

## Spark-Discharge as a Nanoparticle Source to Study Size-Dependent Plasmonic Properties for Photo-electrochemical Water Splitting

Valenti, Marco

**DOI**

[10.4233/uuid:61465ddb-e02e-48a6-969e-5c5c90319d67](https://doi.org/10.4233/uuid:61465ddb-e02e-48a6-969e-5c5c90319d67)

**Publication date**

2018

**Document Version**

Final published version

**Citation (APA)**

Valenti, M. (2018). *Spark-Discharge as a Nanoparticle Source to Study Size-Dependent Plasmonic Properties for Photo-electrochemical Water Splitting*. <https://doi.org/10.4233/uuid:61465ddb-e02e-48a6-969e-5c5c90319d67>

**Important note**

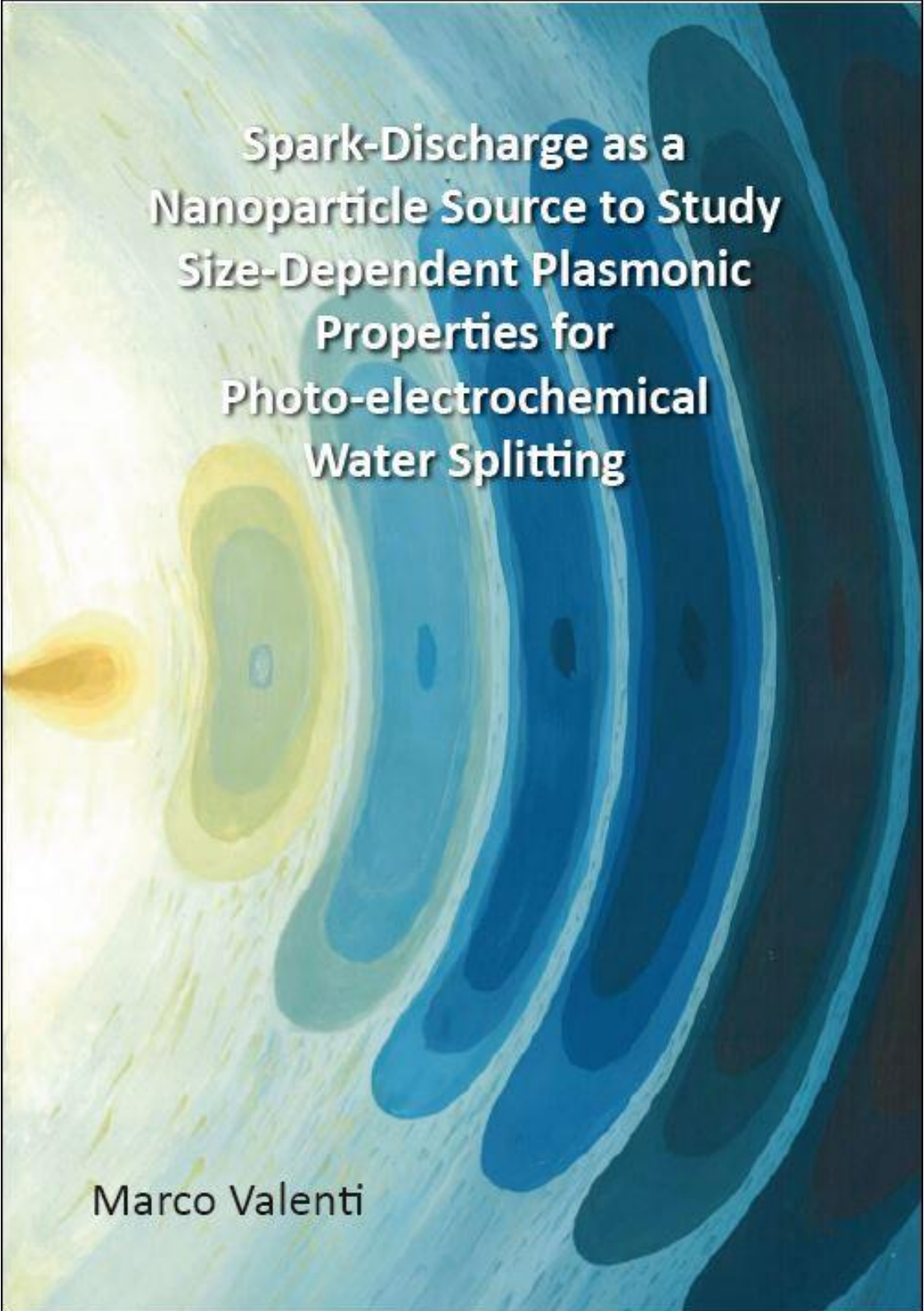
To cite this publication, please use the final published version (if applicable). Please check the document version above.

**Copyright**

Other than for strictly personal use, it is not permitted to download, forward or distribute the text or part of it, without the consent of the author(s) and/or copyright holder(s), unless the work is under an open content license such as Creative Commons.

**Takedown policy**

Please contact us and provide details if you believe this document breaches copyrights. We will remove access to the work immediately and investigate your claim.



**Spark-Discharge as a  
Nanoparticle Source to Study  
Size-Dependent Plasmonic  
Properties for  
Photo-electrochemical  
Water Splitting**

Marco Valenti

# Spark-Discharge as a Nanoparticle Source to Study Size-Dependent Plasmonic Properties for Photo-electrochemical Water Splitting

Dissertation

for the purpose of obtaining the degree of doctor at Delft University of Technology  
by the authority of the Rector Magnificus [prof.dr.ir. T.H.J.J. van der Hagen](#)  
chair of the Board for Doctorates to be defended publicly on  
[Monday 4 June 2018](#) at 12:30 o'clock

by

[Marco VALENTI](#)

[Master of Science / Chemical Engineering, Delft University of Technology, The Netherlands](#)  
born in [Medellin, Colombia](#)

This dissertation has been approved by the promotor.

Composition of the doctoral committee:

Rector Magnificus, chairperson

Prof. dr. A. Schmidt-Ott

Delft University of Technology, promotor

Dr. W. Smith

Delft University of Technology, promotor

Prof. dr. G. Biskos,

The Cyprus Institute, copromotor

Independent members:

Prof. dr. ir. R. van Ommen

Delft University of Technology

Prof. dr. S. Linic

University of Michigan

Prof. dr. E. Garnett

AMOLF

Prof. dr. J. Yeo Boon Siang

National university of Singapore

Prof. dr. F. Mulder

Delft University of Technology, reserve member

Front and back cover by: Nejra Causevic

ISBN number: 978-94-6332-370-3

This research was funded by the NWO-NANO project (11521)



To my parents

Summary .....	5
Samenvatting.....	7
1. Introduction.....	9
2. The electrospray filter for aerosol NP collection into liquid solutions and other nanoparticle immobilization techniques .....	20
3. Plasmonic Nanoparticle-Semiconductor Composites for Efficient Solar Water Splitting (Literature review).....	44
4. Hot Carrier Generation and Extraction of Plasmonic Alloy Nanoparticles .....	100
5. Surface-Induced vs. Phonon-Induced Intraband Excitations for Hot Electron Applications.....	123
6. The Role of Size and Dimerization of Decorating Plasmonic Silver Nanoparticles on the Photoelectrochemical Solar Water Splitting Performance of BiVO <sub>4</sub> Photoanodes.....	143
7. Enhancement of the Photoelectrochemical Performance of CuWO <sub>4</sub> Thin Films for Solar Water Splitting by Plasmonic Nanoparticle Functionalization.....	175
8. Conclusions.....	211
9. List of publications.....	213

## Summary

This work exploits the ability of the spark discharge particle generator (SDG) to produce metallic nanoparticles (NPs) with control over the size, shape and composition, to unravel the plasmonic mechanisms by which NPs can enhance the photoelectrochemical performance of semiconductor photoanodes. Chapter 1 gives an overview of the SDG and the aerosol technology used in this thesis to synthesize the NPs. Chapter 2 summarizes the different aerosol NP immobilization techniques (both on solids and in liquids) and introduces for the first time an electrospray technique to efficiently capture neutral NPs in liquids. In chapter 3, an extensive literature review on plasmonic photoelectrocatalysis is given to introduce the plasmonic mechanisms that are experimentally studied in Chapter 4, 5, 6 and 7. Chapter 4 and 5 are dedicated to study the hot electron injection (HEI) mechanism by which plasmonic NPs create light-induced “hot” charge carriers upon illumination that can drive photoelectrochemical reactions. Chapter 4 reveals that alloying Ag NPs with Au can be used to shift in a control way the absorption and utilization of light to longer wavelengths. However, due to the low interband energy of Au (i.e., 2.3 eV) compared to that of Ag (i.e., 3.6 eV), the alloy NPs exhibited more interband excitations when illuminated with visible light than pure Ag NPs. Such increase in interband excitations resulted in lower hot electron energies and HEI efficiencies in the alloy NPs than in pure Ag NPs. Chapter 5, reveals the HEI size dependency of Ag NPs. It is found that smaller NPs (< 10 nm) where the surface-induced excitations are prominent result in higher HEI efficiencies, while for larger light absorbing NPs (in the range 10-25 nm) a maximum in the performance is found that corresponds well with the size of the Ag NP with the largest nearfield enhancement. Chapter 6, studies the ability of Ag NPs to concentrate and scatter light into thin film semiconductors to enhance their absorption. It is found that most of the solar energy absorbed by pure 15 nm Ag NPs is lost through heat dissipation. However, larger NPs preferentially scatter the incoming light to the neighbour

semiconductor, improving its absorption above their band gap energy. Finally, two configurations of plasmonic NP/semiconductor composites were studied to enhance the semiconductor absorption. In the first configuration the NPs were placed at the semiconductor-electrolyte interface and in the second configuration, the NPs were embedded in the semiconductor at the back-contact/semiconductor interface. It was found that an absorption enhancement at the semiconductor/electrolyte interface was better utilized due to the ability of the surface charge layer to efficiently separate the extra electron holes induced by the plasmonic NPs.

## Samenvatting

Dit werk exploiteert de mogelijkheid van de spark discharge particle generator (SDG) om metallische nanodeeltjes (NDs) te produceren met de mogelijkheid om grootte, vorm, en compositie te controleren. Dit geeft de mogelijkheid om de plasmonische mechanismes die de fotoelektrochemische prestaties van halfgeleider fotoanodes te onderzoeken. Hoofdstuk 1 geeft een overzicht van de SDG en de aerosol technologieën die in deze thesis zijn gebruikt om de NDs te produceren. Hoofdstuk 2 vat de verschillende aerosol ND-immobilisatie technieken (zowel op vaste stoffen als vloeistoffen) samen en introduceert voor het eerst een elektro spray techniek voor de efficiënte afvang van neutrale NDs in vloeistoffen. In hoofdstuk 3, wordt een uitgebreid literatuuronderzoek over plasmonische fotoelektrocatalyse gegeven om de plasmonische mechanismen die experimenteel worden onderzocht in hoofdstuk 4, 5, 6, en 7 te introduceren. Hoofdstuk 4 en 5 zijn gewijd aan de studie van hete elektron injectie (HEI) mechanisme waarbij plasmonische NDs door blootstelling aan licht “hete” ladingdragers creëren die vervolgens fotoelektrochemische reacties kunnen aandrijven. Hoofdstuk 4 laat zien dat het legeren van Ag NDs met Au gebruikt kan worden om op een gecontroleerde manier de absorptie en het gebruik van licht naar langere golflengtes te verplaatsen. Echter, door de lage interband energie van Au (2.3 eV) in vergelijking met die van Ag (3.6 eV), laten de gelegeerde NDs meer interband excitaties zien dan puur Ag NDs bij blootstelling aan zichtbaar licht. Toenames van interband excitaties resulteert in lagere hete elektron energieën, en lagere HEI efficiënties in gelegeerde NDs dan in puur Ag NDs. In hoofdstuk 5 wordt de relatie tussen de HEI en de grootte van Ag NDs aangetoond. Er wordt geconstateerd dat kleinere NDs (< 10 nm) waar oppervlakte geïnduceerde excitaties prominent zijn resulteert in hogere HEI efficiënties, terwijl voor grotere licht absorberende NDs (tussen de 10 en de 25 nm) er een maximum is dat overeenkomt met de grootte waarbij de “near field enhancement” het grootst is. Hoofdstuk 6 bestudeert het vermogen van Ag NDs om licht te concentreren en te verstrooien in dunne-film halfgeleiders waardoor de absorptie verbeterd wordt. Er wordt vastgesteld dat het grootste deel van de zonne-energie geabsorbeerd door Ag NDs van 15 nm verloren wordt door warmte dissipatie. Echter, grotere NDs prefereren om licht te verstrooien richting de aanliggende halfgeleider, waarmee ze de absorptie boven de bandkloof verbeteren. Tot slot zijn 2 configuraties van plasmonische NDs/halfgeleiders bestudeerd om halfgeleider absorptie te verbeteren. In de eerste configuratie zijn NDs op het halfgeleider-elektrolyt raakvlak geplaatst en in de tweede configuratie zijn de NDs

ingesloten in de halfgeleider bij het raakvlak tussen de halfgeleider en de back-contact. Het was vastgesteld dat de absorptie verbetering beter werd gebruikt bij het halfgeleider/elektrolyt raakvlak doordat oppervlakte lading efficiënt de extra gegeneerde elektrongaten scheidt.

## 1. Introduction

The spark-discharge particle generator (SDG) has been significantly investigated due to its ability to generate clean nanoparticles (NPs) of extremely flexible compositions and sizes in the gas phase.[1-3] Moreover, when coupled with a sintering oven and a differential mobility analyser (DMA), an aerosol containing spherical NPs of virtually the same size can be obtained.[4] Such an aerosol can be immobilized in a liquid solution or on a solid substrate in order to study the NPs' unique size-dependant optical, electronic and catalytic properties. While in the last years the flexibility and scalability of the SDG has been demonstrated,[1, 3] less efforts have been directed to exploiting the spark flexibility to study fundamental size-dependent NP properties.

In the last decade significant attention has been given to the study of the localized surface plasmon resonance (LSPR) effect in metallic NPs.[5, 6] The LSPR is the light-induced coherent oscillation of the conduction electrons in the metal. Such coupling between light and the conduction electrons allows to confine the light's electric field to subwavelength dimensions.[7] The promise of plasmonics to manipulate light in the nanoscale has brought significant attention for unique applications such as optical cloaking, optical interconnects, super resolution imaging, plasmonic solar cells, and plasmonic photocatalysis, among others.[7] In order to achieve any of these visionary ideas the electronic and optical properties of plasmonic NPs should be elucidated.

One of the most important challenges in plasmonics is to mitigate the energy loss through heat dissipation which limits the utilization of the plasmonic energy in solar cell and photocatalytic devices.[7] The aim of this thesis is to investigate the mechanisms by which the plasmonic energy can be utilized to produce renewable fuels (e.g., hydrogen) in a photoelectrochemical cell. The main asset of this work to elucidate these mechanisms is the ability to synthesize spherical plasmonic NPs of any composition and size. Such control

is of great importance since most plasmonic NP properties (e.g., light absorption and scattering cross sections) are very sensitive to the NP size, shape and composition. The rest of this introduction is dedicated to explaining the working principle of the SDG and the most important techniques to convert the aerosol coming out of the SDG to an aerosol of monodispersed spherical NPs.

### *1.1. Electrical discharge as a nanoparticle source*

Electricity starts flowing between two metals that are separated by a gas gap when a high enough potential difference is applied between them. This is because at a specific potential difference (breakdown voltage) the gas is ionized, forming a plasma between the two electrodes that contains charge carriers and can conduct electricity from the negatively charged electrode (cathode) to the positively charged electrode (anode). If the potential difference is sustained with a power supply, the ionization and current between the two electrodes is also sustained and this continuous process is called an arc discharge. On the other hand, if the potential difference is applied up to the breakdown voltage but not sustained, the electrodes' potentials readily equalize upon ionization and the process is called a spark discharge. During both processes, electrons and positively charged ions collide with the anode and cathode, respectively. These collisions and the high plasma temperature (up to tens of thousands K) result in ablation of the metallic electrodes, creating a vapour cloud of electrode atoms. If an inert gas carrier flow (e.g., N<sub>2</sub>) is passed in between the gap, the vapour rapidly cools down, forcing supersaturation and subsequent condensation into atomic clusters (< 1 nm). These particles rapidly collide with one another forming bigger aggregates through a coalescence process.[1, 2] The size and shape of these aggregates (or "singlets if round") depend on the material, cooling rate and vapour concentration.[1, 2] While in the arc discharge the cooling rate and vapour concentration can only be tuned through the gas composition, gas flow rate and the



electrode spacing, inducing repetitive spark discharges allows for further tunability (i.e., spark frequency)[8] and a faster cooling, which favours smaller round aggregates (singlets). Nevertheless, for both cases (arc and spark), when the gas flow has been cooled down to approximately room temperature, the aggregates eventually agglomerate to form bigger fractal NPs. In these agglomerates the building blocks are aggregates held together by van der Waals forces.[3] The entire aerosol formation process in an arc discharge or a spark discharge is summarized in Figure 1.

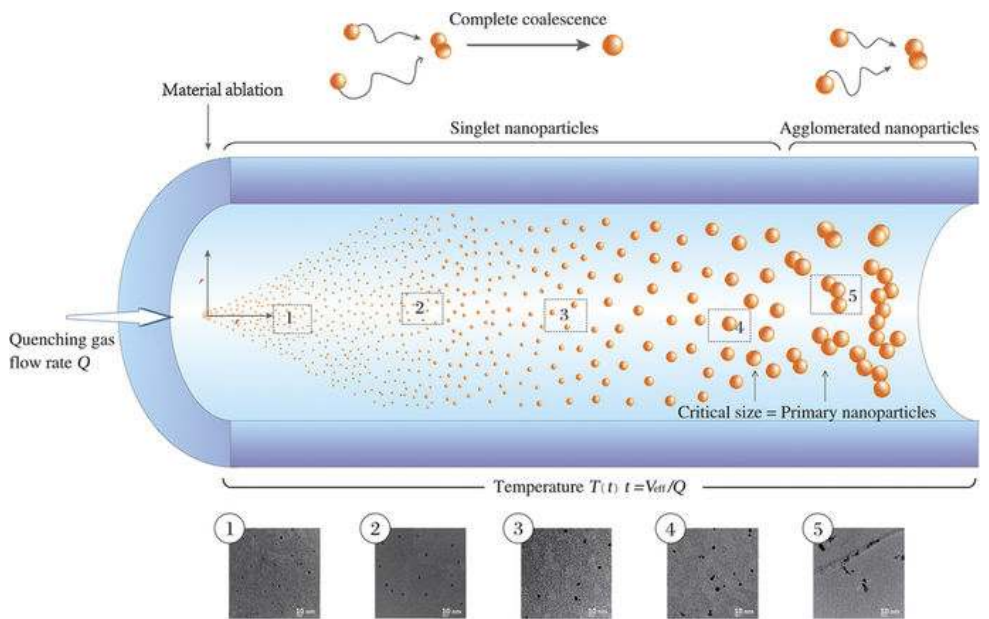


Figure 1. Illustration of formation of singlets and agglomerates in a gas flow due to material ablation at atmospheric conditions. Reprinted with permission from ref. [1]. Copyright 2015, Rights Managed by Nature Publishing Group.

### 1.2. Spark-discharge particle generator (SDG)

Inducing spark discharges at high frequencies results in smaller aggregates and agglomerates than a continuous arc discharge. The spark-discharge particle generator (SDG) is a device that can induce sparks with control over the spark frequency for the generation of size-tunable NPs.[9] A classical SDG consists of a current source, a capacitor and two electrodes with a gas gap, as shown in Figure 2. This way, the capacitor can be charged in a controlled way, up to the discharge voltage to induce the spark. After the spark occurs the capacitor is fully discharged and the process repeats itself with the applied current ( $I$ ) defining the spark frequency ( $f$ ) when the capacitance ( $C$ ) and the spark voltage ( $V$ ) are fixed:

$$f = \frac{I}{CV} \quad (1)$$

The spark voltage (voltage at which the spark is initiated) is in the vicinity of the breakdown voltage and can be monitored with an oscilloscope.

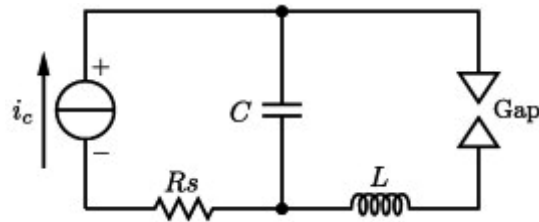


Figure 2. Typical electrical circuit of a SDG

### 1.2.1. Nanoparticle size

The mean size ( $d$ ) of the NPs produced by the SDG depend on the operational SDG parameters as follows:[1]

$$d = \left( \frac{3\beta VC(E-E_0)f}{\rho\pi Q^2} \right)^{1/3} \quad (2)$$

where,  $\beta$  is the coagulation kernel,  $E$  the spark energy,  $E_0$  is the minimum spark energy for producing particles,  $\rho$  is the metal density and  $Q$  is the gas flow rate. The spark energy ( $E$ ) is given by:

$$E = \frac{1}{2}(CV^2) \quad (3)$$

and an estimation of  $\beta$  and  $E_0$  can be obtained from theory, which is discussed elsewhere.[1]

The above formula assumes full coalescence of the NPs upon collision, however at room temperature, depending on the composition, the NPs reach a critical size ( $\sim 5$  nm for Au) from which full coalescence does not occur and agglomerates of NPs with the critical size start forming (Cf. Figure 1). Therefore, Equation 2 can predict the singlets mean size up to the critical size when operated at room temperature. If spherical NPs with a larger NP size are needed, two approaches can be undertaken: (i) the SDG can be heated up to ensure full aggregate coalescence or (ii) agglomeration can be allowed to form large fractal-like NPs, which can be subsequently sintered into spherical NPs in a tube oven. Even though for the former case (i.e., i) Equation 2 can be applied to predict the mean NP diameter, for

both cases the standard deviation of the resulting size distribution is too broad for studying fundamental size-dependant NP properties. Therefore, in order to achieve a monodisperse aerosol, the aerosol coming out of the SDG can be size-selected with great precision directly in the gas phase with a differential mobility analyser (DMA) device, which is discussed in section 1.3.

### *1.2.2. Nanoparticle composition*

If two electrodes of the same composition are used in the SDG, the NPs composition is expected to be the same as that of the electrodes (Figure 3A). However, the SDG can also be operated to induce sparks between two electrodes of different compositions (Figure 3B). The vapours of both electrodes are then mixed and the fast cooling of the spark allows them to condense into NPs with an inter- and intra-particle composition distribution.[10] Therefore, using two electrodes of different compositions allows to mix materials in the nanometre scale and/or atomic scale. Due to the fast quenching of the mixed vapours, NPs with atomically mixed regions are obtained even for immiscible metals by using the configuration shown in Figure 3B.

For applications where is desirable to mix nanoparticles only in the nanoscale, two SDG producing NPs with well-defined compositions and size can be mixed in the gas face where the nanomixing takes place through the agglomeration process as depicted in Figure 3C.

The ability to deliberately alternate (i) between atomic mixing (Figure 3A or Figure 3B) and nano-mixing (Figure 3C) is of particular importance to elucidate and discover complex active sites in catalysis.

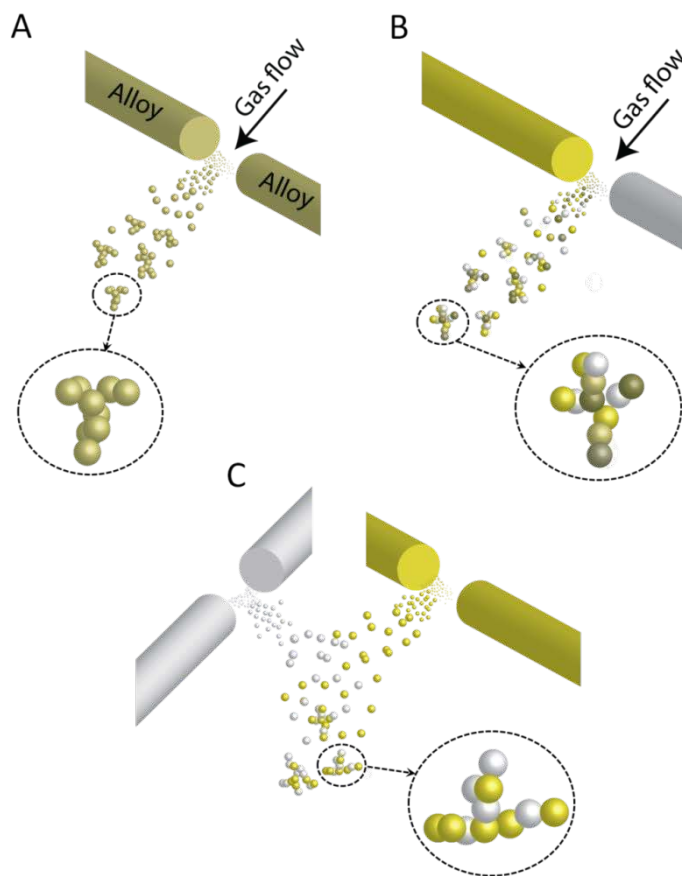


Figure 3. Illustration of three spark configurations. A) Depicts spark ablation between two electrodes of the same composition that produce alloy NPs of the same composition than that of the electrodes. B) Depicts spark ablation between electrodes of two different materials to make alloy NPs with a distribution of compositions. C) Shows that aerosols coming from two different sparks can be mixed to generate agglomerates composed of NPs with two well defined compositions.

### 1.3. Differential mobility analyser

Under atmospheric conditions, the aggregates and agglomerates exiting the SDG have a size distribution that can range from atomic clusters to agglomerates of a few hundreds of nanometres according to the SDG parameters (e.g., gas flow, spark frequency, spark chamber volume etc.).[8] For applications where spherical NPs are needed, the agglomerates can be passed through a tube oven where they can be sintered into spherical NPs. Since a fraction of the NPs exiting the SDG (with diameter smaller than 100 nm) are singly charged, the charged population of spherical NPs of a specific size have a well-defined electrical mobility ( $Z$ ) that is given by the following equation:[11]

$$Z_{NP} = \frac{neC_c}{3\pi\eta d} \quad (4)$$

Where,  $n$  is the number of charges in the NP,  $e$  is the electron charge,  $\eta$  is the gas viscosity,  $d$  is the particle diameter, and  $C_c$  is the Cunningham slip correction factor:

$$C_c = 1 + \frac{\lambda}{d} \left( 2.51 + 0.8e^{-0.55\frac{d}{\lambda}} \right) \quad (5)$$

where,  $\lambda$  is the gas mean free path.

A differential mobility analyser (DMA) is a device that can accurately separate particles of a predefined electrical mobility from a polydispersed aerosol. A classical DMA diagram is shown in Figure 4. When a potential difference ( $V$ ) is applied between the DMA inner electrode rod and outer grounded cylinder, the DMA will deflect to the monodisperse slit only the NP with the opposite polarity that have the following electrical mobility:[4]

$$Z_{DMA} = \frac{Q_{sh}}{2\pi VL} \ln \frac{R_2}{R_1} \quad (6)$$

where,  $Q_{sh}$  is the sheath flow rate,  $L$  is the distance between the polydispersed aerosol inlet and monodispersed aerosol outlet, and  $R_1$  and  $R_2$  are the inner and outer electrode radii, respectively.

If the polydisperse NPs entering the DMA are spherical and singly charged, the DMA voltage ( $V$  in Equation 6) can be tuned to match the electrical mobility of a desired NP size given by equation 4. This way the DMA is an ideal tool to size-select spark-made NPs to obtain monodisperse aerosols of pure NPs that can be immobilized to study their size-dependent properties.

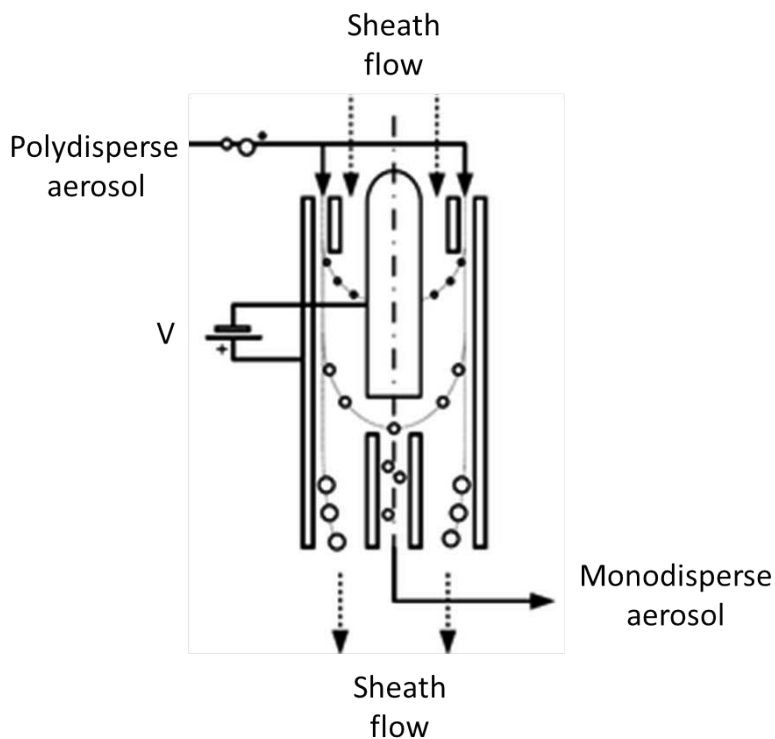


Figure 4. Illustration of a differential mobility analyser

#### 1.4. Thesis outline

In this chapter, the synthesis of tailor-made aerosol metallic NPs with the SDG was discussed. In the chapter 2, the most common NP deposition techniques that allow the immobilization of well-defined monodispersed aerosols in a liquid or on a solid surface are presented, along with the electrospray deposition technique that was developed during this PhD work and introduced for the first time in this thesis.



The third chapter is an extensive literature review that discusses the four mechanisms by which the plasmonic energy in metallic NPs can be utilized, namely, (i) hot electron injection (HEI), (ii) plasmon-induced resonance energy transfer (PIRET), (iii) light scattering, and (iv) light concentration. Chapters 4 and 5 study the role of the composition and size of the NPs on the HEI efficiency, respectively. Chapter 6 studies the light concentration and the light scattering mechanisms, and Chapter 7 studies two important plasmonic NP/semiconductor composite configurations to best exploit the light scattering and concentration mechanisms. Finally, the main conclusions of the experimental work of this thesis is presented in Chapter 8.

## **2. The electrospray filter for aerosol NP collection into liquid solutions and other nanoparticle immobilization techniques**

### Abstract

Well-defined aerosol nanoparticles (NPs) are immobilized in liquid solutions or on solid substrates to study their size-dependent properties or for its integration into a final product (e.g., plasmonic sensor, catalyst or solar cell). This chapter introduces the most common NP immobilization techniques and discusses their size-dependent immobilization/capturing efficiencies. Within this chapter a new electrospray immobilization technique is introduced and characterized. The technique consists on passing an aerosol of metallic NPs through a shower of highly charged micro-droplets generated by an electrospray. It is found that the charged microdroplets can capture neutral aerosol NPs due to attractive image forces. This immobilization technique is more efficient than the standard bubbling technique for NPs with small diffusion coefficients (e.g., spherical NPs larger than  $\sim 20$  nm).

## *2.1. Introduction*

Metallic NPs have unique size-dependent electrical, catalytic and optical properties that makes them promising components for a variety of applications. Generating NPs with control over the size, shape and composition to study such NP properties is possible with liquid chemistry methods[12] and with aerosol technology.[3] Liquid chemistry methods have being extensively investigated and allows the synthesis of metallic NPs with striking geometries such as NP stars, triangles and rods (with control over its diameter and length), which have important optical and catalytic properties. However, the synthesis of NP with different features (e.g., composition and size) require different reactants, surfactants and by-products that need to be removed after the synthesis to be able to study the NP properties. The removal of these chemical impurities is especially important for biological analysis applications and for NP toxicity studies. Therefore, in order to study the size-dependant and composition-dependant properties of NPs made with liquid chemistry methods, different purification techniques must be developed and optimized for each composition and NP size. Aerosol technology offers a more elegant techniques to produce pure spherical NPs of any size and composition to study their size-dependant and composition-dependant properties (Cf. Chapter 1). An important step after the generation of a well-defined monodispersed aerosol is the immobilization of the aerosol NPs on a solid substrate or in a liquid solution. This chapter gives an overview of the most important NP immobilization techniques and introduces a new technique to transfer aerosol nanoparticles into a liquid, where the nanoparticles are directly captured by highly charged micro droplets in an electrospray (ES) filter.

## 2.2. Immobilization techniques

The size-dependent optical, catalytic and toxicity properties of NPs are prominent for sizes smaller than approximately 100 nm. Therefore, to study these properties, techniques that can efficiently immobilize aerosol NPs in this size range are needed. In order to immobilize the aerosol NPs coming out of the SDG or DMA on a solid substrate or in a liquid, the NPs need to be deflected from the gas streamlines to contact the gas/solid or gas/liquid interface. Due to the low NP mass, gravitational and inertial forces will not significantly affect the NP trajectory. However, if the NP has a charge, electrostatic forces can efficiently bring the NP to the interface. Another alternative is to rely on the NP diffusion, where the NPs deviate from the streamlines due to their Brownian motion and contact the interface. In the following subsections techniques to immobilize NPs on solid substrates and in liquids are discussed.

### 2.2.1. Immobilization techniques on solid substrates

#### 2.2.1.1. NP deposition by electrostatic forces

Charged aerosol NPs can be attracted to a metallic or semiconducting substrate by an electric field. If a potential difference is applied between two electrodes, the terminal electrical velocity ( $V_{TE}$ ) induced to a charged NP flowing in between the electrodes is the product between its electrical mobility and the field strength (E):[11]

$$V_{TE} = Z_{NP}E \quad (7)$$

Replacing the electrical mobility for that of spherical NPs (Equation 4), the terminal electrical velocity yields:

$$V_{TE} = \frac{neEC_c}{3\pi\eta d} \quad (8)$$

The electric field strength (E) is defined by:

$$E = \frac{\Delta W}{\Delta X} \quad (9)$$

Where  $\Delta W$  is the potential difference between the electrodes and  $\Delta X$  is the distance between them.

In a horizontal electrostatic precipitator depicted in Figure 5, singly charged NPs of the same size are attracted to the oppositely charged electrode. The NPs that reach the electrode substrate adhere to it by van der Waals forces. As shown in the same figure, NPs having a terminal velocity larger than  $HV_x/L$  will be deposited on the substrate with 100 % efficiency.[11] As long as the NPs are at least singly charged, 100 % deposition efficiency can be obtained on a substrate with length (L) of a few cm by increasing the potential difference between the electrodes ( $\Delta W$ ). The spatial distribution of the deposited NPs can be manipulated by using electrostatic precipitators with different geometries. In this thesis (Chapter 4,5,6 and 7) metallic NPs were deposited with an electrostatic precipitator where the incoming aerosol flow is perpendicular to the substrate, obtaining a nearly homogeneous spatial distribution of NPs on the substrate surface.

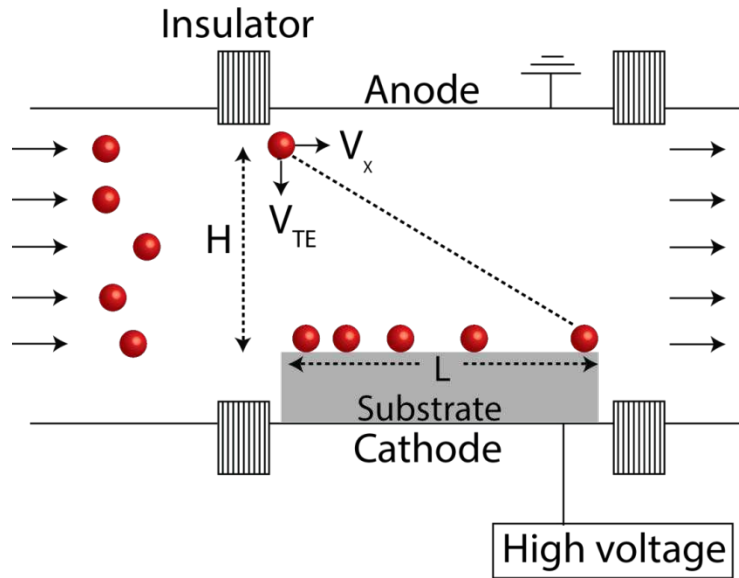


Figure 5. Illustration of the deposition of singly charged aerosol NPs on a flat metallic substrate with a horizontal electrostatic precipitator.

#### 2.2.1.2. NP deposition by diffusion

Aerosol NPs smaller than 100 nm in size significantly deviate from the aerosol gas streamlines due to their Brownian motion. Due to this deviation the NP can contact and adhere to a substrate, leaving the aerosol flow. When an aerosol is passed through a tube or rectangular channel the deposition efficiency  $E_d$  (fraction of entering NPs that deposit on the walls by diffusion) is given by the following simplified expressions (Equation 10 and 11)[11] as a function of the dimensionless deposition parameter  $\mu = \frac{DL}{Q}$ , where  $D$ ,  $L$  and  $Q$  are the aerosol particle diffusion coefficient (Equation 12), tube/channel length and aerosol flow rate, respectively.

$$E_d = -5.5\mu^{\frac{2}{3}} + 3.77\mu \quad \text{for} \quad \mu < 0.007 \quad (10)$$

$$E_d = 1 - 0.819 \exp(-11.5\mu) + 0.0975 \exp(-70.1\mu) + 0.0325 \exp(-179\mu) \quad \text{for} \quad \mu > 0.007 \quad (11)$$

$$D_p = \frac{kTC}{3\pi\eta d} \quad (12)$$

This type of deposition is also present in the piping between the NP source and the deposition chamber, which represents a loss of NPs to the pipe walls. In order to effectively deposit NPs on a substrate by diffusion, the aerosol flow can be forced to pass through a porous substrate with smaller (parallel) channels, which will significantly increase the deposition parameter  $\mu$  (through smaller Q per channel) and allow the complete deposition of the NPs in the substrate by diffusion (Equations 10 and 11). The density of NPs as a function of the channels' length (L) can be tuned by tuning the flow rate, channel dimensions and number of parallel channels of the substrate.

## 2.2.2. Immobilization techniques in liquid solutions

### 2.2.2.1. Bubble column

Separation of NPs from the gas phase to the liquid phase in bubble columns has been investigated mainly for gas cleaning purposes.[13] Diffusion is the main mechanism by

which the NPs reach the gas-liquid interface and are incorporated in the liquid phase.[13] Therefore, the NP concentration in the gas phase decreases exponentially with the residence time of the bubble in the column  $t_r = (z/v_B)$ , where  $z$  is the bubble column height and  $v_B$  is the bubble velocity. The circulation of gas inside the rising bubble (i.e., Hill's vortex) determines the streamline pattern inside the bubble and, therefore, the distance the NPs will approach the gas-liquid interface by convection.[14] The NPs will then be transported by diffusion to the gas-liquid interface from the gas streamlines at the equatorial region, which are the closest to the interface (Figure 6). These phenomena are captured by the Fochs' model[14] that predicts the NP capturing efficiency as a function of the bubble residence time ( $t_r$ ):

$$E = 1 - \exp(-\alpha_D t_r) \quad (13)$$

Where  $\alpha_D$  is the coefficient of diffusional deposition:

$$\alpha_D = 1.8 \sqrt{\frac{D_p v_{rel}}{r_B^3}} \quad (14)$$

Where  $v_{rel}$  is the relative rise velocity of the bubble with respect to the velocity of the liquid and  $r_B$  is the bubble radius.



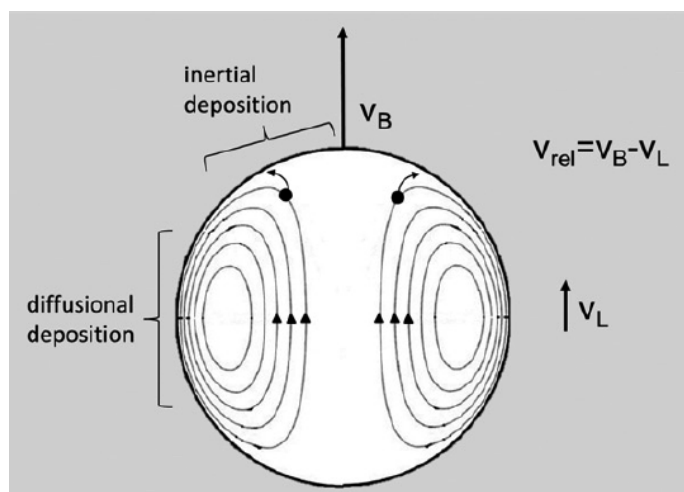


Figure 6. Internal circulation inside a rising gas bubble. Reprinted with permission from ref. [13]. Copyright 2012 Elsevier Ltd.

This model has been verified experimentally and typical column lengths of  $\sim 1$  meter are necessary to capture all NPs of  $\sim 10$  nm.[13] For gas cleaning purposes, increasing the column height to increase the NP capturing is possible. However, if the bubble column technique is used for sampling well-defined NP to subsequently study their size-dependent properties (e.g., toxicity), increasing the column height would dilute the resulting colloidal solution too much for their study. Therefore, in order to increase the efficiency in shorter columns, the bubble size should be decreased by, for example, breaking the bubbles with a sonicator. However, in order to efficiently capture larger NPs  $\sim 90$  nm that have a smaller diffusion coefficient in a small liquid volume, we introduce a new capturing technique in the following chapter.

### *2.3. The electrospray filter for aerosol NP collection into liquid solutions*

Hereby, it is demonstrated that neutral aerosol NPs can be efficiently captured into liquid solutions by passing the aerosol through a cloud of highly charged microdroplets. Such a cloud is created here with an electrospray (ES) device. In this subchapter, the ES principles are introduced, followed by a description of the ES device used in this work, which was designed to capture aerosol NPs into a liquid solution. Subsequently, an overview of the theoretical mechanisms by which the charged microdroplets can capture aerosol NPs are discussed. Finally, the experimental set-up used to measure the ES capturing efficiencies is described and the results are discussed and compared with other existing NP capturing techniques.

#### *2.3.1. Electrospray*

An electrospray device uses electrical forces to induce a liquid jet to break into a spray of highly charged microdroplets (electrospray). In a typical electrospray device a potential difference is applied between a nozzle and a grounded counter electrode as shown in Figure 7. When a liquid flow is forced through the nozzle, different spray modes can be formed according to the strength of the electric stress, surface tension stress and the kinetic energy of the liquid. The objective of most electrospray devices is to deliver the liquid to a target (counter electrode) in a controlled way (e.g., ink-jet printing). However, electrospray has also been used to capture microparticles, mainly for gas cleaning purposes. To the best of our knowledge, electrospray has not yet being used to capture NPs to form a colloid. The main objective of this subchapter is to characterize an electrospray device for its ability to capture aerosol NPs into liquid solutions.

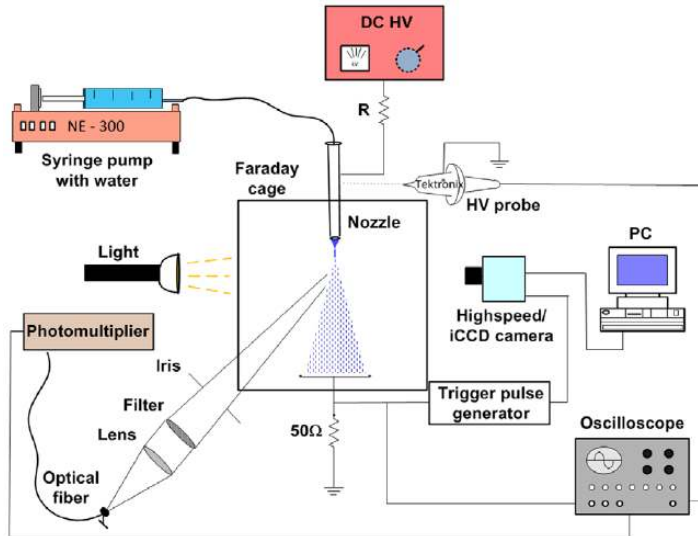


Figure 7. Electro spray set-up with typical equipment used to measure the electro spray properties (e.g., current, droplet size).

The most studied electro spray mode is the cone-jet mode in which the electric field is strong enough to deform a droplet at the end of a capillary tube into a conical shape Taylor cone (Figure 8). At the cone apex a liquid jet emerges, breaking into a spray of highly charged droplets with a narrow size distribution. For a certain liquid there is a minimum flow rate ( $Q_{min}$ ) at which it can be sprayed in this mode:[15]

$$Q_{min} \sim \frac{\epsilon_r \epsilon_0 \gamma}{K \rho} \quad (15)$$

Where,  $\varepsilon_r$  and  $\varepsilon_0$  are the relative dielectric constant of the liquid and the dielectric constant of vacuum, respectively.  $\gamma$ ,  $K$  and  $\rho$  are the liquid surface tension, the liquid conductivity and the density of the liquid, respectively.

In the cone-jet mode, properties like the mean droplet ( $a_d$ ) size and the current ( $I$ ) can be estimated:[16]

$$a_d = C_d \cdot \left( \frac{\rho \cdot \varepsilon_0 \cdot Q_L^4}{I^2} \right)^{\frac{1}{6}} \quad (16)$$

$$I = b \cdot (\gamma \cdot K \cdot Q_L)^a \quad (17)$$

Here,  $C_d$  is a constant equal to two,  $a$  and  $b$  are constants equal to 0.5 and 2.17.

Another important property of the cone-jet mode ES is the droplet charge, which for high applied potentials is close to its fundamental charge limit (Rayleigh limit) before disintegration of the droplet.[17] The fundamental charge limit ( $Q_{RL}$ ) is a function of the droplet radius and surface tension of the liquid:[18]

$$Q_{RL} = \pi \sqrt{(8\varepsilon_0 \gamma a_d^3)} \quad (18)$$



Figure 8. electro spray at the cone-jet mode. [19]

### 2.3.2. *Electrospray filter*

The ES device used in this thesis is shown in Figure 9. It consists of a stainless steel cylindrical case with two side gas inlets and one central liquid inlet at the top. The liquid enters at a high voltage through a one meter long cylindrical channel which is insulated from the grounded case. The liquid comes out of the channel through a stainless steel nozzle as an electro spray cloud due to the potential difference between the nozzle and the stainless steel walls of the case. The microdroplets are precipitated onto the grounded walls as shown in the simulation on the right hand side of the same figure (i.e., Figure 9). The simulation was performed using the exact dimensions of the device and typical electro spray parameters ( $\gamma$ ,  $\rho$ ,  $\epsilon_0$ ,  $Q_L$  and applied potential, see appendix 1), similar to the parameters used in this work to characterize the ES as a NP filter. The aerosol flow needs to cross the electro spray cloud before exiting the device 50 mm below the nozzle through

two side gas outlets. The liquid containing the captured NPs is accumulated at the colloidal reservoir at the bottom of the device.

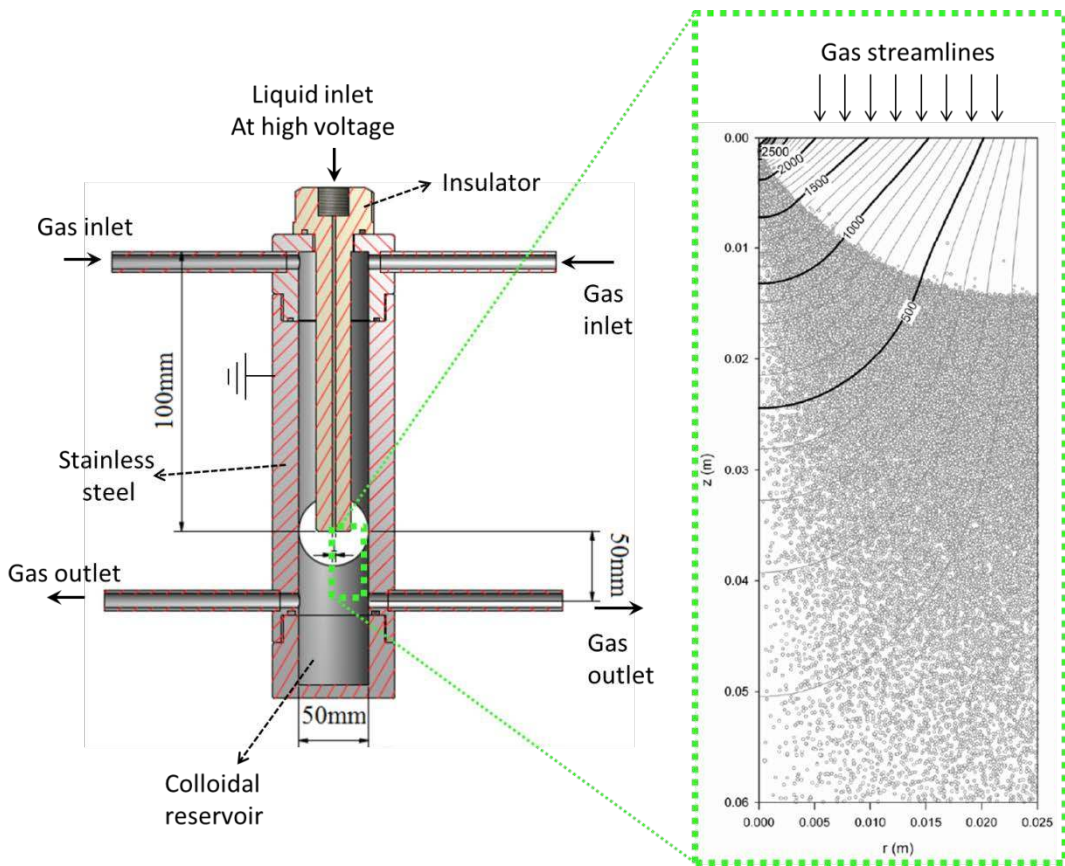


Figure 9. Design of the electro spray NP filter (left) with the simulated droplet spatial distribution (right). The details of the simulation are shown in the appendix 1.

### 2.3.3. Filter model

The theory of submicron particle filtration by spherical collectors is applied here to study the efficiency of the ES filter for capturing particles in the nano range. When the NPs go through the ES curtain, they are collected by the electro spray droplets. According to classical aerosol particle filtration theory, the NP concentration ( $N$ ) drops exponentially along the thickness of a filtering curtain as follows:[20]

$$N = N_{in} e^{-\left(\frac{3\alpha\Sigma\eta}{4a_s}t\right)} \quad (19)$$

where  $N_{in}$  is the initial nanoparticle concentration,  $a_s$  is the droplet radius,  $\alpha$  is the packing density of the filter,  $t$  is the filter thickness and  $\Sigma\eta$  is a sum of single droplet collection efficiencies corresponding to different particle collection mechanisms.

Neutral NPs can be captured on ES droplets mainly by diffusion and by the image force (attracting force between the highly charged droplet and the resulting image in the aerosol NP). Other deposition mechanisms like impaction have a negligible effect, due to the small mass of the NPs. As a result  $\Sigma\eta$  for the case of neutral NPs can be estimated by:

$$\Sigma\eta = \eta_D + \eta_I \quad (20)$$

where  $\eta_D$  and  $\eta_I$  are the single droplet collection efficiency due to diffusion and image force, respectively. These efficiencies can be estimated as follows:[21]

$$\eta_D = 3,97 \left(\frac{D_P}{2a_s U}\right)^{2/3} \quad (21)$$

$$\eta_I = \left(\frac{15\pi}{8} K_P\right)^{0.4} \text{ for } K_P \gg 1 \quad (22)$$

$$\eta_I = 4K_p \quad \text{for } K_p \ll 1 \quad (23)$$

where,  $K_p$  is the dimensionless parameter for image force and is equal to:

$$K_I = \frac{\gamma_p 2Q_d^2 a_p^2 C}{3\varepsilon_0 a_S \mu U} \quad (24)$$

where,  $U$  is the face velocity of the filter,  $Q_d$  is the charge on the droplet,  $\varepsilon_0$  is the permittivity of the free space,  $\mu$  is the dynamic viscosity,  $D_p$  is the particle diffusion coefficient,  $C$  is the slip correction factor,  $\gamma_p$  is the particle polarization coefficient and  $a_p$  is the nanoparticle radius.

Figure 10 shows  $\eta_I$  and  $\eta_D$  (Equation 21 and 22), as a function of the nanoparticle radius using typical ES parameters (e.g. droplet sizes, charges and velocities). Clearly, the image force due to the strong charge on the droplets have single droplets collection efficiencies larger than 1, which means that each droplet can capture NPs that are incident to an area larger than the droplet geometrical cross section. On the other hand, the collection efficiency of the droplets by diffusion is lower than 0.1 for all NP sizes, making its contribution to the overall collection negligible.



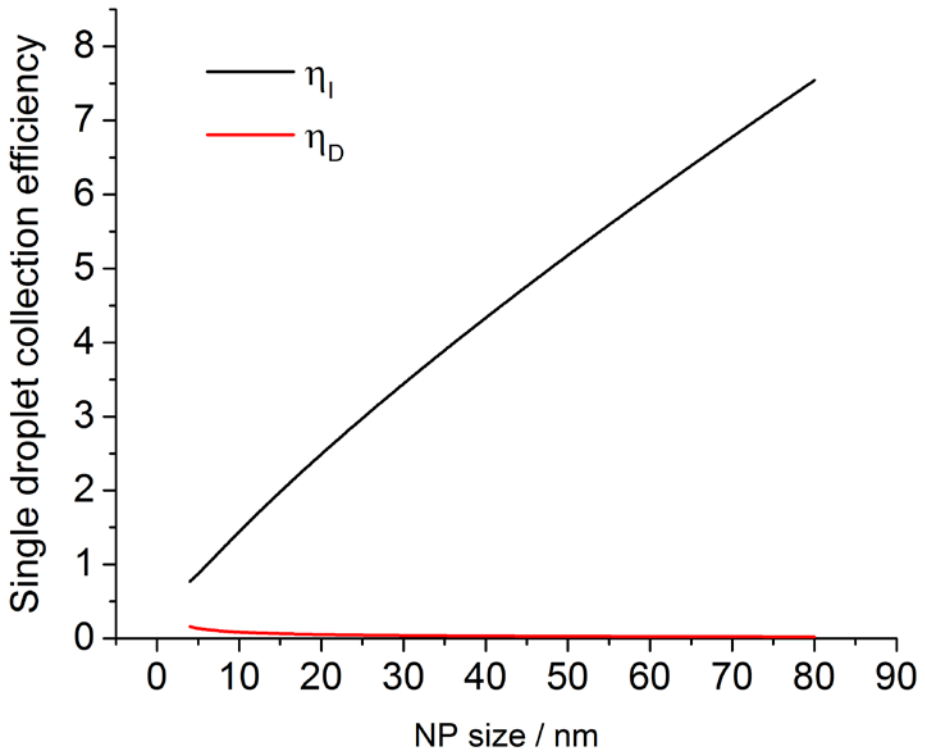


Figure 10. Single droplet collection efficiencies of Au NPs by diffusion and image force, using 1  $\mu\text{m}$  ethanol droplets charged at 80 % of their limit (Rayleigh limit).

In order to calculate the total aerosol NP concentration drop after crossing the ES filter, the packing density of the ES filter (the ratio between the volume of the droplets' and the total filter volume) needs to be defined. The filter volume in which the NP and droplets interact is approximated to be the distance between the nozzle and gas outlet ( $L_F$ ) times the cross sectional area of the filter. On the other hand, the volume of droplets in the filter is the liquid flow rate times the droplets' residence time in the filter volume. This way, the packing density of the ES filter is estimated as follows:

$$\alpha = \frac{V_{droplets}}{V_{filter}} \approx \frac{Q_L \left( \frac{L_F}{U_d} \right)}{\pi r_{ES}^2 L_F} \quad (25)$$

Here,  $Q_L$  is the liquid flow rate fed to the system,  $U_d$  is the droplet velocity and  $r_{ES}$  is the radius of the electro spray cylinder (25 mm). Combining Equations 18 and 24 yields:

$$N = N_{in} e^{-\left( \frac{3Q_L \alpha \Sigma \eta}{8\pi r_{ES}^2 U_d a_s} t \right)} \quad (26)$$

which after rearranging and replacing the filter thickness  $t$  for  $L_F$  yields the capturing efficiency (E) in the ES filter:

$$E = \frac{N_{in} - N_{out}}{N_{in}} \approx 1 - e^{-\left( \frac{3Q_L \alpha \Sigma \eta}{8\pi r_{ES}^2 U_d a_s} L_F \right)} \quad (27)$$

#### 2.3.4. Electro spray filter characterisation

The experimental set-up used to characterize the ES filter is illustrated in Figure 11. Figure 11A shows an overview of the NP synthesis, NP capturing and subsequent counting of the surviving NPs. A close up to the NP synthesis section of the set-up is shown in Figure 11B. The SDG is used as a source of Au NPs and a tube oven is used to sinter the NPs round. In order to test the ES filter ability to capture neutral NPs, the NPs coming out of the tube oven are passed through a neutralizer, which brings the aerosol NPs to the Boltzmann charge distribution (with most of the NPs being neutralized). The small fraction of charged NPs coming out of the neutralizer is completely removed electrostatically and only neutral NPs enter the ES filter. A close up of the characterization section of the set-up is shown in Figure 11C. The surviving neutral NPs coming out of the ES filter are passed through a second neutralizer to singly charge a fraction of the aerosol. A DMA coupled with a

condensation particle counter (CPC) is used to measure the NP concentration of negatively charged NPs as a function of their size.

One of the advantages of the ES filter is that it can be easily turned ON and OFF by either stopping the liquid flow through the nozzle or by turning off the high voltage. This ability of the ES filter to be turned ON and OFF facilitates its characterization, since the NPs captured in the filter can be calculated by subtracting the NPs measured with the CPC when the ES filter is ON from the measured NPs when the filter is OFF. A typical experiment is shown in Figure 11D. In this figure the concentration of NPs measured by the CPC is shown as a function of time. During this experiment the DMA inner rod is left at a constant potential, size-selecting negatively single charged NPs of 30 nm in size. Initially the ES filter is ON and  $\sim 7000$  NPs/cm<sup>3</sup> are measured. Subsequently the ES filter is turned OFF by stopping the liquid flow and the NP concentration raises, reaching a stable concentration of  $\sim 58000$  after  $\sim 100$  seconds. When the filter is turned back ON the concentration drops back to the  $\sim 7000$  NPs/cm<sup>3</sup>, confirming that the NP source (SDG) is producing the same amount of NPs throughout the experiment. The experimental capturing efficiency of the 30 nm NPs can then be calculated as follows:

$$E = \frac{N_{OFF} - N_{ON}}{N_{OFF}} \quad (28)$$

Where,  $N_{OFF}$  is the measured NP concentration when the ES filter is OFF and  $N_{ON}$  is the measured NP concentration when the ES is ON.

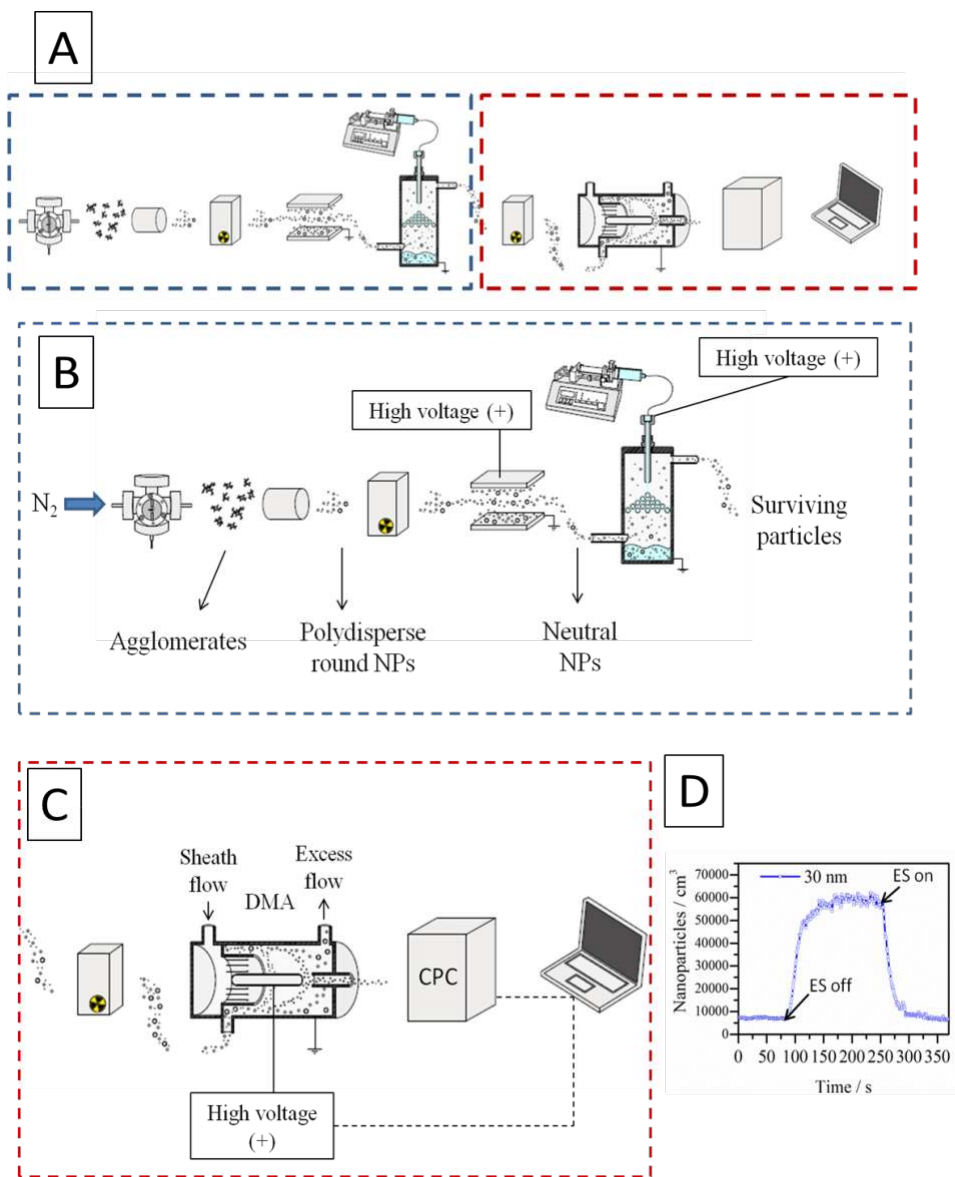


Figure 11. Set-up to measure the neutral aerosol NP capturing efficiency of the ES filter. A) Shows an overview of the set-up, B) Illustrates the NP synthesis and the transferring of the NPs into the liquid phase by the ES filter. C) Illustrates the counting of the surviving NPs as

a function of the NP size. D) Shows a typical experiment that measures the surviving aerosol NPs when the ES filter is ON and OFF.

### 2.3.5. *Results and discussion*

In the experiment shown in Figure 11D, NPs of a range of sizes (8-100 nm) are being captured in the ES filter at the same time, however, each experiment (e.g., Figure 10D) only measures the capturing efficiency of one size by setting the DMA at the corresponding voltage during the measuring of  $N_{OFF}$  and  $N_{ON}$ . The same experiment was repeated at different DMA voltages to obtain the capturing efficiency for all the NP sizes present in the aerosol. Figure 12 shows the capturing efficiency as a function of the NP size for three different applied potentials. Remarkably, nearly all the NPs larger than 40 nm were captured by the ES filter when the largest potential was applied (i.e., 4.5 kV). The obtained colloidal solution collected in the ES reservoir was drop casted onto a TEM grid and inspected by SEM. Figure 13 shows the SEM micrographs and EDS spectrum of the evaporated colloidal solution, which confirms that the spherical Au aerosol NPs were transferred into the liquid solution.

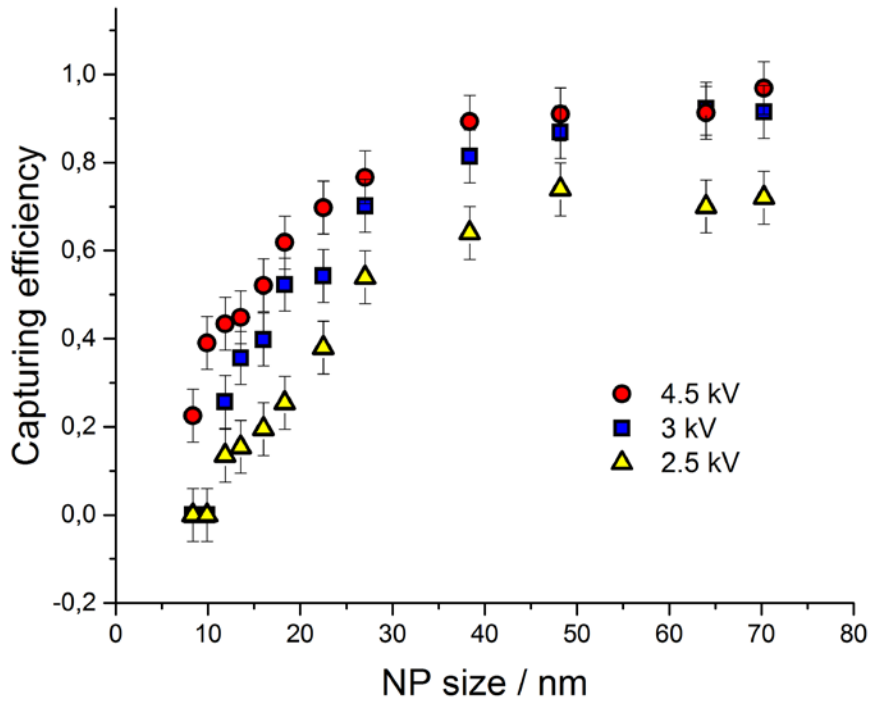


Figure 12. Experimental capturing efficiencies of the ES filter described in section 2.3.2 with the set-up described in section 2.3.4. The three set of experiments were performed at three different needle potentials (2.5, 3 and 4.5 kV) while maintaining the ES case grounded. For all the experiments ethanol was used to feed the ES at a flow rate of 16  $\mu\text{L}/\text{min}$  and  $\text{N}_2$  was used as aerosol medium at a flow rate of 1 L/min containing spark-made neutral spherical Au NPs.

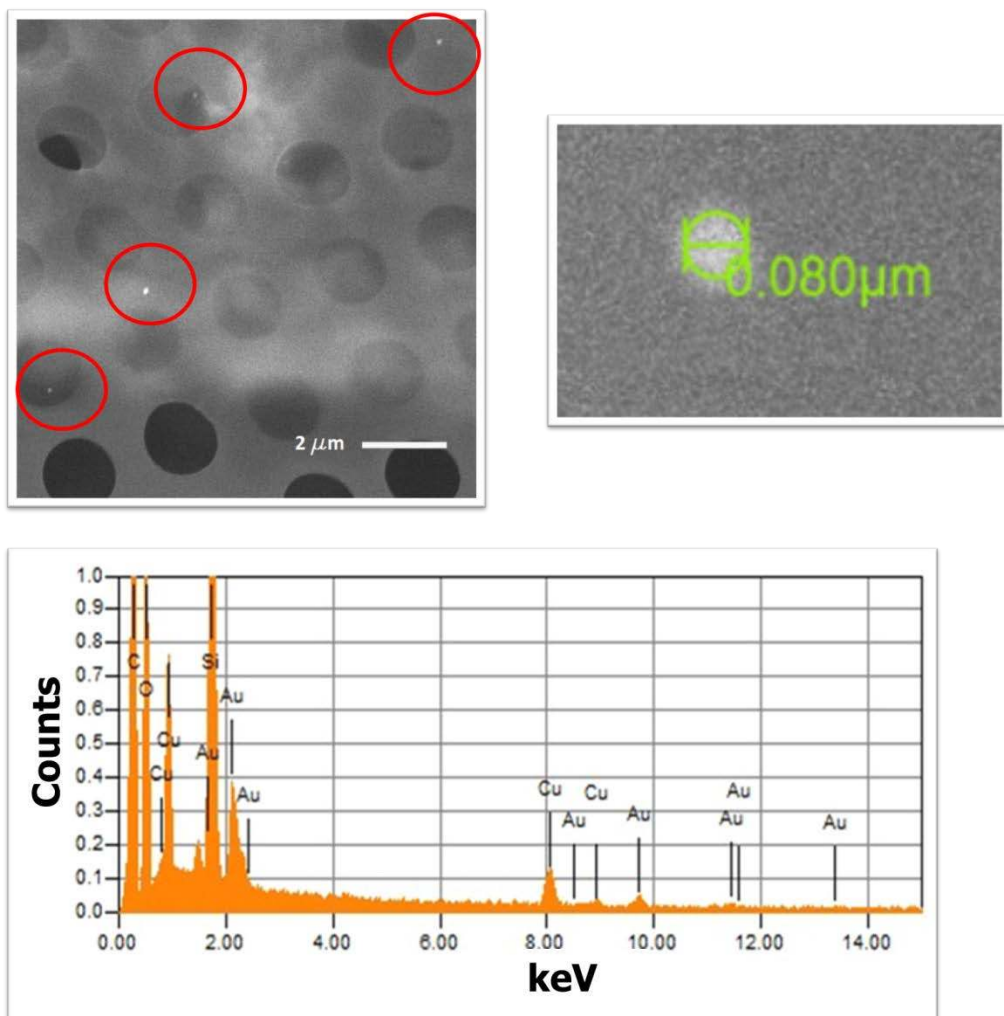


Figure 13. Top: SEM micrographs of a Cu TEM grid onto which a NP colloidal solution obtained with the ES filter was drop casted. Bottom: EDS spectrum of the NPs shown in the top images.

Figure 12 confirms that diffusion does not contribute significantly in the measured capturing efficiencies, since the smallest NP with the largest diffusion coefficient are the least captured for all applied potentials. Instead, the capturing efficiency curves decrease with NP size. This trend can be explained by the image force capturing mechanism, since its single droplet capturing efficiency decreases with the squared of the NP radius (Equations 22, 23 and 24). The capturing efficiency also decrease with decreasing applied voltage. One of the prominent changes in the electrospray when the applied voltage is increased while keeping the liquid flow rate constant is that the droplet size distribution shifts to lower droplet sizes. Here again, the image force is in good agreement with the experimental observation since its single droplet efficiency increases with decreasing droplet size (Equations 22, 23 and 24). In order to confirm the role of the image force in the measured capturing efficiencies, the theoretical capturing efficiency expression for the image force (Equation 27 with  $\sum \eta = \eta_I$ ) was plotted (Figure 14) for three different droplet sizes along with the measured capturing efficiencies. All the parameters used in the model (Equation 27 with  $\sum \eta = \eta_I$ ) are ES parameters (e.g.,  $Q_L$ ) or material properties (e.g.,  $\mu$ ,  $\gamma_p$ ) that are known from the experiment or literature, except the droplet size. The droplet size distribution is usually obtained experimentally with optical equipment that cannot be trivially integrated into the ES filter used here. Typical droplet sizes range from 0.5-4 microns, with its distribution shifting to smaller sizes as the applied potential is increased. From Figure 14 it can be seen that similar values and trends were obtained with the experiments and the model when assuming monodispersed droplets of sizes 1, 1.3 and 1.5 microns. Therefore, the filter model using the image force as capturing mechanism is in good agreement with the experimental values. However, in order to accurately fit the data with the model, the exact size distribution of the droplets and their spatial distribution in the ES filter needs to be known and other electrical effects such as charging of NPs inside the ES need to be taken into account or ruled out. Nevertheless, from the model used here it can be concluded that the smallest droplets (< 1 microns) are the responsible for most of the NP capturing by image force.



Herby it has been demonstrated that NPs can be efficiently captured into liquid solutions with an ES filter. For NPs larger than 20 nm, the ES filter exhibits much higher capturing efficiencies than the commonly used bubble column technique that relies on diffusion. Therefore, ES filter in combination with aerosol technology allows the preparation of pure, well-defined colloidal solutions that is ideal for studying size-dependant NP properties, such as NP toxicity in the liquid phase.

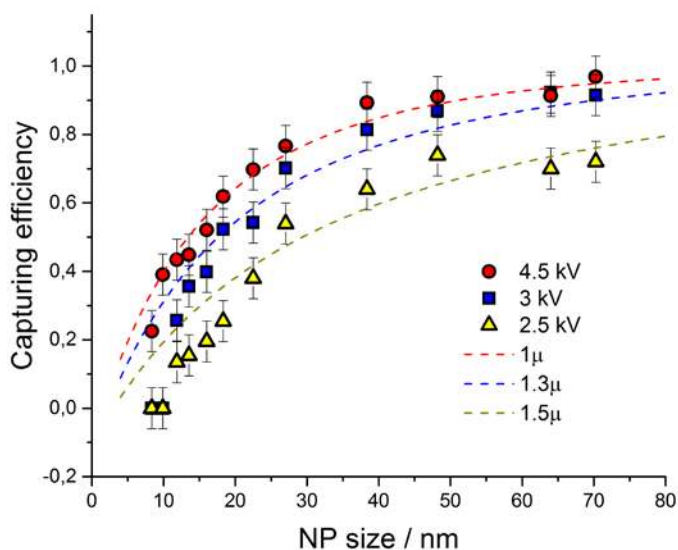


Figure 14. Experimental capturing efficiencies (data points) of the ES filter described in section 2.3.2 with the set-up described in section 2.3.4. The three set of experiments were performed at three different applied potentials (2.5, 3 and 4.5 kV) while maintaining the liquid flow rate and aerosol flow at 16  $\mu\text{L}/\text{min}$  and 1  $\text{L}/\text{min}$ , respectively. The modelled capturing efficiency (Equation 25 with  $\sum \eta = \eta_i$ ) was plotted using different droplet sizes charged at 90 % of their charge limit (Rayleigh limit, Equation).

### **3. Plasmonic Nanoparticle-Semiconductor Composites for Efficient Solar Water Splitting (Literature review)**

#### **Abstract**

Photoelectrochemical (PEC) water splitting is a promising technology that uses light absorbing semiconductors to convert solar energy directly into a chemical fuel (i.e., hydrogen). PEC water splitting has the potential to become a key technology in achieving a sustainable society, if high solar to fuel energy conversion efficiencies are obtained with earth abundant materials. This review article discusses recent developments and discoveries in the mechanisms by which the localized surface plasmon resonance (LSPR) in metallic nanoparticles can increase or complement a neighbouring semiconductor in light absorption for catalytic water splitting applications. These mechanisms can mitigate the intrinsic optical limitations of semiconductors (e.g., metal oxides) for efficient solar water splitting. We identify four types of enhancement mechanisms in recent literature: (i) light scattering, (ii) light concentration, (iii) hot electron injection (HEI), and (iv) plasmon-induced resonance energy transfer (PIRET). (i) Light scattering and (ii) light concentration are light trapping mechanisms that can increase the absorption of light with energies above the semiconductor optical band-edge. These two mechanisms are ideal to enhance the absorption of promising semiconductors with narrow bandgap energies that suffer from limited absorption coefficients and bulk charge recombination. On the other hand, (iii) HEI and the recently discovered (iv) PIRET are mechanisms that can enhance the absorption also below the semiconductor optical band-edge. Therefore, HEI and PIRET have the potential to extend the light utilization to visible and near-infrared wavelengths of semiconductors with excellent electrochemical properties, but with large bandgap energies. New techniques and theories that have been developed to elucidate the above mentioned plasmonic mechanisms are presented and discussed for their application in metal oxide photoelectrodes. Finally, other plasmonic and non-plasmonic effects that do not increase the device absorption, but affect the electrochemical properties of the

semiconductor (e.g., charge carrier transport) are also discussed, since a complete understanding of these phenomena is fundamental for the design of an efficient plasmonic NP-semiconductor water splitting device.<sup>1</sup>

---

<sup>1</sup> This chapter has been based on ref:22. Valenti, M., et al., *Plasmonic nanoparticle-semiconductor composites for efficient solar water splitting*. Journal of Materials Chemistry A, 2016.

### 3.1. Introduction

Photoelectrochemical (PEC) water splitting offers a sustainable and clean way to store solar energy in the form of a chemical fuel, i.e. hydrogen. This process has benefited from over 40 years of research,[23, 24] and many advances have been made with respect to the materials used today,[25, 26] while our overall understanding of the photo physical-chemical processes involved in the overall reaction has improved significantly. The main challenges that remain for PEC water splitting are finding materials that can simultaneously harvest solar irradiation, create and separate electronic charges (electrons and holes), and drive the water reduction and oxidation reactions. Furthermore, in order to bring this technology to a practical level, the entire process must be accomplished by inexpensive earth abundant materials that are stable in an electrochemical environment.

The most successful materials used to drive the solar water splitting reaction are semiconductor photoelectrodes, where metal oxides like  $\text{TiO}_2$ , [23]  $\text{WO}_3$ , [27, 28]  $\text{Fe}_2\text{O}_3$ , [29-31]  $\text{Cu}_2\text{O}$ , [32, 33] and  $\text{BiVO}_4$  [34-37] have received the most attention. These materials have been extensively studied and have emerged as promising candidates for practical applications as they are made from earth abundant materials that are generally stable in aqueous environments. However, metal oxide photoelectrodes often have less than ideal opto-electronic and catalytic properties, exhibited by low absorption coefficients, large band gap energies, short charge carrier diffusion lengths and life-times, and sluggish reaction kinetics at their surface.[25] Therefore, significant efforts have been devoted to functionalize metal oxide semiconductor photoelectrodes to improve their optical, electronic, and catalytic properties.[38-40]

One promising solution is to decorate semiconductors with plasmonic nanoparticles (NPs).[41-43] These metallic NPs can increase the absorption of thin film semiconductor photoelectrodes (with low absorption coefficients) by either confining or scattering the light into the semiconductor (i.e., light trapping).[44]<sup>[42],[43]</sup> In addition, plasmonic NPs can absorb visible light with lower energies (i.e. higher wavelengths) than the semiconductor

band gap and subsequently transfer the absorbed energy to the semiconductor in the form of “*hot electrons*” (electrons with energies higher than the metal Fermi level)[45]<sup>[6]</sup> or in a dipole-dipole interaction,[46] effectively extending the semiconductor absorption range. At the same time, the plasmonic NPs can significantly improve the electronic[47] and catalytic[48] properties of semiconductors when the NPs are placed at the semiconductor-electrolyte interface. All these possibilities have resulted in the synthesis and photoelectrochemical testing of many different plasmonic NP/semiconductor composites, to elucidate the phenomena and exploit their use for solar driven water splitting.[40, 46, 49-52]

Recent reviews[41, 53, 54] on plasmonic photocatalysis have mainly focused on plasmonic mechanisms that enhance the semiconductor absorption. However, less emphasis has been given to plasmonic and non-plasmonic NP effects on the charge transport properties and energetics of the semiconductor. In this review, we discuss how plasmonic NP size, shape, and composition affect the optical properties, charge transport and energetics of semiconductor photoelectrodes for PEC water splitting. Particular emphasis is given to decoupling plasmon-induced and non-plasmon-induced effects that are generated by NP/semiconductor composites, in order to gain mechanistic insights into the structure-functionality relationship of these promising architectures to improve PEC water splitting.

### **3.2. Localized surface plasmon resonance**

Light in the UV-visible wavelength range can induce collective oscillations of the valence electrons in noble metal NPs.[55, 56] This phenomenon is known as localized surface plasmon resonance (LSPR). The oscillating electron cloud (called localized surface plasmon) exhibits a life-time on the order of femtoseconds that is limited by different radiative and non-radiative damping processes.[57] The population of surface plasmons that decays by radiative damping is converted into photons, whereas, the population that

decays by non-radiative damping is converted into electron-hole pairs by interband and intraband excitations (cf. **Figure 15**).[57]

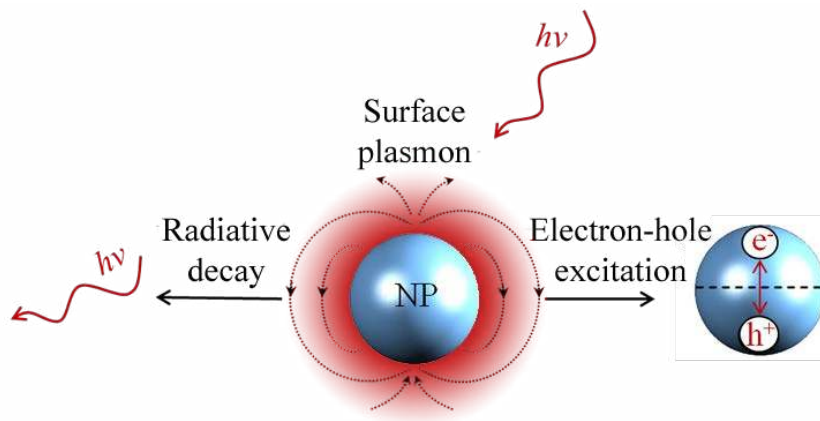


Figure 15. Illustration of radiative (left) and non-radiative (right) decay of the NP surface plasmon. The non-radiative decay occurs due to intraband excitation within the conduction band.

### 3.2.1. Absorption and scattering cross sections

Metal NPs whose surface plasmons mainly decay through non-radiative processes are called light absorbing NPs, since the irradiating energy (e.g., solar radiation) is absorbed by the NPs and subsequently transferred to their surroundings (e.g., by releasing heat). For applications where non-radiative processes are desired, light absorbing NPs with a large absorption cross-section and a small scattering (radiative decay) cross-section are selected. In 1908, Gustav Mie derived analytical expressions for the absorption and scattering cross-sections of spherical NPs of arbitrary size.[55] This theory has evolved to the generalized Mie theory that can also accurately predict the optical behaviour of particles of different shapes, such as ellipsoids and rods.[58] The NP scattering cross section ( $\sigma_{sca}$ ) and absorption cross section ( $\sigma_{abs}$ ) for small spheres can be approximated

using Equations 29, 30 and 31. This approximation is justified by Mie theory for spherical particles in the limit  $ak \ll 1$  and  $|m|ak \ll 1$ , where  $a$  is the radius of the particle,  $k$  is the wave number and  $m$  is the refractive index of the particle relative to that of the medium:[59]

$$\sigma_{abs} = k \cdot Im(\alpha) \quad (29)$$

$$\sigma_{sca} = \frac{k^4}{6\pi} |\alpha|^2 \quad (30)$$

where  $\alpha$  is the particle polarizability, which for a small sphere can be expressed as:[59]

$$\alpha = 3V_p \frac{\varepsilon - \varepsilon_M}{\varepsilon + 2\varepsilon_M} \quad (31)$$

where  $V_p$  is the particle volume, and  $\varepsilon$  and  $\varepsilon_M$  are the wavelength dependent dielectric function of the NP material and surrounding medium, respectively. Resonant enhancement of the polarizability can hence occur for particles of materials with a negative real dielectric function (assuming a relatively small imaginary part). This illustrates why plasmonic excitations are found in metal nanoparticles.

For ellipsoidal NPs, a simple expression for the polarizability along direction  $i=1,2,3$  can be obtained with the, less rigorous, electrostatic approximation (or dipole approximation) for small particles compared with the light wavelength:[59]

$$\alpha_i = V_p \frac{\varepsilon - \varepsilon_M}{\varepsilon_M + L_i(\varepsilon - \varepsilon_M)} \quad (32)$$

where  $L_i$  are geometry factors along direction  $i=1,2,3$  and whose sum should equal 1. For spheres,  $L_i=1/3$ , which reproduce the expression in Equation 3 above.

Equations 29, 30, 31 and 32 clearly show that the absorption and scattering cross sections depend on the NP size ( $V_p$ ), shape ( $L_i$ ) and composition ( $\varepsilon$ ), along with the surrounding media ( $\varepsilon_M$ ). Regarding size, the scattering cross section is proportional to  $V_p^2$ ,

while the absorption cross section is proportional to  $V_p$ . For example, Figure 16 shows that the scattering cross section of a spherical gold NP nearly vanishes when its radius is decreased from 35 nm (Figure 2A) to 10 nm (Figure 2B), while the absorption cross section is decreased to a lesser extent. Therefore, small NPs are used for applications where only non-radiative decays are desired.

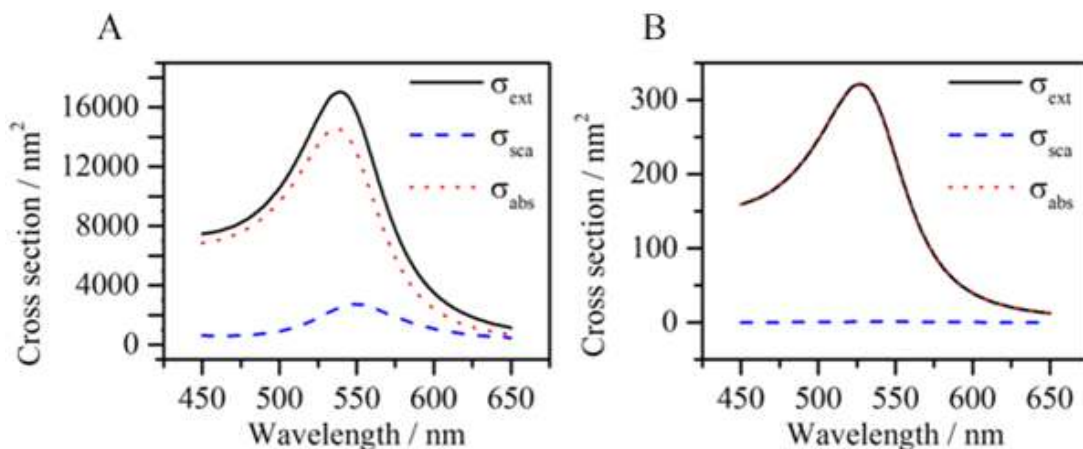


Figure 16. Extinction, scattering and absorption spectra of a gold NP with a radius of 35 nm (A) and a radius of 10 nm (B) calculated using Mie theory. In both cases, the refractive index of the environment is 1.33.

### 3.2.2. Plasmon Resonance frequency

The light frequency at which the NP extinction coefficient is the greatest is called the NP plasmon resonance frequency, and it can be tuned by changing the material composition, shape and size of the NPs as shown in Figure 17. Figure 17A also highlights that noble metal NPs interact significantly with light that is abundant in the solar irradiation spectrum, which makes them excellent candidates to be used in solar energy conversion devices. The NP absorption and scattering spectra are also affected by the dielectric function of the surrounding medium (cf. Equations 29-31). Even though the dielectric function of the surrounding medium is determined by the application (e.g.,



aqueous solution for PEC water splitting), it can be partially modified by coating the NP with a thin semiconducting or insulating layer. The dielectric function and the thickness of the coating can be changed to tune the resonance frequency of the NPs.[60]

Significant tunability of the LSPR extinction spectra has been achieved with metal NP rods and NP dimers (two closely spaced NPs), since they are characterized by two LSPR modes corresponding to excitation at different polarizations (i.e., transversal and longitudinal modes).[61-63] In NP rods, the longitudinal mode can be accurately tuned by modifying the length of the rod,[61] whereas, for NP dimers the longitudinal mode can be tuned by modifying the interparticle distance (cf. Figure 18).[62, 64]

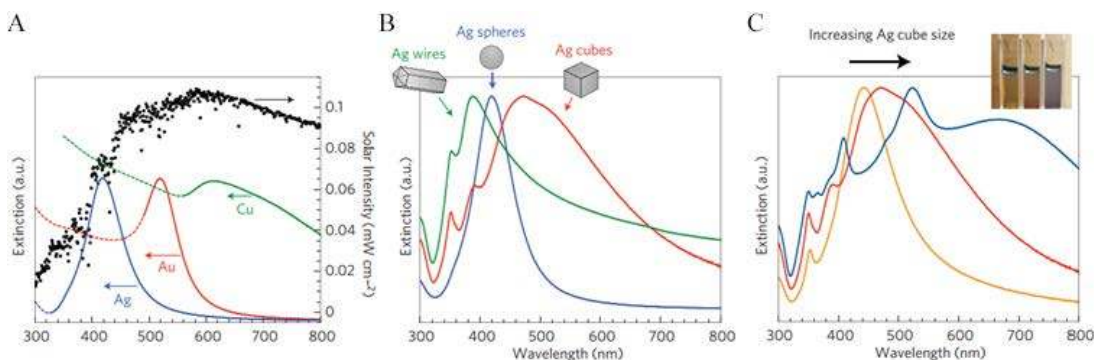


Figure 17. A) Normalized extinction spectra of spherical Ag ( $38 \pm 12$  nm in diameter), Au ( $25 \pm 5$  nm) and Cu ( $133 \pm 23$  nm) particles. The intensity of solar radiation (data for air mass 1.5 solar spectrum from the National Renewable Energy Laboratory, <http://rredc.nrel.gov/solar/spectra/am1.5/>) is also shown, in black. Dashed portions of the metal extinction curves indicate interband transitions (that is, no surface plasmon resonance in these regions). B) Normalized extinction spectra for Ag wire, cube and sphere nanoparticles. Wire-shaped particles are  $90 \pm 12$  nm diameter and  $>30$  aspect ratio, cubic particles are  $79 \pm 12$  nm edge length and spherical particles are  $38 \pm 12$  nm diameter. C) Normalized extinction spectra for Ag nanocubes as a function of size ( $56 \pm 8$  nm,  $79 \pm 13$  nm and  $129 \pm 7$  nm edge lengths correspond to orange, red and blue spectra respectively). The inset shows a photograph of the three nanocube samples suspended in ethanol.[42] Reprinted with permission from ref[42]. Copyright 2011 Macmillan publishers limited.

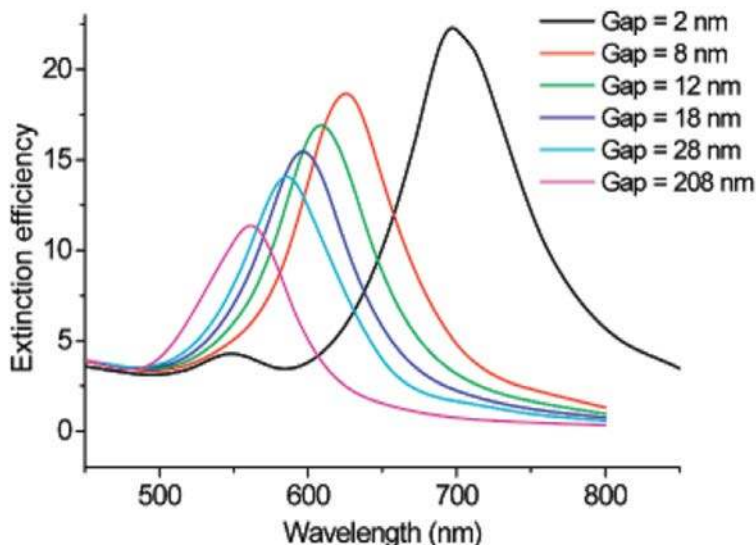


Figure 18. Discrete dipole approximation-simulated extinction efficiency spectra of Au nanodisc pairs for varying interparticle separation gap for incident light polarized parallel to the interparticle axis (longitudinal mode). Reprinted with permission from ref[64]. Copyright 2007 ACS.

### 3.2.3. Light confinement (NP near-field)

An important characteristic of the LSPR is the highly localized electric field enhancement around the plasmonic NP. Figure 19A shows the electric field contours of a silver NP when illuminated with light at the NP resonance frequency. It can be seen that the magnitude of the applied electric field is enhanced by  $\sim 50$  fold at the NP surface. This near-field effect plays an important role in several applications, such as waveguiding along particle chains,[65] surface-enhanced Raman scattering (SERS),[66] light trapping to enhance light absorption in semiconductors[67] (discussed in the following section), among others. Higher field enhancements are achieved with particles having sharp edges, such as the NP rod shown in Figure Figure 19B. Finally, the formation of NP dimers (e.g., spherical[68], rod[69] and triangular prism[68, 70, 71] dimers) give rise to the largest field enhancements that are order of magnitudes larger than the applied field (cf. Figure 19C).

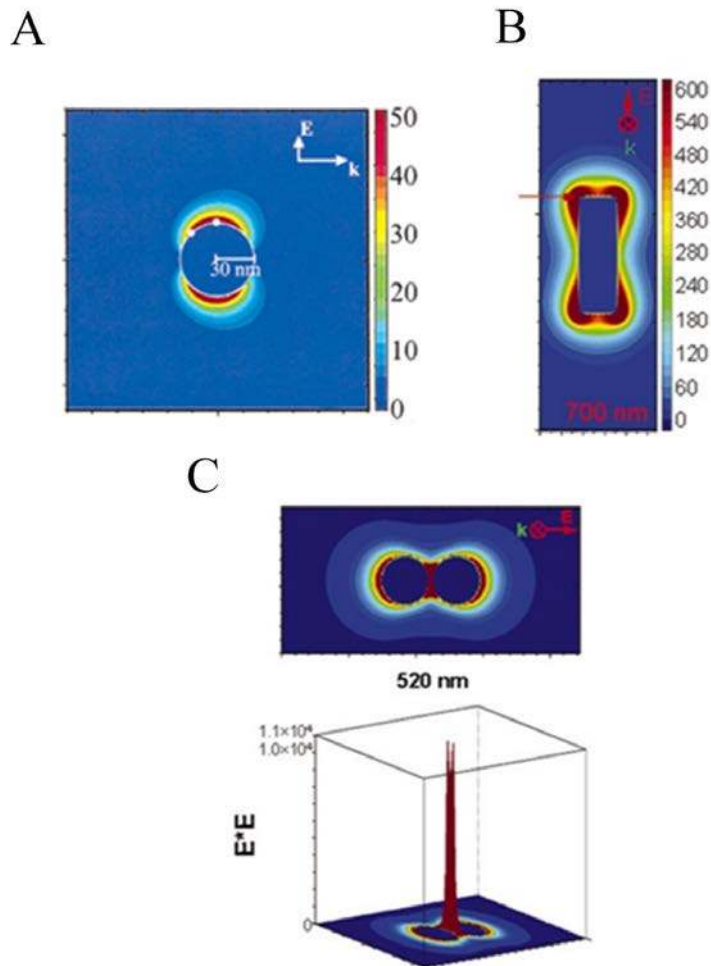


Figure 19. A) Electric field enhancement contours for a Ag sphere. Reprinted in part with permission from ref.[56] Copyright 2002 ACS B) electric field enhancement contours for a rod. Reprinted in part with permission from ref.[68] Copyright 2004 AIP C) electric field enhancement contours external to a dimer of Ag nanoparticles separated by 2 nm, for a plane that is along the inter-particle axis and that passes midway through the two particles. In the 3D plots, the axis perpendicular to the selected plane represents the amount of electric field enhancement around the dimer.[68] Reprinted in part with permission from ref.[68] Copyright 2004 AIP.

### 3.3. Plasmonic NP/semiconductor composites

#### 3.3.1. Harvesting the surface plasmon's energy to drive the water splitting half reactions on semiconductors

For a NP in contact with a semiconductor, (part of) the surface plasmon's energy can be extracted for both radiative damping and non-radiative damping (Figure 20A and B). The surface plasmon energy can be transferred from the NP to the semiconductor and then further converted to chemical energy, for example, to drive the water splitting reactions. This energy transfer is possible through four different mechanisms that form the core of this review. These are (i) light scattering (radiative decay, Figure 20A), (ii) hot electron injection (HEI, Figure 20B), (iii) light concentration (Figure 20C) and (iv) plasmon-induced resonance energy transfer (PIRET, Figure 20D). Light scattering by radiative decay (i) can enhance the effective optical path length in the semiconductor. This leads to corresponding enhanced absorption and generation of charge carriers that can drive the water splitting half reactions (Figure 20A).[44] Instead, when the surface plasmon decays by exciting an electron-hole pair within the NP (non-radiative decay, Figure 20B) (ii), hot electrons can be transferred to the conduction band of the semiconductor. Once the hot electron and hole are separated, they can carry out the corresponding water splitting half reactions.[45] In the third (light concentration) and fourth (PIRET) mechanisms, the highly localized electric field enhancement (i.e., near-field) around the plasmonic NP induces interband excitations in a neighbouring semiconductor (Figure 20C and D).[72]<sup>[73]</sup> In both mechanisms, the plasmon energy transfer to the semiconductor is mediated by coupling between photons, plasmons and excitons (electron-hole pairs) in the NP near-field. Unlike direct light excitation, the near-field can induce excitations not only above, but also below the *optical band gap edge* (OBGE) of the semiconductor. This review distinguishes between near-field effects acting above the OBGE (i.e., light concentration mechanism) and below the OBGE (i.e., PIRET), since they have different implications (cf. section 4.2.2). In the light concentration mechanism (iii) the NPs act as *optical antennas* that localize the

incident electromagnetic field in the neighbouring semiconductor, increasing the electron-hole generation rate in the semiconductor (Figure 20C).[52, 67, 74] In PIRET, the near-field energy is transferred *non-radiatively* to the semiconductor through strong dipole-dipole coupling with band edge states that are optically inaccessible (Figure 20D).[46]

Because the light scattering (i) and the light concentration (iii) mechanisms both effectively guide and/or localize the incoming photons, these mechanisms are referred to as light trapping or photonic effects (Figure 20A and C).[75] While the light trapping mechanisms are only effective with incident photon energies above the OBGE, HEI and PIRET can extend the light utilization to photon energies below the OBGE (Figure 20B and D). These four energy transfer mechanisms (i.e., light scattering, HEI, light concentration and PIRET), allow decorating plasmonic NPs to enhance or complement the insufficient light absorption of bare semiconductors and, therefore, improve the overall performance of conventional water splitting semiconductor devices.

New strategies and materials have been developed in recent years to efficiently exploit the surface plasmon energy in plasmonic NP/metal oxide photoelectrodes in order to mitigate the optical limitations of bare semiconductor metal oxide photoelectrodes (i.e., large bandgap energies and low absorption coefficients).[40, 41, 46-48, 75-77] Recent key publications that have elucidated the roles of each mechanism for the water splitting performance of NP-metal oxide photoelectrodes are reviewed in Section 3.4. along with a more detailed description of the corresponding mechanisms.

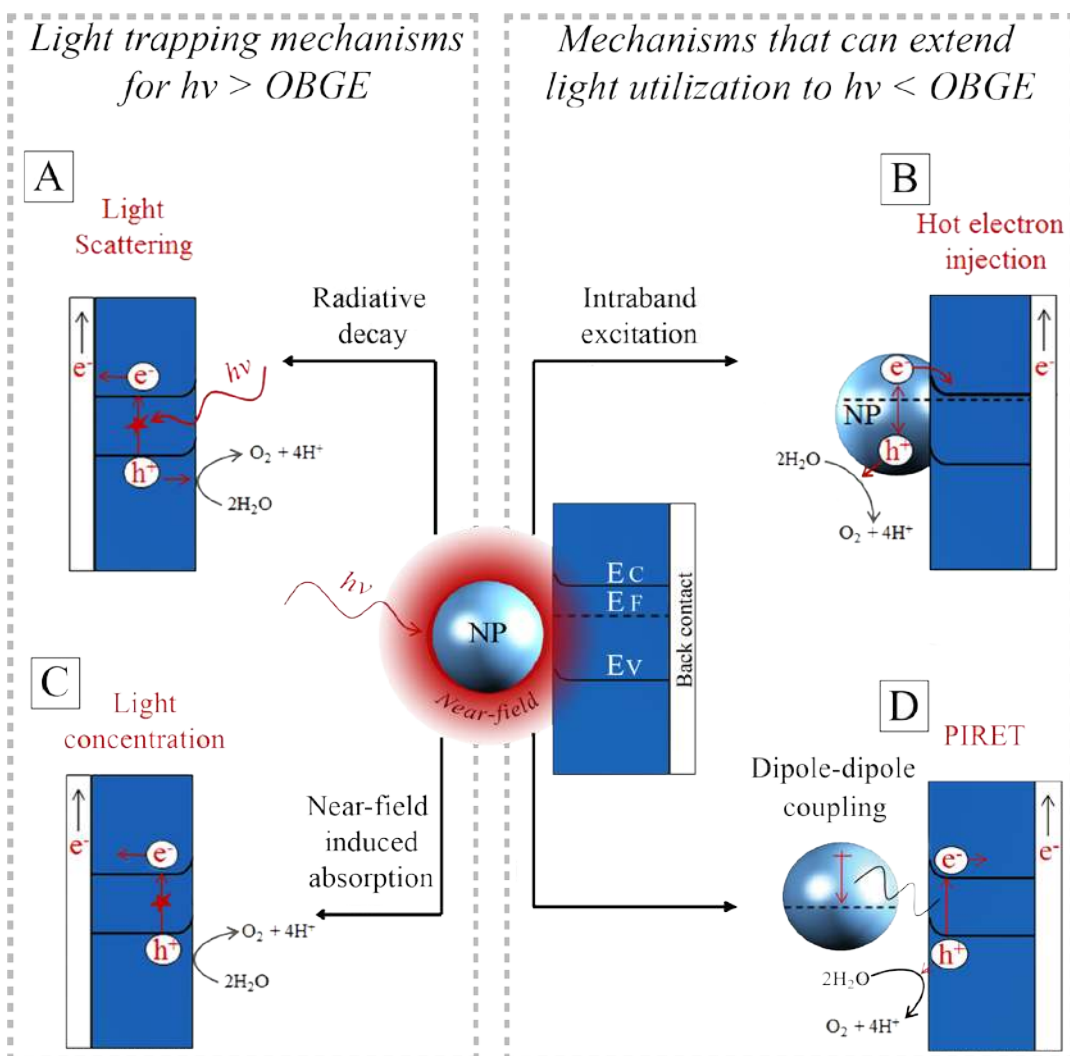


Figure 20. Illustration of four energy transfer mechanisms from a plasmonic NP to an n-type semiconductor to drive water oxidation: A) light scattering, B) hot electron injection, C) Light concentration and D) plasmon-induced resonance energy transfer (PIRET). OBGE denotes the optical band gap edge of the semiconductor.  $E_C$ ,  $E_F$ ,  $E_V$  are the conduction band, Fermi and valence band energies, respectively.

### 3.3.2. Electrochemical effects

The plasmonic mechanisms described above are summarized in Figure 21 together with other metal NP mechanisms, either plasmonic or non-plasmonic, that enhance the performance of semiconductor photoelectrodes. HEI, PIRET and light trapping are the mechanisms by which plasmonic NPs can increase the light absorption in the semiconductor. In addition, decorating plasmonic NPs on semiconductors can also cause other important electrochemical effects that can enhance the water splitting performance of the semiconductor. In turn, these electrochemical effects can be divided into those that affect (i) the semiconductor's charge transport, and (ii) its electronic band energetics (c.f. Figure 21). A significant challenge in plasmonic water splitting research has been to differentiate these two electrochemical effects from the plasmonic mechanisms that can increase the device absorption.[44, 48, 49, 76] Several optical, electrochemical, and computational techniques have been successfully used to distinctly recognize the role of each effect in the water splitting process.[40, 44, 48] Consequently, while this review's main focus is to discuss the recent advances that elucidate the potential of light trapping, HEI and PIRET to enhance the absorption of metal oxide semiconductors, a concluding section (Section 3.5.) is dedicated to discuss other plasmonic and non-plasmonic effects (c.f. Figure 21) that also play an important role in improving the overall performance of the metal NP/semiconductor composite for solar water splitting devices.

	<i>Plasmonic mechanisms</i>	<i>Non-plasmonic mechanisms</i>
<i>Absorption increase</i>	<ul style="list-style-type: none"> <li>➤ Hot electron injection (HEI)<sup>23</sup></li> <li>➤ PIRET<sup>25</sup></li> <li>➤ Light trapping<sup>20</sup></li> </ul>	
<i>Effects on charge transfer</i>	<ul style="list-style-type: none"> <li>➤ Localized heating<sup>57</sup></li> <li>➤ Near- field induced Alignment of adsorbate molecules<sup>58</sup></li> </ul>	<ul style="list-style-type: none"> <li>➤ Improved bulk conductivity<sup>27</sup></li> <li>➤ Improved catalysis<sup>27</sup></li> </ul>
<i>Effects on the energetics and band structure</i>	<ul style="list-style-type: none"> <li>➤ Near-field induced changes in the electronic structure of the semiconductor<sup>26</sup></li> <li>➤ Modification in the Fermi level of the semiconductor due to injected hot electrons<sup>56</sup></li> </ul>	<ul style="list-style-type: none"> <li>➤ Fermi level equilibration<sup>59</sup></li> </ul>

Figure 21. Summary of proposed effects of metal NPs on semiconductors for photoelectrochemical water splitting. [42], [45], [46], [47], [48], [77], [78], [79, 80]



### 3.4. Plasmonic energy transfer mechanisms

#### 3.4.1. Hot electron injection (HEI)

Hot electrons are generated through non-radiative damping and hot electron injection (HEI) is therefore best exploited by light absorbing NPs. Figure 22 shows a more detailed illustration of this mechanism. When the surface plasmons decay through intraband excitations within the conduction band, the excited electrons (hot electrons) obtain energies higher than the metal Fermi energy ( $E_F$ ; cf. Figure 22).[81, 82] For plasmonic NPs smaller than 20 nm the hot electron exhibit energies ( $E_H$ ) within the range  $E_F < E_H < E_F + \hbar\omega$ , while larger particles exhibit much smaller hot electron energies close to  $E_F$ . [83] If the energy of the hot electrons are larger than the interface Schottky energy barrier, the hot electrons can be transferred to the conduction band of the semiconductor.<sup>[45], [72], [84], [85], [82, 86, 87] [88]</sup> Charge neutrality in the metal NP is restored by removing the “hot hole” with an oxygen evolution catalyst (OEC) or an electron-donor solution (in the case of an n-type semiconductor). Excited electrons with energies lower than the Schottky barrier relax through, for instance, electron-electron and electron-phonon collisions (releasing heat).[89] Therefore, the efficiency of the HEI mechanism is expected to decrease with increasing Schottky barrier energies, which depend on the energetics of the selected metal/semiconductor system. However, having energies larger than the Schottky barrier is by no means the only requirement for a hot electron to be injected to the conduction band of the semiconductor. The hot electron also needs to reach the surface of the NP, before undergoing another relaxation process.[6] Further limitations come from the non-ideal electron-acceptor ability of the semiconductor (i.e., limited density of states in the conduction band) and the non-ideal electron-donor ability of the OEC/electrolyte that replaces the injected hot electrons.[6, 90-92] The above limitations significantly affect the efficiency of HEI and it is of great importance to theoretically and experimentally study each limitation individually. One of the main challenges to experimentally study the HEI efficiency comes from the fact that the

measured hydrogen/oxygen evolution in a plasmonic NP/semiconductor photoelectrode not only come from the HEI process (due to the NP light absorption) but also from light absorption of the semiconductor itself. Therefore, strategies must be developed to accurately decouple these two contributions before attempting the optimization of HEI. Two recent publications made key contributions to tackle this issue using two different approaches. Mubeen *et al.*, [45] fabricated a Au nanorod/TiO<sub>2</sub> composite system, where the TiO<sub>2</sub> layer was so thin that its only role was to remove the hot electrons from the nanorod (electron filter) and did not contribute to the measured photocurrent. Chen *et al.* [47] used a different strategy based on a Au NP/ZnO composite and tested its photoelectrochemical ability to split water by illuminating it only with visible light that has lower energies than the ZnO band gap. That ensured that only photocurrent related to the HEI mechanism was measured. We start by reviewing the work by Mubeen *et al.* in detail in order to gain further insights to the HEI mechanism.

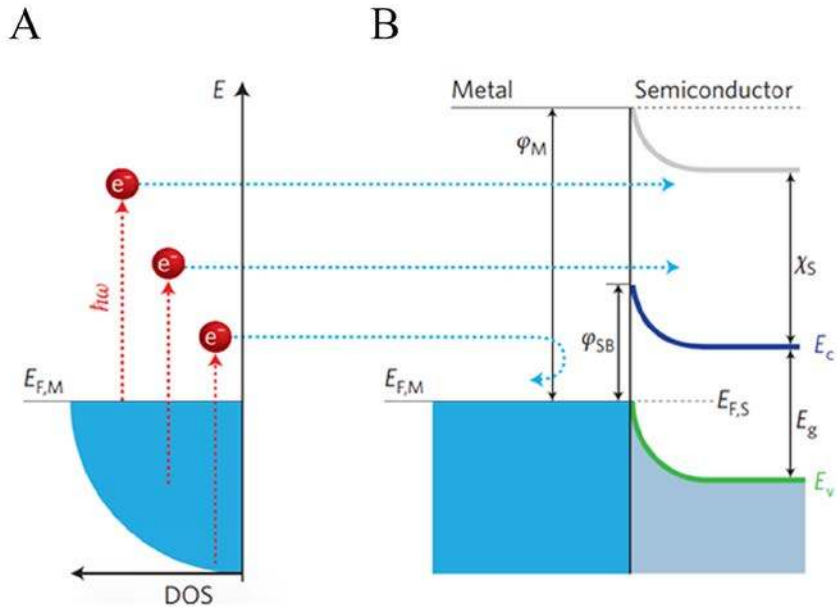


Figure 22. A) Plasmonic energy conversion: electrons from occupied energy levels are excited above the Fermi energy. B) Hot electrons can be injected into a semiconductor by forming a Schottky barrier with the plasmonic nanostructure. Hot electrons with energies high enough to overcome the Schottky barrier  $\phi_{SB} = \phi_M - \chi_S$  are injected into the conduction band  $E_c$  of the neighbouring semiconductor, where  $\phi_M$  is the work function of the metal and  $\chi_S$  is the electron affinity of the semiconductor. Reprinted in part with permission from ref.[6] Copyright 2014 Macmillan publishers limited.

Mubeen *et al.* fabricated an autonomous plasmonic solar water splitting device where the oxygen and hydrogen evolution reaction take place on the NP-semiconductor composite without the use of external wires and without applying a bias voltage. This device consists of an array of vertically aligned gold nanorods in an aluminium oxide template. Figure 23A and B, show an illustration and a transmission electron microscope (TEM) image of one of the nanorods, respectively. The plasmonic rod is capped with a thin layer of crystalline  $\text{TiO}_2$ , which in turn is decorated with a hydrogen evolution catalyst (Pt

NPs). On the side of the nanorod a cobalt-based oxygen evolution catalyst is deposited. In this device, all the charge carriers are derived from surface plasmons (through HEI) and the semiconductor works only as a hot electron filter as depicted in Figure 23C. Using this approach, once the hot electrons and holes are separated, they migrate to the corresponding catalysts to carry out the water splitting half reactions. The autonomous device was operated with a 1 M potassium borate electrolyte (pH 9.6) under visible light illumination ( $\lambda > 410$  nm), exhibiting an external quantum efficiency (EQE) of  $\sim 0.1$  % (averaged over the visible portion of the solar spectrum). Several strategies were taken in this work to confirm that all the charges indeed came from the HEI mechanism and not from conventional  $\text{TiO}_2$  light absorption. One of them is shown in Figure 24, where the hydrogen production of the device was measured under illumination with light of different spectral ranges. Under UV-dominated illumination ( $310 \text{ nm} < \lambda < 520 \text{ nm}$ ), the hydrogen production rate is much lower than when the device is illuminated with visible light ( $\lambda > 410 \text{ nm}$  or  $\lambda > 600 \text{ nm}$ ). The low performance under UV illumination confirms that conventional electron-hole excitation due to light absorption in the  $\text{TiO}_2$  does not contribute to the hydrogen generation under AM 1.5 irradiation, since  $\text{TiO}_2$  only absorbs light up to  $\sim 380$  nm. Therefore, this device is ideal to independently study the different processes that limit the HEI efficiency (e.g., electron-donor ability of the hydrogen evolution catalyst). Finally, this work reports no decrease in activity over 66 hours of solar irradiation. This excellent stability represents a great advantage for plasmon driven water splitting devices when compared with conventional short bandgap metal oxide semiconductors that decrease their performance over time due to corrosion. [93],[94]

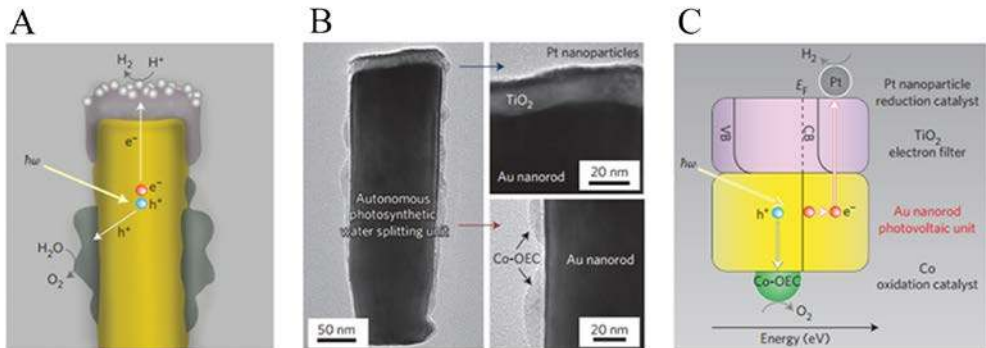


Figure 23. Structure and mechanism of operation of the autonomous plasmonic solar water splitter. a, Schematic of the cross-section of an individual photosynthetic unit showing the inner gold nanorod, the TiO<sub>2</sub> cap decorated with platinum nanoparticles, which functions as the hydrogen evolution catalyst, and the Co-OEC material deposited on the lower portion of the gold nanorod. b, Corresponding transmission electron micrograph (left) and magnified views of the platinum/TiO<sub>2</sub> cap (top right) and the Co-OEC (bottom right). c, Energy level diagram superimposed on a schematic of an individual unit of the plasmonic solar water splitter, showing the proposed processes occurring in its various parts and in energy space. CB, conduction band; VB, valence band; EF, Fermi energy. Reprinted with permission from ref.[45] Copyright 2013 Macmillan publishers limited.

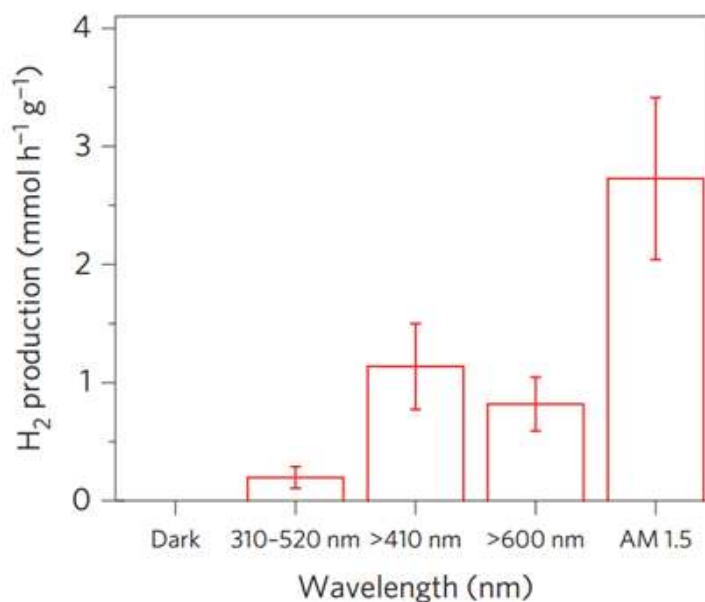


Figure 24. Hydrogen produced per hour with various illumination wavelengths, each determined from an experiment in which the device was continuously illuminated for 9 h. Reprinted with permission from ref.[45] Copyright 2013 Macmillan publishers limited.

More recently, the same authors reported[95] photo-production of hydrogen with a similar system for gold nanorods with different aspect ratios, exhibiting longitudinal absorption modes nearly throughout the solar spectrum ( $\lambda \sim 400 \text{ nm} - 1000 \text{ nm}$ ). In this work, instead of an electron donor oxygen evolution catalyst, methanol was added to the electrolyte as a sacrificial reactant. The authors show that by using nanorods with different aspect ratios the hydrogen production can be doubled compared with a device that uses nanorods of the same dimensions. The device presented a EQE of  $\sim 0.1 \%$  (averaged over the entire solar spectrum) and showed good stability for over 200 hours of continuous operation.

Unlike in the previously described works, Chen *et al.*[47] synthesized a NP/semiconductor composite where the semiconductor absorption contributes significantly to the composite's hydrogen generation. The NP/semiconductor composites used in this work consist of arrays of ZnO nanorods decorated with spherical gold NPs with an average size of less than 5 nm. These composites were used as the working electrode in a three electrode-based photoelectrochemical system, and cyclic voltammetry measurements under AM 1.5 solar simulation irradiation are shown in Figure 25A. It is clear that the performance of the composite device increases with an increase in the plasmonic NP concentration, until an optimum NP loading of 9.8%. Figure 25B, shows a similar type of experiment, but this time the sample was irradiated only with visible light (> 420nm). This visible light has lower energies than the semiconductor band gap and, as expected, no photocurrent was obtained in the cyclic voltammetry of the bare ZnO sample (c.f. Figure 25B). After NP deposition the photocurrent increased up to  $\sim 0.3 \mu\text{A}/\text{cm}^2$  at 1 V vs Ag/AgCl, which the authors attribute to the HEI mechanism. In order to further elucidate the HEI effect, wavelength dependent photocurrent measurements were performed and compared with the NP absorption spectra. Figure 26 shows that the measured photocurrent presents a peak around 2.4 eV, which corresponds well to the NP plasmon absorption mode. This correlation between the photocurrent and the absorption spectra gives further evidence that the obtained photocurrent is due to a plasmonic effect. This type of comparison is now commonly used to prove plasmonic effects and has become an important tool in the plasmon driven water splitting field. However, it should be pointed out that hot electrons with sufficient energy to overcome the Schottky barrier may be excited also without plasmonic effects, via the photoelectric effect. Chen *et al.* also compared the measured photocurrent with the number of photoelectrons that derive from direct light excitation (photoelectric effect) and have sufficient energy to overcome the Schottky energy barrier. These photoelectrons (Fowler hot electrons) are calculated according to Fowler theory:

$$\eta_i = C_f \frac{(hv - \phi)^2}{hv} \quad (33)$$

where  $C_f$  is the Fowler emission coefficient and  $\phi$  is the Schottky energy barrier. Equation 33 was fitted to the obtained photocurrent, as shown in Figure 26. It can be clearly seen that the photocurrent diverges from the Fowler's relation around the NP resonance frequency, confirming that the hot electrons, associated with the surface plasmon resonance effect, significantly contribute to the composite's measured photocurrent (c.f. Figure 25 A and B).

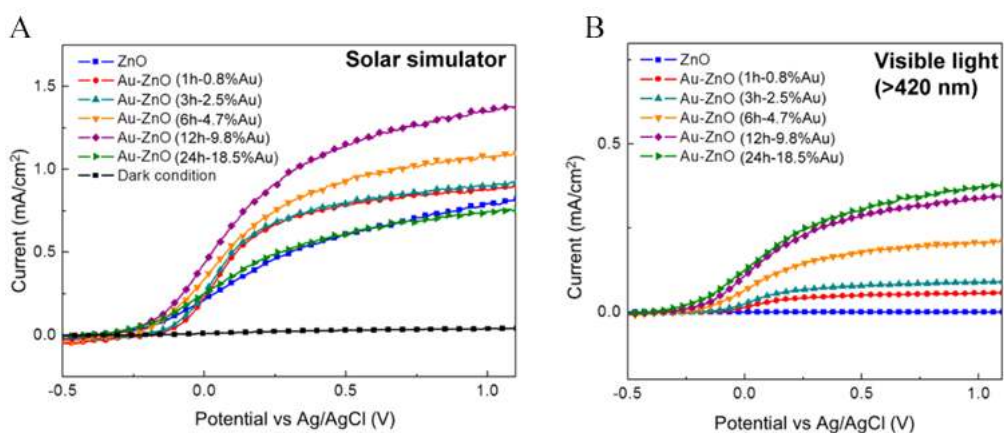


Figure 25. (a) Linear-sweep voltammograms of Au-ZnO photoelectrodes with nanoparticles deposited for various periods, and a dark scan, performed in a 0.5 M aqueous Na<sub>2</sub>SO<sub>4</sub> with a pH of 6.8 under an AM 1.5 solar simulator. (b) Linear-sweep voltammograms of Au ZnO photoelectrodes with nanoparticles deposited for various periods, obtained under illumination by visible light (>420 nm). Reprinted with permission from ref.[47] Copyright 2012 ACS.



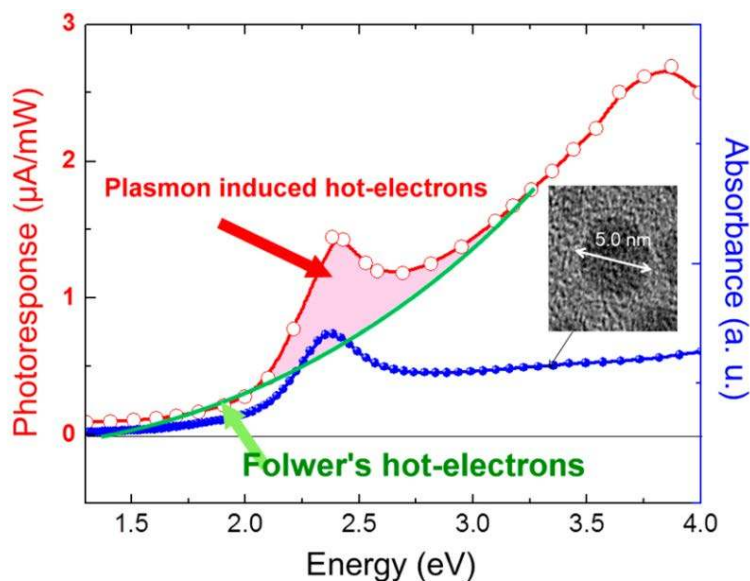


Figure 26. Absorption spectrum of Au nanospheres and plots of photocurrent versus wavelength, fitted to Fowler's law, indicating that photocurrent comprises mainly hot electron flow, with additional contribution from hot electrons that are injected from Au under plasmonic-induced irradiation that is amplified by localized surface plasmon resonance. Reprinted with permission from ref.[47] Copyright 2012 ACS.

### 3.4.2. Transient absorption analysis

A more complex plasmonic composite, containing three light absorbing components, was synthesized by Li *et al.*[40] They used a CdS-Au-TiO<sub>2</sub> sandwich nanorod array as the photoanode in a water splitting PEC cell and studied the role of the plasmonic gold NPs on the composite's performance. The sandwich composite consists of a gold-decorated TiO<sub>2</sub> nanorod with an external coating of CdS quantum dots (QDs), as illustrated in Figure 27. The CdS QDs, like the plasmonic NPs, can be used as photosensitizers to extend the light absorption range of large band gap semiconductors.[96-98] Therefore, in this composite a large fraction of the solar spectrum is absorbed. TiO<sub>2</sub> absorbs light with wavelengths below ~ 400 nm, CdS QDs below ~ 525 nm and the plasmonic NPs below ~

725 nm. Figure 28A shows the incident photon to current efficiency (IPCE) of the composite, with and without the gold NPs. It can be seen that the IPCE is slightly increased in the region of the spectrum around 650 nm, which corresponds to the location of the LSPR mode of the gold NPs. Moreover, at this wavelength neither of the semiconductor components (i.e.,  $\text{TiO}_2$  and CdS QDs) absorb light, which indicates that the photocurrent may be due to the HEI mechanism in the plasmonic NPs. The authors used transient absorption analysis to elucidate the origin of this photocurrent increase. Figure 28B shows the transient absorption signal (bottom of the figure) that corresponds to the  $\text{TiO}_2$  trap state absorptions in the visible region. As expected, under 400 nm illumination for bare  $\text{TiO}_2$  it can be clearly seen the filling of the  $\text{TiO}_2$  trap states by the photogenerated charge carriers (blue line in Figure 28B). What is more interesting is that under 675 nm illumination, filling of the  $\text{TiO}_2$  trap states is also observed in the  $\text{Au-TiO}_2$  and  $\text{CdS-Au-TiO}_2$  composites (green and orange lines in Figure 28B, respectively). Since neither of the semiconductors absorb 675 nm light, the filling of the  $\text{TiO}_2$  trap states must be due to hot electron transfer from the plasmonic NP. Figure 28B (top of the figure) also shows the blue-shift in the gold NP LSPR mode of  $\text{Au-TiO}_2$  compared with  $\text{CdS-Au-TiO}_2$ . From the location in the spectrum of the LSPR and the transient absorption signal (Figure 28B), the authors were able to shed light on the dynamics of the hot electron in the composites (i.e.,  $\text{CdS-Au-TiO}_2$  and  $\text{Au-TiO}_2$ ) upon illumination with light at 675 nm (c.f. Figure 28C). A key observation is that the filling of the  $\text{TiO}_2$  trap states is more efficient in  $\text{CdS-Au-TiO}_2$  than for  $\text{Au-TiO}_2$  (Green and orange lines in Figure 28B). This is consistent with the fact that, in comparison with  $\text{Au-TiO}_2$ , the hot electrons in  $\text{CdS-Au-TiO}_2$  have a lower energy (red-shifted LSPR). As a result the hot electrons are not able overcome the Schottky energy barrier, and are efficiently transferred to the  $\text{TiO}_2$  trap states (green arrows in Figure 28C). On the other hand, the hot electrons in  $\text{Au-TiO}_2$  (with blue-shifted LSPR) exhibit a higher offset energy from the gold Fermi level and can overcome the Schottky energy barrier, reaching the  $\text{TiO}_2$  conduction band (Orange arrows in Figure 28C). Therefore, by looking at the filling of  $\text{TiO}_2$  trap states the authors were able to study the

HEI efficiency of the synthesized plasmonic composites, which makes transient absorption analysis a very powerful tool to study the HEI in complex systems.

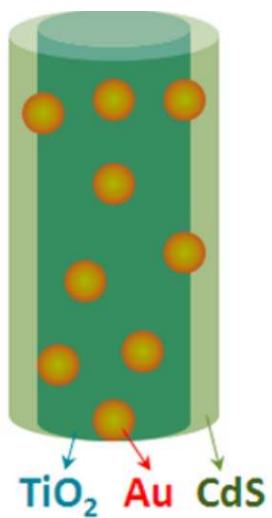


Figure 27. Illustration of the sandwich CdS-Au-TiO<sub>2</sub> composite. Reprinted with permission from ref.[40] Copyright 2014 ACS.

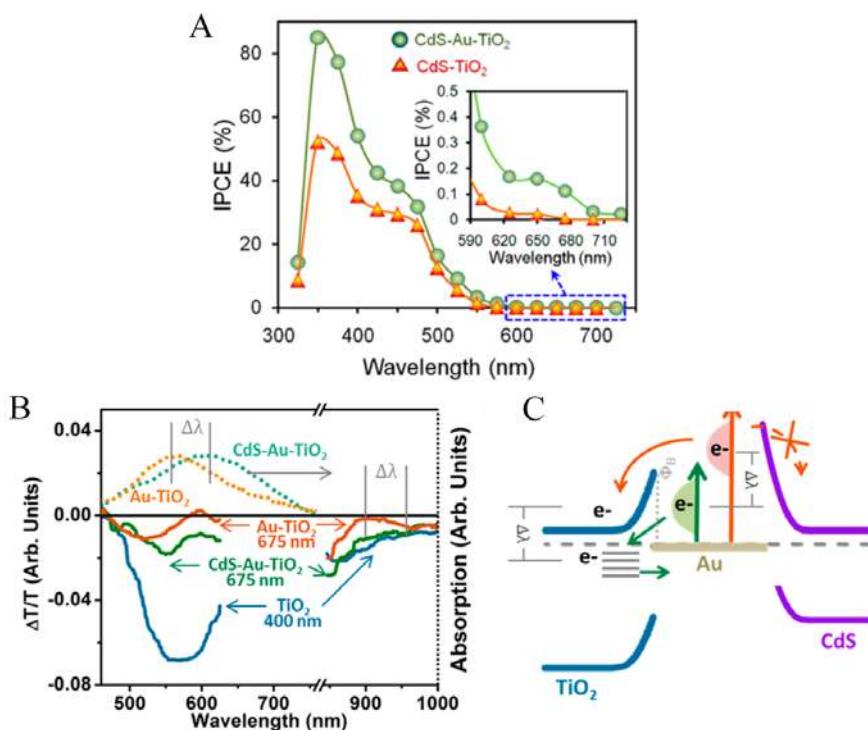


Figure 28. A) IPCE. B) NP absorption in Au-TiO<sub>2</sub> and in CdS-Au-TiO<sub>2</sub> (Top) and full-spectrum transient absorption signal at 20 ps after excitation (bottom). C) The change in back-transfer dynamics and filling of the TiO<sub>2</sub> electron-trap states without charge transfer into CdS is explained by the energy of the hot plasmonic electron distribution relative to the interfacial Schottky barrier. Reprinted with permission from ref.[40] Copyright 2014 ACS.

### 3.4.3. Other design parameters for HEI devices

#### 3.4.3.1. NP composition

As discussed above, the HEI efficiency highly depends on the hot electron energy. Hot electrons can be generated either by intraband or interband transitions. Recent theoretical studies[99-102] have shown that interband transitions induced by visible light (from the d-band) result in high energy hot holes but low energy hot electrons ( $\sim E_F$ ), due to the position of the d-band relative to the Fermi level in noble metals. By contrast, hot

electrons generated by intraband transitions can have energies up to  $E_F + \hbar\omega$ .<sup>[83]</sup> Therefore, it is advantageous to use materials with a relatively large interband energy threshold to maximize the intraband excitation spectrum. Ag exhibits an interband energy of  $\sim 3.7$  eV and, therefore, only intraband transitions are expected when illuminated with visible light. Au on the other hand, has an interband energy of  $\sim 2.3$  eV and its HEI efficiencies may be limited by interband excitations when illuminated with violet, blue and green light.

The above reasoning holds for HEI over the Schottky energy barrier (as illustrated in Figure 22), where the HEI efficiency depends on the hot electron energy. However, it has been recently proposed that low energy hot electrons (generated by interband transitions) can also be transferred to the semiconductor by tunnelling through the Schottky energy barrier.<sup>[103]</sup> Further research must be undertaken to study the efficiency of this hot electron transfer process.

The material composition of the NP is of great importance in the design of HEI water splitting devices, because it affects three important HEI parameters: (i) LSPR frequency, (ii) Fermi level equilibration, and (iii) the energy of the resulting charge carriers. Even though materials other than Au and Ag have been used for HEI applications, including Pt<sup>[104, 105]</sup> and Al<sup>[51]</sup>, we believe that alloy NPs are particularly promising for future HEI devices. The use of alloy NPs allows for fine-tuning of these three important parameters to fit the requirements of specific hot electron acceptor semiconductor for specific applications.

#### 3.4.3.2. NP size

NPs of less than 20 nm are used as hot electron injectors, since their hot electrons exhibit high energies (up to  $E_F + \hbar\omega$ ),<sup>[83]</sup> and can readily reach the NP surface where they are extracted. Since hot charge carriers created by intraband transitions have a mean free path of  $\sim 10$ -40 nm,<sup>[99]</sup> most of the generated hot carriers in these NPs (< 20 nm) are expected to reach the surface before thermalization. In contrast, hot carriers created by

interband excitations are expected to have much shorter mean free paths ( $\sim 1$  nm)[99] and, therefore, even smaller NPs (2-3 nm) are required for charge extraction. Particles smaller than 2 nm in size are called metal clusters, and exhibit a discrete molecule-like band structure. It has been reported that Au clusters with distinct highest occupied molecular orbital (HOMO)-lowest unoccupied molecular orbital (LUMO) gap can act like a semiconductor with short band gap.[106] Even though this review focuses on plasmonic NPs, it is important to highlight that metal clusters can also be used as co-absorbers to enhance the absorption of metal oxides.[107]

#### 3.4.3.3. NP shape

Varying particle shape enables tuning of the NP LSPR frequency, which makes possible to absorb and utilize light throughout the complete solar spectrum. In addition, it has been suggested that NP shape also affects the amount and location of generated hot carriers within the NP.[108, 109] Harutyunyan *et al.*[108] studied the hot charge carrier dynamics with standard pump-probe measurements for different nanostructure geometries and reported ultrafast dynamics in nanostructures with “hot spots” (areas with greatly enhanced electromagnetic field). The authors ascribed this ultrafast response to an efficient generation of hot electrons from hot spots. In good agreement with this, Sousa-Castillo *et al.*[109] showed that the photochemical response of  $\text{TiO}_2$  is enhanced to a larger extent when functionalized with nanostars than when functionalized with nanorods or spherical NPs. The high photocatalytic activity was ascribed to hot spots present around the spikes of the NP, which promotes the hot carrier generation near the NP-semiconductor interface and the subsequent HEI to the semiconductor.

As will be explained in the following section, the HEI mechanism is the only known plasmonic mechanism that can expand the absorption of a semiconductor water splitting device to longer wavelengths without depending on spectral overlap with the semiconductor. Therefore, if well-defined plasmonic NPs that absorb light beyond the semiconductor absorption edge are used, the HEI can be studied independently, as was

done in the works discussed above. However, in most reports on plasmonic water splitting, an overlap between the semiconductor absorption and the NP absorption/scattering may give rise to many other plasmonic and non-plasmonic effects that simultaneously affect the semiconductor absorption and electrochemical properties.[48],[49],[76],[110],[111],[112],[113],[114],[115-117],[77],[118] These ideas are discussed in the context of recent literature reviewed in the following two sections.

### **3.4.2. Light scattering, light concentration and PIRET**

Unlike the HEI mechanism, the light scattering, light concentration and PIRET mechanisms do not transfer the plasmon energy by charge transfer, but radiatively or by a dipole-dipole interaction, inducing interband excitations in a neighbouring semiconductor. The benefits of these mechanisms in photoelectrochemical water splitting are illustrated in Figure 29 for backside illumination (light reaching the semiconductor first). Most bare semiconductor films exhibit incomplete absorption and the transmitted light is unexploited (Figure 29A). When the semiconductor is decorated with light scattering NPs (c.f. Figure 29B), the transmitted light interacts with the metal NPs, inducing surface plasmons that subsequently decay by scattering the photons back into the semiconductor. As a result, the optical path length through the semiconductor is increased, which increases its absorption and water splitting performance.[44] Figure 29C illustrates a similar principle, where the transmitted light induces LSPR in the metal NP, which generates a highly localized electric field in the vicinity of the NP. This NP near-field can locally excite additional electrons from the valence band of the semiconductor to the conduction band (i.e., through the light concentration and PIRET mechanisms), again, improving the device performance.

Essentially, light concentration and light scattering only increase the interaction of light with the semiconductor by concentrating it and by increasing its path through the semiconductor. Therefore, these mechanisms are called light trapping or photonic enhancement mechanisms. They can increase the absorption of the semiconductor for

plasmonic NP systems with resonances with energies above the optical band gap edge (OBGE) of the semiconductor.[67, 72] PIRET, as with light concentration and light scattering, also occur at wavelengths that overlap with the semiconductor's absorption spectra. However, PIRET has also been demonstrated to generate electron-hole pairs below the semiconductor OBGE, suggesting strong dipole-dipole coupling with band edge states that are optically inaccessible (see section 4.2.2).[46],[95]



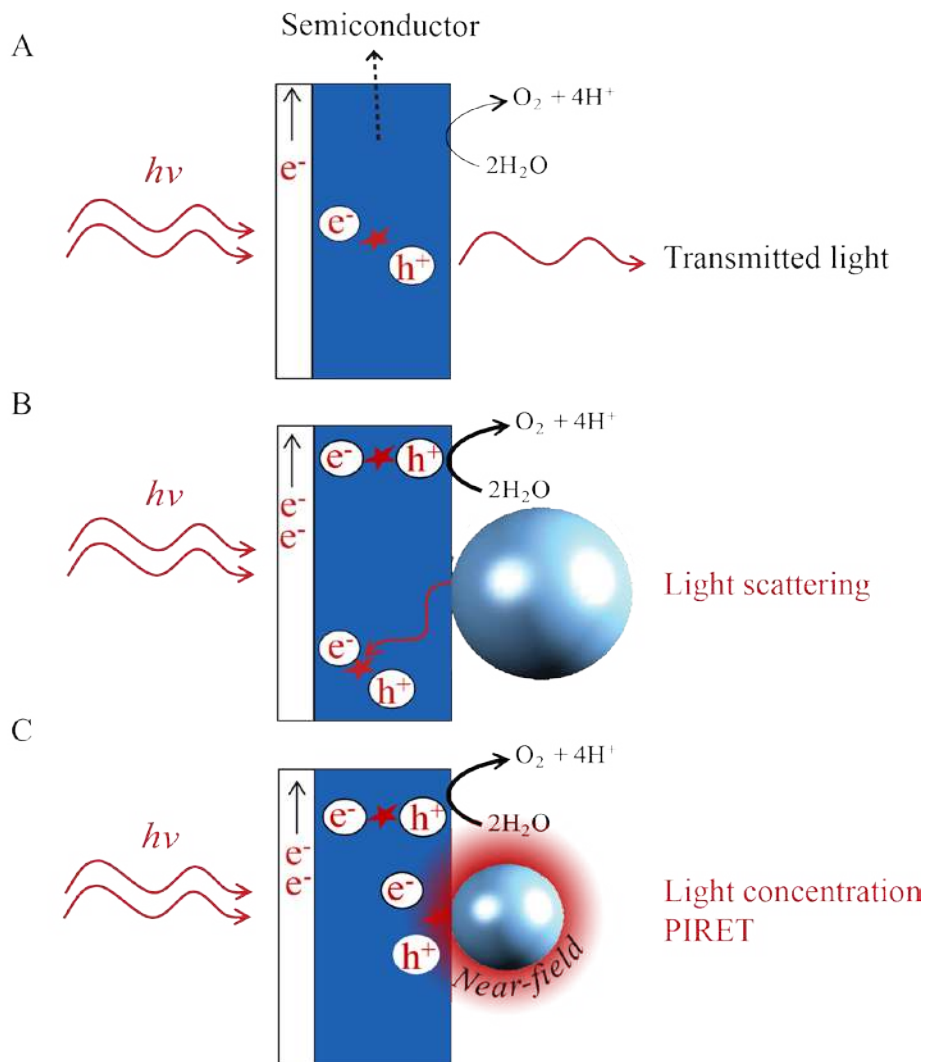


Figure 29. Illustration of absorption enhancement in a water splitting photoanode due to light scattering, light concentration and PIRET.

### 3.4.2.1. Light scattering

An important characteristic of light scattering plasmonic NPs is that the light is scattered preferentially towards the surrounding material that has the largest refractive index.[119] Therefore, when a metal NP is placed on the semiconductor/electrolyte interface (Figure 29B), light is scattered preferentially towards the semiconductor, since they generally have a larger refractive index (RI, e.g., RI  $\sim$  2.5 for BiVO<sub>4</sub>, RI  $\sim$  2.6 for TiO<sub>2</sub> and RI  $\sim$  2.9 for Fe<sub>2</sub>O<sub>3</sub>) than an aqueous electrolyte (RI  $\sim$  1.3). We recently[44] demonstrated a purely scattering effect by decorating the surface of BiVO<sub>4</sub> photoanodes with light scattering 65 nm silver NPs. Figure 30A shows the increase in absorption of  $\sim$  100 nm BiVO<sub>4</sub> grains after NP deposition. It can be clearly seen that the absorption increases only within the semiconductor light absorption range and according to the absorption coefficients of the semiconductor. This suggests that the NPs only absorb negligible light on their own and preferentially scatter the light back to be absorbed by the semiconductor. If the decorating NPs would, instead, be absorbing light and subsequently releasing the energy to the surroundings (e.g., releasing heat), the measured absorption increase would be expected to be only proportional to the surface plasmon resonance curve and not to the semiconductor absorption spectrum. In order to investigate the effect of this absorption increase on the conversion efficiency of the device, IPCE measurements were carried out with and without adding a hole scavenger in the electrolyte (c.f. Figure 30B). The IPCE increase upon NP functionalization without the hole scavenger may be due to the contribution of two beneficial effects: (i) surface effects (e.g., increase catalysis) and (ii) bulk effects (e.g., absorption increase due to the light scattering mechanism). On the other hand, with the addition of the hole scavenger, the hole transport from the semiconductor surface to the electrolyte (i.e., surface effects) is no longer rate limiting and, therefore, any change in the IPCE after NP deposition can be assigned to a bulk effect (e.g., increase in absorption).[120] We therefore assigned the IPCE increase with H<sub>2</sub>O<sub>2</sub> (hole scavenger) shown in Figure 30B to the absorption increase

shown in Figure 30A. In the same work, an even larger absorption increase ( $\sim 6\%$ ) was obtained for front illumination (light reaching the NPs first), demonstrating that the preferential scattering mechanism can reduce the reflected light at the semiconductor-electrolyte interface.

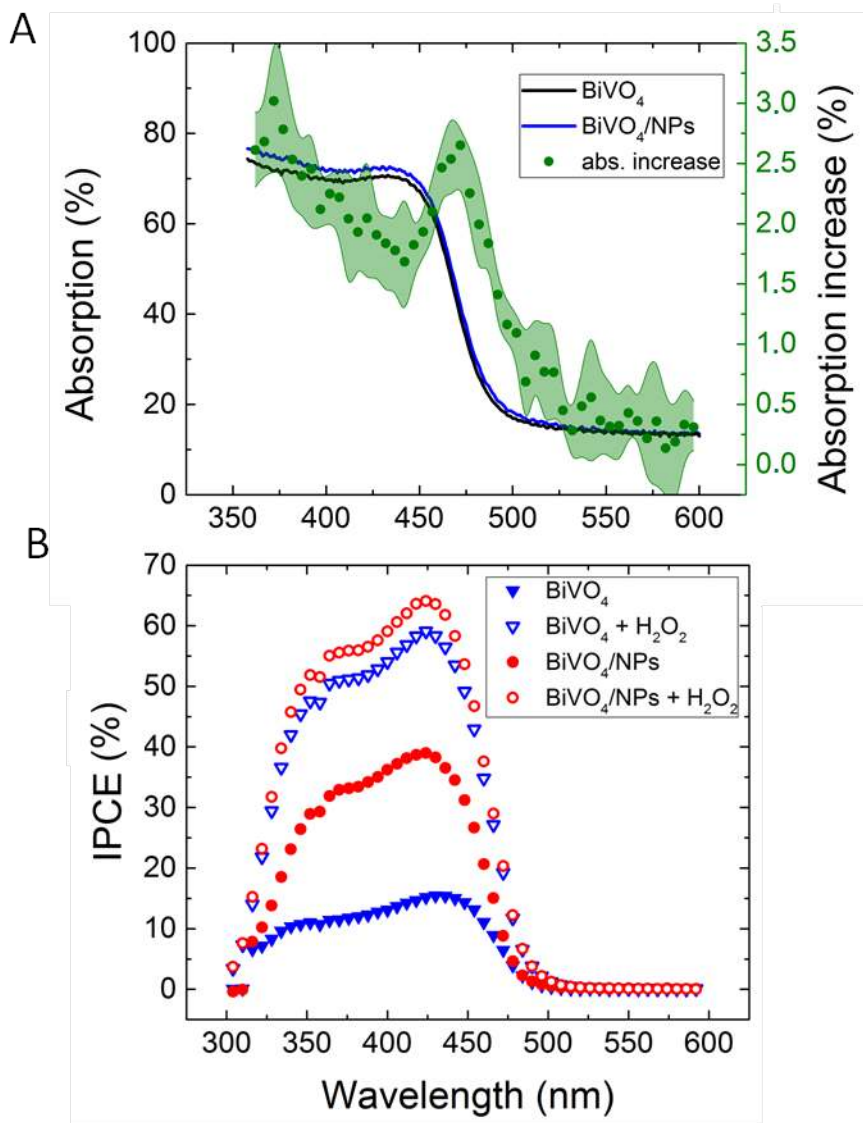


Figure 30. A) Back illumination absorption increase in the BiVO<sub>4</sub> spectra upon deposition of 65 nm Ag NPs. B) Back illumination *Incident* photon to current conversion efficiency (IPCE) measurements before and after 65 nm Ag NP functionalization. Reprinted with permission from ref.[44] Copyright 2016 Wiley-VCH.

### 3.4.2.2. Near-field effects: Light concentration and PIRET

Plasmonic NPs with large absorption cross sections can act as efficient light concentrators.[72, 121-123] In the light concentration mechanism the NP near-field energy is radiatively transferred to the semiconductor, locally generating electron-hole pairs in the semiconductor.[42] As with direct light excitation, in this near-field effect the electron-hole formation rate in the semiconductor is proportional to the local intensity of the electric field (i.e.,  $|E|^2$ ). This is an important feature of this mechanism, since it allows the ability to locally increase the electron-hole generation by orders of magnitude due to the extreme field enhancements that can be achieved around plasmonic NPs.[74] Moreover, concentrating the light allows the ability to promote electron hole pair generation in specific/predefined regions of the semiconductor film, where the photogenerated charge carriers are expected to be efficiently separated (e.g., space charge region, see discussion below). Since this plasmon-induced absorption occurs due to the near-field interaction with the semiconductor, the probability of absorption is expected to increase with the plasmon life-time.[124] Moreover, it was suggested that for this mechanism to be effective, the reciprocal of the surface plasmons life-time (decay rate) must be smaller than the rate of absorption of the semiconductor.[72] Therefore, this antenna effect is limited by the decay of the surface plasmons through other competing damping processes (e.g., intraband and interband excitations in the metal).[43]

Cushing *et al.*[46] discovered that, unlike direct light excitation, the plasmon's strong dipole moment can also locally induce excitations below the OBGE, extending the light utilization of the semiconductor to longer wavelengths. In this near-field mechanism, called PIRET, the surface plasmon decays through a non-radiative dipole-dipole energy transfer to the semiconductor, resulting in electron-hole excitations in the semiconductor. This mechanism was studied in an Au-SiO<sub>2</sub>-Cu<sub>2</sub>O sandwich NP (Figure 31A) by transient absorption spectroscopy (TAS) and wavelength dependent photocatalysis. In this study the

insulating SiO<sub>2</sub> layer prevent HEI from the metal to the semiconductor outer layer (i.e., Cu<sub>2</sub>O), while the near-field can still penetrate the SiO<sub>2</sub> layer and interact with the semiconductor. Wavelength dependent photocatalytic measurements showed a clear enhancement in the conversion efficiency at energies both above and below the semiconductor OBGE (Figure 31B) when compared with the efficiency of the bare semiconductor (Figure 31C). These results, accompanied by transient analysis and theoretical calculations, lead the authors to identify the PIRET mechanism as being responsible for the observed enhancement. Two important advantageous characteristics of PIRET are that (i) unlike light trapping mechanisms, it allows for absorption enhancement of the semiconductor at energies below its OBGE due to dipole-dipole coupling to weak band edge states (yet still requiring a spectral overlap with the semiconductor absorption) and (ii) unlike HEI, it does not require specific band energy alignment of the semiconductor with respect to the Fermi level of the plasmonic NP. The discovery of PIRET modifies the previous understanding of the light concentration mechanism since the localization of the incident electromagnetic field in the vicinity of the NP (NP near-field) cannot only induce electron hole-pairs radiatively (proportionally to the square of the electric field) but can also non-radiatively induce electron-hole pairs below the OBGE in the near-field through a dipole-dipole interaction (PIRET). Since PIRET is a relatively new discovery, most water splitting publications that use small light absorbing NPs to locally increase the semiconductor absorption discuss their results solely under the context of the light concentration mechanism, and should be revisited including PIRET in the interpretation.

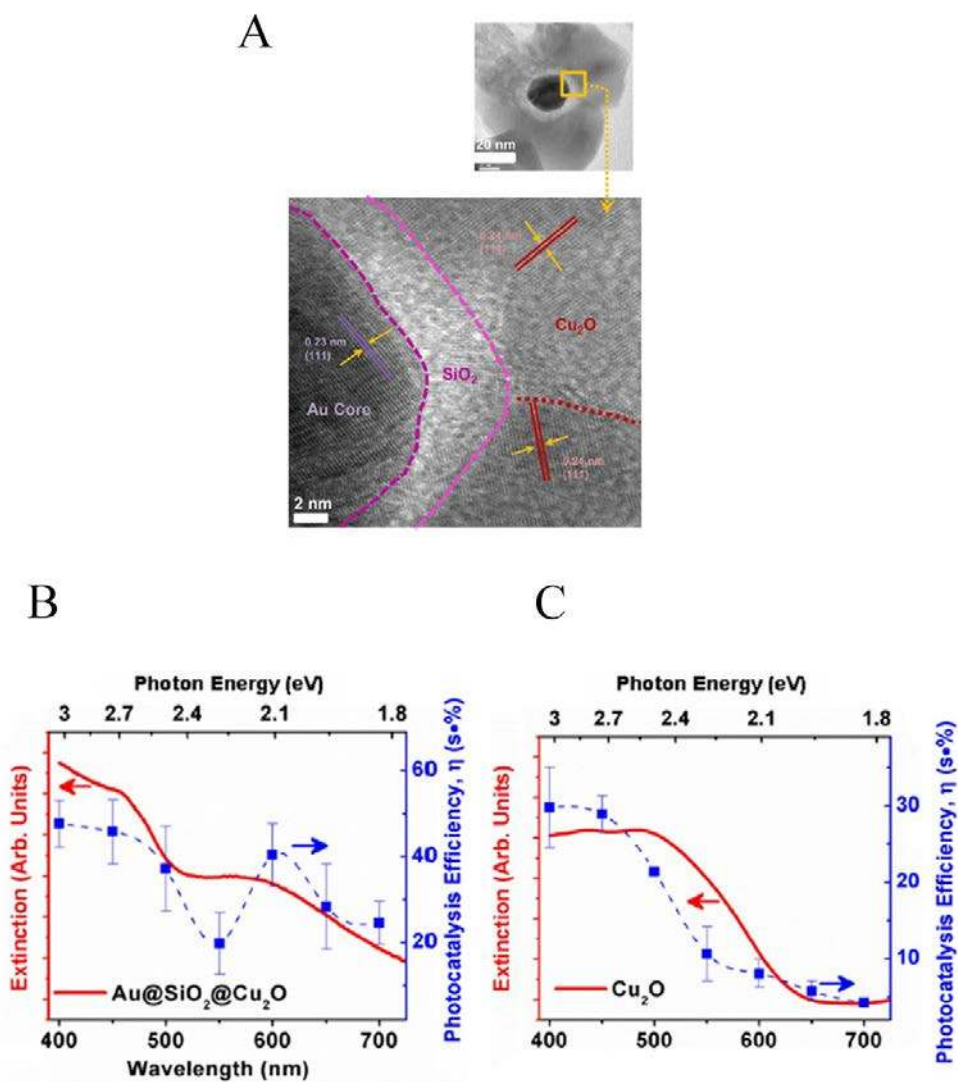


Figure 31. A) Au@SiO<sub>2</sub>@Cu<sub>2</sub>O sandwich structure (top) and an enlargement of the micrograph for the interface regions of the sandwich structure shows the various crystal orientations (bottom). Ultraviolet–visible spectra and photocatalytic action spectra for B) Au@SiO<sub>2</sub>@Cu<sub>2</sub>O and C) Cu<sub>2</sub>O. Reprinted with permission from ref.[46] Copyright 2012 ACS.

For small light absorbing NPs, it is still not clear what percentage of the surface plasmons energy is transferred to the semiconductor through near-field mediated energy transfer (e.g., PIRET) and what percentage is through HEI. However, recently, Cushing *et al.*[75] shed light on this issue by studying the charge carrier dynamics in TiO<sub>2</sub> coated silver NPs with transient absorption spectroscopy (TAS). The authors report that in these coated NPs, HEI and PIRET take place simultaneously, with PIRET being the more prominent mechanism. This points out the fact that the HEI is generally more limited than PIRET, due to its strict dependence on several operating parameters (c.f. Section 4.1., e.g., Schottky energy barrier). In the same work, Cushing *et al.*, also studied other coated NP architectures with transient absorption analysis, finding the conditions needed for HEI and PIRET to occur in a plasmonic NP/semiconductor composite as summarized in Figure 32. Their findings confirm that i) unlike HEI, PIRET only takes place at the region of the spectrum where there is spectral overlap between the semiconductor and the NP and ii) unlike HEI, PIRET can occur even when there is not direct contact between the NP and the semiconductor, since the NP near-field can penetrate through a thin insulating layer. Due to the latter, plasmonic NPs with an insulating coating block the HEI mechanism and, therefore, facilitates the study of PIRET and the light concentration mechanisms. Combined with additional reasons described below, this has led to a significant number of publications that use plasmonic NPs coated with an insulating layer in NP/semiconductor composite water splitting devices.[76]<sup>[110, 125]</sup>





Figure 32. Variables that control the possible plasmonic enhancement near-field mechanisms for extending photoconversion. Connecting the line between the properties of the given core@shell nanoparticle gives the corresponding enhancement mechanisms present. Reprinted with permission from ref.[75] Copyright 2015 ACS.

Thomann *et al.*,[125] functionalized  $\text{Fe}_2\text{O}_3$  films with 50 nm gold NPs coated with a 10 nm shell of  $\text{SiO}_2$  in two configurations that have the (i) NPs embedded in the film and (ii) the NPs at the semiconductor-electrolyte interface. Both configurations showed a clear enhancement in the wavelength dependent photocurrent compared with the bare semiconductor sample. The spectra of this photocurrent enhancement closely followed the simulated absorption increase due to the plasmonic NPs, which evidenced a plasmonic

effect for both configurations. This photocurrent enhancement was assigned, with the help of full-field electromagnetic simulations, to the semiconductor absorption increase in the vicinity of the plasmonic NPs. However, for configuration ii (NPs at the semiconductor surface) a background wavelength independent enhancement was seen, which could not be explained by plasmonic mechanisms such as PIRET or light trapping. The authors speculate that such wavelength independent enhancement arise from surface effects such as catalytic effects on water oxidation by the NPs.

Abdi *et al.*,[76] decorated the surface of BiVO<sub>4</sub> photoanode films with 50 nm SiO<sub>2</sub> coated Ag NPs and found a 2.5-fold photocurrent enhancement under simulated sun illumination at 1.23 V vs. RHE. The authors ascribed this enhancement to both catalytic and optical effects due to the decorating plasmonic NPs. By adding a hole scavenger (H<sub>2</sub>O<sub>2</sub>) in the electrolyte, the authors were able to identify the absorption enhancement contribution to the total IPCE enhancement. An absorption enhancement of 33% was in good agreement with full-field electromagnetic simulations and was ascribed to far-field (light scattering) and, in a lesser extent, to near-field effects. As can be seen in Figure 33, the IPCE increase reported in this work is larger than 15 % IPCE at ~ 425 nm. Such a large IPCE enhancement can be explained by the significant overlap between the semiconductor and the plasmonic NPs absorption spectra, which is a requirement for the light trapping mechanisms (concentration and scattering of light) and PIRET. In order to increase such spectral overlap, the NPs' geometry,[110] composition[110] and their spatial distribution (e.g., dimer formation[44, 51]) can be modified. As example, Erwin *et al.*[110] synthesized Au-Ag core-shell nanostructures to expand the absorption overlap of the NP with the semiconductor. When compared with the absorption of spherical NPs, the Au-Ag core-shell nanostructures (e.g., nanopyramids) exhibited a second absorption mode and broader absorption spectra. These particles were coated with a thin insulating layer of SiO<sub>2</sub> and embedded in mesoporous TiO<sub>2</sub> photoanodes. The absorption of the bare TiO<sub>2</sub>, Au-Ag core-shell nanostructures/TiO<sub>2</sub> composite and spherical Au NPs/TiO<sub>2</sub> composite are shown in Figure 34A. The Au-Ag core-shell nanostructures clearly increased the absorption

of the photoanode in a larger extent than the spherical Au NPs, throughout the measured range. Accordingly, the IPCE enhancement (Figure 34B) was also increased in a larger extent for the Au-Ag core-shell nanostructures/TiO<sub>2</sub> composite. This shows that broadening the absorption overlap between the NP and the semiconductor by modifying the NP geometry and composition can efficiently extend the action of light trapping and PIRET. However, the obtained IPCE increase was low (~ 0.01 %, Figure 34B) due to the poor visible light absorption of TiO<sub>2</sub> (Figure 34A). In the same work, the authors also characterized their samples by measuring the photocurrent under solar simulated light, modulated at different light intensities (i.e., from 50 mW cm<sup>-2</sup> to 300 mW cm<sup>-2</sup>). While the bare photocurrent of the semiconductor showed a half order dependency to the light intensity, the photocurrent of the functionalized composites showed a first order dependency. This phenomenon was previously reported[67] for TiO<sub>2</sub> samples functionalized with Ag NPs, and can be explained by the near-field mechanisms.[42] These mechanisms concentrate the light at the semiconductor/electrolyte interface, increasing the generation of charges near the semiconductor surface where the space charge region is located. Therefore, all the near-field induced charges are efficiently separated due to the built-in electric field in the space charge layer. Consequently, in composites where the near-field induced charges are prominent contributors to the total photocurrent, the bulk charge separation is not a limiting step and the photocurrent shows a first order dependence on light intensity. This important feature of promoting the generation of charges at the space charge region was also studied by Valenti *et al.*,[49] by comparing the light absorption increase of CuWO<sub>4</sub> films when plasmonic NPs were deposited either (i) at the back contact/semiconductor interface or (ii) at the semiconductor/electrolyte interface. It was found that the increase in absorption was more effectively extracted as photocurrent when the NPs were placed at the surface of the semiconductor (ii). This result can again be explained by the efficient separation of the near-field induced charges at the space charge region. Naldoni *et al.*[126] also studied the effect of plasmonic NPs at the semiconductor-electrolyte interface and their findings suggest that both decreasing

the interparticle distance and partially embedding the NPs in the semiconductor can enhance the light concentration in the semiconductor and its photocatalytic activity.

It is important to highlight that the near-field induced charge carriers are not only well separated (due to the electric field of the space charge region) but also the hole (in the case of n-type semiconductors) can readily reach the semiconductor/electrolyte interface in the vicinity of the NP, where other plasmonic or non-plasmonic effects can enhance its injection efficiency to the electrolyte (c.f. section 5.1). Therefore, the light concentration and PIRET effects are promising tools that could effectively enhance the absorption, bulk separation and injection efficiency to the electrolyte.

In addition to discrete NPs, nanotextured and flat metallic films have also been used to increase the semiconductor light absorption at specific regions of a neighbouring semiconductor.[111, 127, 128] The increase in absorption for such systems is (i) related to the evanescent fields of the surface plasmon polaritons (SPPs) of nanotextured films,[111, 129] or (ii) due to the ability of metal films to reflect light and generate resonant cavity modes.[128] In both cases, the films can also be used as back contact current collector in the water splitting device.[111, 128] A synergetic approach combines the LSPR effects provided by plasmonic NPs at the electrolyte-semiconductor interface with additional enhancement mechanisms provided by a metallic film used as back contact. Fang *et al*.[127] showed that this configuration enables light to be efficiently trapped by scattering-reflecting back and forth through the semiconductor between Au nanodisk and a Au mirror film.

Table 1 summarizes the most important physical, optical and electronic characteristics of the above described LSPR mechanisms (i.e., light scattering, light concentration, HEI and PIRET) that can increase the overall absorption of a semiconductor photoelectrode. This table can be used in the design of a plasmonic NP/semiconductor composite photoelectrode to optimize the performance of the semiconductor or to further elucidate the nature of these plasmonic mechanisms.

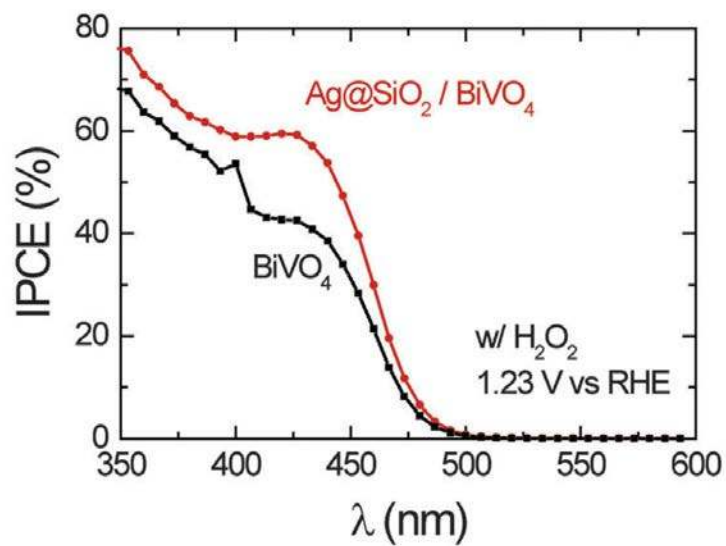
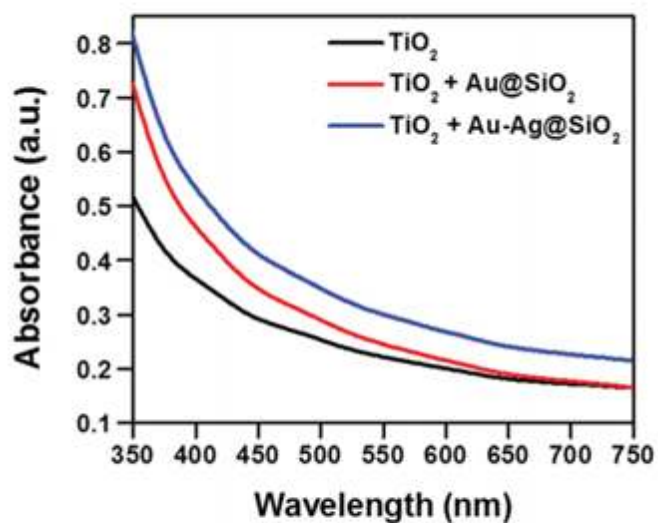


Figure 33. IPCE of bare  $\text{BiVO}_4$  and  $\text{Ag@SiO}_2/\text{BiVO}_4$  at 1.23 V vs. RHE in the presence of 0.5 M  $\text{H}_2\text{O}_2$  in the electrolyte. Reprinted with permission from ref.[76] Copyright 2014 RSC.

A



B

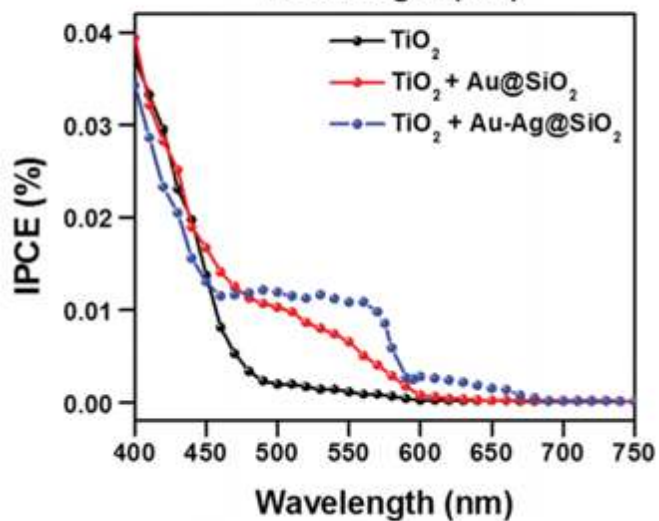


Figure 34. A) Absorption spectra showing enhancement in light absorption with Au-Ag@SiO<sub>2</sub> nanostructures (blue) and Au@SiO<sub>2</sub> nanoparticles (red) embedded within the mesoporous TiO<sub>2</sub> photoanodes relative to TiO<sub>2</sub> only anodes (control, black). B) IPCE curves of nonenhanced (TiO<sub>2</sub> only) and plasmon enhanced photoanodes. The plasmon enhanced

photoanodes are at the optimized concentration. Reprinted with permission from ref.[110] Copyright 2014 RSC

**Table 1.** Optical, physical and electronic characteristics of the plasmonic mechanisms that increase the overall absorption of semiconductor photoelectrodes.

	Light scattering	Light concentration	PIRET	HEI
Origin of enhancement	Photonic enhancement		Dipole-dipole energy transfer	Charge transfer
NP-semiconductor spectral overlap	Required		Required	Not required
Enhancement above optical bandgap edge	✓		✓	✓
Enhancement below optical bandgap edge	✗		✓	✓
NP-semiconductor contact	Not required		Not required	Required
Alignment of band energies	Not required		Not required	Required

### 3.5. Electrochemical effects

Besides light absorption, plasmonic NP can also induce effects in the semiconductor's charge transfer properties (c.f. Subsection 3.5.1), energetics (c.f. Subsection 3.5.2), and band structure (c.f. Subsection 3.5.2.3). In this section we discuss these plasmon-induced and non-plasmon-induced NP effects that do not increase light absorption, but instead facilitate the electrochemical processes in a semiconductor-based water splitting device.

### 3.5.1. Effects on charge transfer

Depending on where the plasmonic NPs are placed in the semiconductor device (embedded or on the surface), the NPs can affect the bulk and/or surface charge transfer processes that the photogenerated charge carriers undergo in the semiconductor to carry out the water splitting half reactions.[48, 49] In the case of n-type semiconductor photoanodes, the photogenerated holes first move through the semiconductor towards the semiconductor surface (bulk charge transport). Subsequently, the hole needs to be transferred from the valence band to the semiconductor surface, where the hole is injected to the electrolyte to evolve oxygen. In particular this last step (charge injection from the semiconductor surface to the electrolyte) has often been ascribed as main responsible for photocurrent increase upon plasmonic NP functionalization.<sup>[44, 48], [49], [50, 130-134]</sup> Haro *et al.*,[48] obtained a significant increase in the catalysis and, in a lesser extent, an increase in the bulk conductivity after embedding gold NPs in a mesoporous TiO<sub>2</sub> photoanode. After discarding HEI and light trapping mechanisms (based on PEC characterization), the authors studied the influence of the NPs on the bulk conductivity, chemical capacitance and surface charge transfer resistance of the TiO<sub>2</sub> with electrochemical impedance spectroscopy (EIS) analysis. In this technique, the impedance (complex voltage to current ratio) spectrum of the system is obtained by applying a bias AC voltage to the PEC cell at different frequencies and recording the current response. Subsequently, the impedance spectrum is modelled with an equivalent circuit (EC), consisting of capacitors and resistors, that represents the limiting transport processes in a well-known PEC system. Haro *et al.*,[48] used a well-established transmission line model as EC to fit the impedance spectra at different applied potentials. The parameters for the surface charge transfer, chemical capacitance and bulk conductivity were extracted from the fittings, as shown in Figure 35. It can be clearly seen that the charge transfer resistance at the surface progressively decreased with the NP load in the photoanode. The chemical capacitance also increased upon NP functionalization, which is explained in this



work by the increase of the density of states due to the gold NPs. Finally, Figure 35C shows that the bulk conductivity slightly increased with the NP load.

The increase in the charge carrier injection to the electrolyte could be due to the inherent catalytic properties of the metal, Fermi level equilibration[80] (cf. Section 5.2.1.) or due to plasmonic effects, such as plasmonic heating,[78] improved adsorption of polar molecules that align in the direction of the NP near-field[79] and hot electron induced activation of co-catalysts.[135] While EIS is a powerful tool that allows the ability to quantify the resistance of the charge injection to the electrolyte, other techniques must be developed in order to elucidate and distinctly recognize the different plasmonic and non-plasmonic effects that facilitate the charge transport processes. These charge transfer effects are of extreme importance when they occur in combination with plasmonic mechanisms that increase the absorption of the semiconductor, since for this case the NP plays the dual role of (i) light absorber and (ii) co-catalyst. This dual effect has already been demonstrated in different NP/semiconductor systems where the NP facilitate the charge carrier transport and also enhance the absorption through HEI[40] or light trapping.[44] <sup>40</sup> In particular for near-field effects (light concentration and PIRET) occurring near the semiconductor surface, the additional plasmonic induced charge carriers i) are well separated due to the space charge region, ii) more readily reach the semiconductor surface, and iii) exhibit enhanced charge injection to the electrolyte due to the enhanced catalysis near the NP. In this way, near-field induced charge carriers are expected to efficiently contribute to the overall photocurrent.

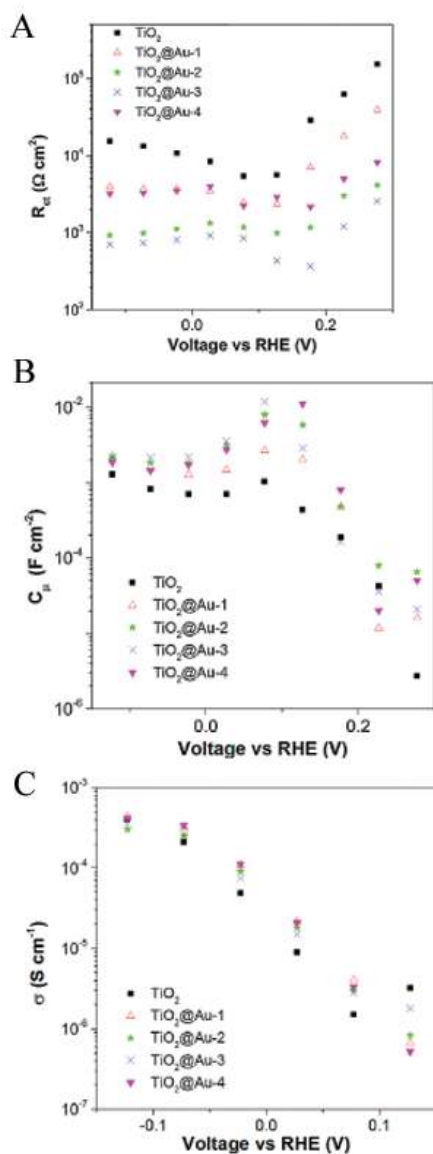


Figure 35. A) Charge transfer resistance, B) chemical capacitance, and C) conductivity of mesoporous  $\text{TiO}_2$  films without and with different loading of Au NPs under illumination at  $100\text{mW}\cdot\text{cm}^{-2}$ . The conductivity has been only calculated in the potential range where the transmission line is observed. Reprinted with permission from ref.[48] Copyright 2014 Elsevier Ltd.

### 3.5.2. Effects on energetics

#### 3.5.2.1. Semiconductor-metal Fermi level equilibration

In a photoelectrochemical cell, the semiconductor photoelectrode Fermi level equilibrates with the redox couple in the electrolyte (n-type semiconductors equilibrate with oxidation potentials and p-type semiconductors equilibrate with reduction potentials). When a n-type semiconductor is illuminated with light, electron-hole pairs are generated and the Fermi level shifts to more negative potentials. The difference between the Fermi level in the dark and under illumination determines the internal photovoltage.[136] Similarly, when a metallic NP/semiconductor composite photoelectrode is used, the Fermi level equilibrates between the metal, semiconductor and redox couple. Interestingly, when the metallic NP/semiconductor composite is illuminated, the Fermi level of the composite can have an even larger negative shift (compared to the bare semiconductor) due to the ability of metallic NPs to store the photogenerated electrons coming from the semiconductor (cf. Figure 36).[80] The transfer of electrons from the excited semiconductor to the NP continues until photoequilibrium between the metal and the semiconductor is obtained. Such a metallic NP induced negative shift in the Fermi level results in an increased photovoltage and photocatalytic activity (cf. Figure 36).[80, 137]

A clear correlation between the extent of the negative induced Fermi level shift and the increased catalytic activity was shown by Subramanian *et al.*[80] The authors decorated TiO<sub>2</sub> NPs with Au NPs of different diameters (i.e., 3-, 5- and 8 nm) and found that decreasing NP size consistently increased the Fermi level negative shift and the photocatalytic activity of the composite. The increase of the Fermi level shift with decreasing NP size could be explained by the discrete nature of the energy levels in Au NPs, which results in a larger shift in energy level per stored electron for the smaller NPs.[80]

This subsection shows that metallic plasmonic NPs can not only increase the absorption of the semiconductor and improve its charge transfer properties, but they can also alter its electronic band energetics. Since properties like the plasmonic NP size determine the efficiency of both (i) plasmonic mechanisms that increase the semiconductor absorption, and (ii) non-plasmonic mechanisms that improve the energetics, a trade-off typically needs to be made according to the specific semiconductor limitations.

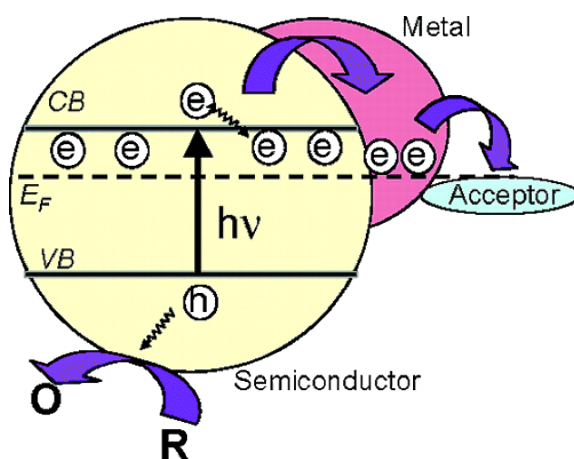


Figure 36. Fermi Level Equilibration in a Semiconductor–Metal Nanocomposite System. Reprinted with permission from ref.[80] Copyright 2004 ACS.

### 3.5.2.2. HEI induced Fermi level shift

The work of Chen *et al.*[47] and Mubeen *et al.*[45] (see section 4.1.) demonstrate that the oxygen and hydrogen evolution reactions on NP/semiconductor composite photoelectrodes can be driven by hot holes and hot electrons, respectively. However, Shi *et al.*[77] recently suggested that hot electrons and holes can improve the performance of water splitting electrodes in other ways apart from directly driving the water splitting half reactions. They report an increase in the electrocatalytic activity (i.e. higher current at

lower over-potentials) for the hydrogen evolution reaction on MoS<sub>2</sub> upon gold nanorod decoration. This increase is explained by a change in the MoS<sub>2</sub> Fermi level due to hot electron injection from the illuminated gold nanorods to the semiconductor (i.e., MoS<sub>2</sub>). The absorption spectra of the materials synthesized in this work are shown in Figure 37A. The nanorod-decorated material (Au-MoS<sub>2</sub>) exhibit a LSPR longitudinal absorption mode of the gold nanorods at 813 nm. The electrocatalytic activity of the synthesized materials without illumination, using a typical three-electrode configuration, is shown in Figure 37B together with the activity of the Au-MoS<sub>2</sub> composite under illumination with an 808 nm laser. The result of interest for this review is the positively shifted onset potential (from -0.22 to -0.16 V vs. RHE) when the composite electrode (i.e., Au-MoS<sub>2</sub>) is illuminated with the 808 nm laser. The activity of this composite was also tested with 532 nm and 650 nm lasers but no activity improvement was observed. The fact that activity only improved under illumination with the light energy that corresponds to the LSPR mode (i.e., 808 nm, c.f. Figure 37A), strongly suggests a surface plasmon resonance effect. Moreover, *in-situ* electrochemical LSPR scattering measurement under a dark-field microscope suggest hot electron injection from the Au nanorod to the MoS<sub>2</sub> semiconductor. Based on these results, Shi *et al.* propose the mechanism illustrated in Figure 38A (following the processes I, III and V) to explain the observed enhancement (Figure 37B). Process I represents the hot electron-hole formation due to the non-radiative SPR decay. The hot electron could then recombine within the NP (process II), be injected to the conduction band of the semiconductor (process III) and be injected to the electrolyte to drive the hydrogen evolution reaction (process IV). The authors discard this last option (IV) as a main process, since gold is not a good hydrogen evolution catalyst. The hot electron injection to the semiconductor's conduction band (process III) is a more likely process to occur due to the low Schottky barrier between gold and MoS<sub>2</sub>. Once in the semiconductor conduction band, the hot electron could then be injected back into the electron-deficient NP (process V in Figure 38A). The continuous hot electron injection to the conduction band of the semiconductor increases its Fermi level (c.f. Figure 38B), bringing it closer to the energy

level of the redox pair  $H^+/H_2$ . This effect can decrease the overpotential of the semiconductor for the hydrogen evolution reaction as observed by the authors (c.f. Figure 37B). Finally, different hole scavengers were added to the electrolyte in order to avoid charge recombination in the gold nanorod (process II in Figure 38A), which would in turn promote the hot electron injection to the semiconductor. In accordance with the suggested mechanism, the use of hole scavengers (e.g., ethanol, methanol, glucose) provided higher current densities. More specifically, ethanol further lowered the onset potential of the composite under laser illumination as much as -0.12 mV. These results show that plasmonic NP decoration can also increase the catalytic activity of semiconductors and promises to be a key component towards the replacement of precious metals (e.g., platinum) as catalyst electrodes for the hydrogen evolution reaction in water splitting devices.

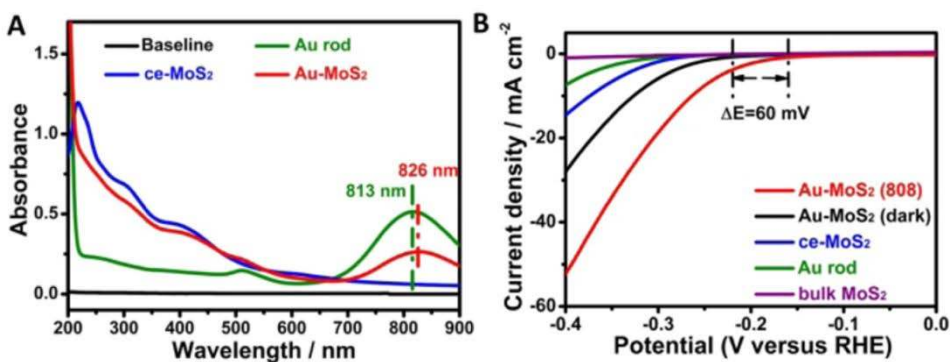


Figure 37. A) UV-vis spectra of MoS<sub>2</sub> (ce-MoS<sub>2</sub>) nanosheet, gold nanorod and Au-MoS<sub>2</sub>. B) Hydrogen evolution reaction polarization curves obtained on several catalysts as indicated. Reprinted with permission from ref.[77] Copyright 2015 ACS.

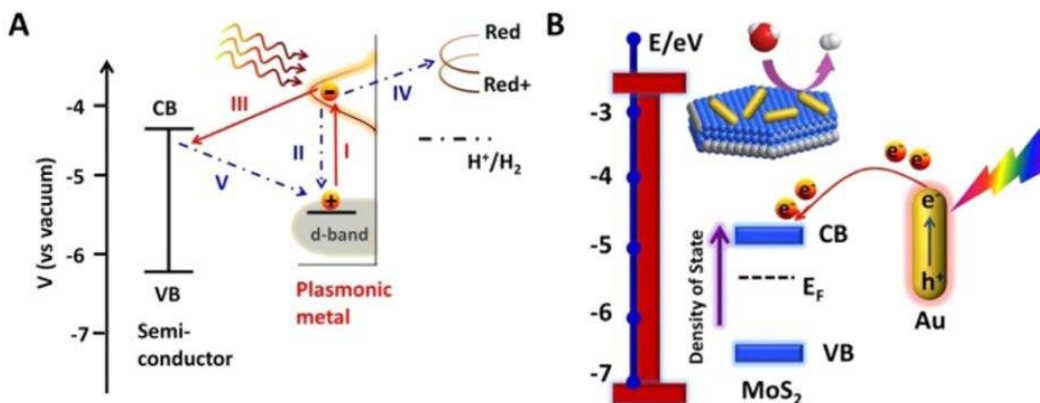


Figure 38. A) Different plausible hot electrons transfer pathways likely to occur during SPR. B) Schematic Au-MoS<sub>2</sub> and energy level diagram illustrating hot electrons injection and change of MoS<sub>2</sub> Fermi level. Reprinted with permission from ref.[77] Copyright 2015 ACS.

### 3.5.2.3. Effects on band structure

Finally, Chen *et al.*,<sup>[47]</sup> studied the influence of gold NPs' near-field on the conduction/valence band of ZnO nanorods (same system discussed above in section 3.4.1) with X-ray absorption near edge structure (XANES). In this study, the gold NPs (with sizes of  $4.7\text{nm} \pm 0.7\text{nm}$ ) were sitting uniformly on the surface of the ZnO nanorods. With XANES the authors observed a significant increase in the ZnO conduction band vacancies under plasmon-induced illumination, which can promote the separation of photogenerated electrons and holes. Such changes in the band structure near the NP/semiconductor interface were ascribed to the NP near-field. Therefore, the authors show that two advantageous plasmonic effects can occur in a plasmonic NP/semiconductor composite: (i) near-field induced generation of vacancies in the conduction band, and (ii) absorption increase through HEI.

### 3.6. Conclusions and outlook

Significant progress has been made in the last several years to elucidate the mechanisms (i.e., light scattering, light concentration, PIRET and HEI) by which plasmonic NPs can improve the solar light utilization of semiconductor photoelectrodes for efficient solar water splitting. Research on metal oxide water splitting photoelectrodes, which exhibit good catalytic activity and stability in aqueous media, benefits particularly from these new plasmonic mechanistic insights to circumvent the specific optical weaknesses of the different metal oxides. Table 1 summarizes some of the most important characteristics of each plasmonic mechanism that can enhance the light utilization in NP/semiconductor water splitting devices. As shown in this table, PIRET and HEI are mechanisms that can extend the light utilization of metal oxide photoelectrodes with large bandgap energies to the visible and near-infrared light. In particular, the HEI mechanism, whose efficiency is independent of the semiconductor absorption, allows for light harvesting of the entire solar irradiation spectrum by, for example, using rod NPs with different geometrical aspect ratios that collectively absorb light throughout the solar irradiation spectrum. However, the HEI mechanism suffers from many requirements, including the adequate alignment of the semiconductor band energies with respect to the Fermi level of the metal NP, which restricts its use to a limited number of material combinations. By contrast, photonic enhancements and PIRET do not require any band alignment, but their efficiency strongly depends on the NP-semiconductor spectral overlap. Therefore, following the great advances in the synthesis of well-defined NPs and NPs systems (e.g., NP dimers, NP-metallic films systems, etc) with predefined absorption spectra, more research needs to be directed towards ideal spectral overlap to achieve complete light absorption in promising new metal oxides with short band gaps by means of photonic enhancement and PIRET.

While significant progress has been made in the understanding of the mechanisms to increase the light utilization of metal oxides, less attention has been paid to other roles



that plasmonic NPs play when used in high performing metal oxide photoelectrodes (e.g., as a catalyst, co-catalyst, recombination centers, etc). In particular, metal oxide photoelectrodes operating at low applied biases are often limited by poor bulk or interfacial charge transfer processes that are highly sensitive to the presence of metal NPs. In order to obtain a real optical contribution of plasmonic NP in efficient plasmonic NP/semiconductor water splitting devices, a better understanding of the NP charge transfer and energetics effects in the semiconductor must be further elucidated.

### **Acknowledgements**

Financial support from the following institutions is gratefully acknowledged: NWO (VENI project granted to Dr. Wilson A. Smith), the Wenner-Gren Foundations, the Swedish Research Council, the Swedish Foundation for Strategic Research, the Royal Swedish Academy of Sciences, the ÅForsk Foundation and the Swedish Government Strategic Research Area in Materials Science on Functional Materials at Linköping University (Faculty Grant SFO-Mat-LiU No 2009 00971).

#### 4. Hot Carrier Generation and Extraction of Plasmonic Alloy Nanoparticles

##### Abstract

The conversion of light to electrical and chemical energy has the potential to provide meaningful advances to many aspects of daily life, including the production of energy, water purification and optical sensing. Recently, plasmonic nanoparticles (PNPs) have been increasingly used in artificial photosynthesis (e.g. water splitting) devices in order to extend the visible light utilization of semiconductors to light energies below their bandgap. These nanoparticles absorb light and produce hot electrons and holes that can drive artificial photosynthesis reactions. For n-type semiconductor photoanodes decorated with PNPs, hot charge carriers are separated by a process called hot electron injection (HEI), where hot electrons with sufficient energy are transferred to the conduction band of the semiconductor. An important parameter that affects the HEI efficiency is the nanoparticle composition, since the hot electron energy is sensitive to the electronic band structure of the metal. Alloy PNPs are of particular importance for semiconductor/PNPs composites, because by changing the alloy composition their absorption spectra can be tuned to accurately extend the light absorption of the semiconductor. This work experimentally compares the HEI efficiency from Ag, Au and Ag/Au alloy nanoparticles to TiO<sub>2</sub> photoanodes for the photoproduction of hydrogen. Alloy PNPs not only exhibit tunable absorption, but can also improve the stability, electronic, and catalytic properties of the pure metal PNPs. In this work, we find that the Ag/Au alloy PNPs extend the stability of Ag in water to larger applied potentials while, at the same time, increasing the interband threshold energy of Au. This increasing of the interband energy of Au suppresses the visible-light-induced interband excitations, favoring intraband excitations that result in higher hot electron energies and HEI efficiencies.<sup>2</sup>

---

<sup>2</sup> This chapter has been based on ref:138. Valenti, M., et al., *Hot Carrier Generation and Extraction of Plasmonic Alloy Nanoparticles*. ACS Photonics, 2017.

## Introduction

Photoelectrochemical (PEC) water splitting is a promising approach to produce hydrogen as a sustainable fuel from abundant resources.[25, 139] In a PEC water splitting cell based on a single photoelectrode, semiconductors are used to absorb light and generate charge carriers (electron-hole pairs), which are subsequently separated to carry out the oxygen and hydrogen evolution reactions on the semiconductor surface and corresponding metal counter electrode. N-type metal oxide semiconductors have been extensively investigated as water splitting photoanodes due to their excellent stability in aqueous solutions and their ability to catalyze the oxygen evolution half reaction.[25] However, an important limitation of metal oxide semiconductors is their poor visible light absorption due to their relatively large band gaps. Decorating metal oxide semiconductors with plasmonic nanoparticles (PNPs) that absorb visible light can extend the hydrogen generation of metal oxide water splitting devices to light energies below the semiconductor *optical* band gap edge (OBGE).[140] These metallic PNPs are characterized by the light-induced collective oscillation of their free electrons (surface plasmons). The below OBGE light harvesting ability of the decorating PNPs has been explained by two mechanisms, (i) hot electron injection (HEI),[140] and (ii) plasmon induced resonance energy transfer (PIRET).[141] HEI (i) is the process in which plasmon induced hot electrons (electrons with energies higher than the metal Fermi level) in the metallic PNPs are transferred to the conduction band of a contacting semiconductor. In the case of a semiconductor photoanode, the hot electron transferred to the conduction band migrates to the metal counter electrode (e.g., Pt) to evolve hydrogen. The “hot” hole, left behind in the metal PNP, can be extracted with an electron acceptor catalyst to evolve oxygen[140] or by adding a sacrificial agent in the electrolyte.[142] PIRET (ii), on the other hand, is a mechanism in which the surface plasmon decays by inducing electron hole pairs directly in the semiconductor through a dipole-dipole interaction with a transient exciton.[143] One important advantage of the HEI mechanisms is that, unlike PIRET, its efficiency does not

depend on the semiconductor's absorption band edge,[141] allowing the ability to extend the light utilization of the device to even longer wavelengths (e.g., near infrared). However, the efficiency of the HEI mechanism is significantly limited since the plasmon induced hot electrons/hot holes need to efficiently undergo several processes: (i) the charges need to reach the surface of the PNP, (ii) the hot electrons must have sufficient energy, above the metal Fermi level, to cross the metal/semiconductor Schottky energy barrier and (iii) the hot holes need to be efficiently extracted to continuously maintain charge neutrality in the metal PNP upon the HEI process.[144] Due to the poor overall efficiency of these processes, most of the plasmon induced hot electrons are not harvested, but instead decay by releasing heat. The efficiency of the above mentioned processes strongly depend on the size, shape and composition of the PNPs. These dependencies need to be studied independently in order to reveal the true potential of the HEI mechanism. Of particular importance is the PNP composition, since it not only affects the metal/semiconductor Schottky energy barrier[145] but also determines the plasmon-induced hot electron energies.

Recent theoretical studies[145-149] show that the energy profile of the plasmon-induced hot electrons is extremely sensitive to the composition of the particle, which determines the amount of hot electrons that can cross the Schottky energy barrier (process ii). These studies find that intraband excitations (e.g., within the conduction band) induced by visible light can produce high energy hot electrons and holes, while visible-light-induced interband excitations (e.g., from the d band to unoccupied states above the Fermi level) produce high energy holes but low energy electrons ( $\sim$  Fermi energy). Two metals which have been used extensively as PNP's are Ag and Au. Figure 39A illustrates that when Ag is illuminated with visible light only intraband transitions occur, generating highly energetic hot electrons. In contrast to this, Figure 39B illustrates that when Au is illuminated with visible light, interband transitions occur due to its relatively lower interband energy ( $\sim$  2.3 eV), resulting in the generation of hot electrons with low energies.[149] Therefore, the visible-light-induced interband transitions limit the

production of highly energetic electrons in Au, making it a less attractive hot electron injector material than Ag for solar driven applications. However, small light absorbing Ag PNPs exhibit resonance frequencies in the violet region of the visible spectrum, overlapping with the absorption of most promising metal oxides. Ideally, the PNP absorption should be tuned to absorb light with energies below the metal oxide band gap to extend the light absorption of the semiconductor. One promising way to red-shift the resonance frequency of Ag PNPs in a controlled way is by alloying the Ag nanoparticles with Au.[150] Since the resonance frequency of Ag/Au nanoparticles depends on its composition, the resonance frequency can be tuned to a predefined region of the spectrum that accurately extends the light absorption of a specific semiconductor. However, while significant attention has been given to study the hot electron energy and the hot electron injection ability of pure metal PNPs,[145-149] the hot electron energies and injection efficiencies of alloy PNPs are still unknown. This work experimentally explores the HEI ability of Ag/Au alloy PNPs to increase the PEC efficiency of TiO<sub>2</sub> photoanodes. Moreover, we compare the HEI efficiencies of the alloy PNPs with their pure metal counterparts (Ag and Au PNPs) by using PNPs of the same shape and size.

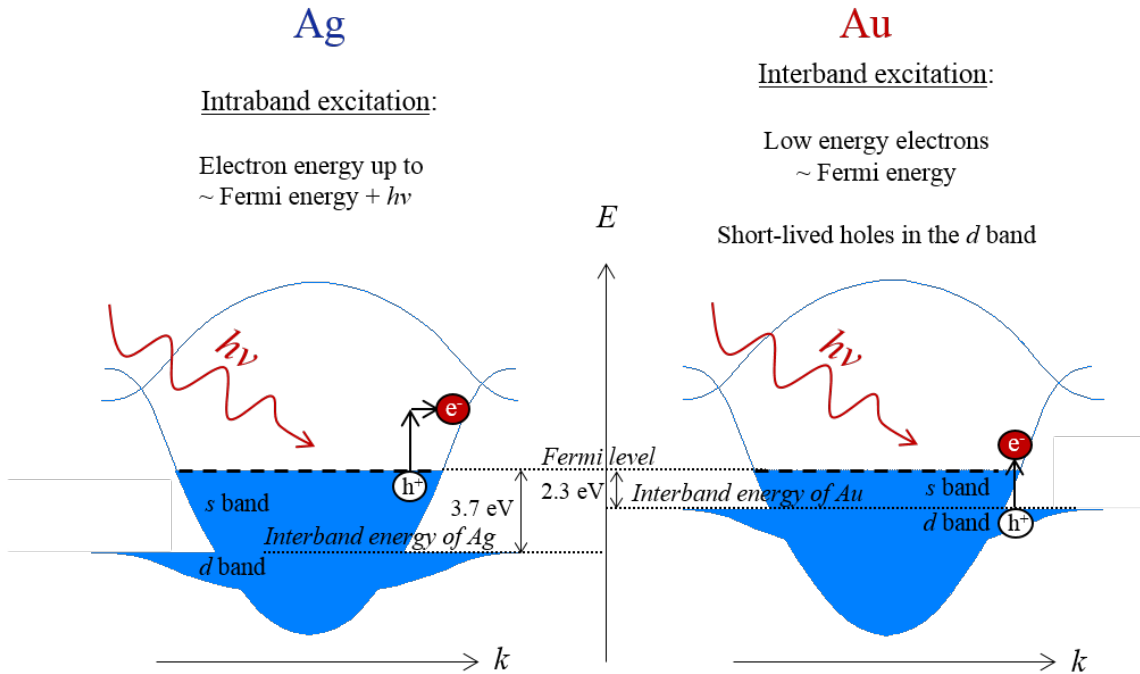


Figure 39. Illustration of the phonon-assisted intraband electronic transitions in Ag PNPs (A) and interband electronic transition in Au PNPs (B) when illuminated with visible light. In specific, interband transitions in Au are caused by violet, blue and green light in the visible spectrum, which have higher energies than the interband energy threshold of Au. Phonon-assisted intraband transition (A) is given here as an example, however other competing processes can also assist intraband transitions, such as direct absorption (for PNPs smaller than  $\sim 10$  nm) or electron-electron scattering (prominent for light with shorter wavelengths within the visible range). Only phonon-assisted and direct intraband transitions result in energetic hot electrons.[151]

### Results and Discussion.

Ag, Au and Ag/Au alloy PNPs were produced in the gas phase with a spark discharge particle generator,[152] where high frequency electrical discharges are induced between two closely spaced metal rods of the corresponding metals (i.e., Au, Ag and 50-50 atomic % Au/Ag alloy). The metallic vapor produced in each electrical discharge is

dragged with a nitrogen gas flow, where the vapor condensates into nanoparticles,[153] which subsequently agglomerate to form larger fractals. These fractal particles were then made spherical by passing them through an oven, and size selected to 15 nm with a differential mobility analyzer.[154] The round morphology and size (i.e., 15 nm) of the synthesized PNPs are confirmed with transmission electron microscopy (TEM) as shown in Figure 40.

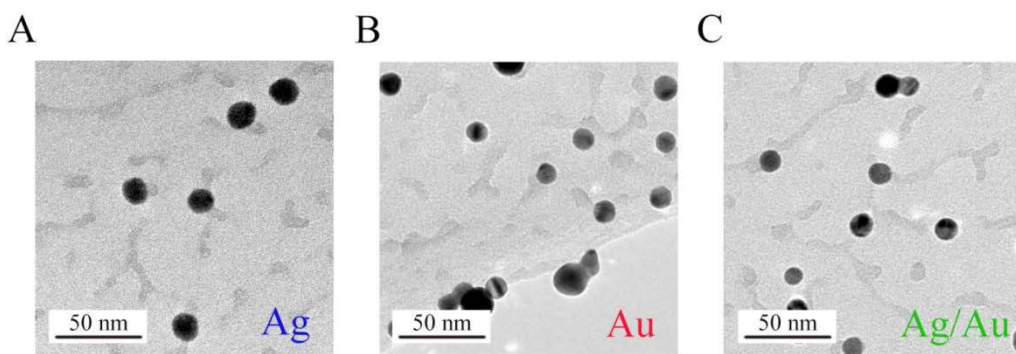


Figure 40. TEM micrographs of the synthesized Ag (A), Au (B) and alloy (C) PNPs.

In order to study the effect of the synthesized PNPs on the PEC properties of  $\text{TiO}_2$ , the PNPs of the three compositions were deposited from the gas phase onto the surface of ultrathin  $\text{TiO}_2$  films. Three electrode PEC measurements were carried out in a water/methanol solution. In these experiments the methanol acts as a sacrificial agent, removing the (i) photogenerated holes (due to  $\text{TiO}_2$  interband excitations) that reach the surface of the semiconductor and the (ii) plasmon induced “hot” holes generated in the PNPs. The most likely reactions to occur on the photoanode are the oxidation of methanol to formaldehyde and, to a lesser extent, further oxidation of formaldehyde to formate. On the other hand, the corresponding electrons migrate to a Pt counter electrode to drive the hydrogen evolution reaction.

Cyclic voltammetry measurements under solar illumination for the bare  $\text{TiO}_2$

sample and the PNPs decorated samples are shown in Figure 41. In the anodic sweep of the Ag PNP decorated sample, a Ag oxidation peak can be clearly seen at  $\sim 0.5$  V vs. SHE, which limits the plasmonic effects of Ag PNPs to devices that operate at lower applied potentials ( $< 0.5$  V vs. SHE). In the cathodic sweep the corresponding reduction peak can be seen at  $\sim 0.25$  V vs. SHE. In the anodic sweep of the sample decorated with alloy PNPs, the oxidation peak exhibits an anodic shift with respect to that of the Ag sample (cf. Figure 41). Therefore, alloying Ag with Au extends the stability of Ag to a larger range of applied potentials. On the other hand the sample decorated with Au PNPs does not present an oxidation peak at the applied potentials.

At applied potentials below the beginning of the oxidation peak of the corresponding decorating metal PNPs (below  $\sim 0.5$  V vs. SHE for Ag, below  $\sim 0.8$  V vs. SHE for Ag/Au and the full measured range for Au), a clear enhancement on the photocurrent density can be observed for all the decorated samples when compared with the bare TiO<sub>2</sub> sample. The origin of this photocurrent density enhancement can be a contribution of optical and electrochemical PNP effects acting below and above the semiconductor's OBGE. The wavelength dependent incident photon to current efficiency (IPCE) of the bare TiO<sub>2</sub> film is shown in Figure 42, together with the IPCE of a TiO<sub>2</sub> film decorated with Ag PNPs. The bare TiO<sub>2</sub> sample exhibits photocurrent response only below 380 nm, which is consistent with its OBGE energy. On the other hand, the sample decorated with Ag PNPs not only increased the performance of the bare semiconductor above its OBGE (i.e., below  $\sim 380$  nm) but also extended the photoresponse of the semiconductor device to the visible region of the spectrum (from 380 nm to 540 nm), below the semiconductor OBGE energy. The photocurrent enhancement above the OBGE could be due to (i) a plasmonic effect (e.g., photonic enhancement[155]), (ii) a surface effect that facilitates the charge transfer from the surface to the electrolyte (e.g., improved catalysis[48]) or due to a contribution from both (i) and (ii). On the other hand, the enhancement below the OBGE of TiO<sub>2</sub> can only be explained by plasmonic effects, such as the HEI mechanism,[144] PIRET mechanism[143] or by a contribution of both. Therefore, we discuss both possible



enhancements (i.e., below and above the OBGE) separately in the following two subsections for samples decorated with Ag, Au and alloy (Ag/Au) PNPs.

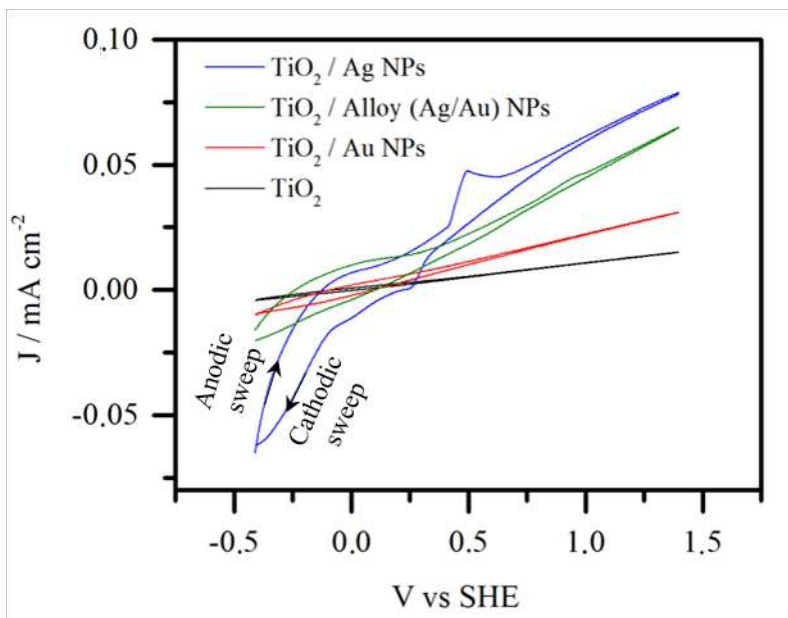


Figure 41. Anodic and cathodic cyclic voltammetry sweeps under solar illumination for the  $\text{TiO}_2$  films with and without decorating PNPs. The corresponding cyclic voltammetry sweeps in the dark are shown in Figure S1 (*Supporting information*).

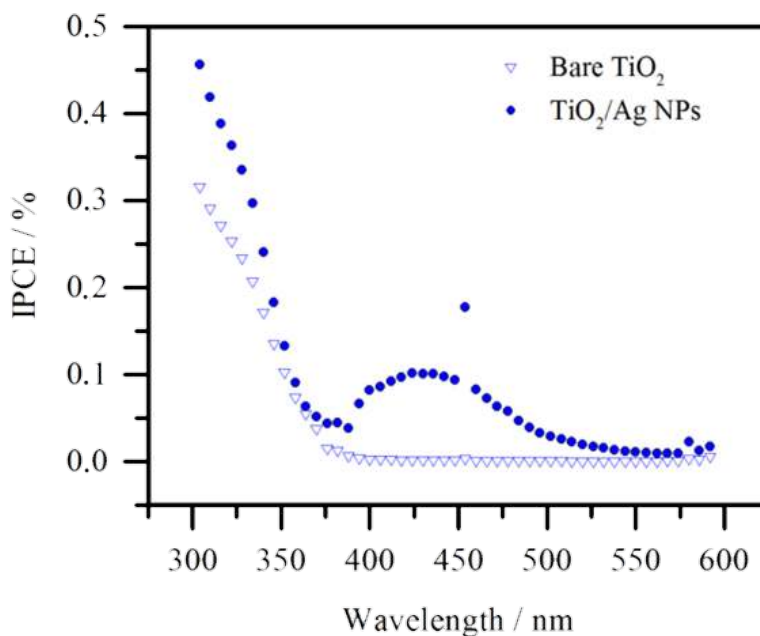


Figure 42. IPCE values of a TiO<sub>2</sub> film with and without decorating 15 nm Ag PNPs at -0.1 V vs. SHE.

**Enhancement below the TiO<sub>2</sub> optical band edge energies.** Figure 43A shows the IPCE increase ( $\Delta$ IPCE) in the visible region of the spectrum for TiO<sub>2</sub> films after decoration with either Ag, Au or alloy (Ag/Au) PNPs. Figure 43B shows the corresponding absorption increase of the samples after the PNP deposition, which shows the surface plasmon resonance modes of the PNPs at  $\sim$  405 nm for Ag,  $\sim$  525 nm for Au and  $\sim$  450 nm for the alloy, which are in good agreement with other studies on alloy (Ag/Au) PNPs.[156] Clearly, the IPCE values increased upon PNP deposition in distinct regions of the spectrum that correspond to the surface plasmon resonance mode of each PNP material. It is observed, however, that the IPCE peaks are red shifted (by  $\sim$  25 nm) with respect to the absorption peaks, which is explained by the change in the PNP surrounding media refractive indexes used in the absorption (air) and IPCE (water/methanol solution) measurements.[157] The IPCE enhancement for each of the materials tested exhibited an almost symmetrical shape

with a mode at the corresponding surface plasmon resonance frequencies. If PIRET would be playing a major role in the enhancement, the IPCE increase ( $\Delta$ IPCE) curve would not only be proportional to the surface plasmon resonance curve but also to the TiO<sub>2</sub> absorption bands, which increases with decreasing wavelength. Instead, the enhancements in Figure 43A are only proportional to the surface plasmon resonance absorption modes and, therefore, it can be concluded that the HEI mechanism, which is independent on the semiconductor absorption, is the most prominent contributor to the enhancements. Therefore, the IPCE values below the TiO<sub>2</sub> band gap are proportional to the Fowler theory modified by the plasmon absorption spectrum (cf. Equation 1)[158, 159] that predicts the number of hot electrons with sufficient energy to overcome the metal/semiconductor energy barrier:

$$IPCE \sim C_F \frac{(h\nu - q\phi_B)^2}{h\nu} S(\nu) \quad (34)$$

where,  $C_F$  is the Fowler emission coefficient,  $h\nu$  is the energy of the excitation light,  $q\phi_B$  is the metal/semiconductor interfacial energy barrier, and  $S(\nu)$  is the plasmon absorption spectrum.

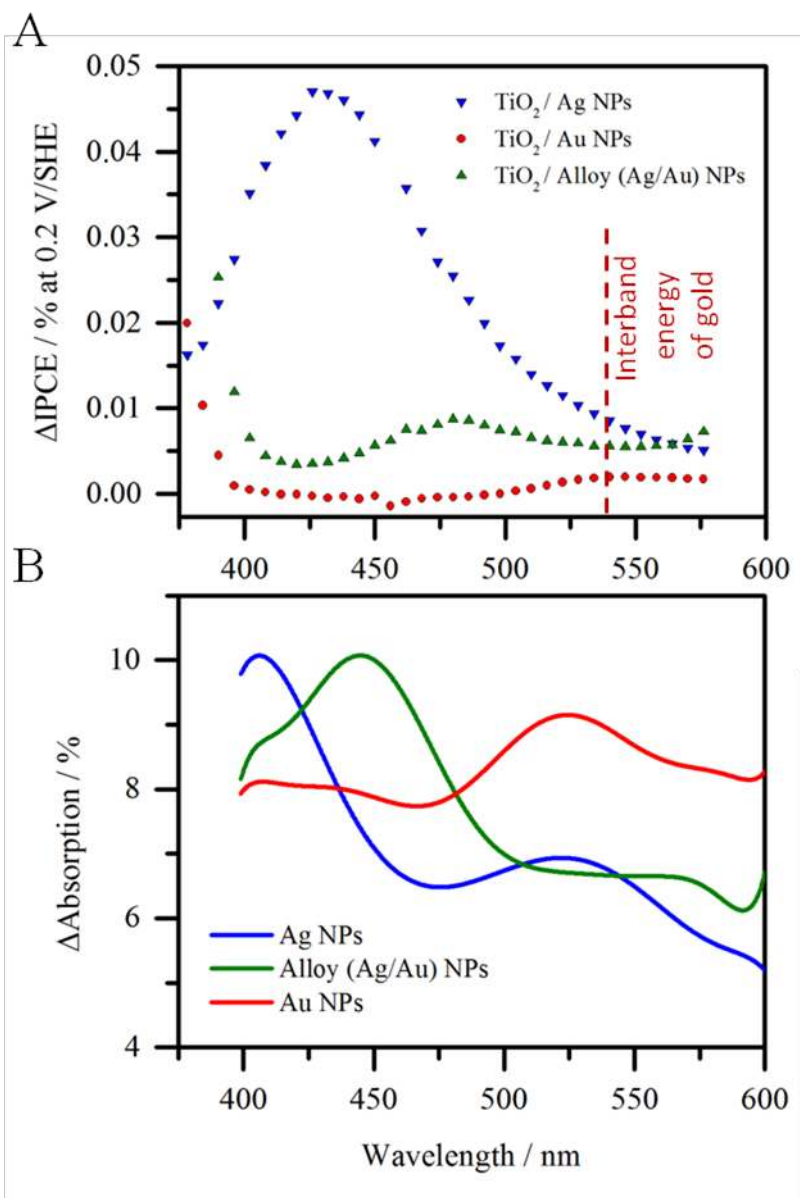


Figure 43. A) IPCE enhancement of TiO<sub>2</sub> films when decorated with 15 nm Ag, Alloy (Ag/Au) and Au NPs at 0.2 V vs. SHE. B) Corresponding absorption increase.

Even though each of the TiO<sub>2</sub> samples decorated with PNPs of different compositions (i.e., Ag, Au and Ag/Au) increased their visible light absorption by ~ 10 % at the PNPs' resonance frequencies (Figure 43B), the corresponding IPCE increase differed significantly (cf. Figure 43A). Namely, Ag exhibited an IPCE increase of ~ 0.05 % at ~ 430 nm, while the alloy exhibited an increase of ~ 0.01 %, and Au an increase of less than 0.01 % at their corresponding resonance frequencies. If the IPCE values in Figure 43A would be limited by light absorption, each of the PNPs with different compositions (Ag, Au and alloy) should exhibit the highest IPCE values at their corresponding resonance frequencies, where they absorb the most light (generating the largest hot electron populations). However, the Ag PNPs' IPCE increase is larger than that for the Au and alloy PNPs throughout the measured spectrum (cf. Figure 43A). At the resonance frequency of the alloy PNPs (i.e., ~ 475 nm) and the resonance frequency of the Au PNPs (~ 550 nm), where the Ag PNPs absorb less light than its counterparts, Ag exhibits larger IPCE values. Therefore, the IPCE values of the alloy and Au PNPs in Figure 43A must not be limited by a low population of plasmon-induced hot electrons (light absorption,  $S(\nu)$  in Equation 1) but, instead, by a non-efficient hot electron injection process. A plausible explanation for the low HEI efficiency of Au is that above its interband energy of ~ 2.3 eV (below ~ 539 nm) hot electrons are mainly created by interband excitations and have low energies (~ Fermi energy) as explained above (cf. Figure 39). Therefore, Au hot electrons generated by light energies below ~ 539 nm do not surpass the interface energy barrier and, thus, no photocurrent is produced in this range (red data points in Figure 43A). More interestingly, the alloy PNPs, unlike the Au PNPs, exhibit IPCE response below ~ 539 nm (above the interband energy of Au), which suggests that the alloy PNPs interband energy threshold is shifted to lower wavelengths, allowing energetic intraband-induced hot electrons to cross the interfacial energy barrier. The interband energy threshold of the Ag/Au alloy is expected to be located around 3 eV (~ 413 nm), between that of Ag (~ 3.7 eV) and that of Au (~ 2.3 eV).[160] However, unlike the pure metals, the Ag/Au alloy does not exhibit a

sharp threshold energy of interband transition,[160] and its hot electron energies have not been predicted or studied. The interband transition threshold energies of the synthesized PNPs are studied here by X-ray photoelectron spectroscopy (XPS) in order to investigate the origin (i.e., interband or intraband) of the generated hot electrons. The valence band XPS spectra of the Ag, Au and alloy PNPs are shown in Figure 44. The sharp intensity increase in the XPS spectra of Ag and Au correspond to their d-band energies (with respect to the Fermi level of the metal), which are in good agreement with the optical interband energy thresholds of the pure metals ( $\sim 2.3$  eV for Au and 3.7 eV for Ag). Unlike the pure metallic PNPs, the alloy PNPs exhibit a valence band spectrum without a sharp intensity increase and, therefore, a distinct interband energy threshold cannot be assigned to them. Instead of a sharp transition, the alloy d-band density of states increases progressively (Figure 44) from  $\sim 2.3$  eV (interband energy threshold of Au) to  $\sim 3.7$  (interband energy threshold of Ag). Within this transition energy region the alloy is expected to generate less visible-light-induced interband excitations than Au due to the decrease in the d-band density of states revealed by the XPS spectra (cf. dashed arrow in Figure 44). A decrease in interband excitations increases the probability of intraband excitations (generation of energetic hot electrons), which can explain the visible light HEI response between  $\sim 450$  nm and  $\sim 520$  nm of the alloy PNPs (green data points in Figure 43A). Nevertheless, even though the XPS spectrum of alloy PNPs exhibits a more limited d-band density of states than Au in the visible region energy, only the Ag PNPs with a well-defined threshold energy of  $\sim 3.7$  eV ensure that only intraband transitions are generated in the visible region. Therefore, while in the alloy PNPs a fraction of the hot electrons is generated by interband excitations and does not cross the interfacial barrier due to their low energy ( $\sim$  Fermi energy), in Ag PNPs only energetic intraband hot electrons are created, resulting in larger HEI efficiencies (Figure 43A). Figure 45 illustrates the relation between the d-band energy with respect to the metal Fermi level (revealed by XPS, Figure 44) and the efficiency of the HEI process (Figure 43A), which explains the decrease in HEI efficiencies with increasing Au composition in the tested PNPs.

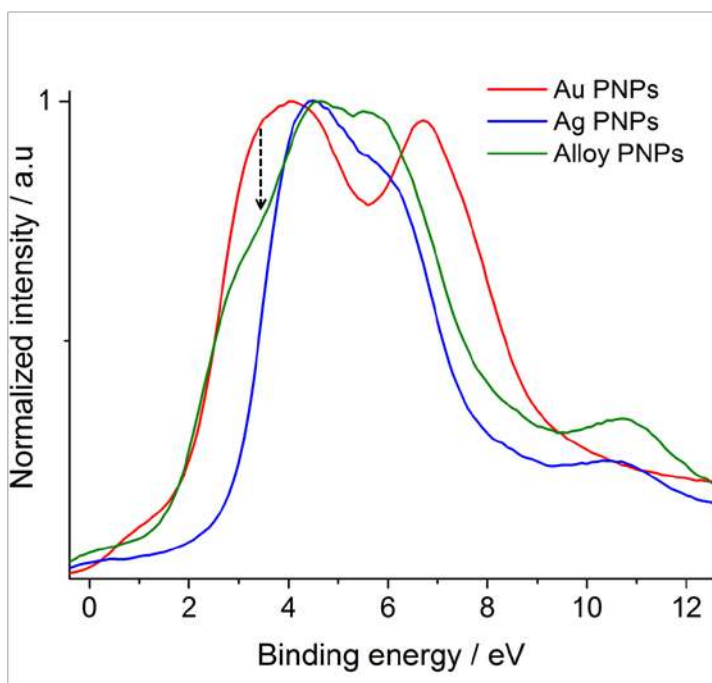


Figure 44. Valence band XPS spectra of the synthesized PNPs.

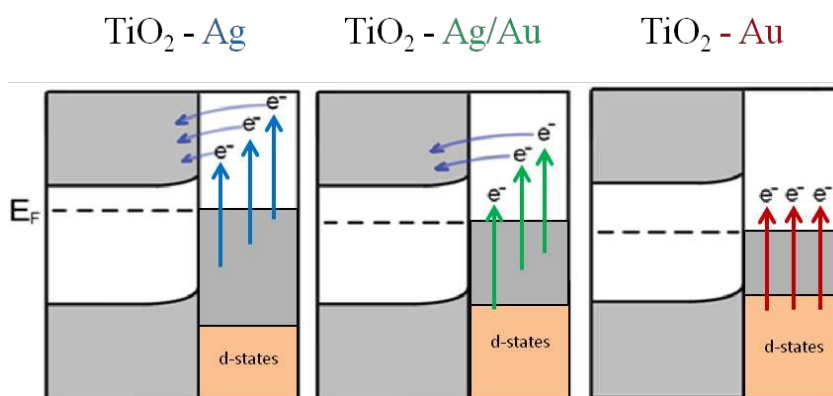


Figure 45. Illustration of the relative Fermi equilibration energies ( $E_f$ ) and hot electron energy (above the Fermi level equilibration) of Ag, alloy (Ag/Au) and Au PNPs when

illuminated with visible light. When Ag is illuminated, only intraband transitions occur, since the energy difference between the position of the d-states and the Fermi level is larger than that of the irradiating visible light. On the other hand, Au allows for prominent interband excitations when illuminated with violet, blue and green light, due to its relatively shorter distance between the d-states and Fermi level. When Ag/Au is illuminated, it undergoes less interband excitations than Au, since its d-states are shifted further away from the Fermi level. Interband excitations exhibit low hot electron energies ( $\sim$  Fermi energy), limiting the HEI process.

Moreover, the energetic intraband hot electrons in the alloy PNPs are also expected to have a lower HEI efficiency than those generated in the Ag PNPs, due to the higher interfacial energy at the alloy/TiO<sub>2</sub> interface when compared to that of Ag/TiO<sub>2</sub>. According to the Schottky-Mott rule, the interfacial energy barrier can be estimated by the difference between the work function of the metal ( $\sim$  4.26 eV for Ag and  $\sim$  5.1 eV for Au)[161] and the electron affinity of the semiconductor ( $\sim$  3.9 eV for TiO<sub>2</sub>)[162]. Therefore, it is expected that the interfacial energy barrier of the alloy/semiconductor interface will increase with increasing Au composition due to the larger work function of Au when compared to Ag. Such an increase in the interfacial barrier with increasing Au composition would decrease the HEI efficiency (cf. Equation 1) of the energetic intraband hot electrons.

Another material-dependent process that can affect the HEI efficiencies is the hot electron charge transport from the excitation point to the extraction point (i.e., PNP / semiconductor interface). However, the average intraband charge carrier mean free paths are expected to be  $\sim$  20 nm for both Au and Ag,[146, 149] which is more than the double of the radius of the particles used in this work. These mean free path values virtually ensure that the hot carriers reach the PNP surface and can be extracted. Therefore, the differences in the hot electron energies between the PNP materials are a more plausible explanation to the material-dependent HEI efficiencies shown in Figure 43A.

In order to estimate the injection efficiency of visible-light-induced intraband hot electrons obtained in this work, the absorbed photon to current conversion efficiency



(APCE) was calculated by correcting the IPCE (Figure 43A) for the absorbed light (Figure 43B). Ag PNPs exhibited an APCE of  $\sim 0.5\%$  when illuminated with 425 nm light. Therefore, while this work clearly shows that visible-light-induced intraband hot carriers can be extracted more efficiently than interband hot carriers, the intraband HEI efficiency ( $\sim 0.5\%$ ) of the tested 15 nm Ag PNPs has been proven to be too limited for any solar-to-fuel energy conversion application. The low efficiency indicates that most of the visible light energy absorbed by the 15 nm Ag PNPs is dissipated thermally.

**Enhancement above the TiO<sub>2</sub> optical band edge.** Figure 46 shows the TiO<sub>2</sub> IPCE enhancements upon deposition of Ag (Figure 46A), Au (Figure 46B) and alloy (Figure 46C) PNPs for 5 different applied potentials (namely, - 0.1, 0.2, 0.5, 0.8 and 1.1 V vs. SHE). While increasing the applied potential does not significantly change the enhancement below the OBGE, the enhancement above the OBGE increases progressively. In addition, the enhancement above the OBGE is orders of magnitude larger than that of the HEI below the OBGE, which indicates that any contribution from the HEI mechanism above the OBGE is not significant compared to other effects. Above the OBGE, light trapping mechanisms such as light concentration and light scattering can play an important role. However, the extinction of light by the small PNPs used in this study is primarily due to light absorption and not due to light scattering. Therefore, in our experiments, light trapping due to the concentration of light around the decorating PNPs is the only relevant mechanism that could play a role in the measured enhancement. However, light trapping mechanisms occur only in the region of the spectrum where the absorption of the PNP and the absorption of the semiconductor overlap. According to this interpretation, the sample decorated with Ag PNPs should exhibit the most pronounced light trapping effect, since its surface plasmon resonance is positioned approximately at the TiO<sub>2</sub> band gap edge region and, therefore, traps light that can be absorbed by the semiconductor. On the other hand, the samples decorated with Au and alloy PNPs exhibit a surface plasmon resonance at longer wavelengths, trapping light below the OBGE of the semiconductor.

Clearly, the enhancement above the OBGE shown in Figure 46 is more significant for the alloy than for the pure metals (i.e., Ag and Au), which suggests that the light trapping mechanism is not the most prominent contributor to the measured enhancement. Moreover, this lack of correlation between the PNP/semiconductor absorption overlap and the IPCE enhancement suggests that the enhancement above the OBGE is not due to any plasmonic effect but, instead, due to a co-catalytic property of the metallic PNP that facilitates the charge transfer from the semiconductor surface to the electrolyte. In order to unravel the origin of this co-catalytic effect, more electrochemical experiments (e.g., electrochemical impedance spectroscopy measurements) must be carried out.

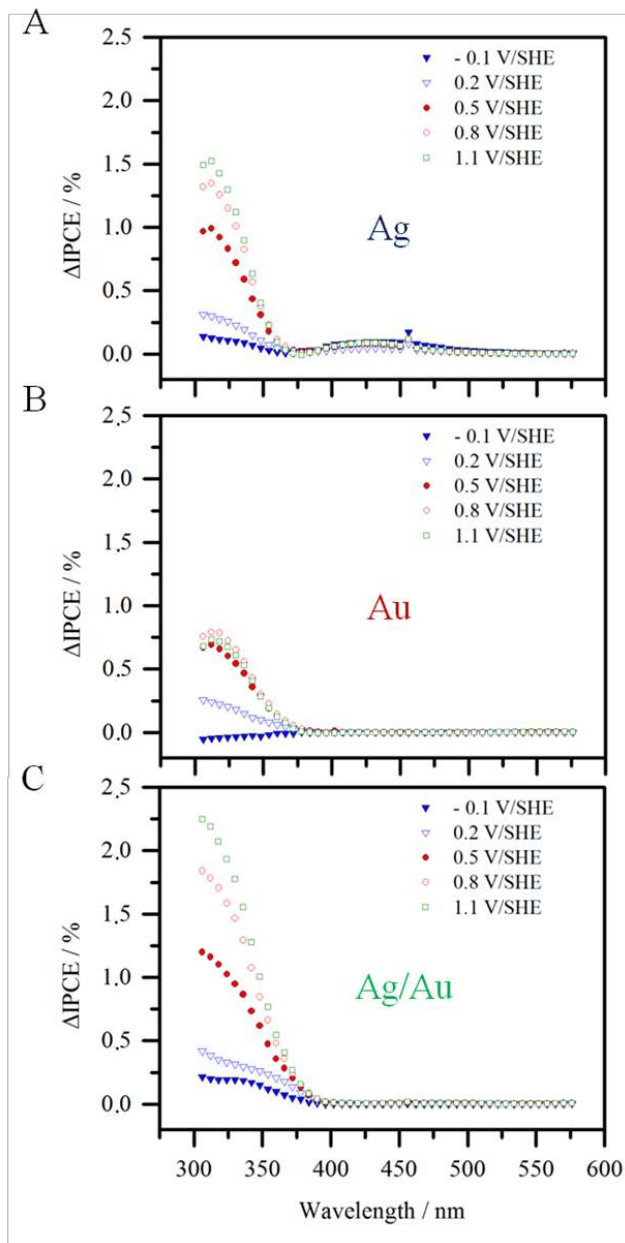


Figure 46. Wavelength dependent IPCE enhancement curve of  $\text{TiO}_2$  films when decorated with 15 nm Ag (A), Au (B) and Alloy (Ag/Au, C) PNPs at different applied potentials.

In summary, hot electron injection efficiencies from Ag/Au alloy PNPs to TiO<sub>2</sub> photoanodes were compared to those of Ag and Au PNPs by measuring the photoelectrochemical conversion efficiencies of the composite photoanode below the TiO<sub>2</sub> OBGE. Our results revealed that Ag/Au alloy PNPs exhibit higher efficiencies than Au and significantly lower efficiencies than Ag (by ~ 8-fold). Since the PNPs used in this work are smaller than the mean free path of the hot electrons, the measured hot electron injection efficiencies are not limited by hot charge transport to the PNP surface. Instead, the measured hot electron injection efficiencies are expected to be limited by low hot electron energies and high interfacial energy barriers between the TiO<sub>2</sub> and the different metals. It is well known that Au PNPs undergo interband electronic transitions when illuminated with visible light, which results in low energy hot electrons and, therefore, low hot electron injection efficiencies. In this work, we assign the higher hot electron injection efficiency of the Ag/Au (when compared to Au) to a decrease in visible-light-induced interband transitions. Au presents an interband energy threshold shift to higher energies (lower wavelengths) when alloyed with Ag. This shift increases the visible-light-induced intraband excitations, which results in higher hot electron energies and injection efficiencies. However, unlike the pure PNPs, the threshold energy of the alloy PNPs is not sharp and the d-band density of the states decreases progressively in a transition region. Therefore, we conclude that alloying Ag with Au decreases the interband excitations in the visible region, but does not suppress them entirely. This interband transition region was revealed here by XPS and explains the lower HEI efficiencies of the alloy PNPs when compared to the Ag PNPs. Nevertheless, the Ag/Au PNPs not only exhibit higher hot electron injection efficiencies than Au, but, unlike their pure counterparts, also allow to tune their absorption spectrum by changing their Ag/Au composition ratio. Such tunability can be used to perfectly extend the light utilization of semiconductors to lower light energies (< OBGE).

Despite the advantages in stability and absorption tunability of PNPs, the HEI efficiencies measured in this work (e.g., APCE of  $\sim 0.5\%$  for 15 nm Ag PNPs at 425 nm) are too low for any photoelectrochemical solar-to-fuel energy conversion applications (e.g., water splitting, CO<sub>2</sub> reduction). From the measured efficiencies we conclude that most of the absorbed visible light in 15 nm Ag, Au and alloy (Ag/Au) PNPs dissipate without generating energetic hot electrons.

Finally, the photoelectrochemical conversion efficiency of the TiO<sub>2</sub> film was also studied by irradiating light with energies above the semiconductor's OBGE. In this region of the spectrum ( $\lambda < \sim 380$  nm), the photocurrent of the PNP/TiO<sub>2</sub> composites is mainly due to TiO<sub>2</sub> interband excitations. When the metal PNPs were deposited, the IPCE of the semiconductor significantly increased. This increase cannot be caused by light trapping effects due to the lack of absorption overlap between the PNPs and the semiconductor. Instead, the photocurrent increase is ascribed here to a more efficient charge transfer across the semiconductor electrolyte interface upon the metallic PNP deposition. However, the origin of this charge transport effect must be further investigated.

## **Methods.**

**PNPs synthesis.** The 15 nm Ag, Au and Ag/Au PNPs were synthesized in the gas phase with a spark discharge particle generator coupled with a differential mobility analyzer as described briefly above, and in detail elsewhere.[49] In the spark discharge particle generator electrodes of Ag, Au and Ag/Au alloy (50-50 atomic %) were used for the PNPs synthesis of the corresponding compositions. The electrodes, having a purity of 99.95%, were purchased from Goodfellow Cambridge Limited.

**TiO<sub>2</sub>/Metallic PNP composite electrodes synthesis.** A 10 nm film of Ti was deposited on FTO (fluorine tin oxide) coated glass substrates by magnetron sputter deposition. The samples were annealed in a tube oven at 500 °C for 5 hours under flowing air (20 ml/min) to oxidize the Ti films to TiO<sub>2</sub>. Charged metallic PNPs were deposited electrostatically from the gas phase to the TiO<sub>2</sub> surface.

**Photoelectrochemical measurements.** The photoelectrochemical measurements were carried out in a methanol / water (50 v/v %) solution in an electrochemical cell using a three-electrode configuration: a working electrode whose potential was controlled by a potentiostat (EG&G PAR 283), a reference Ag/AgCl electrode (XR300, saturated KCl + AgCl solution (KS120), Radiometer Analytical), and a coiled Pt wire as a counter electrode. The photocurrent measurements shown in Figure 41A and S1 were performed under simulated AM1.5 solar illumination with a Newport Sol3A Class AAA solar simulator (type 94023A-SR3). The monochromatic photocurrents (IPCE) were measured using a 200 W quartz tungsten-halogen lamp coupled into a grating monochromator with a 6 nm step, as described in detail elsewhere.[163]

**Absorption measurements.** The absorption spectra measurements of the PNPs shown were carried out with a PerkinElmer-Lambda 900 spectrometer equipped with an integrated sphere device. Measurements were conducted before and after PNP deposition, so that the influence of the PNPs on the TiO<sub>2</sub> absorption spectra could be determined.

### **Acknowledgment**

This work is supported by an NWO VIDI grant awarded to Wilson A. Smith. We thank Nejra Causevic for making the table of contents image, Joost Middelkoop for the TEM measurements, Herman Schreuders for the magnetron sputter deposition and Bart Boshuizen for the XPS measurements.

## Supporting information

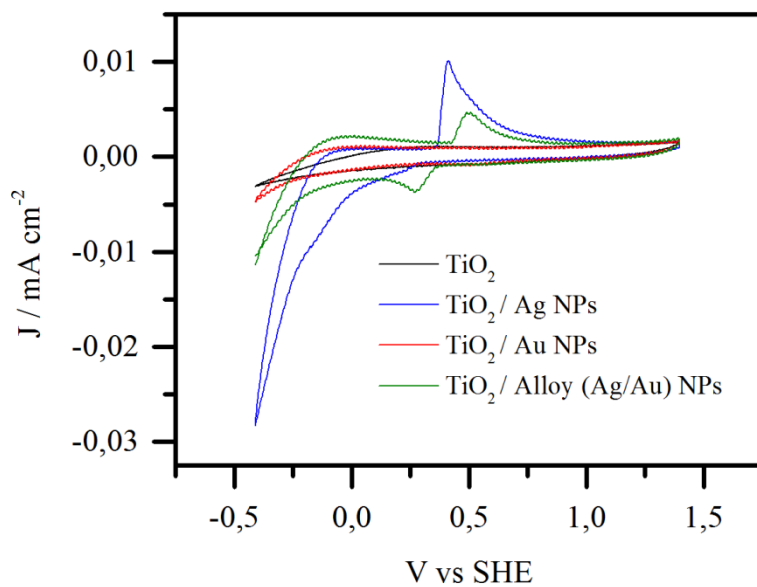


**Figure S1.** Anodic and cathodic cyclic voltammetry sweeps in the dark for the  $\text{TiO}_2$  films with and without decorating plasmonic PNPs.

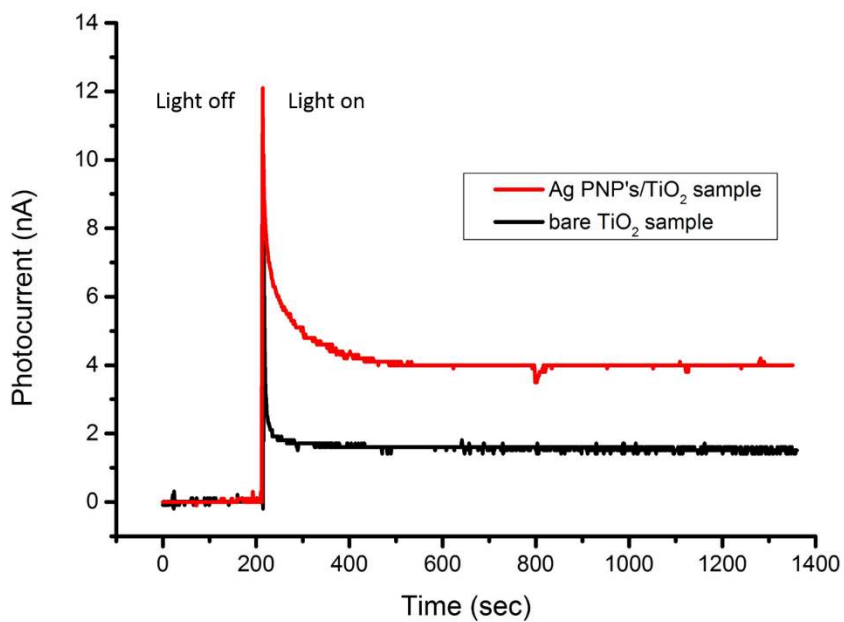


**Figure S2.** Photocurrent stability measurements of the bare TiO<sub>2</sub> and TiO<sub>2</sub>/Ag PNPs photoelectrodes when illuminated with monochromatic light ( $\lambda = 430$  nm) at 0.2 V vs SHE with methanol-phosphate buffer (50 % v/v) as electrolyte.



## 5. Surface-Induced vs. Phonon-Induced Intraband Excitations for Hot Electron Applications

Herein, the generation and extraction of plasmon-induced hot electrons (HEs) in Ag plasmonic nanoparticles (PNPs) has been studied. Such efforts are motivated by the ability of absorption-tunable arrays of PNPs to generate HEs throughout the entire solar spectrum, which can improve the visible and near infra-red efficiency of solar energy conversion devices. Theoretical studies predict higher HE energies (that favor the hot electron extraction) for intraband excitations compared to those for interband excitations. The mechanisms by which the electron momentum is conserved in intraband excitations (i.e., surface-induced and phonon-induced excitations) alter the HE energies, but it is unclear to what extent the HE extraction can benefit from promoting or suppressing one of these mechanisms. In this work we study the Ag PNP size-dependent HE injection into the TiO<sub>2</sub> conduction band in a photoelectrochemical cell. We distinguish two distinct size regimes in which different momentum conservation mechanisms (i.e., surface-induced and phonon-induced excitations) dictate the extraction efficiency. In the phonon-induced regime (Ag PNP diameters > 10 nm) a maximum in the HE injection efficiency is obtained with ~ 22 nm PNPs, while in the surface-assisted damping regime (Ag PNP diameters < 10 nm) the HE extraction increased with decreasing size. The maximum efficiency in the phonon-induced regime coincides with the maximum electric field enhancement, revealing the role of the electric field confinement on promoting the generation and extraction of HEs. This work adds to the fundamental understanding of HE generation and transport, which can be applicable to any localized surface plasmon resonance application.

The harvesting of solar energy has the potential to have far reaching impacts on almost every facet of everyday life. Converting sunlight to electricity or fuels and chemicals can provide an effective route to power the world and produce vital commodity chemicals in a sustainable and potentially carbon-neutral process. One important area of solar energy conversion involves using metallic nanoparticles to produce plasmon resonance energy, which can then be further converted to electricity or chemical energy.[6, 162, 163]

When the light-induced localized surface plasmon resonance (LSPR) decays in plasmonic nanoparticles (PNPs), hot electrons (HEs) with energies up to that of the incident light can be generated. In PNPs the LSPR can be tuned to (i) produce HEs in a predefined narrow range of light wavelengths for light sensing applications,[84] or to (ii) fabricate a PNP array that produces HEs throughout the entire solar spectrum for solar energy conversion applications (e.g., solar cells and photocatalytic/photoelectrochemical devices).[95] For these applications the HE must be readily extracted from the PNPs before it loses its energy in electron-electron scattering processes within the PNP. If the HEs are not readily extracted, its energy is dissipated thermally (see hot electron transport section below), making the PNPs ideal for photothermal therapy applications.[61] Whether the application involves the HE extraction or not, the HE generation process must be better understood in order to determine the real potential of these HE applications. In this work, we study the size dependency of the HE generation and extraction in spherical Ag PNPs in a photo-electrochemical cell. While the technique used here is ideal for plasmonic photo(electro)chemical devices (e.g., water splitting, CO<sub>2</sub> electro-reduction, etc.), our findings add to the fundamental understanding of the generation of HEs that can be used for any HE application.

When a PNP is in contact with a semiconductor the light-induced HE in the PNP is transported to the PNP surface where it must have sufficient energy to cross the metal-semiconductor energy barrier.[6, 22] Once the hot charge carriers are separated, they can carry out half reactions (e.g., oxygen and hydrogen evolution reactions). However, the HE-driven solar energy conversion is limited due to (i) low HE populations and (ii) short HE lifetimes.[164] The HE populations and life-time depend on the nature of the electronic excitation.[164] HEs are generated due to the surface plasmon decay through interband or

intraband excitations. Visible-light-induced interband excitations occur in metals such as Au and Cu, due to their relatively low interband energies. Interband excitations involve the formation of electrons above the Fermi level and the corresponding holes left in the d-band. Since the d-band is highly populated, the holes in the d-band are short-lived and recombine before they can reach the surface of the PNP to drive a reaction.[100, 102] In contrast to this, intraband excitations not only have longer HE life-times but also higher HE energies.[102] Unlike Au, Ag has the d-band located well below its Fermi level ( $\sim 3.7$  eV) and, therefore, when illuminated with visible light, only intraband excitations occur. Because of this, Ag is an excellent material to study the generation of HEs through intraband excitations, both theoretically[101] and experimentally.[138]

**Hot electron generation in Ag PNPs.** The visible-light-induced surface plasmon resonance in Ag PNPs decay by the emission of a photon (radiative decay) or by producing hot charge carriers through intraband excitations (non-radiative decay). The non-radiative decay is a consequence of different physical processes that allow for momentum conservation in the intraband electronic transition, namely, electron-electron scattering, electron-phonon scattering and electron-surface scattering. While electron-electron scattering produces two electrons with up to half the energy of the excitation photon (up to  $h\nu/2$ , where  $h$  is the Planck constant and  $\nu$  is the light frequency), electron-phonon scattering and electron-surface scattering can result in the generation of hot electrons with energies up to  $h\nu$ . Figure 47 depicts the momentum conservation of these two excitations mechanisms. In the electron-phonon scattering process, the electron absorbs a phonon, obtaining the necessary momentum for the transition without significantly changing its energy (Figure 47A). Figure 47B shows that an electron can also directly obtain the energy and momentum from the plasmon by surface scattering. Surface-induced excitations are also explained by the field confinement at the metal-insulator interface that generates a Lorentzian distribution in the momentum of the plasmon normal to the surface that allows for direct transitions (Figure 47B).[100]

The electron-phonon scattering is an intrinsic property of the material and is nearly size-independent.[165] In contrast, surface-induced excitations and radiative decay are only prominent for small ( $< \sim 10$  nm) and large ( $> \sim 40$  nm) PNPs, respectively. These

mechanisms are recognized and studied experimentally by a spatial modulation spectroscopy technique that allows the ability to study the linewidth of the localized surface plasmon decay of a single PNP.[165] The linewidth ( $\Gamma$ ) is related to the dephasing time  $\tau$  of the surface plasmon, which depends on the surface plasmon dephasing mechanisms as follows:

$$\Gamma = \frac{2\hbar}{\tau} = \Gamma_{\text{int}} + \Gamma_{\text{rad}} + \Gamma_{\text{e-surf}} = \frac{2\hbar}{\tau_{\text{int}}} + \frac{2\hbar}{\tau_{\text{rad}}} + \frac{2\hbar}{\tau_{\text{e-surf}}} \quad (35)$$

where,  $\Gamma$  is the linewidth in eV,  $\hbar$  is the reduced Plank constant,  $\Gamma_{\text{int}}$ ,  $\Gamma_{\text{rad}}$  and  $\Gamma_{\text{e-surf}}$  are the linewidth contribution of the intrinsic damping (i.e., electron-phonon scattering and resistive losses), radiative decay and electron-surface scattering mechanisms, respectively, and  $\tau_{\text{int}}$ ,  $\tau_{\text{rad}}$  and  $\tau_{\text{e-surf}}$  are the corresponding dephasing times.

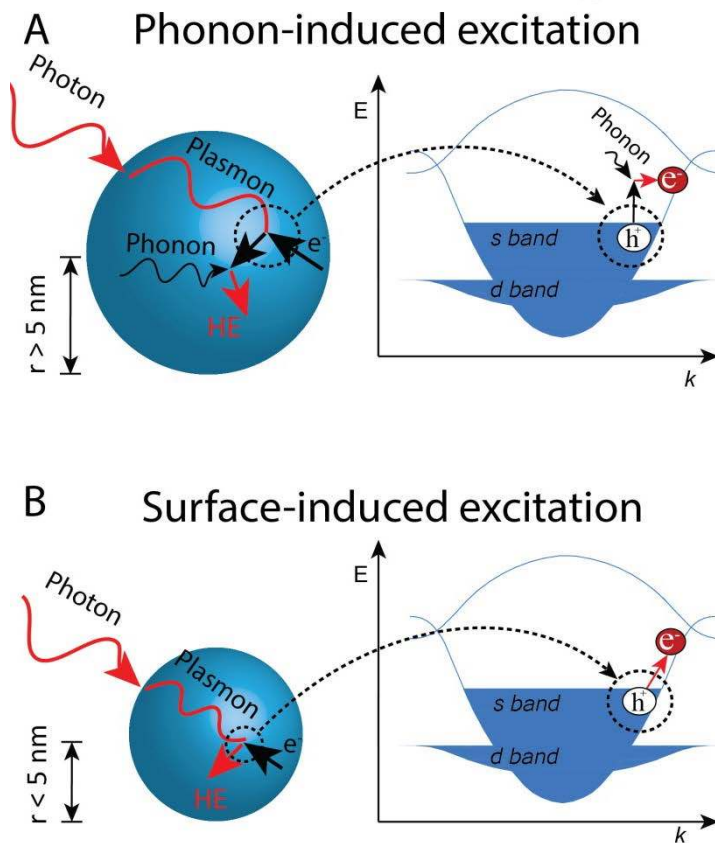


Figure 47. Illustrates the light-induced plasmon excitation in Ag PNPs and two alternative intraband electronic excitations (i.e., Figure A and B) by which the excited plasmon decays and generates a HE. While all the physical processes involved in the two excitations are depicted on the left of the figures, the conservation of energy and momentum of the excitations are shown explicitly on the right of the figures in simplified band diagrams. Figure A, shows a phonon-induced transition where the necessary momentum for the electronic transition is provided by a phonon. Figure B, shows a surface-induced transition where both the energy and the momentum are directly provided by the plasmon.

While,  $\tau_{\text{int}}$  has mainly been estimated with *Ab-initio* simulations,[100] a good estimation of  $\tau_{\text{rad}}$  and  $\tau_{\text{e-surf}}$  can be obtained with the following simple empirical relations:[165, 166]

$$\frac{1}{\tau_{\text{rad}}} = \kappa_{\text{rad}} V \quad (36)$$

$$\frac{1}{\tau_{\text{e-surf}}} = g_s \frac{v_F}{D} \quad (37)$$

where,  $\kappa_{\text{rad}}$  is the radiation damping constant,  $V$  is the PNP volume,  $g_s$  is the surface factor,  $v_F$  is the fermi velocity and  $D$  is the PNP diameter.  $g_s$  has been estimated for silver with spatial modulation spectroscopy techniques and is  $\sim 0.7$ . [165]

The contribution of the surface-induced excitations to the broadening of the silver PNP linewidth is plotted in Figure 48 by using the above relation. In the same figure the experimental value of  $\Gamma_{\text{int}}$  for Ag PNP in this size range is shown as reference (black dashed line). [165] Clearly, when the surface plasmon is restricted to oscillate in small PNP's (diameter  $< 10$  nm), it obtains sufficient momentum to induce direct excitations (surface-induced excitations) without the need of absorbing a phonon. This is shown by a larger  $\Gamma$  for the e-surface interaction than for the intrinsic damping in this range. At PNP diameters of  $\sim 10$  nm, the surface-induced excitations become of the same magnitude as intrinsic damping (phonon-induced excitations and resistive losses). When intrinsic damping is prominent (diameter  $> 10$  nm), phonon-induced excitations (that generate HE's) compete with resistive losses that dissipate thermally without generating HEs. [100] According to this analysis, decreasing the PNP size to  $< \sim 10$  nm where most of the HE come from surface-induced excitations would be a

promising strategy to decrease the intrinsic resistive losses and thus increase the HE generation and potential extraction rates.

However, efficient generation of hot carriers has also been associated with electric field hot spots. These regions within and around the PNP where the electric field is highly amplified (i.e., intensities up to  $\sim 10^4$  times larger than that of the incident light for PNP dimers)[68] are more pronounced in PNPs with sharp edges and in PNP dimers.[68] However, even when a single spherical PNP embedded in water is put in contact with a substrate with a higher refractive index than water, a hot spot is created at the substrate-PNP interface.[167] Figure 49 shows the electric field enhancement calculated with COMSOL Multiphysics<sup>®</sup> in/around a PNP embedded in water before (Figure 49A) and after (Figure 49B) it is put in contact with a TiO<sub>2</sub> substrate. Clearly, a hot spot is formed at the PNP- substrate interface (Figure 49B). The amplitude of the field depends strongly on the species adsorbed onto the PNP, contact angle between the PNP and the semiconductor, and the electronic nature of the PNP surrounding environment (i.e., chemical interface damping).[168] Since the LSPR dephasing time is directly proportional to the electric field enhancement,[169] the dependence of the electric field enhancement on the PNP size is best estimated by direct measurement of the dephasing time in spherical Ag nanoparticles with an insulating SiO<sub>2</sub> layer around them (well-defined environment). These measurements were carried out for different PNP sizes by Baida *et al.*[165] with a spatial modulation spectroscopy technique, and are shown in Figure 49C. Clearly, the largest dephasing time and, therefore, field enhancement is obtained with  $\sim 22$  nm Ag PNPs. In smaller PNPs than 22 nm, the LSPR dephases more promptly due to an increase of e-surface scattering, and in larger PNPs the LSPR dephases more promptly due an increase in the radiative decay.[170]

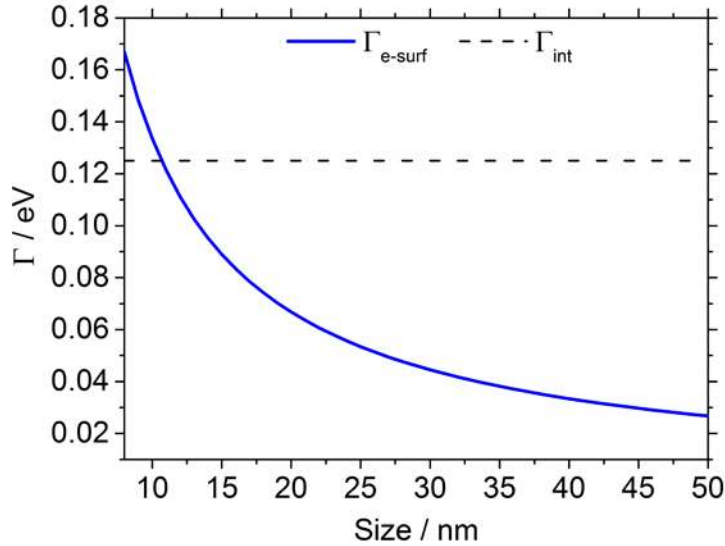


Figure 48. An estimation of the contribution of the surface-induced and intrinsic damping mechanisms to the linewidth of the surface plasmon.  $\Gamma_{e\text{-surf}} = \frac{2\hbar}{\tau_{e\text{-surf}}}$  and  $\Gamma_{\text{int}} = \frac{2\hbar}{\tau_{\text{int}}}$ .

Few works have suggested that the hot spots can increase the generation and extraction of hot electrons.[108, 109] Harutyunyan et al.[108] measured anomalous ultrafast electron relaxation kinetics in plasmonic nanostructures with hot spots. In that work, the authors explained the anomalous relaxation kinetics by ultrafast electron-electron scattering of hot electrons, suggesting that hot spots enhance the generation of hot electrons. Other works have compared the hot electron extraction (photocurrent) from plasmonic structures with and without hot spots, finding that the structures with hot spots yield the largest



photocurrent.[109] However, systematic experiments that clearly show a correlation of the field strength with the hot electron generation and extraction are lacking. A good platform to systematically study the role of the field enhancement are size-tunable spherical Ag nanoparticles on a TiO<sub>2</sub> film, which was used in our work. This system brings several advantages: (i) the field enhancement can be tuned by varying the PNP size (Figure 49C), (ii) the hot spot is created at the interface between the hot electron source (i.e., PNP) and the hot electron acceptor (TiO<sub>2</sub>), allowing the hot electrons generated in the hot spots to readily transfer to the TiO<sub>2</sub> conduction band, and (iii) all the visible light excitations in the PNP are of intraband nature, which allows the hot electrons to reach energies up to the energy of the irradiating light. Furthermore, the absorption range of the Ag PNPs fall outside the absorption range of TiO<sub>2</sub> ( $E_g = 3.2$  eV/380 nm), allowing the ability to decouple the absorption of light from the two materials.

As explained above, for PNPs smaller than 10 nm, intraband surface-induced excitations are prominent and can decrease the resistive losses,[100] however these same excitations decrease the strength of the electric field that is associated with efficient HE generation.[108] Our results shed light on the understanding of these two counteractive effects by systematically studying the size-dependent HE injection efficiency from spherical Ag PNP's to the conduction band of TiO<sub>2</sub> to oxidize methanol in an photoelectrochemical cell. The size-dependency was studied between 8 to 27 nm where the radiative decay was negligible and the transition from phonon-induced to surface-induced excitations can be studied directly in the environment envisioned for photoelectrochemical applications (e.g., water splitting and CO<sub>2</sub> reduction). Systematically decreasing the PNP size while maintaining its spherical geometry allows the ability to tune the PNP nearfield, which is key to understand its role in the HE generation process. With this unique approach, it was shown that within the phonon-

induced size range ( $\sim 10 - 30\text{nm}$ ) the hot electron injection efficiencies are determined by the hotspot field amplitude with a maximum extraction efficiency at diameter  $\sim 22 \text{ nm}$ .

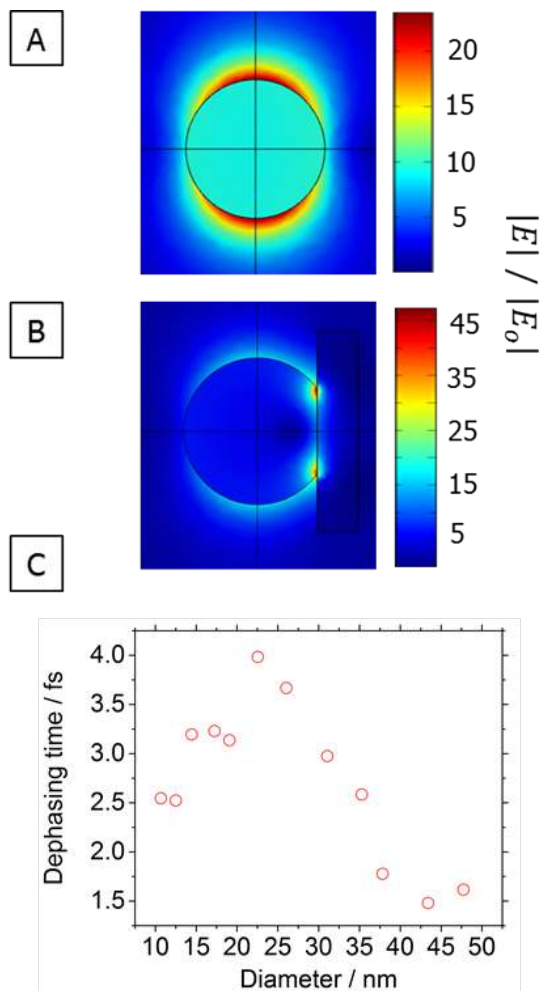


Figure 49. Near-field of a PNPs embedded in water before (A) and after (B) contacting a  $\text{TiO}_2$  substrate. C) Dephasing time of the LSPR as a function of the PNP size as reported by ref.[165]

**Hot electron transport.** Another size-dependent effect in the HE injection is the HE transport to the extraction point. After a HE is generated, it can scatter with other electrons below the Fermi level, losing its energy in the formation of a new electron hole pair. Therefore, the HE should reach the PNP surface before scattering processes occur in order to have enough energy for the extraction. The average distance of Ag HEs between two electron-electron collision events (i.e., mean free path) has been estimated to be  $\sim 20$  nm.[100] If the size of the PNP is larger than the electron mean free path, the HE energy drops rapidly creating a thermal distribution of electrons with a higher electronic temperature (Figure 50), which subsequently relaxes thermally by emitting phonons.[171]

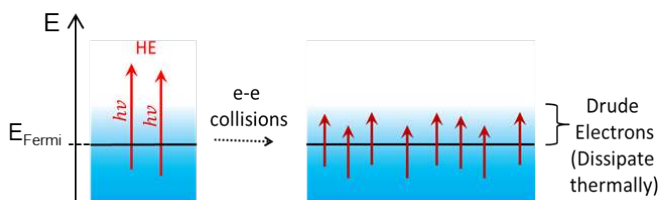


Figure 50. Energy distribution of HE before and after undergoing e-e collisions.

**Results and discussion.** Negatively charged spherical Ag PNPs were synthesized in the gas phase with a spark-discharge particle generator and size selected with a differential mobility analyzer (DMA). The monodispersed aerosol PNPs exiting the DMA were electrostatically deposited on TEM grids for characterization. Figure 51 shows a typical TEM image of the synthesized PNPs, confirming its spherical shape. With the same methodology, the Ag PNPs were electrostatically deposited on  $\text{TiO}_2$  films that, in turn, were grown (see Methods section) on fluorine doped thin oxide (FTO) coated glass. These composite electrodes were used as photoanodes in an electrochemical cell as depicted in Figure 52.

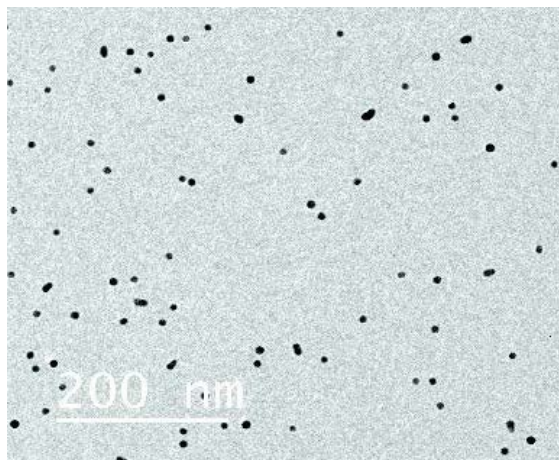


Figure 51. Show TEM micrograph of the synthesized Ag nanoparticles.

Dissolved  $O_2$  in the electrolyte was removed by purging the aqueous solution with  $N_2$  to avoid the oxidation of the Ag PNPs. In a three electrode configuration (cf. Figure 52), the photoanode potential was fixed to 0.15 V vs. SHE (below the oxidation potential of Ag to  $Ag^+$ ) and illuminated with monochromatic light to measure the wavelength dependent incoming photon to current conversion efficiency (IPCE, Figure 53). The IPCE response of the Ag PNPs in this region of the spectrum (below the optical band gap edge of the semiconductor) can be assigned to the injection of HE from the PNPs into the  $TiO_2$  conduction band. The hot hole left behind is scavenged away by methanol to form formaldehyde, a reaction which is thermodynamically more favorable than the self-oxidation of Ag (cf. Figure 52). The IPCE response in Figure 53 has a mode around 420 nm, which corresponds to the plasmon resonance absorption mode shown in the same figure. The red shifted IPCE mode with respect to the absorption mode is explained by the larger refractive index of water compared to that of air, where the absorption measurements were performed.

While the correlation between the Ag PNPs' absorption and IPCE confirms that the photocurrent is plasmon-induced, other mechanisms besides HE injection, such as light trapping mechanisms and light screening may also be present around the bandgap edge of TiO<sub>2</sub> (~ 400 nm). Since the present work is concerned exclusively to the HE generation and extraction, the following analysis and experiments are limited to excitation light with wavelengths longer than 420 nm (where the absorption of TiO<sub>2</sub> is negligible) to minimize the contribution of any other plasmonic effects (e.g., light trapping effects) or direct semiconductor photoelectrochemistry. In order to estimate the hot electron injection efficiency, the IPCE response can be combined with the absorption spectra to obtain the absorbed photon to current conversion efficiency (APCE, Figure 54). If the measured APCE is due to plasmon-induced hot electron injection across a metal-semiconductor energy barrier (as shown in Figure 52), the APCE should have the same wavelength dependency as the photoelectron emission theory (Fowler theory) across a metal-semiconductor energy barrier (Schottky barrier):[172]

$$APCE \sim C_F(h\nu - q\phi_B)^2 \quad (38)$$

where,  $C_F$  is the Fowler coefficient and  $q\phi_B$  is the Schottky energy barrier.

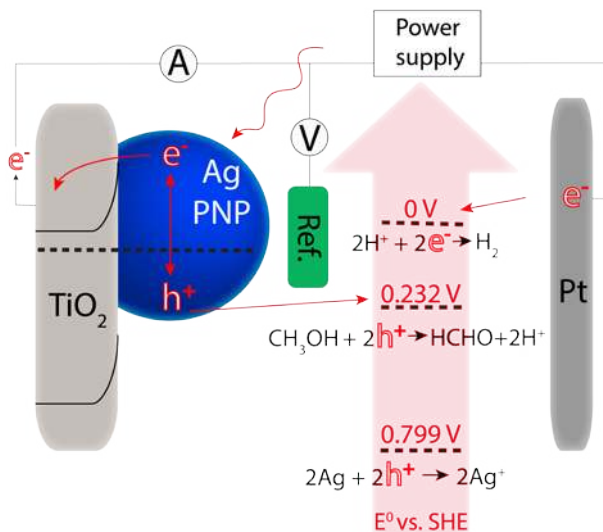


Figure 52. Schematic illustration of the hot electron injection from the PNP to the conduction band of TiO<sub>2</sub> and the corresponding hot charge carrier-driven reactions.

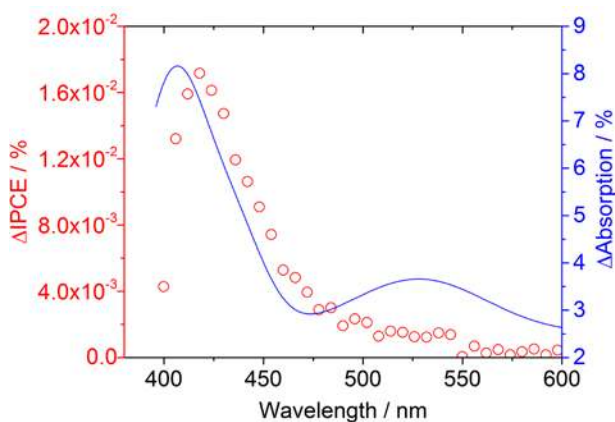


Figure 53. IPCE and absorption of the 15 nm Ag PNPs.

As discussed above, the HE generation in Ag PNPs results from intraband excitations. Fowler's relation holds for a process in which the hot electron injection is limited by the

Schottky barrier height. From the good fit of the measured APCE data with Fowler's relation (cf. Figure 54) it can be inferred that the injection of intraband-induced electrons are limited by their low energies (i.e., low HE populations).

IPCE measurements were also carried out for different PNP sizes (namely,  $8.5 \text{ nm} \pm 0.7 \text{ nm}$ ,  $9.5 \text{ nm} \pm 0.9 \text{ nm}$ ,  $11.8 \text{ nm} \pm 1.6 \text{ nm}$ ,  $14.8 \text{ nm} \pm 1.3 \text{ nm}$ ,  $18.4 \text{ nm} \pm 1.8 \text{ nm}$ ,  $20.3 \text{ nm} \pm 2.3 \text{ nm}$ ,  $23.4 \pm 2.2$ ,  $25.4 \pm 2.5 \text{ nm}$ ; see TEM micro-graphs and particle size distributions in the supplementary information). The corresponding APCE values also followed Fowler's relation. The wavelength dependent APCE values for all the tested PNP sizes are plotted in Figure 55 for three different excitation wavelengths (namely, 430-, 472- and 538 nm). The difference in APCE between PNP sizes can be assigned either to a (i) difference in the generated HE populations between the different PNP sizes or (ii) a difference in the HE energy loss involved in their transport to the extraction point. The wavelength dependent curves follow the same trend for the three excitation wavelengths, indicating that the same effects determine the size-dependent efficiency at the different wavelengths. This is in good agreement with the fact that  $\text{TiO}_2$  interband excitations are not prominent at these wavelengths and only HE injection effects are observed in Figure 55.

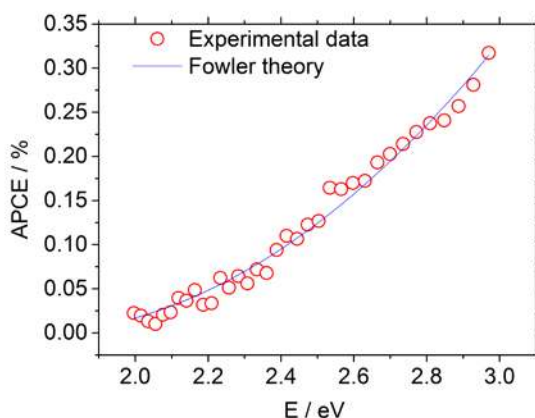


Figure 54. APCE of the 15 nm Ag PNPs.

To gain further insights to the process, we divide the size-dependent APCE curve into two regions according to the nature of the main HE excitation mechanism. For PNP sizes below 10 nm the APCE corresponds mainly to the surface-induced HE, while from 10 nm to 26 nm the HE are mainly generated through phonon-induced excitations.

Within the surface-induced excitations region, the APCE increases with decreasing size, which can be explained by a decrease in resistive losses as predicted by Brown *et al.*[100] However, above 10 nm, where the phonon-induced excitations are more prominent, the APCE increases from  $\sim 10$  nm to  $\sim 22$  nm. Such increase is explained here by the increase in the amplitude of the electric field at the hot spot. The APCE increases up to  $\sim 22$  nm (near the measured electric field maximum, dashed line in Figure 55) and then significantly decreases. The sharp decrease above  $\sim 22$  nm can be explained by two phenomena: (i) decrease of the field amplitude in the hot spot, and (ii) charge transport limitation since the theoretically estimated mean free path for Ag PNP hot electrons is  $\sim 20$  nm. [100, 102]

A consequence of the results presented in Figure 55 is that PNPs of 20 nm with less surface to volume ratio (or surface to absorption ratio, since absorption is  $\propto V_{\text{PNP}}$ ) than 12 nm PNPs generates more HE per absorbed photon. This is surprising since surface scattering is thought to be the main contributor for the generation of HE.[100] Therefore, the superior electric field confinement of the larger PNP can compensate for their limited surface area. In fact, Figure 55 reveals that the electric field of larger PNP can play a greater role than the surface in the production of HE's.

To conclude, the present work finds that the spherical Ag PNPs with the highest HE injection efficiencies are 8 nm PNPs (or smaller) and 22 nm PNP. Since small PNPs (e.g., 8 nm) have a relatively small absorption cross section  $\sigma_{\text{abs}} \propto V_{\text{PNP}}$ , they must be synthesized and/or deposited in large areal densities on a nanostructured semiconductor electron acceptor (with small Schottky energy barrier) to achieve a PNP system where all the energetic surface-induced HE are utilized. For applications where such large surface densities are not feasible, the optimal 22 nm size found in this communication can be used



to maximize the extraction, taking advantage of their superior electric field confinement. Therefore we have shown a rational guide for creating PNPs that can be tailored base on the needs of the application. To further increase the HE injection efficiency of the 20 nm PNP, their shape can be modified to geometries containing sharp edges, which further enhances the electric field confinement.

Finally, the hot electron efficiency curve measured in this work (within the phonon-induced excitation region) corresponds well with the measured dephasing time curve, which is proportional to the electric field enhancement. Therefore, this work suggests that the photo-electrochemical device described above to measure the hot electron injection efficiency can potentially be used to measure the field enhancement of nanostructures, which is of paramount importance for SERS applications.

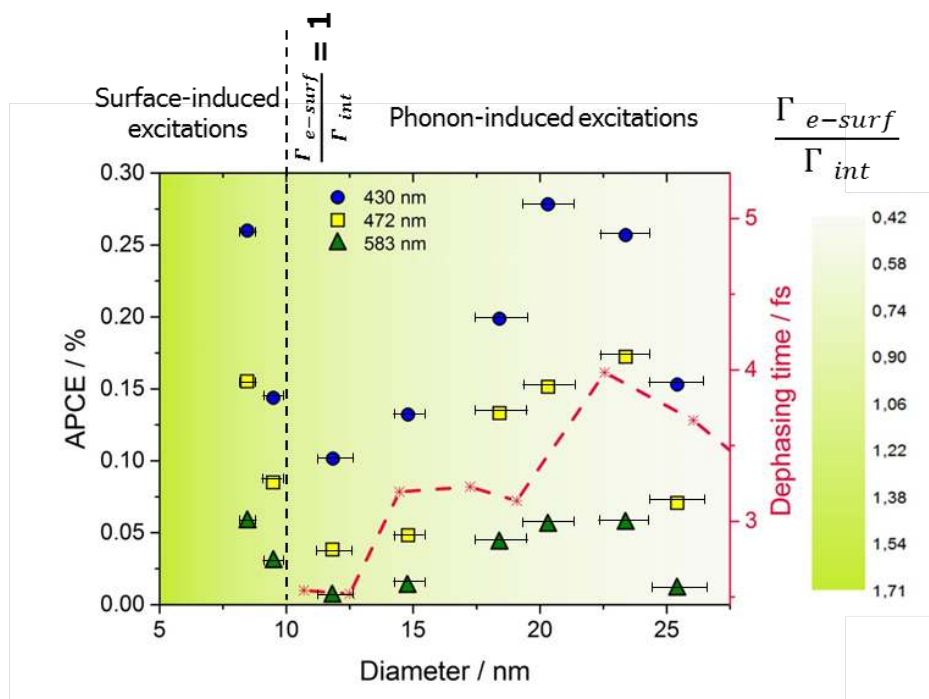


Figure 55. Size-dependent HE injection efficiency (APCE) of Ag PNPs as a function of diameter. The dephasing times (red data points) were taken from ref.[165]

## Methods

**10 nm TiO<sub>2</sub> layer synthesis** – A 10nm titanium layer was sputtered onto a cleaned fluorine-doped tin oxide (FTO) coated glass substrate (TEC-15, Hartford Glass Co.), using a magnetron sputtering system (ATC Orion) with titanium targets. A portion of the glass substrate was masked before the sputtering step, to provide a back contact to the sample during the photoelectrochemical testing. The sputtered deposited samples were annealed under flowing air (~100 sccm), in a tube oven at 500 °C for 5 hours at steps of 5 °C/min, to produce an anatase TiO<sub>2</sub> layer.

**Ag PNP synthesis** - Silver nanoparticles were manufactured using a high frequency spark discharge particle generator, principles of which are described in detail elsewhere.[173] Silver rods (>99.95% purity, purchased from Goodfellow Cambridge Limited) were used in the system and nitrogen gas was used as the carrier gas. A tube oven was used to coalesce the particle agglomerates exiting the spark generator into spheres. The negatively charged particles were subsequently size selected using a differential mobility analyser and were electrostatically deposited on to the TiO<sub>2</sub> surface. PNP depositions for TEM measurements were done on 200 mesh copper microgrids coated with foamvar/carbon (TED Pella).

**Absorption measurements** – The absorption spectra of the silver PNP's of different sizes were recorded using a PerkinElmer-Lambda 900 spectrometer. The measurements were performed inside an integrating sphere with front illumination of the sample. Readings were taken before and after the PNP deposition on the TiO<sub>2</sub> substrate, to determine the absorption contribution of the PNP's.

**Photoelectrochemical measurements** – The tests were performed in a custom made photoelectrochemical cell. A solution of methanol (>99.9% purity, Sigma

Aldrich) – 0.1 M phosphate buffer (pH – 7), in a ratio 50% v/v, used as the electrolyte. Before the tests, the electrolyte solution was bubbled with nitrogen gas, at high flowrates, to remove any dissolved oxygen. A three electrode arrangement was chosen for the experiments, with a coiled platinum wire serving as the counter electrode and an Ag/AgCl (XR 300, Radiometer Analytical) reference electrode. The working electrode potential was controlled using a EG&G PAR 283 potentiostat. The IPCE measurements were performed using a 200 W quartz-halogen lamp coupled with a grating monochromator and a software controlled shutter arrangement. Optical cut-off filters were used to avoid any secondary wavelengths from the monochromator.

## Supplementary information

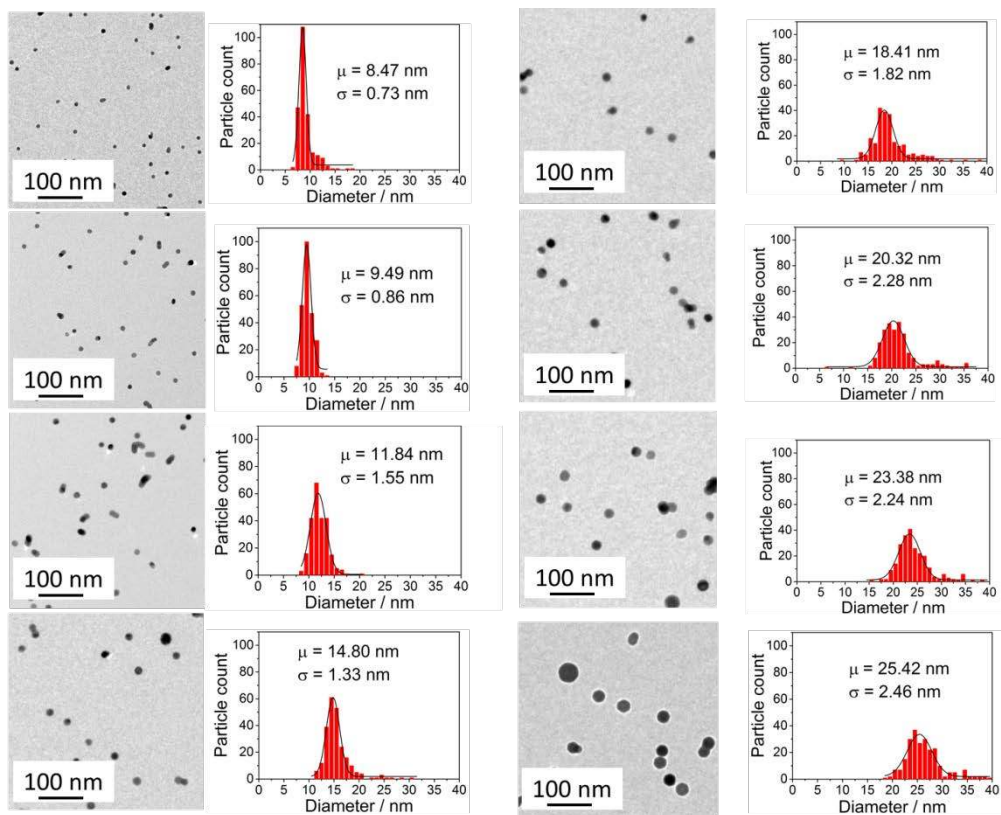


Figure S1. Micrographs of the PNPs deposited in TEM grids and their particle size distribution for different sizes of silver nanoparticles used in this study.

## 6. The Role of Size and Dimerization of Decorating Plasmonic Silver Nanoparticles on the Photoelectrochemical Solar Water Splitting Performance of BiVO<sub>4</sub> Photoanodes

### Abstract

Ag nanoparticles (NPs) are deposited on BiVO<sub>4</sub> photoanodes to study their effect on the photoelectrochemical (PEC) water splitting performance of the semiconductor. 15 nm light absorbing NPs and 65 nm light scattering NPs were studied separately to compare their light trapping ability for enhancing the semiconductor's absorption through light concentration and light scattering, respectively. The 15 nm NPs enhanced the BiVO<sub>4</sub> external quantum efficiency throughout the semiconductor's absorption range (e.g., ~ 2.5 fold at  $\lambda = 400$  nm). However, when a hole scavenger was added to the electrolyte, no enhancement was observed upon NP deposition, indicating that the NPs only facilitate the injection of holes from the semiconductor surface to the electrolyte but do not enhance its absorption. On the other hand, the 65 nm scattering NPs not only facilitated hole injection to the electrolyte, but also enhanced the absorption of the semiconductor (by ~ 6%) through light scattering. Such a dual effect, i.e., of enhancing both the surface properties and the absorption of the semiconductor, makes light scattering Ag NPs an ideal decoration for PEC water splitting photoelectrodes.<sup>3</sup>

---

<sup>3</sup> This chapter has been based on ref: 174. Valenti, M., et al., *The Role of Size and Dimerization of Decorating Plasmonic Silver Nanoparticles on the Photoelectrochemical Solar Water Splitting Performance of BiVO<sub>4</sub> Photoanodes*. ChemNanoMat, 2016. **2**(7): p. 739-747.

The collective oscillation of valence electrons in metal nanoparticles (NPs) resulting from their electromagnetic interaction with light is known as surface plasmon resonance (SPR). As a result of this phenomenon, metal NPs can either absorb or scatter the irradiating light.[56] The photon frequencies in which the SPR takes place (i.e., the resonant frequencies) depend on the material, shape and size of the NPs.[56] Noble metal NPs (e.g., Ag and Au) exhibit resonance frequencies within the visible spectrum and are great candidate materials in solar energy conversion devices (e.g., photovoltaic and photocatalytic).[175],[72],[67],[41],[176]

It has been shown that the incident energy absorbed by plasmonic NPs can be transferred to a nearby semiconducting photoelectrode, thereby enhancing its performance.<sup>[72],[67],[41],[43],[46],[6]</sup> As a result, many noble metal NP / semiconductor systems have been studied to date, in particular to improve the rate of solar photoelectrochemical reactions (e.g., water splitting for hydrogen generation and phenol degradation for water purification).[67],[46],[177],[178],[179],[180],[117],[181],[182],[183] In many of these studies, the improvement of the semiconductor's performance, upon plasmonic NP functionalization, has been explained by a light trapping mechanism called local electromagnetic field enhancement or light concentration. In this mechanism, the SPR significantly enhances the intensity of the incoming electromagnetic field (e.g., solar radiation) in the vicinity of the NP, which locally increases the absorption in a nearby semiconductor.[72],[67],[41],[43] Increasing the absorption in the vicinity of the NPs is advantageous when the NPs are placed at the semiconductor-electrolyte interface since, in this case, the absorption increase takes place in the semiconductor space-charge layer where the electron-hole pairs are more efficiently separated. In order to maximize this light concentration mechanism in a NP-semiconductor composite, the morphology and

spatial distribution of the NPs could be modified to achieve higher light confinement in so-called hot spots. Such hot spots have been achieved in NPs with different geometries that have sharp edges (e.g., NP triangles[68]). Another way to create hot spots is by bringing two NPs together to a distance of less than few nanometers (NP dimer). It has been shown that the near-field of dimer NPs undergo electromagnetic coupling and as a result a hot spot is created in the dimer junction.[184] This hot spot creation by near-field coupling can be of great interest for the NP-semiconductor photocatalyst design because: 1) the hot spot formation by NP coupling offers the largest field enhancements, and has been demonstrated in NPs of different geometries (e.g., spherical[184], rod-like[69] and triangular[68] NP dimers), and 2) the near-field coupling effect could become unavoidable in a final NP-semiconductor photocatalyst device with a high NP areal density on the semiconductor surface. However, it is not yet known to what extent the concentration of light in these dimer hot spots can influence the light absorption of a nearby semiconductor.

Small NPs (e.g., Ag NPs having diameters < 30 nm) with a large cross section of absorption are ideal to trap light through the light concentration mechanism,<sup>[72],[43]</sup> however, larger plasmonic NPs (e.g., Ag NPs having diameters > 50 nm) with a large scattering cross section could also trap light and enhance the absorption of semiconductors by preferentially scattering the irradiated light towards the semiconductor.<sup>[72],[43]</sup> These scattering NPs, when placed at an interface between two media, preferentially scatter light towards the medium with a higher refractive index.[119] Metal oxide semiconductors generally have a larger refractive index than water. Therefore, if scattering NPs are placed at the semiconductor-electrolyte interface, light will be scattered preferentially towards the semiconductor. This effect has the potential to increase the semiconductor absorption either for front illumination (i.e., light hitting the NPs first) or for back illumination. For front illumination, the incoming light will be preferentially scattered by the NPs towards the semiconductor, decreasing the reflection

of light off the photoelectrode (in the case of a reflective photoelectrode film). For back illumination, the light goes first through the semiconductor and the remaining non-absorbed light could then be preferentially back-scattered by the NPs, increasing its path length through the semiconductor and its absorption probability. Moreover, the preferentially scattered light will enter the semiconductor at a wide angular distribution, increasing the light's average path length through the semiconductor, thereby increasing the probability of absorption.

While the decorating NPs essentially scatter or concentrate the light, the scattered/concentrated light must have enough energy to excite electron hole pairs in the semiconductor in order to improve the device efficiency. In other words, for light concentration or preferential scattering to trap light in the semiconductor, the NPs must absorb/scatter light with energies larger than the semiconductor bandgap energy. Therefore, it is also important to have the capability of tuning the NP resonance frequencies to specific regions of the solar spectrum that match the absorption profile of the neighboring semiconductor. It is well known that the NP resonance frequency can be tuned through particle size, morphology and composition.[56] An alternative way to tune the resonance frequency with great flexibility is, again, by the formation of dimers[185]<sup>[186]</sup> or other small groups of closely spaced particles, since they are characterized by multiple resonant modes, whose positions and intensities are also highly dependent on the inter-particle distance. For instance, when two identical spherical NPs (homodimer) are brought close together (at distances of a few nanometers), their resonance mode splits into two distinctive hybridized modes, which correspond to a longitudinal (parallel to the axis of the homodimer)  $\sigma$  bonding hybridized mode (cf. Figure 56) and a transversal  $\pi^*$  antibonding hybridized mode (perpendicular to the axis of the homodimer; cf. Figure 56).[187]<sup>[63]</sup> The position of the longitudinal  $\sigma$  mode in the spectrum has been extensively studied and is red shifted as the inter-particle distance is decreased.[62]<sup>[188],[189]</sup> Therefore, these hybridized modes (i.e.,  $\sigma$  and  $\pi^*$ ), arising from the



interaction of two NPs, could offer great absorption tunability and light confinement (see above) in the design of semiconductor-NP composite photocatalysts.

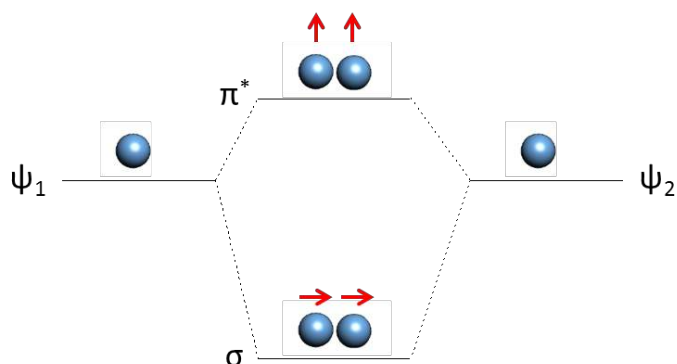


Figure 56. Homodimer hybridization model.

In this work, we study the plasmon resonance coupling effect on the water splitting performance of bismuth vanadate ( $\text{BiVO}_4$ ) photoanodes by depositing spherical 15 nm Ag NPs, produced in the gas phase,[190] onto the surface of the semiconductor at different concentrations. By increasing the concentration of the NPs, dimers were formed on the semiconductor surface and the ensemble of deposited NPs exhibited hybridized absorption modes that overlap with the  $\text{BiVO}_4$  absorption spectrum. The effect of the 15 nm singlet and dimer light-absorbing NPs on  $\text{BiVO}_4$  absorption is studied by analyzing the *incident* photon to current conversion efficiency (IPCE), or external quantum efficiency (EQE), as a function of excitation wavelength and by cyclic voltammetry (CV).

Moreover, we also tested the ability of 65 nm Ag NPs to preferentially scatter light and, therefore, increase the absorption of the semiconductor. Finally, the results using the

15- and the 65 nm Ag NPs are compared to give a comprehensive overview of the effects of size tunable pure Ag plasmonic NPs in the enhancement of solar water splitting photoelectrodes.

## Results and discussion

**Structural and optical characterization of Ag NPs.** Ag aerosol NPs, synthesized with the spark discharge particle generation technique,[191] were sintered into spheres by passing them through a tube furnace, and size selected with a differential mobility analyzer (DMA)[154] directly in the gas phase.[190] The NPs coming out of the DMA are all negatively charged and have a narrow particle size distribution. These well-defined charged aerosol NPs were electrostatically precipitated onto a TEM grid for their structural characterization. The size and morphology of the deposited NPs are shown in Figure 57a and b. Evidently, the NPs are uniform and spherical, thus making them excellent candidates for distinct SPR absorption. From the particle size distribution shown in Figure S1 (Supporting information), it can be seen that the size of the NPs is  $15 \pm 3$  nm. The measured particle coverage on the grid is  $\sim 7$  NP /  $\mu\text{m}^2$ . Figure 57c shows another TEM grid sample with a higher NP coverage ( $\sim 35$  NP /  $\mu\text{m}^2$ ). At this higher NP surface densities, closely spaced and touching NP dimers are observed on the TEM grid surface (cf. Figure 57c and d). The formation of touching NP dimers is expected, since the synthesized Ag NPs are virtually pure and do not have any coating or capping agent that could hinder the contact when a NP lands within the cross section of another already deposited NP. However, from Figure 57d it cannot be accurately determined if the contact between the NPs is point-like or if they partially merge together a few nanometers. The SPR modes of touching dimers significantly depend on the dimer junction geometry[189] and, therefore, further information about the NP junction is obtained (cf. discussion below) by comparing the measured and simulated absorption spectra of the dimers. In order to study the

absorption spectra of the synthesized dimers (with interparticle distances of less than 5 nm, as shown in Figure 57c and d), the Ag NPs were also deposited under the same conditions onto the surface of a transparent fluorine doped tin oxide (FTO) coated glass substrates (Figure 58a) at different NP coverages.

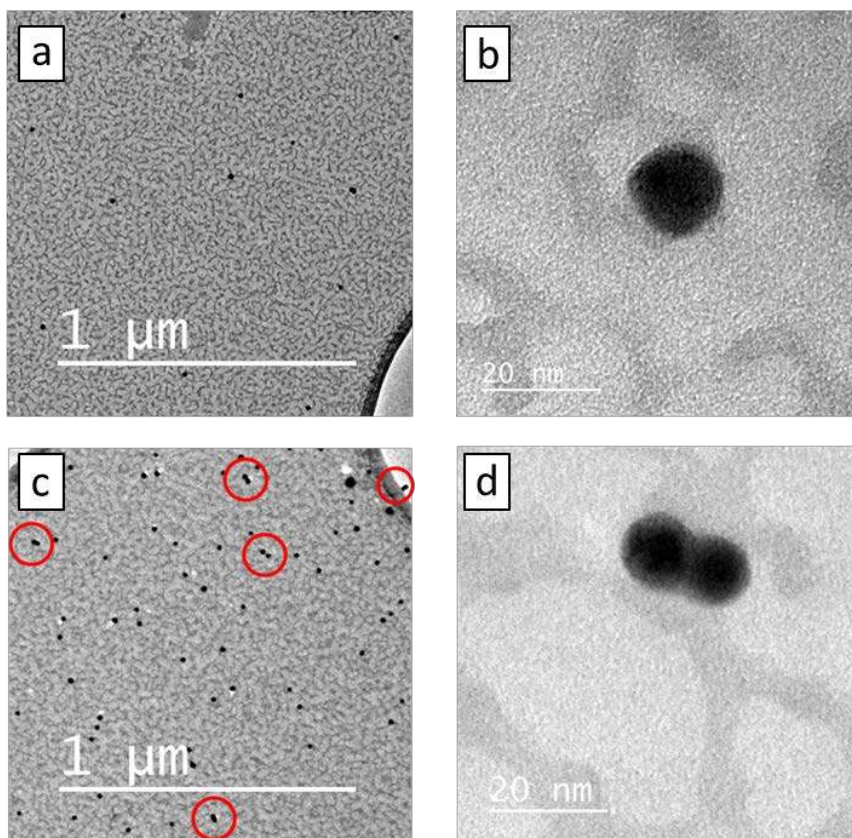


Figure 57. TEM image of the synthesized NPs deposited electrostatically on a TEM grid. a), and b) the morphology and NP spatial distribution at a low NP coverage ( $\sim 7 \text{ NP} / \mu\text{m}^2$ ). c) and d) show the formation of closely spaced NP dimers and touching dimers (highlighted by red circles) at a high NP coverage ( $\sim 35 \text{ NP} / \mu\text{m}^2$ ).

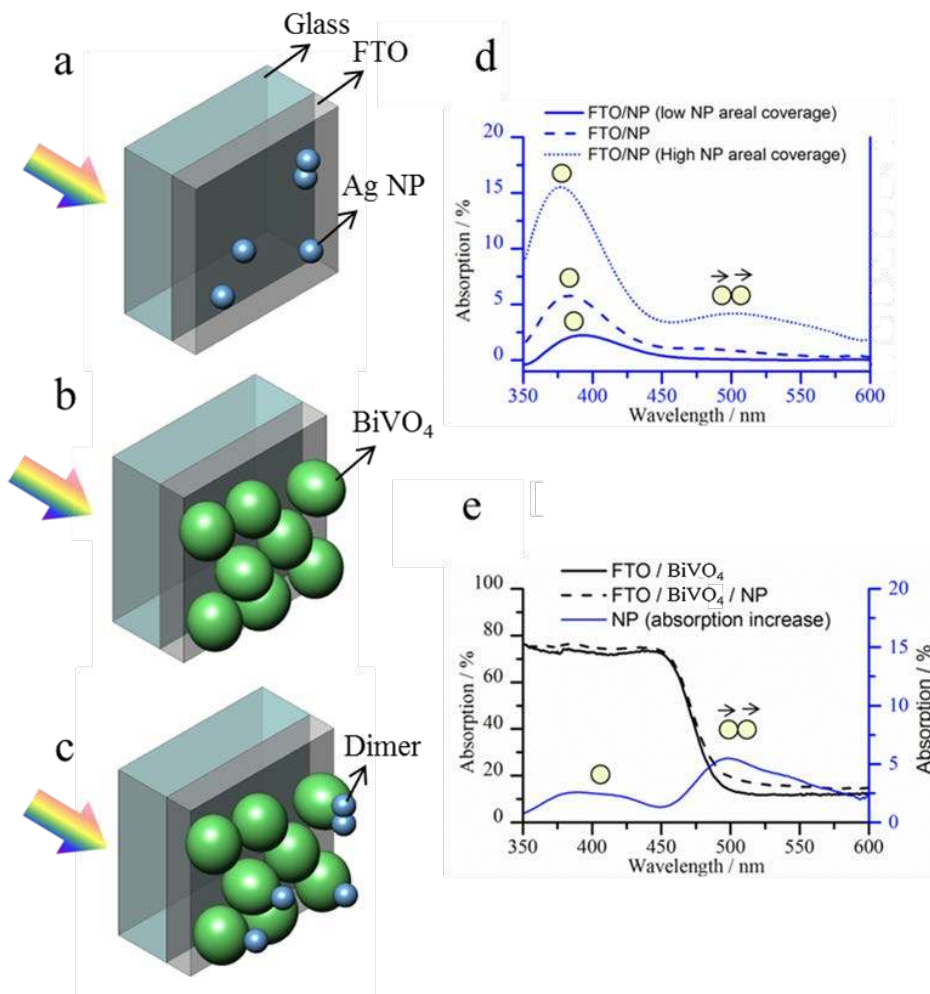


Figure 58. Illustration of the sample configurations a) FTO / NP, b) FTO / BIVO<sub>4</sub> and c) FTO / BIVO<sub>4</sub> / NP together with their corresponding back illumination absorption spectra (d and e).

The absorption spectra of three FTO / NP samples with increasing NP coverage are shown in Figure 58d. It can be observed that the sample with the lowest NP coverage

only shows one well defined absorption peak at  $\sim 380$  nm that corresponds to the SPR mode of isolated Ag NPs.[56] However, as the NP coverage is increased, a second absorption peak is observed at  $\sim 500$  nm. The appearance of this second peak is explained by the NP coupling effect, since, at high areal densities the inter-particle distance decreases leading to electromagnetic interaction between two or more NPs, which gives rise to hybridized plasmonic modes. The position in the spectrum of the observed hybridized absorption peak ( $\sim 500$  nm, Figure 58d) is of particular importance since it expands the NP absorption overlap with a semiconductor's absorption to longer wavelengths ( $\lambda > 450$  nm). BiVO<sub>4</sub>, for instance, has a low absorption coefficient near its optical bandgap edge situated at  $\sim 510$  nm. Therefore, due to the appearance of the hybridized absorption peak, the decorating NPs have the potential to also increase the absorption of BiVO<sub>4</sub> near its optical absorption edge, where it has low absorption and poor photoelectrochemical conversion efficiency.

Consequently, the 15 nm Ag NPs were deposited on the surface of BiVO<sub>4</sub> photoanodes. The back illumination (i.e., light incident from the substrate side) absorption spectra of the sample, before and after NP deposition (Figure 58b and c, respectively), are shown in Figure 58e together with the estimated NP absorption contribution. From this figure, it can be clearly seen that the absorption of the BiVO<sub>4</sub> photoanode was increased at  $\sim 500$  nm by approximately 5%. As hypothesized above, an absorption increase in this region of the spectrum can be explained by the formation of closely spaced and touching particles (i.e., NP dimers) that are characterized by a red shifted longitudinal plasmonic mode.[187] In order to verify this hypothesis, the composite sample (FTO / BiVO<sub>4</sub> / NP) was inspected with high resolution scanning electron microscopy (HRSEM, Figure 59). The HRSEM micrographs show that Ag NPs were deposited, approximately uniformly, on top of the BiVO<sub>4</sub> grains. The NP coverage is found to be  $\sim 40$  NP /  $\mu\text{m}^2$  from the analysis of 172 NPs. From these particles  $\sim 13$  % were forming dimers with an interparticle distance of less than  $\sim 5$  nm. This dimer formation on the surface of the BiVO<sub>4</sub> grains explains the

measured absorption peak at  $\sim 500$  nm (Figure 58d), since it corresponds well to the red shifted longitudinal mode of Ag dimers.[187]<sup>[188]</sup> This is a critical observation, as it reveals that a significant enhancement in optical absorption can be obtained through careful manipulation of not only the NP size, but also by the spatial distribution of the NPs on the semiconductor surface. Moreover, this dimerization can 1) extend the spectral range of the optical enhancement from individual NPs to higher wavelengths and 2) exhibit a highly localized field enhancement (hot spot) at the NP dimer junction,[192] thus potentially strengthening the role of NP functionalization on photoactive semiconductor materials.

It is important to highlight that even though most of the NPs on the  $\text{BiVO}_4$  do not form dimers (cf. Figure 59), the absorption of the singlet NPs does not contribute significantly to the overall back illumination absorption of the composite (Figure 58e). This is because isolated NPs absorb light at  $\sim 380$  nm (cf. Figure 58d) and when the composite (FTO /  $\text{BiVO}_4$  / NP) is illuminated from the back (Figure 58c), most of the light with wavelengths below  $\sim 450$  nm is absorbed by the  $\text{BiVO}_4$  before reaching the NPs. Therefore, the interaction of light with the isolated NPs is limited by low light intensities, whereas the dimers can absorb light beyond 450 nm that is not screened by the  $\text{BiVO}_4$  and thus they contribute to a larger extent on the total composite absorption (Figure 58e).

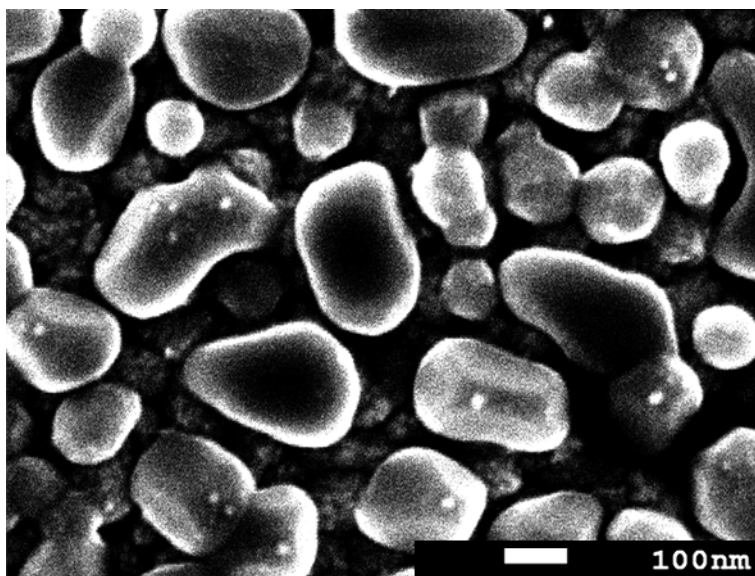


Figure 59. Top view HRSEM micrograph of the  $\text{BiVO}_4$  / NP composite.

**Finite difference time domain (FDTD) simulations.** In order to further elucidate the absorption contribution of the dimers to the total composite absorption, FDTD simulations were carried out to calculate the absorption spectra of the NP dimers sitting on a  $\text{BiVO}_4$  substrate. Figure 60 shows the calculated absorption spectra of Ag NP dimers with different inter-particle distances, including touching dimers (with point-like and overlapping contacts). The size and morphology of the separated and touching particles used in the simulation are derived from the TEM images shown in Figure 57. As expected, when excited with light polarized along the dimers (longitudinal), all the simulated absorption spectra of the dimers exhibit a red shifted absorption peak in comparison with the absorption peak of an isolated Ag NP (cf. Figure S2). However, as explained above in the measured NP absorption spectra (Figure 58e), the  $\text{BiVO}_4$  screen the light with wavelengths below  $\sim 450$  nm and, therefore, only those dimers that exhibit an absorption mode near the band-gap edge region (i.e.,  $\sim 450$  nm) significantly contribute to the composite absorption. As shown in Figure 60, the main contributors to the measured

composite absorption (Figure 58e) at  $\sim 500$  nm are the dimers that are touching (with either point-like or overlapping contacts), which exhibit a longitudinal absorption peak in this same region of the spectrum. Moreover, the measured non-zero absorption shown in Figure 58e at  $\sim 550$  nm, is predicted only by the dimers that exhibit a 1 to 5 nm overlap at the junction (cf. Figure 60). This suggests that the resulting dimers do not have a point-like contact in the NP dimer junction but instead the NPs partially merge over a few nanometers.

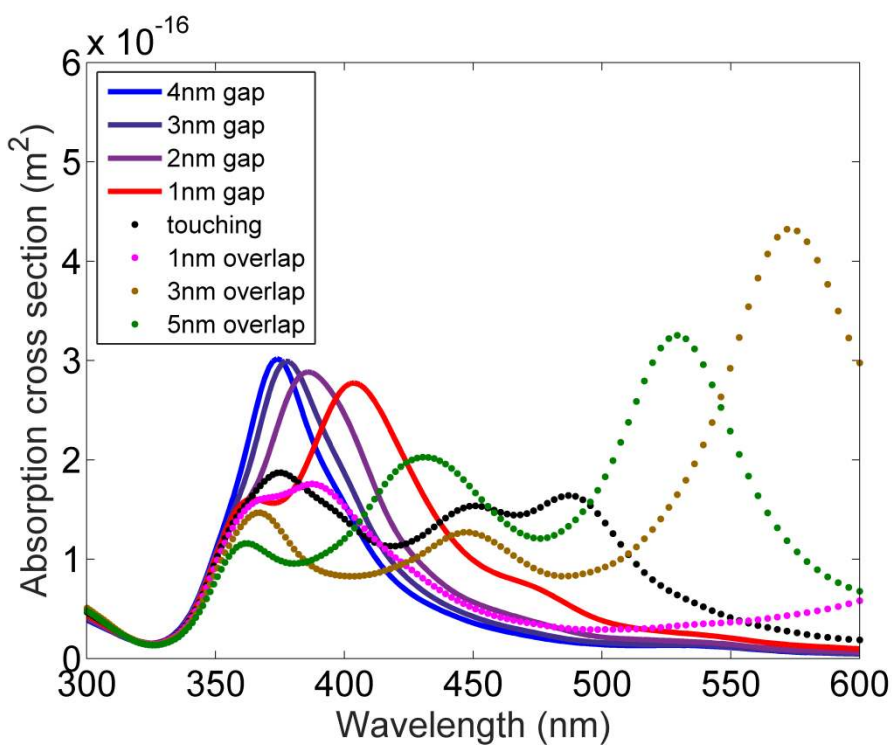


Figure 60. Simulated absorption spectra of two closely spaced or touching 15 nm NPs sitting on a BiVO<sub>4</sub> substrate at different inter-particle distances.



**Water splitting performance of BiVO<sub>4</sub> / 15 nm Ag NP composite.** In order to determine the effect of the Ag NPs on the water splitting photo conversion efficiency of BiVO<sub>4</sub>, the photocurrent generation before and after functionalization with 15 nm Ag NPs was tested as a function of excitation wavelength (Figure 61a). Figure 61b shows the corresponding absorption increase of the sample after NP deposition to compare the optical and photoelectrochemical enhancement effects. A clear increase in the IPCE is obtained upon NP functionalization throughout the wavelengths above the optical band-gap edge energy of the semiconductor. In order to better visualize the relative IPCE increase as a function of wavelength, the IPCE enhancement factor ( $f = IPCE_{BiVO_4 + Ag\ NPs} / IPCE_{BiVO_4}$ ) is plotted in Figure 62 for two samples of different NP coverage (i.e., one with 20 NPs/ $\mu\text{m}^2$  and the other with  $\sim 40$  NPs/ $\mu\text{m}^2$ ). The corresponding NP absorption spectra are also shown in the same figure. A good correlation is observed between the NP absorption and the measured enhancement factor, which suggests that the photoelectrochemical enhancement can be related to a plasmon excitation in the NPs. One important observation is that the enhancement factor, for both NP coverages, rapidly decreases to 1 as it approaches the BiVO<sub>4</sub> optical bandgap edge ( $\sim 510$  nm). This observation is in agreement with the enhancement resulting from the plasmonic light concentration mechanism, because this is also proportional to the semiconductor absorption that rapidly decreases around  $\sim 450$  nm.[72][43] In other words, just as in ordinary photoexcitation, plasmon-excited electron hole pairs also depend on the semiconductor's absorption coefficient. In order to test this hypothesis, IPCE measurements before and after NP deposition were again carried out, but this time a hole scavenger (H<sub>2</sub>O<sub>2</sub>) was added to the electrolyte (cf. Figure 63a). The hole scavenger ensures that all minority charge carriers (i.e., the holes) reaching the BiVO<sub>4</sub>-electrolyte interface are injected to the electrolyte before any surface recombination occurs.[120] Therefore, any IPCE enhancement under these conditions can be ascribed to a bulk effect (e.g., increase in absorption through plasmonic light trapping). Under these conditions, no IPCE enhancement was observed after NP deposition (Figure 63a). This result indicates

that the NP enhancement mechanism (shown in Figure 62) only facilitates the charge carrier injection to the electrolyte and does not enhance the semiconductor absorption through the light concentration mechanism. Figure 63b shows the absorption increase of the same sample upon NP deposition. Figure 63a and b, explicitly show that neither the NP absorption peak at  $\sim 380$  nm (SPR of NP singlets) nor the second absorption peak at  $\sim 500$  nm (mainly due to the absorption contribution of dimers) increase the photocurrent of the semiconductor in the presence of a hole scavenger. Therefore, it can be concluded that there is no significant energy transfer (e.g., through the light concentration mechanism) from the 15 nm Ag NPs (singlets or dimers) to the semiconductor that effectively increases its absorption. This low (or non-existent) efficiency of the light concentration mechanism can be explained by the fact that, in this work, pure NPs are used and the direct contact between the surface plasmon and the semiconductor leads to a significant decrease of the surface plasmon lifetime due to interfacial damping.[193] Decreasing the surface plasmon lifetime is expected to decrease the probability of plasmon induced excitations in the semiconductor.[72],[124] In order to elucidate the role of this direct contact between the semiconductor and the surface plasmon of pure metal NPs, separate experiments need to be carried out, where the same NPs are coated with a thin insulating layer (e.g.,  $\text{SiO}_2$ ) that mitigates the interfacial damping effect. Nevertheless, the significant enhancement in the conversion efficiency (Figure 62) shows that the pure Ag NPs are playing an important role in enhancing the minority charge carrier transfer from the semiconductor surface to the electrolyte. Such a surface effect is also reflected in the cyclic voltammetry measurements under simulated solar irradiation (Figure 64). A remarkable increase from  $\sim 0.6$  to  $\sim 1.7$   $\text{mA}/\text{cm}^2$  at 1.23V vs. RHE was achieved upon NP deposition. Consistently with the monochromatic measurements (Figure 63a), the photocurrent in the cyclic voltammetry measurements under simulated solar irradiation with the presence of a hole scavenger in the electrolyte does not show any enhancement upon NP functionalization (Figure 64), confirming that the 15 nm Ag NPs only affect the surface properties of the semiconductor.

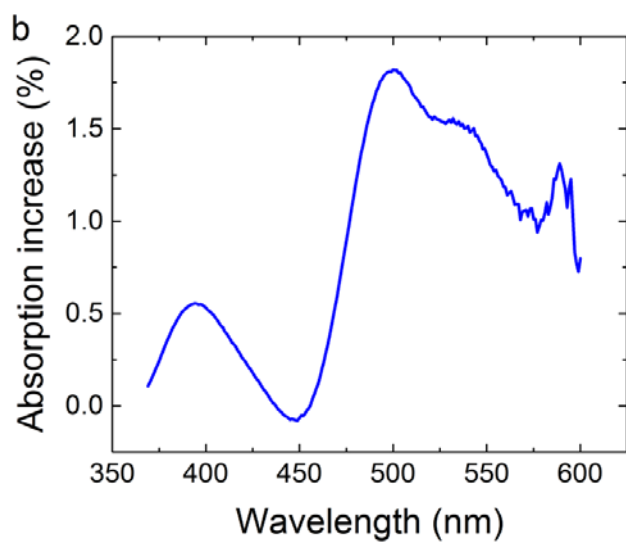
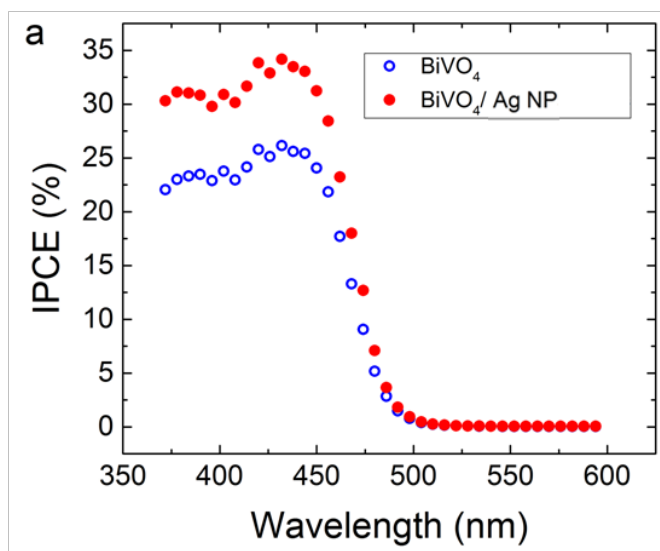


Figure 61. a) Back illumination *Incident* photon to current conversion efficiency (IPCE) measurements at 1.23 V vs. RHE before and after NP functionalization. b) Absorption increase upon NP functionalization

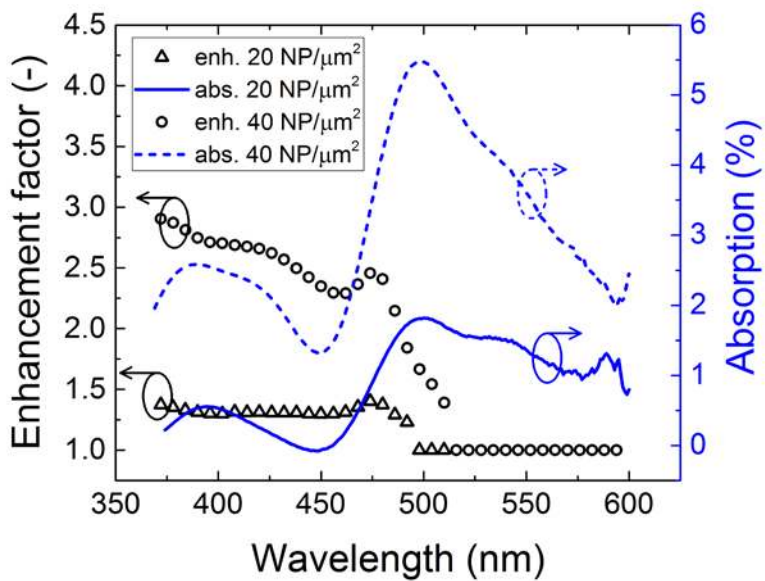


Figure 62. Correlation between the BiVO<sub>4</sub> absorption increase and photoelectrochemical enhancement factor obtained upon NP functionalization for two NP surface coverage

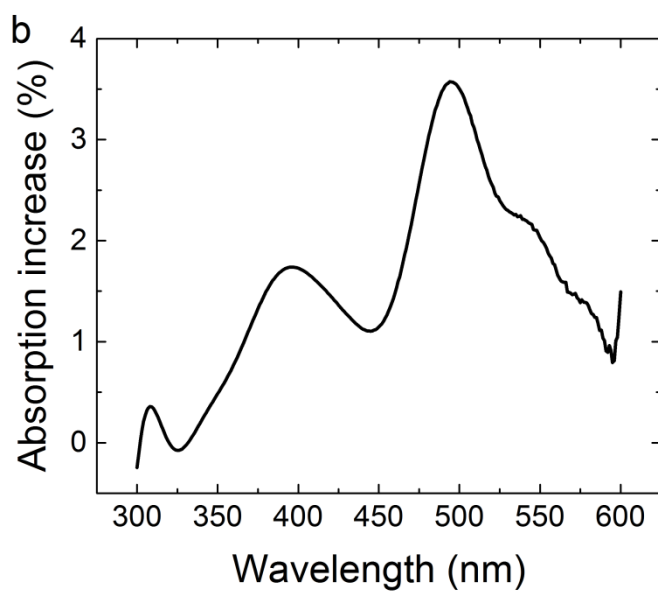
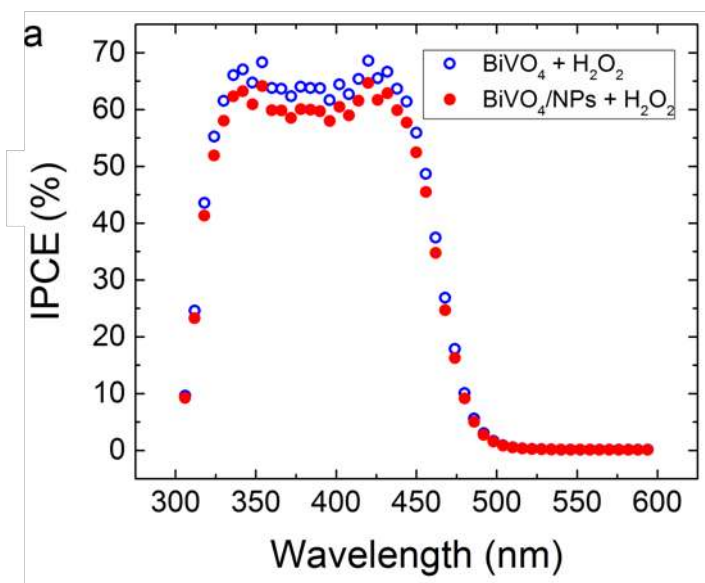


Figure 63. A) IPCE curves at 1.23 V vs RHE with  $\text{H}_2\text{O}_2$  in the electrolyte before and after NP deposition. B) Absorption increase upon NP deposition.

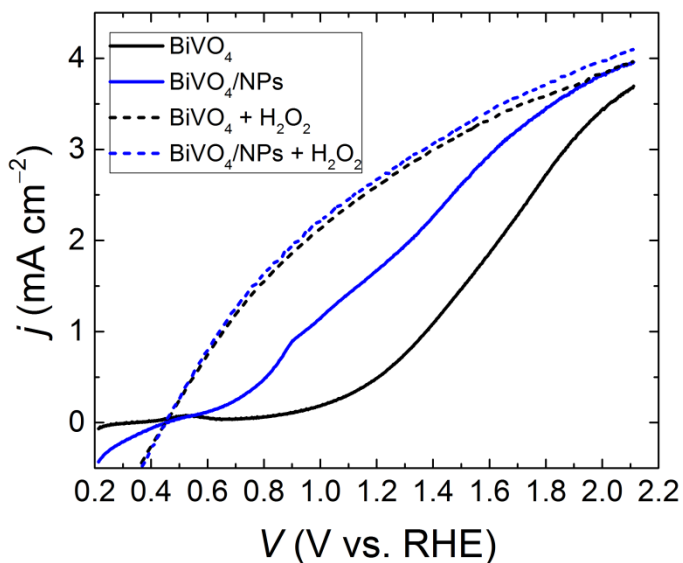


Figure 64. Three electrode AM1.5 photocurrent versus voltage ( $j$ - $V$ ) curve of  $\text{BiVO}_4$ , before (black) and after (blue) NP functionalization, with (dashed lines) and without (solid lines)  $\text{H}_2\text{O}_2$  in the electrolyte.

Cyclic voltammetry measurements under simulated solar irradiation were also carried out for front illumination (i.e., light reaching the NPs first) with and without the presence of  $\text{H}_2\text{O}_2$  (cf. Figure S3). In this case, the photocurrent was decreased, with  $\text{H}_2\text{O}_2$  in the electrolyte, which suggests that the light absorbing NPs partially screened the light to the semiconductor, decreasing its light absorption. On the other hand, without the presence of the hole scavenger, the photocurrent was increased due to a surface effect.

Plasmonic effects that increase the absorption of the semiconductor (e.g., light trapping) have been ruled out with the IPCE measurements performed with the presence of a hole scavenger. However, other plasmonic effects acting on the surface of the

semiconductor can also facilitate the charge transport and may also be playing an important role in the conversion enhancement, in particular considering the correlation between the conversion enhancement (at 1.23 V vs RHE) and the NP (singlets and dimers) absorption peaks (Figure 62). A plasmonic mechanism through which the NPs can influence the oxidation reaction catalysis is by locally increasing the temperature in the NPs vicinity.[78] Such temperature increase may enhance the reaction rate and the resulting photocurrent. However, a simple calculation (see Equations S1 and S2, *supporting information*) indicates that the temperature increase due to plasmonic heating of the 15 nm Ag NPs is not significant (less than 0.1 K). Other plasmonic surface effects are (i) improved adsorption of polar molecules due to their alignment with the NP nearfield[79] and (ii) local changes in the conduction/valence band due to its interaction with the NP nearfield.[177] Specially, the latter mechanism (ii) has been studied by X-ray absorption near edge structure (XANES), demonstrating that the NP nearfield can modify the electronic structure of the semiconductor by increasing the semiconductor conduction band vacancies, and thus promoting the separation of photogenerated electrons and holes.[177] Recognizing the contribution of any plasmonic mechanism taking place on the semiconductor surface would be of great value and a separate work should be undertaken to further elucidate the enhancement shown in this work (cf. Figure 62 and 64).

**Water splitting performance of BiVO<sub>4</sub> / 65 nm Ag NP composite.** BiVO<sub>4</sub> samples were also functionalized with 65 nm Ag NPs in order to test their ability to increase the BiVO<sub>4</sub> absorption through preferential scattering of light. Figure 65 shows back illumination absorption spectra of a BiVO<sub>4</sub> sample before and after NP deposition. In the same figure, the device absorption increase upon NP deposition is plotted in order to analyze the origin of its enhancement. The absorption increase is observed only within the semiconductor's absorption range, decreasing steeply to zero at the BiVO<sub>4</sub> band-gap edge.

This can be explained by an absorption increase due to light scattering, since some of the light that is not initially absorbed by the semiconductor is scattered back by the plasmonic NPs and absorbed according to the absorption coefficients of  $\text{BiVO}_4$ .

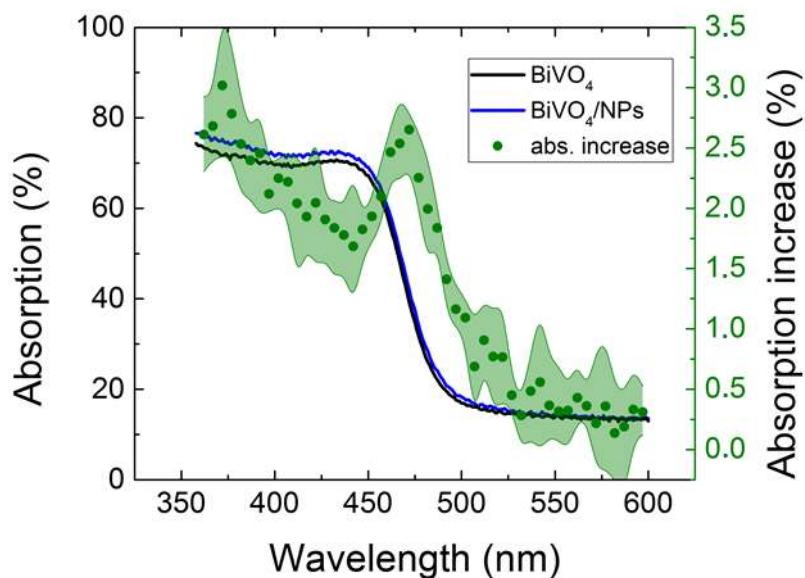


Figure 65. Back illumination absorption increase in the  $\text{BiVO}_4$  spectra upon deposition of 65 nm Ag NPs.

In order to study the effect of the absorption increase on the conversion efficiency of the semiconductor, IPCE measurements were carried out with and without a hole scavenger ( $\text{H}_2\text{O}_2$ ), before and after NP functionalization (cf. Figure 66). Once again, an enhancement is observed without the addition of  $\text{H}_2\text{O}_2$  in the electrolyte. However, unlike for the smaller 15 nm NPs, the 65 nm Ag NPs system shows a clear enhancement also with the presence of a hole scavenger. This is evidence of an increase in the semiconductor's absorption due to the NPs. The IPCE enhancement under  $\text{H}_2\text{O}_2$  is smaller ( $\sim 4\%$ ) than without it ( $\sim 20\%$ ). This is expected since the IPCE increase without the hole scavenger



encompasses both the enhancement due to an absorption increase associated with the light path and beneficial surface effects.[179],[182]

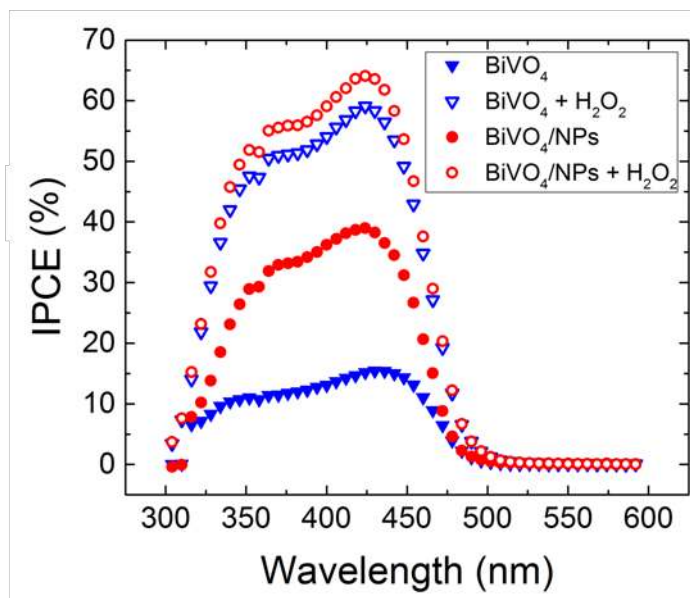


Figure 66. Back illumination *Incident* photon to current conversion efficiency (IPCE) measurements before and after 65 nm Ag NP functionalization.

The increase in the back illuminated BiVO<sub>4</sub> absorption is limited to ~ 2 %, due to the fact that most of the light is absorbed by the semiconductor before it reaches the light scattering NPs. Unlike smaller light absorbing NPs, their larger counterparts do not screen the light to the semiconductor when the sample is illuminated from the front (with the light hitting the NPs first). On the contrary, they can act as an antireflective medium by preferentially scattering the incoming light towards the BiVO<sub>4</sub> that exhibits a larger refractive index (~ 2.45) than water (~ 1.3), as explained above. Figure 67 shows the front illumination absorption increase of the device upon NP functionalization along with the IPCE enhancement factor under the presence of H<sub>2</sub>O<sub>2</sub> ( $f = \text{IPCE}_{\text{BiVO}_4 / \text{Ag NPs}}^{\text{H}_2\text{O}_2} /$

IPCE<sub>BiVO<sub>4</sub></sub><sup>H<sub>2</sub>O<sub>2</sub></sup>). An absorption increase of ~ 6 % is obtained for front illumination, which is larger than that for back illumination due to the fact that for front illumination the light is preferentially scattered before being absorbed by the semiconductor. Moreover, also for front illumination an increase is obtained in the IPCE in the presence of a hole scavenger in the electrolyte (Figure S4) and the corresponding enhancement factor follows the absorption increase due to the 65 nm Ag NPs functionalization (Figure 12). This correlation suggests that the increase in the IPCE is caused by the increased semiconductor absorption due to preferential scattering of light. Further evidence is given in Figure S5, where the IPCE of the bare and functionalized samples are corrected for the absorbed light, to yield the *absorbed* photon to current conversion efficiency (APCE). The APCE curves in Figure S5 are almost identical, showing that once the IPCE curves (Figure S4) are corrected for the light absorption (i.e., IPCE (%) / Absorption (%)), the performance is reconciled. Therefore, from Figure 67 and S5 we conclude that the increase in the IPCE under the presence of H<sub>2</sub>O<sub>2</sub> corresponds exclusively to the obtained absorption increase, which is in turn ascribed to the preferential light scattering mechanism of the 65 nm NPs.

Therefore, it is clear that 65 nm Ag NPs enhance the water splitting conversion of the BiVO<sub>4</sub> by facilitating the hole injection to the electrolyte and by enhancing the absorption of the semiconductor through preferential light scattering. Despite the fact that the 15 nm NPs did not increase the semiconductor's absorption, the surface effect studied above can be exploited to a larger extent with the 15 nm NPs than with the 65 nm NPs due to the fact that more semiconductor surface area in contact with the Ag NPs, can be covered with smaller NPs. This way, the selection of the particle size in a final device must be determined according to the semiconductor's limitations. If the semiconductor is limited by light absorption, larger particles should be used. On the other hand, if the semiconductor is limited by high surface resistance, smaller Ag NPs are preferred.

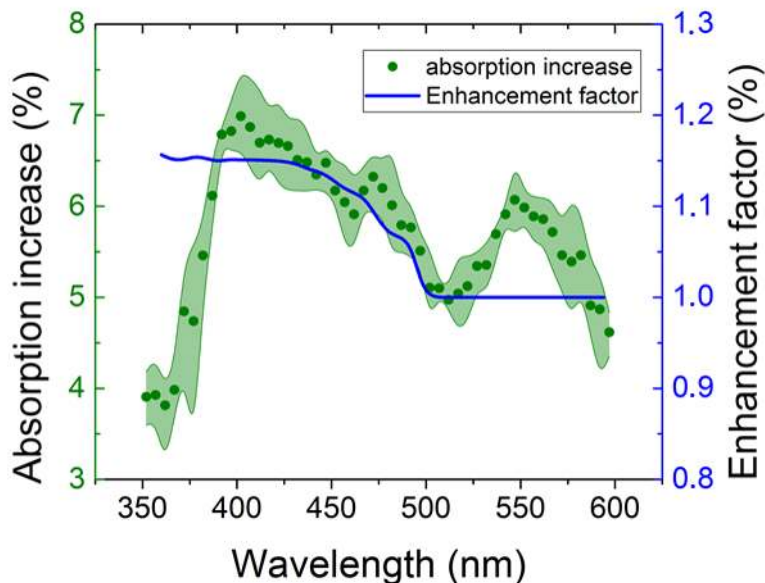


Figure 67. Front illumination absorption increase upon 65 nm Ag NPs deposition (black circles), along with the IPCE enhancement factor (calculated with the data shown in Figure S4) with the presence of  $\text{H}_2\text{O}_2$  in the electrolyte (Blue line).

## Conclusions

Depositing pure 15 nm Ag NPs on the semiconductor-electrolyte interface significantly increased the  $\text{BiVO}_4$  water splitting photocurrent under simulated solar irradiation. A PEC analysis, using a hole scavenger, revealed that the photocurrent increase is due to the improved charge carrier (i.e., hole) injection from the semiconductor surface to the electrolyte. A clear correlation between the wavelength dependent IPCE enhancement factor and the Ag NPs (singlets and dimers) absorption spectra suggests that the photocurrent increase at 1.23 V vs RHE is due to a plasmonic effect taking place at the semiconductor surface that facilitates the surface charge carrier

injection to the electrolyte. Further experiments are needed to discretely identify this enhancement mechanism.

Despite the fact that the  $\text{BiVO}_4$  / 15 nm Ag NP composite exhibits a higher absorption than the bare semiconductor, the composite PEC performance under 100% surface charge injection efficiency conditions was identical to that of the bare semiconductor. Therefore, we conclude that the decorating 15 nm Ag NPs (singlets and dimers) do not transfer the absorbed energy to the semiconductor (e.g., through the light concentration mechanism), but instead the SPR decays by releasing heat. The poor efficiency of the light concentration mechanism is explained by the fast interfacial damping of the SPR due to the direct contact between the pure metallic NPs and the semiconductor.

On the other hand, decoration with 65 nm Ag NPs was found to increase the light absorption of the semiconductor by preferential scattering of light. Such an effect was found to be even more effective for front illumination (i.e., light reaching the NPs first) than for back illumination, since, for the latter the semiconductor absorbs a fraction of the light first, reducing the amount of light to be scattered by the decorating NPs. The increase in the absorption after decoration with 65 nm NP is effectively translated into an increase in the IPCE.

This work provides a comprehensive study where the effects of pure spherical Ag NPs on the water splitting performance of  $\text{BiVO}_4$  semiconductors are elucidated using photoelectrochemical, optical and computational techniques, such as cyclic voltammetry, UV-Vis spectroscopy and FDTD. The results presented here can be viewed as a reference point to any future work with more complex plasmonic Ag nanostructures (e.g., coated Ag NPs, Ag based alloy NPs, Ag nano rods, etc) and their enhancement of PEC performance of semiconductor photoelectrodes.

## Materials and methods

**Fabrication of BiVO<sub>4</sub> photoanodes.** Fluorine doped Tin Oxide (FTO) coated glass (TEC-15, Hartford Glass Co.) was used as a substrate for the photoanode synthesis, after repetitive cleaning with soap, water, distilled water, acetone and isopropanol. The BiVO<sub>4</sub> solution (4 mM) was prepared by mixing the two solutions of the main precursors. Bi-(NO<sub>3</sub>)<sub>3</sub>·5H<sub>2</sub>O (98%, Alfa Aesar), diluted in acetic acid (98%, Sigma-Aldrich), was mixed with an equimolar amount of vanadium in the form of VO(AcAc)<sub>2</sub> (99%, Alfa Aesar) dissolved in absolute ethanol. The prepared BiVO<sub>4</sub> solution of the semiconductor was sprayed, with a chemical spray pyrolysis setup, on the substrate. The FTO glass substrate was placed at a distance of 20 cm from the spray nozzle on a heating surface. The temperature during the spraying process was kept at 480 °C. The BiVO<sub>4</sub> solution was sprayed in 100 cycles, through the nozzle of the atomizer driven by an overpressure of 0.6 bar of N<sub>2</sub> gas. The spraying flow rate of the solution per cycle was 0.2 ml/s with a delay time of 55 s, so that the solvent can fully evaporate. Before the deposition of BiVO<sub>4</sub> on the substrate, SnO<sub>2</sub> solution was sprayed at a temperature of 450 °C for 5 cycles with the same flow rate as the BiVO<sub>4</sub> solution. The SnO<sub>2</sub> solution was prepared by mixing SnCl<sub>4</sub> (0.1 M) with ethyl acetate (99.5% J.T.Baker). In that case, the precursor solution (SnO<sub>2</sub>) was placed 30 cm above the substrate. The purpose of the addition of SnO<sub>2</sub> between the substrate and the semiconductor was to prevent the recombination of the charge carriers at the FTO/BiVO<sub>4</sub> interface.[194] For the crystallization of the deposited BiVO<sub>4</sub> thin films, the samples were annealed in a tube furnace at 460 °C for 2 h.

**Synthesis of nanoparticles.** In order to synthesise pure Ag NPs having diameters within a very narrow range and deposit them on the surface of the photoanode, a spark discharge particle generator coupled with a differential mobility analyzer (DMA) was used.[191] A N<sub>2</sub> flow of 2 l/min was passed through the spark discharged particle generator where NPs are synthesized by inducing electrical discharges at high frequencies between two Ag rods (Goodfellow Cambridge Limited). The aerosol coming out of the

spark discharge particle generator is then passed through a tube furnace at 870 °C in order to sinter the particles into spheres. Subsequently, the NPs were size selected with a custom-made DMA[154], using a closed loop sheath flow of 9 l/min. The negatively charged particles coming out of the DMA were then deposited electrostatically to the BiVO<sub>4</sub> photoanode.

**UV-Vis Absorption measurements.** A spectrometer PerkinElmer-Lambda 900 was used for the UV-Vis absorption measurements of the BiVO<sub>4</sub> thin films. The incident light beam was concentrated on the sample, which was placed in an integrating sphere. This way, the transmittance and diffuse reflectance of each BiVO<sub>4</sub> sample, before and after the NP deposition, were measured simultaneously for wavelengths between 350 and 600 nm.

**Photoelectrochemical measurements.** The photoelectrochemical measurements of the semiconductor, with and without nanoparticles, were carried out in an aqueous 0.1 M potassium phosphate buffer solution (pH ~7) in a photoelectrochemical cell. A three electrode configuration was used; a working electrode controlled by a potentiostat (EG&G PAR 283), a reference Ag/AgCl electrode saturated in KCl + AgCl solution and a Pt wire as a counter electrode. A 200 W quartz tungsten-halogen lamp coupled with grating monochromator was used for the wavelength dependent measurements, following the method described in detail elsewhere.[163] The white-light photocurrents were measured under AM1.5 solar illumination (100 mW/cm<sup>2</sup>) with a Newport Sol3A Class AAA solar simulator (type 94023A-SR3). Cyclic voltammetry was used to determine the photocurrent for different voltage values. According to the basic principles of this technique, voltage is swept between two values (from 0.4 to 1.5 V with a scan rate of 50 mV/s) and the resulted photocurrent can provide information about the kinetics of the reaction (water oxidation). The photocurrent density was calculated by

dividing the photocurrent values with the active surface area of the semiconductor ( $0.283 \text{ cm}^2$ ) and plotted as a function of the voltage vs RHE ( $V_{\text{RHE}}$ ).

**Finite difference time domain (FDTD) simulations.** The optical properties of 15 nm Ag dimers were modeled using the FDTD method (FDTD Solutions, Lumerical Solutions, Inc., Canada). Two Ag spheres with varying gap (or overlap) were placed on a substrate with a refractive index of 2.45 and illuminated normal to substrate using a total-field scattered-field source. The optical absorption cross section was calculated as the net power flux into a monitor box surrounding the dimer.

### **Acknowledgements**

Financial support from VENI project (granted to Dr. Wilson A. Smith) by NWO is gratefully acknowledged.

Financial support from the NWONANO project (11521), in which the particle production method was optimized, is gratefully acknowledged.

We thank Joost Middelkoop and Frans Oostrum for the TEM and SEM measurements, respectively.

## Supporting Information

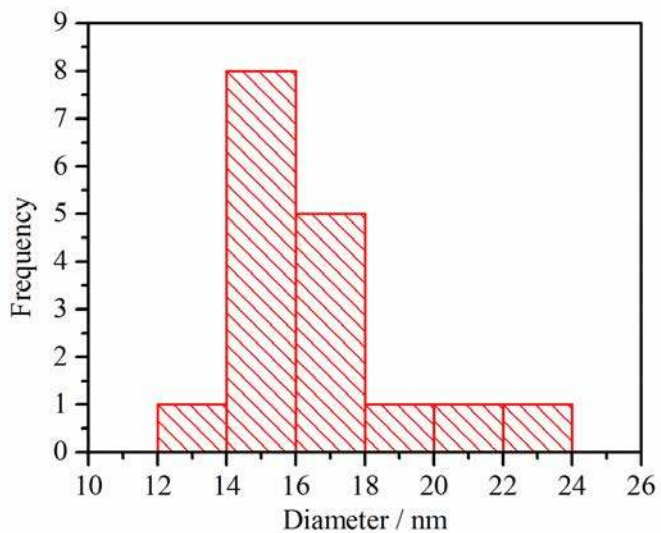


Figure S1. Particle size distribution of the Ag NPs shown in Figure 2A.

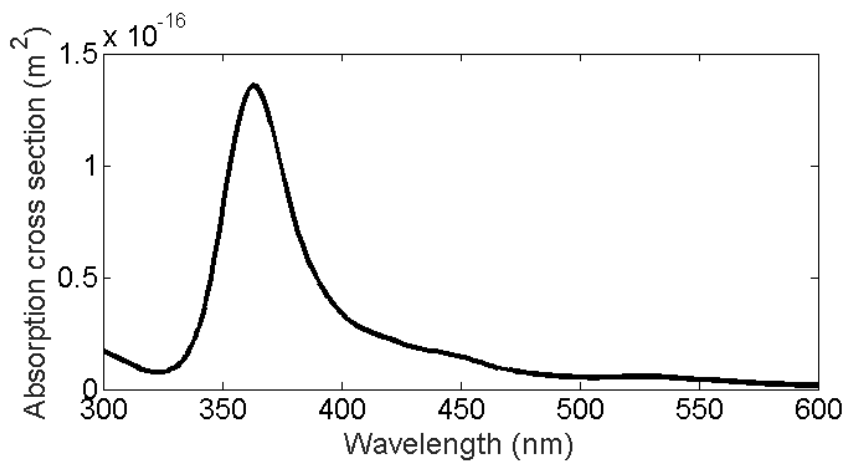


Figure S2. Simulated absorption spectra of a Ag NP on a BiVO<sub>4</sub> substrate.



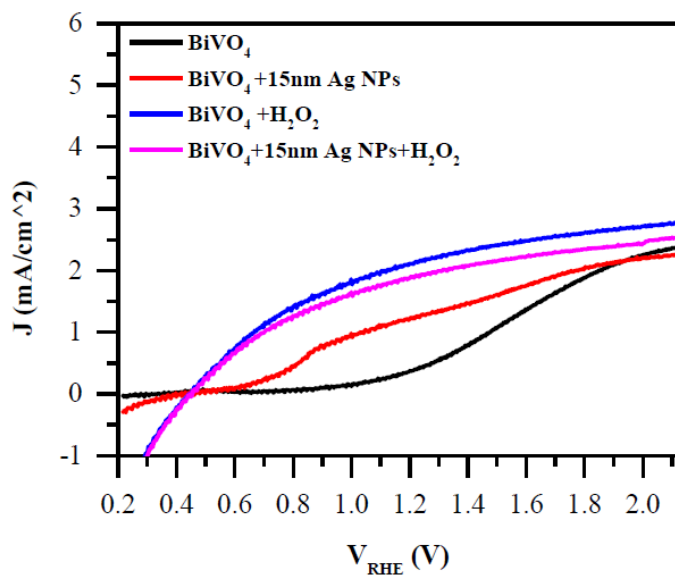


Figure S3. Front illumination (AM1.5) photocurrent versus voltage (j-V) curve of BiVO<sub>4</sub>, before (black) and after (blue) NP functionalization, with (dashed lines) and without (solid lines) H<sub>2</sub>O<sub>2</sub> in the electrolyte.

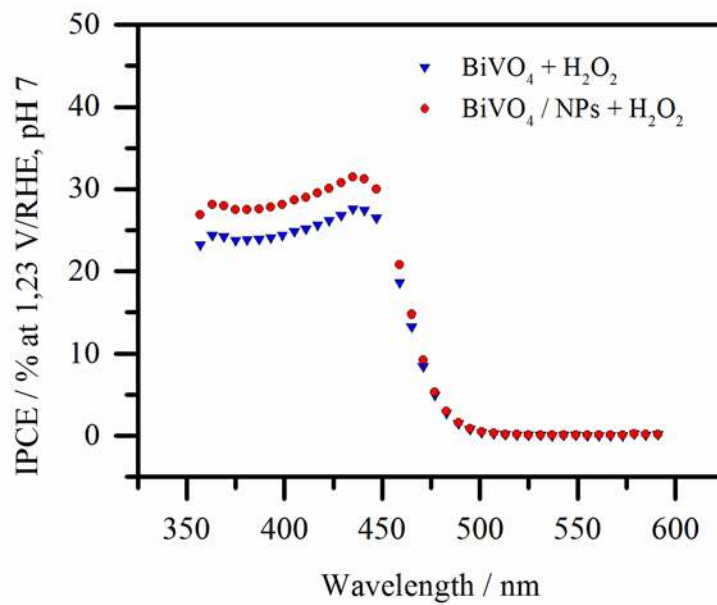


Figure S4. Front illumination IPCE curves for a  $\text{BiVO}_4$  sample before and after 65 nm Ag NP deposition.

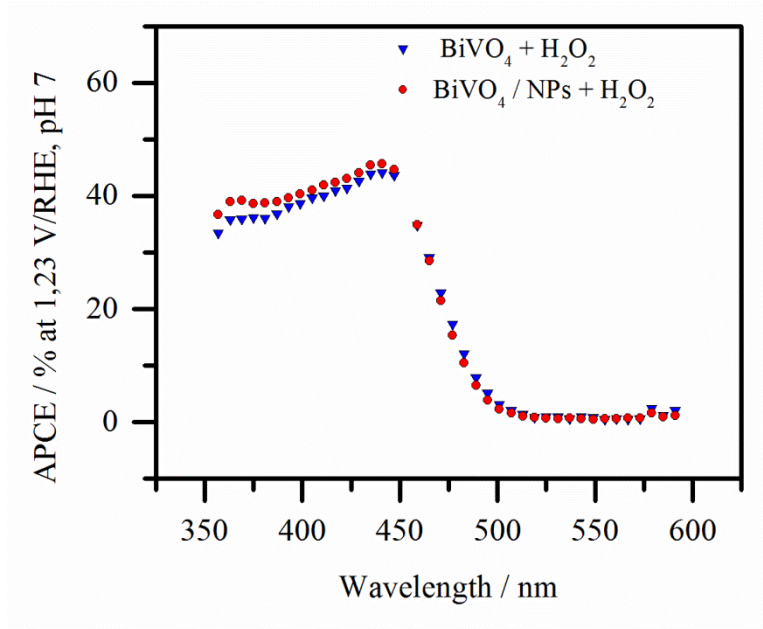


Figure S5. APCE curves for a BiVO<sub>4</sub> sample before and after 65 nm Ag NP deposition.

The power ( $P$ ) absorbed by the plasmonic NP can be estimated with the following relation:[78]

$$P = \sigma I \quad \text{Equation 1S}$$

Where,  $\sigma$  is the absorption cross section of the plasmonic NP ( $\sim 3 \cdot 10^{-16} \text{ m}^2$  at 400 nm, see Figure 5) and  $I$  is the light intensity ( $\sim 1200 \text{ W/cm}^2$ ).

The change in temperature ( $\delta T$ ) due to an spherical plasmonic NP can be computed with the following analytical solution:[78]

$$\delta T = P / (4\pi kR) \quad \text{Equation 2S}$$

Where,  $k$  is the thermal conductivity of the medium (0.6 W/mK for water) and  $R$  is the radius of the particle (7.5 nm in this work), which results in a  $\delta T$  of less than 0.1 K.

## 7. Enhancement of the Photoelectrochemical Performance of CuWO<sub>4</sub> Thin Films for Solar Water Splitting by Plasmonic Nanoparticle Functionalization

The effect of plasmonic nanoparticles (NPs) on the photoelectrochemical water splitting performance of CuWO<sub>4</sub> is studied here for the first time. CuWO<sub>4</sub> thin films were functionalized with well-defined Au NPs in two composite configurations: with the NPs I) at the CuWO<sub>4</sub> – electrolyte interface, and II) at the CuWO<sub>4</sub> back contact. In both cases, the incident photon to current conversion efficiency of the film was increased (~ 6-fold and ~ 1.2-fold for configurations I and II (at  $\lambda = 390$  nm), respectively). Two important advantages of placing the NPs on the CuWO<sub>4</sub> – electrolyte interface are identified: 1) Au NPs, coated with a 2-nm TiO<sub>2</sub> layer, are found to significantly enhance the surface catalysis of the film, decreasing the surface charge recombination from ~60% to ~10%, and 2) the NP's near-field can promote additional charge carriers within the space charge layer region, where they undergo field-assisted transport, essentially avoiding recombination. Our study shows that Au NPs, coated with a 2-nm TiO<sub>2</sub> layer, can significantly mitigate the catalytic and optical PEC limitations of CuWO<sub>4</sub>. An increase from 0.03 mA cm<sup>-2</sup> to 0.1 mA cm<sup>-2</sup> in the water splitting photocurrent was measured for a 200-nm film under simulated solar irradiation at 1.23 V vs RHE.<sup>4</sup>

---

<sup>4</sup> This chapter has been based on ref: 49. Valenti, M., et al., *Enhancement of the Photoelectrochemical Performance of CuWO<sub>4</sub> Thin Films for Solar Water Splitting by Plasmonic Nanoparticle Functionalization*. The Journal of Physical Chemistry C, 2014.

## Introduction

Harvesting and storing solar energy in chemical bonds is an ideal alternative to fossil fuels and an answer to the continuously growing need for clean, renewable, and sustainable energy. One of the most promising ways to convert solar energy directly into fuel is by photoelectrochemical (PEC) water splitting, which can be achieved by light absorbing semiconductors driving the oxygen and hydrogen evolution reactions.

Metal oxides are promising materials for solar water splitting applications due to their low cost and high stability in aqueous environments. Nevertheless, their optoelectronic and catalytic properties result in a limited overall reaction efficiency, which needs further improvement. A large number of metal oxides have been investigated as photoelectrodes for water oxidation and reduction reactions. The most studied metal oxides (i.e.,  $\text{TiO}_2$ ,  $\text{WO}_3$ ,  $\text{Fe}_2\text{O}_3$ ) suffer from poor solar to hydrogen (STH) conversion efficiencies due to their large band gap energies (e.g., 3.2 eV for  $\text{TiO}_2$ <sup>[195]</sup> and 2.8 eV for  $\text{WO}_3$ <sup>[196]</sup>), and extremely short charge carrier diffusion lengths (e.g., 2 nm in  $\text{Fe}_2\text{O}_3$ )<sup>[197]</sup>.  $\text{CuWO}_4$  and  $\text{BiVO}_4$  have recently attracted attention due to their relatively smaller band gap energies (2.4 eV for  $\text{BiVO}_4$  and 2.25 eV for  $\text{CuWO}_4$ ), and improved charge mobility characteristics.

In particular, poly-crystalline  $\text{CuWO}_4$  is a promising photoanode material.<sup>[198]</sup><sup>[199]</sup> The band gap of  $\text{CuWO}_4$  is close to ideal for PEC water splitting (i.e., between 2.0 and 2.25 eV),<sup>[200]</sup> corresponding to a theoretical STH efficiency of  $\sim 13\%$  (assuming 100% Faradaic efficiency) achieved at photocurrent density of  $10.7 \text{ mA cm}^{-2}$ .<sup>[201]</sup> Despite that, the PEC performance of  $\text{CuWO}_4$  is significantly hindered by its low light absorption coefficient (e.g.  $\sim 10^3 \text{ cm}^{-1}$  for  $\text{CuWO}_4$ ,<sup>[198]</sup> and  $\sim 10^5 \text{ cm}^{-1}$  for  $\text{Fe}_2\text{O}_3$ <sup>[202]</sup> at  $\lambda=500\text{nm}$ ) and high bulk

charge transfer resistance,[199][203]<sup>[204, 205]</sup> which results in lower than theoretically possible photocurrent densities for this material.

Functionalizing semiconductors with plasmonic nanoparticles (NPs) can help mitigate some of their PEC water splitting limitations (e.g., low light absorption, and charge carrier diffusion).[206] Under visible light irradiation, valence electrons in noble metal NPs undergo a collective oscillatory motion. This phenomenon, called surface plasmon resonance (SPR), can enhance the PEC performance of nearby semiconductors by several mechanisms including 1) plasmon resonance energy transfer (PRET),[206] 2) hot electron injection[207] and/or 3) light scattering, which will be described in subsections 1.1, 1.2, and 1.3, respectively.

Plasmon enhanced solar water splitting has been studied for different systems including Fe<sub>2</sub>O<sub>3</sub>,[181] TiO<sub>2</sub>,[206, 208] and BiVO<sub>4</sub>,[76] but so far it has not been used on CuWO<sub>4</sub>. Thimsen *et al.*[181] functionalized iron oxide (Fe<sub>2</sub>O<sub>3</sub>) platelets with Au NPs (~ 45 nm in diameter). Due to the small overlap of the light absorption spectra of the NPs and the semiconductor used in that study, only a small increase in the normalized IPCE (~25%) was observed. It should be noted that the relative enhancement reported in that study was measured only at the wavelengths where the absorption spectra of the NPs and semiconductor overlapped. On the other hand, Ingram *et al.*[206] reported significant improvement in the solar hydrogen formation of an N-doped TiO<sub>2</sub> film (~ 750-nm thick) after functionalization with Au NPs or Ag nanocubes. The explanation provided by the authors is that the NP functionalization increased the surface charge carriers concentration in the semiconductor, which is particularly important for semiconductors, like TiO<sub>2</sub>, that suffer from high bulk charge transfer resistance.

In either case, the above-mentioned studies highlight 1) the importance of tuning the NPs plasmon resonance through their size and shape control (according to Mie theory) so as to match the absorption spectra of the applied semiconductor, and 2) that NP

functionalization can be an adequate way to improve significantly the semiconductors' performance and therefore mitigate their main inherent limitations.

In this work we investigate the possibilities of mitigating the inherent limitations of  $\text{CuWO}_4$  (low absorption coefficient and large charge transfer resistance) by functionalizing relatively thin (200 – 400-nm)  $\text{CuWO}_4$  films with plasmonic NPs. We deposit tailored 35-nm Au NPs, synthesized with a novel gas-phase technique, on  $\text{CuWO}_4$  films in order to enhance their light absorption in the region near the band-gap edge (i.e.,  $\sim 540$  nm) where the semiconductor exhibits its lowest absorption and PEC performance. According to Mie theory, spherical 35-nm Au NPs exhibit resonance frequencies around 540 nm.

Different mechanisms for plasmon enhanced solar water splitting are briefly described below as background for interpreting the results obtained in this study and to determine the most likely mechanisms for the enhancement of  $\text{CuWO}_4$  water splitting performance.

#### **Plasmon resonance energy transfer (PRET)<sup>5</sup>**

An important characteristic of SPR is the enhancement of the incident electric field around the NP (NP near-field). When the NP is in contact or within a few nm from the semiconductor, its near-field penetrates the semiconductor as illustrated in Figure 68. In this region, the NP near-field acts as a light concentrator, locally enhancing the electron-hole generation rate in the semiconductor. This plasmon resonance energy transfer (PRET) enhancement mechanism is effective only for NPs with resonance frequencies that correspond to energies within the semiconductor's band-gap.[181][43]<sup>[67]</sup>

---

<sup>5</sup> This mechanism is the same as the "light concentration effect" described in chapter 3 of this thesis. Since this chapter was published before the PIRET mechanism (near-field effect acting below the optical band-gap edge of the semiconductor) was well known in the field, there was no need to differentiate between the light concentration mechanism (near-field effect acting above the optical band-gap edge of the semiconductor) and PIRET.



When the plasmonic NPs are placed on the semiconductor-electrolyte interface, the enhancement in the electron-hole formation rate will take place at the space charge layer (SCL). As a consequence, all the additional charge carriers formed due to the PRET, will undergo field-assisted transport and contribute to the photocurrent. Hence, when the thickness of the film is larger than the SCL width, the PRET contribution is expected to be more significant when the NPs are placed near the semiconductor-electrolyte interface than at the semiconductor back contact.

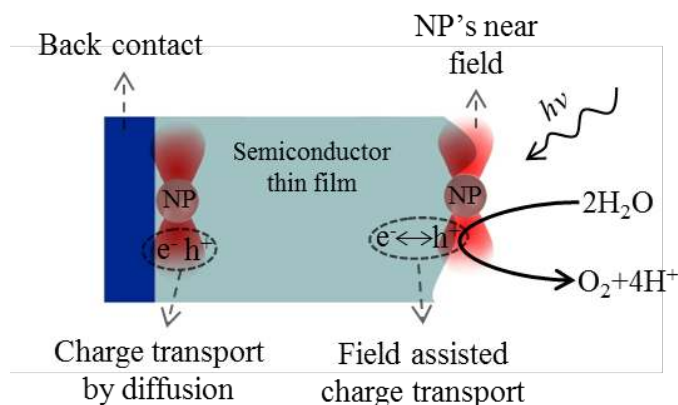


Figure 68. Illustration of the PRET enhancement mechanism induced by NPs placed on the semiconductor - electrolyte interface (right hand side) and on the  $\text{CuWO}_4$  back contact (left hand side).

### Light scattering

When the SPR decays, light is either scattered or absorbed.[56] According to Mie theory, if Au NPs are larger than 60-nm their scattering cross section in an aqueous environment becomes significant ( $> 800 \text{ nm}^2$  at a wavelength of 540 nm). When the NPs are placed at an interface between two different materials more light is scattered into the material with a larger refractive index (RI).[119] Since most metal oxides have a larger RI than water, plasmonic NPs placed at the semiconductor-electrolyte interface can reduce the amount of light that is reflected off the surface, by scattering the incident light into the

semiconductor (Figure 69 A). If the RI of the semiconductor is also larger than the RI of the conducting back contact material, NPs placed at this interface will again have a preferential scattering towards the semiconductor (Figure 69B). Besides this antireflection effect, scattering of light at the surface of the semiconductor can also increase the light's pathlength through the semiconductor, which is critical for thin films with in-direct band-gap energies and small absorption coefficients.

Overall, the light scattering mechanism induced by the NPs can increase the incident photon to current conversion efficiency (IPCE) of the semiconductor by increasing the light absorption. However, unlike the previously described enhancement mechanism (PRET), scattering does not enhance the *absorbed* photon to current conversion efficiency (APCE). Hence, APCE is a key measurement technique to distinguish between these two enhancement mechanisms.

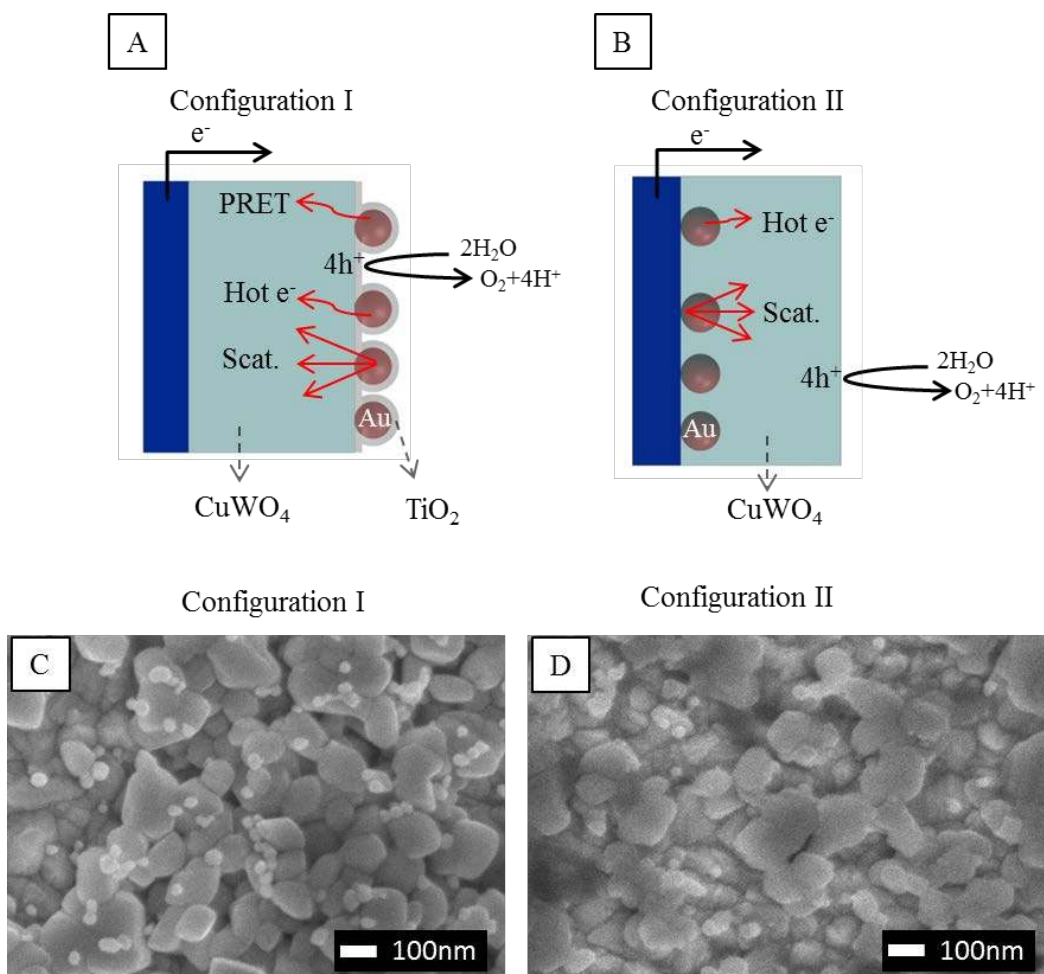


Figure 69. A) and B) Illustration of two  $\text{CuWO}_4$  - NP composite configurations in contact with an electrolyte. In Configuration I,  $\text{TiO}_2$  coated Au NPs are placed at the  $\text{CuWO}_4$  - electrolyte interface, whereas in Configuration II the Au NPs are at the back contract. The most relevant optical effects are illustrated in each configuration. Scat. – Scattering. C) and D) Corresponding SEM top view images for the fabricated composite configurations.

### Direct hot electron injection

Small noble metal NPs having a large cross section of absorption can transfer the energy of resonating photons to the surrounding medium by the formation of charge

carriers,[209] namely hot electrons and holes. If the energy of the hot electron/hole is larger than the energy barrier at the NP-semiconductor interface, they can be transferred to the semiconductor's conduction/valence band and take part in the corresponding water splitting half reactions.[207]

An important feature of this mechanism is that it can take place outside the semiconductor band gap energy, expanding the spectrum of usable light to longer wavelengths. This feature is used in this work to distinguish the hot electron injection mechanism from the aforementioned mechanisms (i.e. PRET & light scattering).

## **Experimental**

### **Spray Deposition of CuWO<sub>4</sub> Thin Film Photoanodes**

Thin films (200 – 400-nm) of CuWO<sub>4</sub> were deposited on fluorine doped tin oxide (FTO) substrate (TEC-15, Hartford Glass Co.) using an easy to scale-up spray pyrolysis technique. Prior to the CuWO<sub>4</sub> deposition, the substrate was cleaned by subsequent ultrasonication in triton, acetone and isopropanol solution for ca. 20 min, dried under compressed N<sub>2</sub> flow and slowly heated up to 300 °C. The precursor solution was prepared by mixing pre-prepared 0.2 M aqueous solutions of copper sulphate pentahydrate (CuSO<sub>4</sub>·5H<sub>2</sub>O, 99%, Acros Organics) and sodium tungstate dihydrate (Na<sub>2</sub>WO<sub>4</sub>·2H<sub>2</sub>O, 99%, Merck KGaA) and diluting with milliQ water to a concentration of 0.005 M. The pH of the final solution was adjusted to 10.5 by adding appropriate amount of ammonia water (NH<sub>4</sub>OH, 25%, Sigma Aldrich). The spray deposition was carried out using an automated spray setup with Quickmist air atomizing spray nozzle driven by an overpressure of 0.06 MPa of nitrogen gas. The distance between nozzle and substrate was fixed at 30 cm. Each spray cycle (5 cycles for 200-nm film) consisted of 2 s of spray time and 58 s of delay time to allow solvent evaporation. The resulting thin films were subsequently annealed for 4 hours under air flow (20 ml min<sup>-1</sup>) in a tube furnace at 500 °C, to ensure that the CuWO<sub>4</sub> is fully

crystalline. The mean thickness ( $\pm 20\%$ ) of the films was determined using a profilometer (DekTak 3).

### **NP synthesis**

Au NPs were synthesized in the gas phase with a spark discharge particle generator.[210] In brief, sparks between two gold electrodes are repeatedly formed with a frequency of 300 Hz using a power supply coupled with a capacitor. Gold vapors produced during every spark are carried away and cooled down in a  $N_2$  gas flow ( $2 \text{ L min}^{-1}$ ). As a result, the gold vapors condense into clusters that grow to NPs and agglomerate. The agglomerated NPs are sintered into spherical NPs by heating the aerosol flow in a tube furnace ( $\sim 900 \text{ }^\circ\text{C}$ ). The spherical NPs are then brought to the Boltzmann equilibrium charge distribution[211] by passing them through a neutralizer. The charged NPs leaving the neutralizer are mostly singly charged (e.g.  $> 95\%$  for 50-nm NPs). A custom-made differential mobility analyzer (DMA,[154]) downstream from the neutralizer is then used to separate the NPs according to their electrical mobility, which for singly charged NPs corresponds to the NP size (see Equation S1 and S2 in the supporting information).

By adjusting the operating conditions (i.e. voltage and flows) of the DMA, we selected 35-nm Au NPs, which were then deposited on the  $\text{CuWO}_4$  film (or bare FTO substrate) for 15 min, using an electrostatic precipitator (EP). An illustration of the whole process of Au NP synthesis, size selection and deposition is shown in Figure 70.

The size-selected Au NPs were also collected on a carbon polymer microgrid (supported on a copper grid) for characterization by transmission electron microscopy (TEM). From the TEM micrographs the NPs' cross-sectional areas were measured with the software *imagej* (Research Services Branch, National Institutes of Health), regardless of their shape. The effective NPs' diameters were then calculated from their corresponding areas by

assuming spherical NPs ( $Diameter = 2 \cdot \left( \sqrt{\frac{Area}{\pi}} \right)$ ). With this method, the sizes of 276 NPs were used to calculate the mean size of the synthesized NPs.

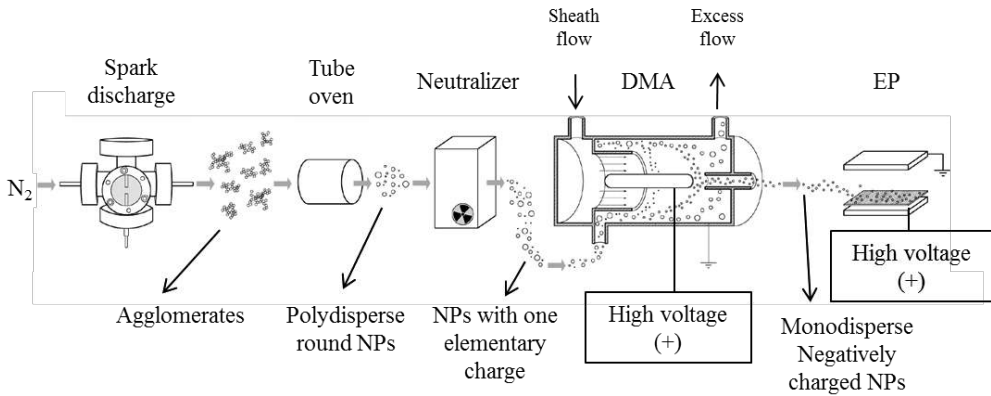


Figure 70. Schematic illustration of the synthesis and deposition of the monodisperse (35 nm in diameter) spherical Au NPs.

### TiO<sub>2</sub> deposition

A thin titanium dioxide layer with a thickness of 2.3 nm (determined by Ellipsometry) was deposited on top of the CuWO<sub>4</sub>/Au NP films by Atomic Layer Deposition (ALD) using tetrakis-dimethylamino titanium (TDMAT) and H<sub>2</sub>O as precursors. ALD is a variant of chemical vapor deposition (CVD) used for growing ultra-thin and high quality films.[212] The ALD equipment used for TiO<sub>2</sub> deposition is described in detail elsewhere.[213] The pulse sequences for depositions were 30 s for purge, 5 s for TDMAT precursor, 30 s for purge and finally 10 ms for H<sub>2</sub>O precursor. The deposition temperature was kept constant at 150 °C.

### **UV Vis absorption and film thickness measurements**

The UV-Vis absorption spectra of the  $\text{CuWO}_4$  films were measured using a spectrometer (Perkin-Elmer-Lambda 900) equipped with an integrated sphere device allowing simultaneous recording of both transmittance and diffuse reflectance of the sample. Measurements were conducted for back illumination, before and after Au NP and  $\text{TiO}_2$  layer deposition, so that the influence of each component on the overall absorption spectra could be determined.

### **Photoelectrochemical measurements**

The photoelectrochemical characterization of the samples, before and after their functionalization with NPs (cf. subsection 2.2 & 2.3), was carried out in an aqueous 0.1 M potassium phosphate buffer solution ( $\text{KPi}$ ,  $\text{K}_2\text{HPO}_4$  and  $\text{KH}_2\text{PO}_4$ , 99.5% Fluka,  $\text{pH} \sim 7$ ) in an electrochemical cell using a three-electrode configuration: a working electrode whose potential was controlled by a potentiostat (EG&G PAR 283), a reference Ag/AgCl electrode (XR300, saturated KCl + AgCl solution (KS120), Radiometer Analytical), and a coiled Pt wire as a counter electrode. White-light photocurrent measurements were performed under simulated AM1.5 solar illumination with a Newport Sol3A Class AAA solar simulator (type 94023A-SR3) (irradiation spectrum, Figure S1). The monochromatic photocurrents (IPCE and APCE) were measured at 1.23 V vs RHE using 200 W quartz tungsten-halogen lamp coupled into a grating monochromator with a 6-nm step following the method described in details elsewhere.[163] IPCE measurements provide information about the number of photons incident on the photoelectrochemical cell that are effectively converted into photocurrent as a function of wavelength. This value is, however, understated due to losses associated with incident light reflection and imperfect absorption, and is referred to as the external quantum efficiency.[214] The APCE is the IPCE value corrected with regard to the UV-Vis absorption spectra of each sample and provides values closer to the real conversion efficiency, i.e. the internal quantum efficiency.

## Results and discussion

The size and shape of the Au NPs was measured by TEM (cf. Figure 71). The size ( $39 \pm 7$ -nm) is in good agreement with that selected by the DMA (set to select 35-nm particles). The 4-nm difference between the targeted and obtained mean size can be explained by the errors involved in assuming the NPs are perfectly round. This inexact assumption (see elongated shape in Figure 71 bottom) was made in the gas phase size selection (cf. Equation S1 in the supplementary information) and in the NP size measurements (see subsection 2.2). According to Mie theory, the  $\lambda_{\text{max}}$  of absorption (the wavelength where the absorption is the greatest) of an isolated 39-nm round Au particle does not deviate significantly (less than 2-nm) from the  $\lambda_{\text{max}}$  of the targeted 35-nm particles. Hence, we still expect that the synthesized particles, having the particle size distribution shown in the inset of Figure 71, exhibit a  $\lambda_{\text{max}}$  at the  $\text{CuWO}_4$  band gap edge ( $\sim 540$  nm).



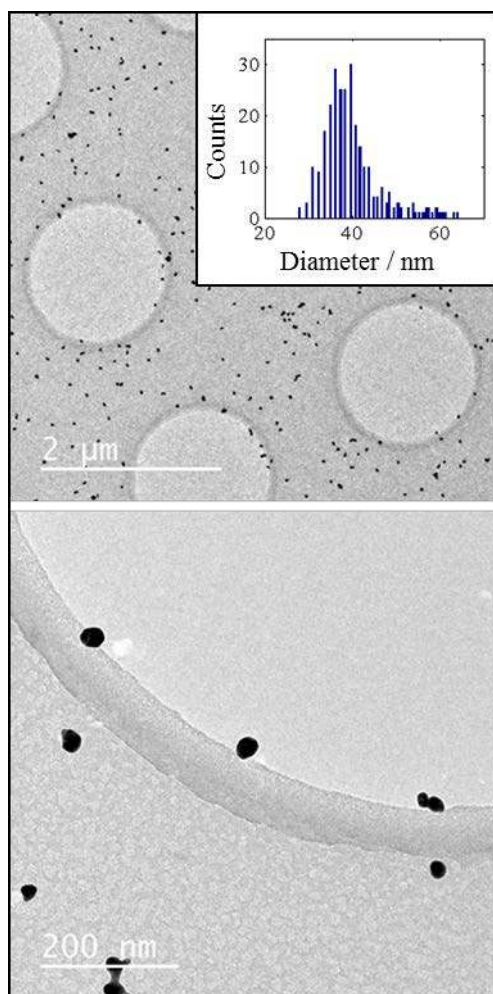


Figure 71. TEM micrographs of Au NPs produced by the spark discharge generator and selected by the DMA (as described in Figure 70). Inset figure: Size histogram of the top image.

Two configurations of  $\text{CuWO}_4$  – NP composites were constructed (cf. Figure 69). Configuration I (cf. Figure 69A), was fabricated by spray deposition of  $\text{CuWO}_4$  on a FTO substrate, followed by Au NP deposition and  $\text{TiO}_2$  atomic layer deposition. For Configuration II (cf. Figure 69B), first Au NPs were deposited on the FTO substrate,

followed by  $\text{CuWO}_4$  spray deposition on top of them. Top view SEM images of the resulting composite samples are shown in Figure 69C (Configuration I) and Figure 69D (Configuration II).

The role of the  $\text{TiO}_2$  layer in Configuration I is twofold: 1) to fix the NPs on the  $\text{CuWO}_4$  surface and 2) to coat the NPs in order to enhance their SPR interaction with light (Mie theory). The conduction of holes through this ultra-thin insulating film is possible via tunneling.[215]

Figure 72A shows the effect of the NPs and the  $\text{TiO}_2$  layer on the composite's (Configuration I) light absorption. The bare Au NPs increased the light absorption of  $\text{CuWO}_4$  only ~7% (at 520 nm). However, a clear red shift and increase in the peak of absorption (e.g. ~ 12% at 544 nm) was obtained after the  $\text{TiO}_2$  was deposited. This change is attributed to the expected effect of the SPR absorption when the NPs are coated (cf. Figure 72B). As a consequence, the coated NPs' SPR enhanced the light absorption of the  $\text{CuWO}_4$  film along a larger range in the spectrum. Therefore, the SPR enhancement mechanisms (e.g. PRET) can be active over a larger range in the  $\text{CuWO}_4$  thin film absorption spectra. Moreover, the  $\lambda_{\text{max}}$  of absorption is located exactly at the band gap edge of  $\text{CuWO}_4$  (i.e., between 540 – 550 nm). Obtaining the SPR peak of absorption in this region, has two main advantages: 1) It allows to identify the contribution, if any, of the hot electron injection mechanism, since any PEC enhancement at energies beyond the  $\text{CuWO}_4$  band gap would indicate hot electron injection from the NPs to the semiconductor (cf. subsection 1.3.). On the other hand, if the enhancement is restricted to the absorption range of  $\text{CuWO}_4$ , despite the large NP absorption beyond the band gap edge, the hot electron mechanism can be excluded. 2) Since bare  $\text{CuWO}_4$  exhibits an extremely low light absorption coefficient at these wavelengths (490 – 550-nm), a larger NP coverage could be used to significantly enhance the absorption in this region (through scattering or PRET

mechanisms), without blocking the light at wavelengths where  $\text{CuWO}_4$  efficiently absorbs light (e.g. 350 nm).

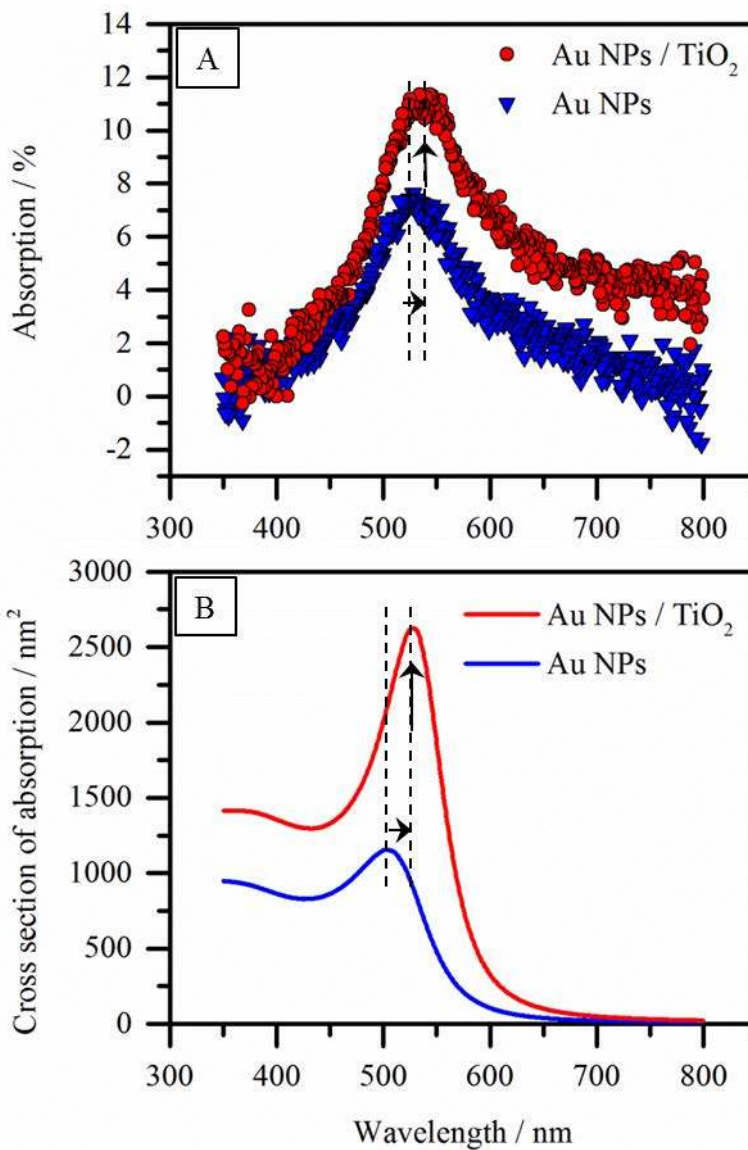


Figure 72. Measured NPs' SPR absorption peak before (blue) and after (red) deposition of a TiO<sub>2</sub> layer of 2-nm. B) SPR absorption cross section of coated and uncoated 39-nm NPs, according to Mie theory. The arrows indicate the red shift and the increase of the measured (top) and calculated (bottom) peak of absorption.

Although the  $\lambda_{\max}$  of absorption (cf. Figure 72A) agrees with the theory (cf. Figure 72B), the width of the peak of absorption is much broader than for the isolated particle model. This can be explained by the distribution of NP sizes present on the composite (cf. Figure 71) and by the formation of dimers and larger agglomerates during the NPs deposition, as shown by SEM (cf. Figure 69C). The latter also explains the absorption intensity at longer wavelengths (e.g. 700nm) since dimers, for instance, give a second peak of absorption at longer wavelengths.[62]

The IPCE measurements for a 200-nm  $\text{CuWO}_4$  film before and after functionalization with NPs (Configuration I) are shown in Figure 73A, together with their corresponding absorption spectra (Figure 73B). The absorption contribution of the  $\text{TiO}_2$ -coated Au NPs is added in Figure 73B as a reference. A significant increase in the IPCE was achieved for Configuration I. The IPCE values in Figure 73 can be used to compute the NP enhancement factor ( $f_{total}$ ) as a function of the wavelength (cf. Equation 1). The largest IPCE increase is observed at a wavelength of  $\sim 390$  nm with an enhancement factor as large as 6-fold.

$$f_{total} = \frac{IPCE_{CuWO_4 / Au NPs / TiO_2}^{H_2O}}{IPCE_{CuWO_4}^{H_2O}} \quad (1)$$

Where, the  $IPCE_{CuWO_4 / Au NPs / TiO_2}^{H_2O}$  and  $IPCE_{CuWO_4}^{H_2O}$  are the water splitting IPCE measurements for the composite and bare  $\text{CuWO}_4$ , respectively.

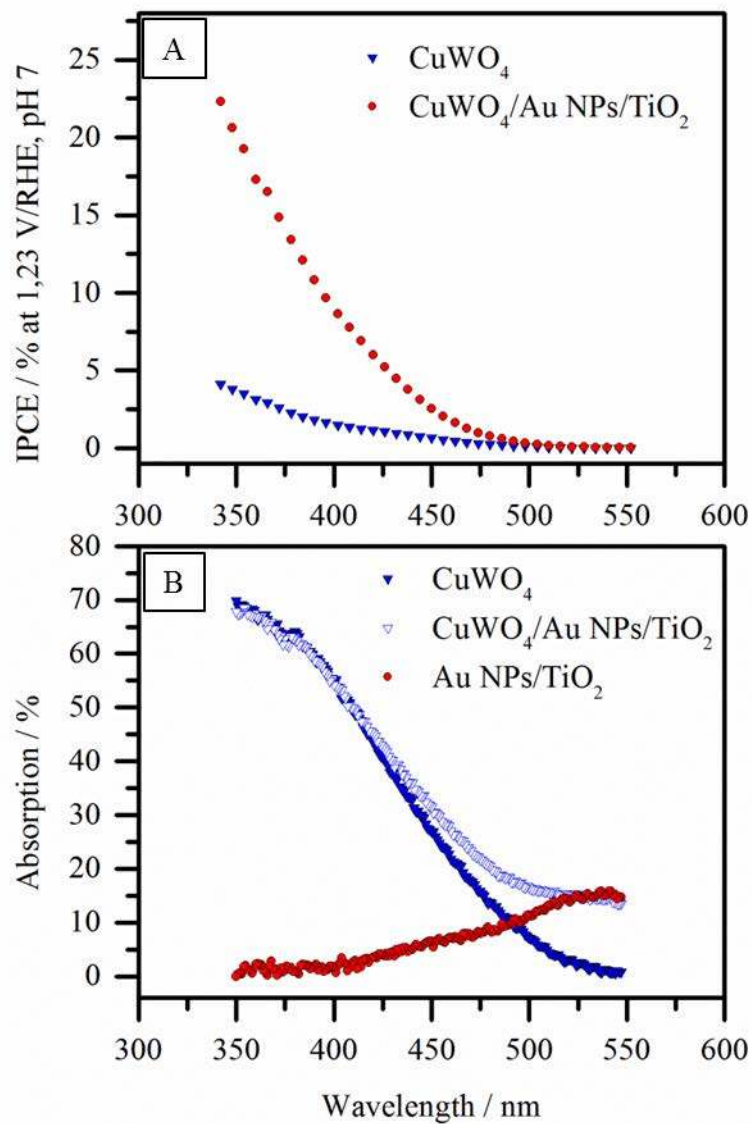


Figure 73. A) Back illumination IPCE for the 200-nm  $\text{CuWO}_4$  before and after NP functionalization (Configuration I) B) Corresponding absorption spectra.

The enhancement of the photocurrent density ( $J_{photocurrent}^{H_2O}$ ) of the  $CuWO_4$  film is a consequence of a surface (e.g. catalytic) and/or a bulk (i.e. absorption or charge separation enhancement) effect due to the semiconductor's interaction with the decorating NPs, as stated in the following equation[120]:

$$J_{photocurrent}^{H_2O} = J_{absorbed} \times P_{charge\ separation} \times P_{charge\ injection} \quad (2)$$

where,  $J_{absorbed}$  is the rate of photon absorption,  $P_{charge\ separation}$  is the charge separation yield of photogenerated charge carriers and  $P_{charge\ injection}$  is the charge injection yield to the electrolyte.

In order to distinguish between these contributions (surface and bulk effects) we used the following strategy that was first used by Dotan et al[120] to quantify bulk and surface recombination in  $Fe_2O_3$ , and more recently by Abdi et al[76] to distinguish between the catalytic effect and plasmonic effect of  $Ag@SiO_2$  core-shell NPs in  $BiVO_4$ .

By adding  $H_2O_2$  (an easily oxidized hole scavenger) to the electrolyte, it is reasonable to assume that the surface catalytic efficiency is 100% ( $P_{charge\ injection} = 1$  in Equation 2).[120] This way, the IPCE performance of bare  $CuWO_4$  ( $IPCE_{CuWO_4}^{H_2O_2}$ ) and the composite ( $IPCE_{CuWO_4 / Au\ NPs / TiO_2}^{H_2O_2}$ ) can be compared under 100% surface catalytic efficiency conditions. Any photocurrent enhancement, under these conditions ( $P_{charge\ injection} = 1$ ), could be then ascribed to an increase in the absorption and/or charge separation yield through a NP plasmonic effect[76]:

$$f_{Plasmonic} = \frac{IPCE_{CuWO_4 / Au\ NPs / TiO_2}^{H_2O_2}}{IPCE_{CuWO_4}^{H_2O_2}} \quad (3)$$

where  $f_{plasmonic}$  is the plasmonic enhancement factor.

The catalytic enhancement ( $f_{catalytic}$ ) can be computed by comparing the actual enhancement factor ( $f_{total}$ , cf. Equation 1) and the plasmonic enhancement factor ( $f_{plasmonic}$ ):

$$f_{catalytic} = \frac{f_{Total}}{f_{Plasmonic}} \quad (4)$$

Figure 74 shows the computed IPCE enhancement factors. The surface catalytic effect is found to be the predominant effect in the total enhancement, increasing the IPCE more than 3-fold at a wavelength of 390 nm. The shape of this enhancement ( $f_{catalytic}$  vs. wavelength) follows to the light intensity spectrum used in the IPCE experiments (See Figure S2), with both curves presenting a peak at ~390nm. This can be explained by the fact that for bare  $CuWO_4$ , having a low catalytic efficiency, more hole surface accumulation and subsequent recombination take place when more holes are available at the surface (i.e. at wavelengths with a large incident photon flux and a corresponding higher absorption in the films). Therefore, we see that after NP functionalization the catalytic efficiency is enhanced, hindering the hole recombination in a larger extent at wavelengths (350 – 425 nm) with a large number of incoming photons and a relatively large  $CuWO_4$  absorption coefficient.

On the other hand, the curve of the calculated plasmonic enhancement factor ( $f_{plasmonic}$  vs. wavelength) does not increase with the intensity of the incoming light nor with the absorption of the semiconductor but with the absorption of the plasmonic NPs. Interestingly, the enhancement threshold of  $f_{plasmonic}$  is limited to the wavelength range at which the bare  $CuWO_4$  absorbs light. Therefore, we conclude that the hot electron injection mechanism does not play a relevant role in the measured enhancement.



In order to distinguish between the remaining plasmonic mechanisms (i.e. PRET and light scattering), the APCE enhancement factors were calculated, analogously to the IPCE enhancement factor calculations (cf. Equation 1, 3 and 4). The APCE plasmonic enhancement factor is found to be larger than 1 (cf. Figure S4). An increase in the APCE, due to a plasmonic effect, cannot be explained by the scattering mechanism<sup>6</sup> since its only contribution is to increase the absorption in the bulk of the material. The PRET mechanism, on the other hand, is characterized by a strong localized electric field (NP's near-field) that can enhance the rate of electron/holes formation of the semiconductor when the NPs are sitting on the semiconductor-electrolyte interface (near the SCL region).<sup>[67]</sup> This strong interaction between the NP's near-field and the SCL region, could explain the APCE plasmonic enhancement factor shown in Figure S4. This scenario is realistic for a semiconductor whose bulk charge carrier transport is the limiting step in the PEC performance. In this case, the charge carriers formed in the bulk have a high probability for recombination and only the electron-hole created near the surface, which undergo efficient separation due to the SCL, contribute significantly to the total photocurrent. Hence, if this is the case for CuWO<sub>4</sub>, concentrating the light intensity at the SCL with plasmonic NPs (via PRET) lead to an enhancement in the concentration of well-separated charge carriers and thus an observable APCE enhancement.

---

<sup>6</sup> Assuming that the recombination properties of CuWO<sub>4</sub> are not absorption dependent.

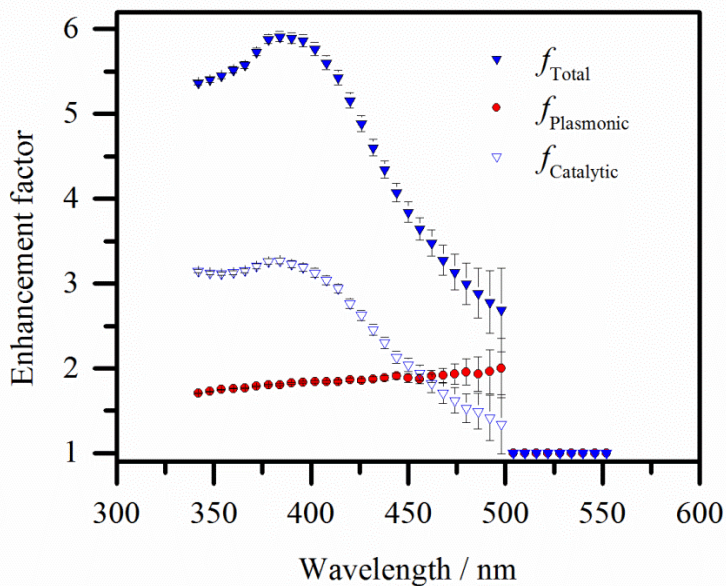


Figure 74. IPCE enhancement factors after NP functionalization (Configuration I), calculated with Equations 1,3 and 4 from the IPCE values plotted in Figure S3. The error bars represent the sensitivity of the IPCE enhancement factors to the experimental uncertainties.

To further elucidate the effect of plasmonic NPs on the  $\text{CuWO}_4$  water splitting PEC performance, a second composite (Configuration II) was tested. For this configuration, the PRET enhancement mechanism is expected to have a much smaller effect, since the NP near-field does not concentrate the light at the electrolyte interface where the charge carriers are separated more efficiently (cf. section 1.1.). Therefore, the effect of other enhancement mechanisms (e.g. scattering) that might enhance the performance to a smaller extent, can be observed and studied independently.

The IPCE results of Configuration II are shown in Figure 75A, together with their corresponding absorption spectra (cf. Figure 75B). Unlike for Configuration I, for Configuration II is not possible to measure the performance of the  $\text{CuWO}_4$  film before and after NP functionalization, since for this configuration (II) the NPs had to be deposited first (See Figure 69B). Therefore, Figure 75. shows the IPCE and absorption of two different samples, synthesized under exactly the same conditions, with the only difference that the spray pyrolysis deposition of the bare  $\text{CuWO}_4$  sample was made on a clean FTO surface, while the spray deposition of the composite was made on a FTO surface decorated with NPs. The maximum absorption of the bare  $\text{CuWO}_4$  sample (350-nm) is 7% larger than the composite sample. This small absorption deviation comes from the thickness deviation between different spray pyrolysis depositions. The IPCE of the bare  $\text{CuWO}_4$  sample and the composite (Configuration II) are almost identical (cf. Figure 75A). Nevertheless, the composite shows a small enhancement at shorter wavelengths (350 – 420) as shown in Figure 76. This enhancement increases with decreasing wavelength and is non-existent at the wavelengths where the semiconductor's absorption overlaps with the NP's absorption. Therefore, we conclude that unlike for Configuration I, Configuration II exhibits no plasmonic enhancement.

In order to explain the small increase in the performance of Configuration II, the catalytic efficiency ( $C_{eff}$ , see Equation S3 in the supporting information) of the samples was investigated (cf. Figure S5). It is observed that the composite sample has a larger catalytic efficiency, which explains the small increase in the IPCE for Configuration II (cf. Figure 76). This catalytic effect can still come from the NPs, despite the fact that for Configuration II the NPs are on the back contact. This is because the  $\text{CuWO}_4$  film is quite porous, and some of the NPs on the back contact can still be in contact with the electrolyte and the  $\text{CuWO}_4$  grains, playing a catalytic role. This explanation is supported by SEM (Figure 69D), where some of the NPs on the FTO are still observable between the  $\text{CuWO}_4$  grains.

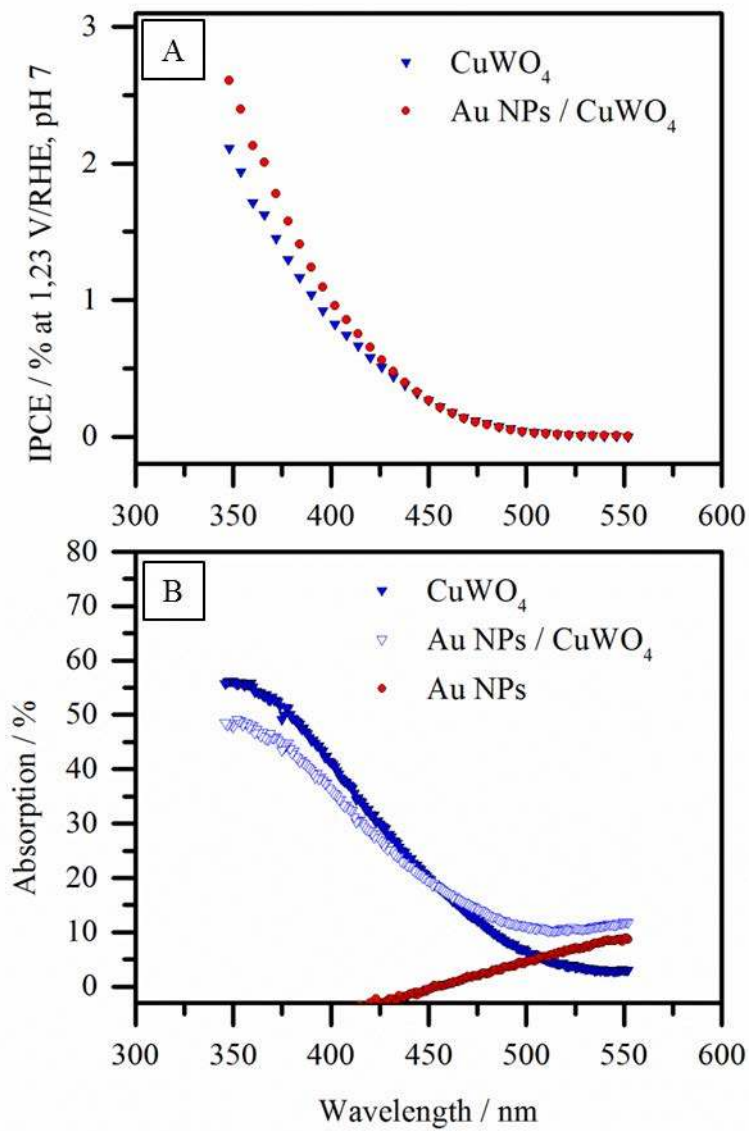


Figure 75. A) Back illumination IPCE for bare 200-nm  $\text{CuWO}_4$  and functionalized (Configuration II) 200-nm  $\text{CuWO}_4$  B) Corresponding absorption spectra.

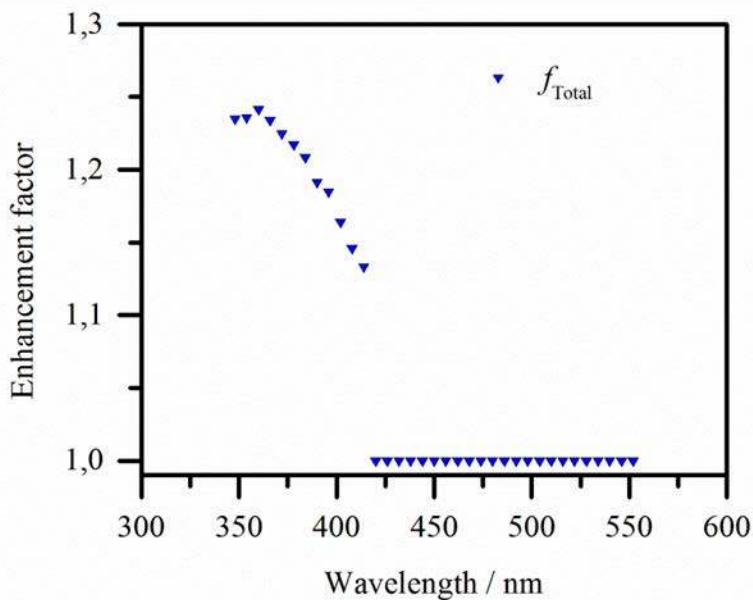


Figure 76. IPCE enhancement factor due to NP functionalization (Configuration II), calculated with Equations 1, from the IPCE values plotted in Figure 75A.

The IPCE enhancement observed for Configuration I, is found to be a contribution between a surface (NP catalytic effect) and a bulk (plasmonic effect). The plasmonic enhancement is explained here by a PRET-induced localized increase in the charge carrier yield at the SCL. This charge carrier increase at the SCL plays an important role in the  $\text{CuWO}_4$ 's improved photocurrent due to excellent charge separation in this region. This theory is supported by a second configuration (Configuration II) where the particles were embedded toward the back of the semiconductor, away from the SCL, and no plasmonic enhancement was observed. Furthermore, the significant plasmonic enhancement factor, obtained in this work (Figure 74), can be explained by the fact that  $\text{CuWO}_4$  exhibits high bulk charge carrier recombination.[199] Since, in this case, any charge carrier increase at

the SCL leads to a significant increase of the overall photocurrent. The PRET effect, at the SCL, has already been observed for TiO<sub>2</sub>, [206] which also suffers from high bulk charge carrier recombination. [216]

It is important to highlight that PRET, as any plasmonic enhancement mechanism, is only active in the region of the spectrum where the NPs interact with light. In this work, the measured plasmonic enhancement factor increases with the wavelength (Figure 74), following the trend of the NP's absorption spectra. However, at shorter wavelengths (i.e. 350 – 400 nm) the measured NP absorption vanishes, while the enhancement factor does not decrease to unity. This enhancement in the UV region cannot be explained by a plasmonic mechanism, unless, even small NP absorptions (below the noise level of the used spectrometer) can have a PRET effect in the ultraviolet region of the spectrum due to the optimum absorption of the semiconductor in this region. This explanation is supported by the Mie theory calculations that show that Au NPs with a thin TiO<sub>2</sub> coating exhibit an absorption cross section at these wavelengths (i.e. 350-nm – 400-nm, Figure 72B). Nevertheless, other non-plasmonic contributions can also be playing a role in the presented enhancement and further work must be carried out to determine them.

In addition to the plasmonic enhancement effect, an outstanding IPCE increase (3-fold at wavelengths between 350-410nm) in the surface catalysis of the semiconductor was achieved for Configuration I. As shown in Figure S3, the fabricated composite exhibits nearly 100 % catalytic efficiency.

The total IPCE enhancement factor for Configuration I ranged from 6 to 3-fold throughout the band gap energies of the semiconductor. This increase in the external quantum efficiency was reflected in the output photocurrent under solar simulated irradiation (see cyclic voltammetry measurements in Figure 77) with an outstanding increase of 4-fold at, for instance, 1.23 and 1.9V vs RHE. Furthermore, in order to investigate the

stability/photocorrosion properties of Configuration I, the bare and the composite samples were illuminated with AM 1.5 irradiation under a constant applied potential (1.23 V vs. RHE), while recording the current density as a function of time (cf. Figure 78). It can be observed that both samples decrease their performance over time. Nevertheless, the photocurrent density of the functionalized sample is  $\sim 3$  time larger than that for the bare sample for the duration of the measurement (1 h). The instability of  $\text{CuWO}_4$ , under the conditions used in this work, has already been shown by Yourey et al.[205] The decrease in the performance of Configuration I is found to be similar to state of the art  $\text{CuWO}_4$  films that produce similar photocurrents.<sup>33</sup> Therefore, we conclude that the instability of the composite sample (Configuration I) is typical of  $\text{CuWO}_4$  under these conditions.

Finally, It is important to highlight that the main objective of this work was not to achieve the highest performing  $\text{CuWO}_4$ , but to investigate the potential plasmonic NP mechanisms that can improve the PEC performance of the material. However, we have shown that plasmonic NPs can increase significantly the photocurrent of  $\text{CuWO}_4$  films. Specifically, we enhanced the photocurrent density (under simulated solar irradiation) of a 200-nm spray pyrolysis deposited  $\text{CuWO}_4$  film from  $0.03 \text{ mA}\cdot\text{cm}^{-2}$  to  $0.1 \text{ mA}\cdot\text{cm}^{-2}$  (cf. Figure 77 and 78) at the thermodynamic potential for water oxidation (1.23 V vs RHE) in a pH 7 M KPi solution, which is comparable to the state of the art bare  $\text{CuWO}_4$  film ( $0.15 \text{ mA}\cdot\text{cm}^{-2}$ ), prepared by spin casting a sol-gel-like precursor.[205] To achieve higher photocurrents, further work must be carried out to optimize the NP's coverage concentration, size and material to achieve a higher enhancement factor.

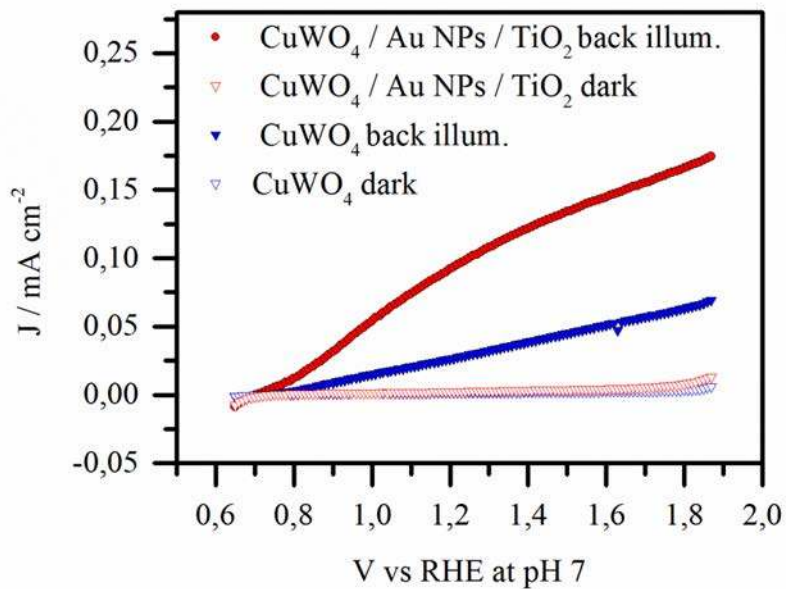


Figure 77. Three electrode AM1.5 photocurrent versus voltage ( $j$ - $v$ ) curve of bare 200-nm  $\text{CuWO}_4$  and functionalized (Configuration I) 200-nm  $\text{CuWO}_4$  at pH  $\sim 7$ .



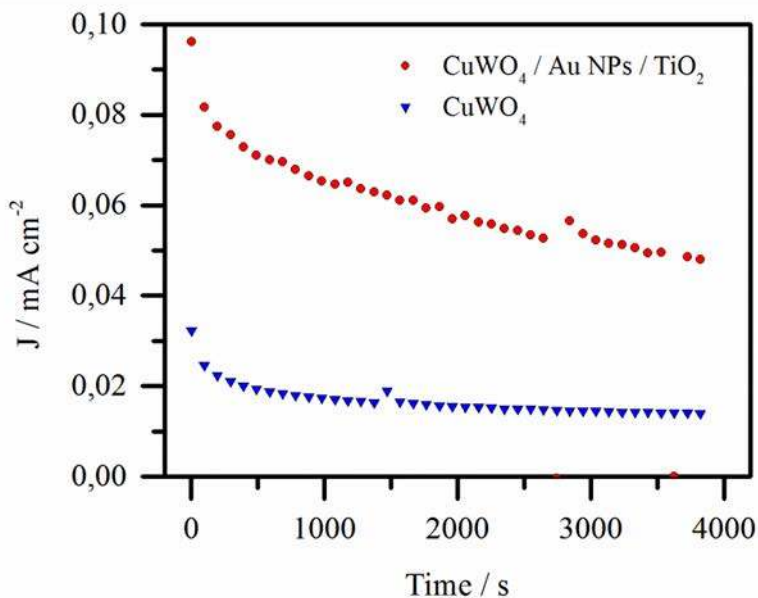


Figure 78.  $j$ - $t$  curves for  $\text{CuWO}_4$  and functionalized (Configuration I)  $\text{CuWO}_4$ , carried out in 0.1 M  $\text{KPi}$  buffer (pH  $\sim 7$ ) at 1.23 V vs RHE under AM 1.5 irradiation.

#### 4. Conclusions

An elegant gas phase methodology for the synthesis and subsequent deposition of metal NPs on semiconductors has been introduced. This method was found to be an ideal way to functionalize a semiconductor surface with plasmonic NPs that interact with light in a predefined region of the spectrum. In this work, Au NPs, with a SPR  $\lambda_{\text{max}}$  of absorption located at the same position as the  $\text{CuWO}_4$  band-gap edge, were deposited on the  $\text{CuWO}_4$  surface (Configuration I) or at its back contact (Configuration II).

The presented results indicate that decorating  $\text{CuWO}_4$  film surface (configuration I) with  $\text{TiO}_2$  coated Au NPs can enhance significantly the PEC water splitting performance of

CuWO<sub>4</sub> films. The nature of this enhancement is found to be a contribution of a surface catalytic effect and a plasmonic effect.

The plasmonic contribution was quantified by comparing IPCE performance of the bare and functionalized samples under 100 % surface catalytic conditions. When the particles were placed at the semiconductor-electrolyte interface (Configuration I), a plasmonic enhancement factor of ~2 was achieved. This enhancement is explained here by a PRET-induced increase in the formation of charge carriers at the SCL, where the charge carriers are separated efficiently. When NPs were placed at the back contact of the CuWO<sub>4</sub> film (Configuration II), no plasmonic enhancement was observed. This can be explained by the fact that for Configuration II, unlike Configuration I, the formation of additional charge carriers through PRET takes place at the bulk of the CuWO<sub>4</sub> film, where charge recombination is predominant.

Overall, this work is expected to have a relevant influence on future research towards improving the PEC performance of CuWO<sub>4</sub> and other semiconductors with indirect band-gap. Additionally, the method we introduced provides an easy way to distinguish the contributions of the two abovementioned NP enhancement mechanisms (scattering and PRET), by comparing IPCE and APCE of the functionalized samples (Configuration I and II).

### **Acknowledgements**

Financial support from the VENI project (granted to Dr. Wilson Smith) by NWO is gratefully acknowledged. Financial support from the NWO-NANO project (11521), in which the particle production method was optimized, is gratefully acknowledged. We thank Phaedra Oikonomopoulou for the illustrations, Timo van Drenth for valuable discussions and Joost Middelkoop for the TEM measurements.

### Supporting Information

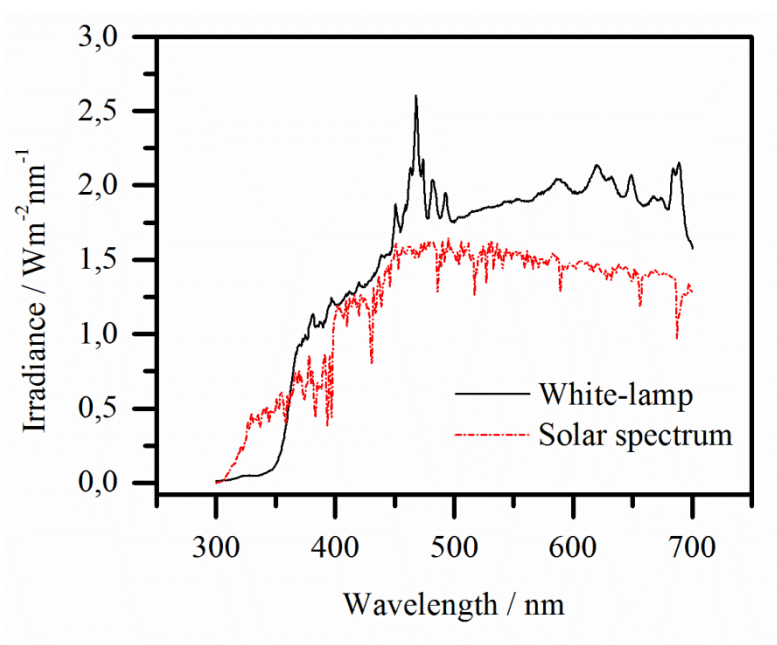


Figure S1. Irradiance spectra of white-light used for photocurrent measurements, recorded at 12 cm distance and Solar Light Irradiance Spectrum.

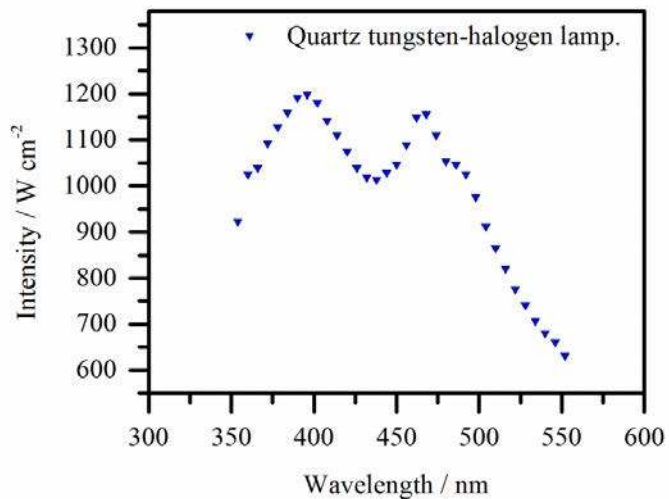


Figure S2. Intensity of the quartz tungsten-halogen lamp used in the IPCE measurements.

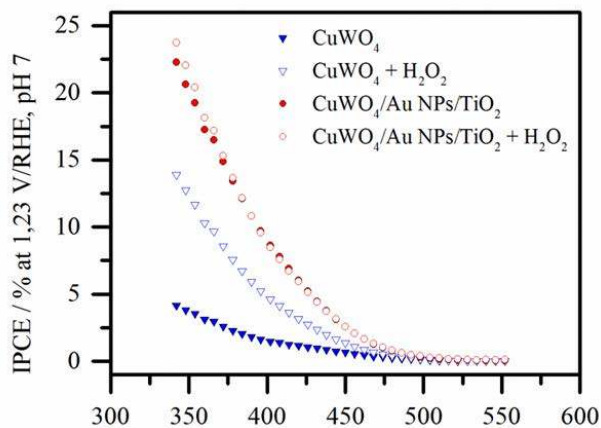


Figure S3. Back illumination IPCE for bare 200-nm  $\text{CuWO}_4$  and functionalized (Configuration I) 200-nm  $\text{CuWO}_4$  with and without  $\text{H}_2\text{O}_2$  in the electrolyte.

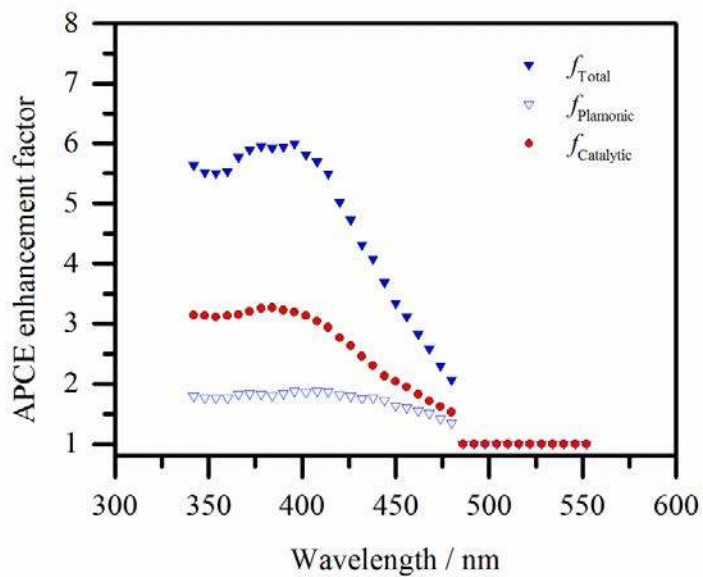


Figure S4. APCE enhancement factors after NP functionalization (Configuration I), calculated with Equations 1,3 and 4.

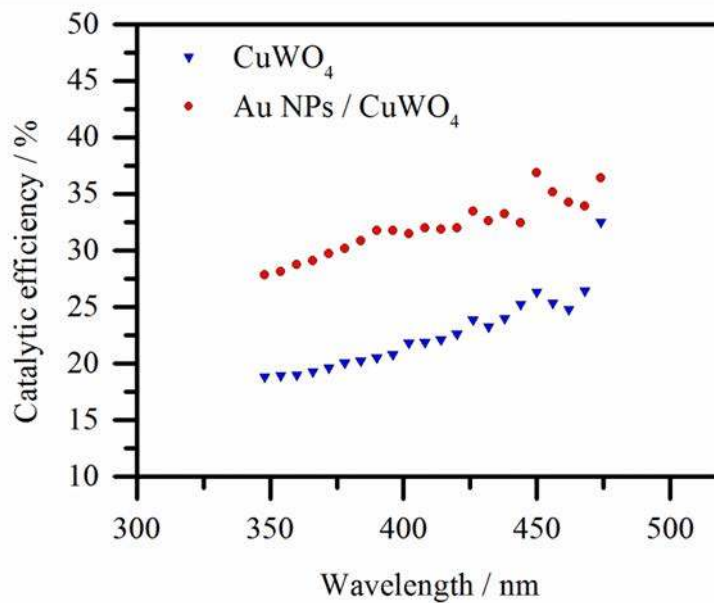


Figure S5. Catalytic efficiency of bare 200-nm CuWO<sub>4</sub> and functionalized (Configuration II) 200-nm CuWO<sub>4</sub>, calculated with Equation S3 from the IPCE values plotted in Figure S6.

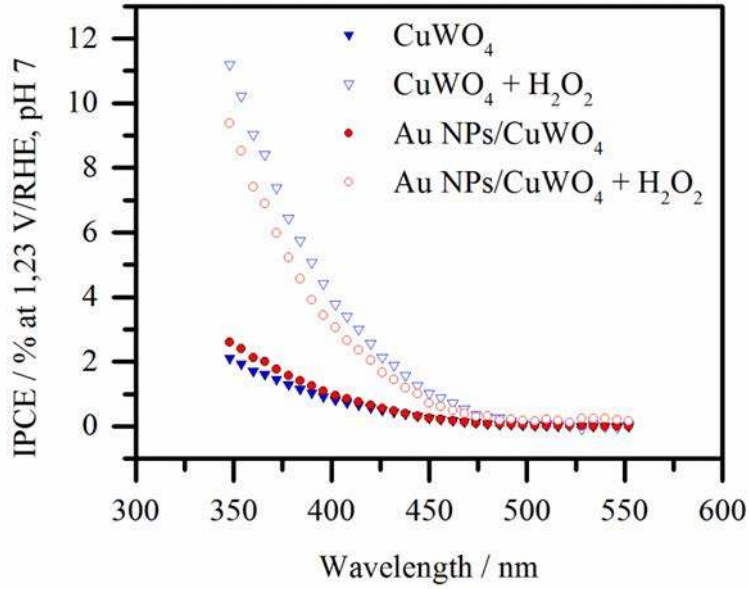


Figure S6. Back illumination IPCE for bare 200-nm  $\text{CuWO}_4$  and functionalized (Configuration II) 200-nm  $\text{CuWO}_4$  with and without  $\text{H}_2\text{O}_2$  in the electrolyte.

$$z = \frac{e \cdot C_c(d)}{3 \cdot \pi \cdot \mu \cdot d}, \quad (S1)$$

Here  $e$  is the elementary unit charge,  $\mu$  is the dynamic viscosity of the gas,  $d$  is the NP's diameter, and  $C_c$  is the Cunningham slip correction factor given by:

$$C_c(d) = 1 + 2.492 \cdot \left(\frac{\lambda}{d}\right) + 0.84 \cdot \left(\frac{\lambda}{d}\right) \cdot \exp\left(-0.43 \cdot \left(\frac{d}{\lambda}\right)\right), \quad (S2)$$

where  $\lambda$  is the mean free path of the gas.

$$C_{eff} = \frac{IPCE^{\text{H}_2\text{O}}}{IPCE^{\text{H}_2\text{O}_2}}, \quad (S3)$$

where, the  $IPCE^{H_2O_2}$  and  $IPCE^{H_2O}$  are IPCE measurements with and without  $H_2O_2$  in the electrolyte, respectively.



## 8. Conclusions

This thesis demonstrates that the spark discharge particle generator is a powerful tool for the production of single size spherical metallic nanoparticles to study their unique size-dependant properties. Even though this is the demonstrated in this thesis for plasmonic properties, there is a range of catalytic, electrochemical, optical, and toxicological size-dependent properties that could be elucidated by using the spark discharged particle generation as particle source.

In Chapter 1 of this thesis, the electrospray nanoparticle filter was introduced and characterized by its ability to capture nanoparticles from the gas phase into the liquid phase. The main advantage of this nanoparticle filter in comparison with capturing the nanoparticles by diffusion in a bubble column is that it has a higher capturing efficiency for nanoparticles larger than  $\sim 60$  nm in diameter.

In Chapter 3 we conclude that the limiting factor in the hot electron generation and extraction in Au/Ag alloy nanoparticles are the interband excitations that increase with Au composition. Pure Ag nanoparticles exhibits only intraband excitations when illuminated with visible light, resulting in high hot electron energies and hot electron injection efficiencies. Therefore, tuning the absorption range of hot electron injection devices by alloying Ag nanoparticles with Au significantly compromises the efficiency of the devices.

In Chapter 4, we show the size-dependant hot electron injection efficiencies of pure Ag nanoparticles. It is shown that for nanoparticles with diameters smaller than 10 nm, surface-induced excitations are the main contributors to the hot electron generation and extraction and, in this size range, the extraction efficiency increases with decreasing nanoparticle size. For nanoparticles with sizes larger than 10 nm, where the phonon-

inuduced excitations are more prominent, the hot electron injection efficiency increases with the amplitude of the field at the hot spot, which is located in the vicinity of the extraction point.

Chapter 5, shows that light trapping by 15 nm Ag plasmonic nanoparticles due to the light concentration effect is not efficient since the plasmonic energy is release as heat before absorption takes place in the semiconductor (i.e., BiVO<sub>4</sub>). On the other hand, larger light scattering Ag nanoparticles (~ 65 nm) can trap light by extending the light path in the neighbouring semiconductor, increasing its light absorption (~ 6 % for front illumination).

Finally, in Chapter 6, we show that Au plasmonic nanoparticles can trap light at the semiconductor (CuWO<sub>4</sub>)-electrolyte interface, increasing the light absorption of the semiconductor at the surface charge layer, where the plasmon-induce electron hole pairs are efficiently separated and contribute significantly in the device photocurrent.

The experimental results found in this thesis systematically expose the limitations of plasmonic nanoparticles to (i) directly harvest the solar energy into current or fuels or (ii) to trap light in neighbouring metal oxide semiconductors. The main limitation is that most of the plasmonic energy is release through heat dissipation and other energy transfer mechanisms to usable electricity or fuels are too inefficient for any solar energy conversion application.

## 9. List of publications

- 1) Valenti M, Dolat D, Biskos G, Schmidt-Ott A, Smith WA. Enhancement of the Photoelectrochemical Performance of CuWO<sub>4</sub> Thin Films for Solar Water Splitting by Plasmonic Nanoparticle Functionalization. *The Journal of Physical Chemistry C* 2015, 119(4): 2096-2104.
- 2) Valenti M, Venugopal A, Tordera D, Jonsson MP, Biskos G, Schmidt-Ott A, , Smith WA. Hot Carrier Generation and Extraction of Plasmonic Alloy Nanoparticles. *ACS Photonics* 2017.
- 3) Valenti M, Jonsson MP, Biskos G, Schmidt-Ott A, Smith W. A. Plasmonic nanoparticle-semiconductor composites for efficient solar water splitting. *Journal of Materials Chemistry A* 2016.
- 4) Valenti M, Kontoleta E, Digdaya IA, Jonsson MP, Biskos G, Schmidt-Ott A, , Smith WA. The Role of Size and Dimerization of Decorating Plasmonic Silver Nanoparticles on the Photoelectrochemical Solar Water Splitting Performance of BiVO<sub>4</sub> Photoanodes. *ChemNanoMat* 2016, 2(7): 739-747.
- 5) Valenti M, Venugopal A, Joost Meijers, Biskos G, Schmidt-Ott A, , Smith WA. Momentum Conservation of Hot Electrons in Ag Plasmonic Nanoparticles. *Submitted to Nanoscale*.

## 10. Acknowledgment

**Professor Ruud van Ommen** replied to an email sent to all professors in the chemical engineering department saying that he has a project that may suit a Jong Bachelor student that just arrived from Colombia. **Ruud**, finally I have a good chance to tell you how much it meant to me the welcoming environment that existed in the Proeffabriek and your always positive and constructive attitude during every meeting we had in my Erasmus project, without that and without your advice and recommendation I would have never started the master in the faculty and certainly I would not have this PhD thesis. Thank you!

**Andreas Schmidt-Ott**, it is difficult to put together a thank you note for you since it has been so much time that we have worked together, so many advices, discussions, conferences, teas, projects and good times. Therefore, I have decided to focus in the one most important thing I slowly learnt from you, which is the curiosity and enjoyment for everything around a scientific experiment.

**George Biskos**, thank you for all the knowledge and advices you gave me. I truly enjoy learning aerosol technology from the best.

**Wilson Smith**, I remembered walking into a couple of professor's offices explaining how much I was excited to explore the plasmonic properties of my single-size spherical metallic nanoparticles. After a five minute chat with you, the faith of this thesis was decided. Your amazing energy, sharpness and an incredible drive to make a difference in society, were the key ingredients I needed to work hard towards this thesis. During these four years working together I tried to learn many things from you professionally, to realize that the most important lesson I would learn from you was a simple reminder: Family first.

**Diana Dolat**, meeting you was a turning point in my carrier. You welcome me to photoelectrochemistry and taught me openly all you knew and showed me clearly what you did not know that would be interesting to know, and why. That unselfishness in teaching I have adopted with my students, trying to give them all I have, from knowledge to my passions and aspirations in science. It has made this trip worthwhile for me. Thank you.

**Herman Schreuders** and **Joost Middelkoop**, thank you for so many advices, work related and family related. I cannot count how many times you got me our of troubles. Your dedication and your great attitude are key for every PhD student. Thank you.

**Bernard Dam**, since the first time I assisted to the group meetings on Wednesdays. I saw in you a true leader, clearly demanding the highest quality of research and ethics that science needs. I embraced that responsibility and share it with my students in a daily basis. Thank you. Only in the last months I had the opportunity to discuss science with you directly, precisely in the topic that I enjoy the most. It was a true pleasure.

Thanks to **Kostis** and **Tobias** for all the good times at the lab and on conferences, and for all the help you gave me in the nanolab. Thanks to all the MECS group for the great time I had during my PhD. Thanks **Digda, Ming, Moreno, Nienke, Jicheng, Fahimeh, Kai, David, Divya, Steffen, and Recep**, it was really nice learning and having really fun chats about everything in the lab, offices, corridors and scientific trips. Thanks to **Wil, Karen** and **Heleen** for all the nice chats, all the help and the great attitude during all these years.

Teaching and learning from my students, **Angeliki, Jenny, Wouter, Anirudh, Timo, Florian, Varsha, Manju, Nitin, Piyush, Joost, Laurence**, and all the LO1-2, was extremely inspiring. It was truly fun. Thank you.

Finally, and most importantly, I would like to thank my family. Thanks to my **parents** and **Cate** for supporting me and encouraging me with every journey I have chosen to undertake, despite the fact that sometimes that journey makes me a bit absent, physically and mentally. You have always been and always will be my inspiration and role models. Thanks to my **grandmother**, aunties **Soco** and **Pato, Dani, Maria, Jose, Juan** for always being there taking care of me and loving me, despite the distance.

Thanks to **Riccardo, Danilo, Laura, Sami** and **Hernando** for being there to inspire me every time.

Thanks **Nejra** for all the illustrations and for the cover of this thesis, you are incredibly talented. Thanks to **Fikret, Indira** and **Tarik** for the support.

Thanks to my **Gabriel** for making me so happy and thanks to **John** for your support and friendship.

I also would like to thank my two loves, **Selma** and **Luca** that make me wake up full of dreams for an ever happier and brighter future.

## References

1. Feng, J., G. Biskos, and A. Schmidt-Ott, *Toward industrial scale synthesis of ultrapure singlet nanoparticles with controllable sizes in a continuous gas-phase process*. 2015. **5**: p. 15788.
2. Feng, J., et al., *General Approach to the Evolution of Singlet Nanoparticles from a Rapidly Quenched Point Source*. *The Journal of Physical Chemistry C*, 2016. **120**(1): p. 621-630.
3. Pfeiffer, T.V., J. Feng, and A. Schmidt-Ott, *New developments in spark production of nanoparticles*. *Advanced Powder Technology*, 2014. **25**(1): p. 56-70.
4. Knutson, E.O. and K.T. Whitby, *Aerosol classification by electric mobility: apparatus, theory, and applications*. *Journal of Aerosol Science*, 1975. **6**(6): p. 443-451.
5. Mayer, K.M. and J.H. Hafner, *Localized Surface Plasmon Resonance Sensors*. *Chemical Reviews*, 2011. **111**(6): p. 3828-3857.
6. Clavero, C., *Plasmon-induced hot-electron generation at nanoparticle/metal-oxide interfaces for photovoltaic and photocatalytic devices*. *Nat Photon*, 2014. **8**(2): p. 95-103.
7. Khurgin, J.B., *How to deal with the loss in plasmonics and metamaterials*. 2015. **10**: p. 2.
8. Tabrizi, N.S., et al., *Generation of nanoparticles by spark discharge*. *Journal of Nanoparticle Research*, 2008. **11**(2): p. 315.
9. Schwyn, S., E. Garwin, and A. Schmidt-Ott, *Aerosol generation by spark discharge*. *Journal of Aerosol Science*, 1988. **19**(5): p. 639-642.
10. Tabrizi, N.S., et al., *Generation of mixed metallic nanoparticles from immiscible metals by spark discharge*. *Journal of Nanoparticle Research*, 2010. **12**(1): p. 247-259.
11. Hinds, W.C., *Aerosol Technology: Properties, Behavior, and Measurement of Airborne Particles*. 2nd Ed. 1999: John Wiley & Sons, Inc., New York.
12. You, H., et al., *Synthesis of colloidal metal and metal alloy nanoparticles for electrochemical energy applications*. *Chemical Society Reviews*, 2013. **42**(7): p. 2880-2904.
13. Koch, D. and A.P. Weber, *Separation of gas-borne nanoparticles in bubble columns*. *Journal of Aerosol Science*, 2012. **53**(Supplement C): p. 61-75.
14. Fuchs, N.A., *The Mechanics of Aerosols*. 1964, Oxford: Pergamon Press.

15. Gañán-Calvo, A.M., J. Dávila, and A. Barrero, *Current and droplet size in the electro spraying of liquids. Scaling laws*. Journal of Aerosol Science, 1997. **28**(2): p. 249-275.
16. De La Mora, J.F. and I.G. Loscertales, *The current emitted by highly conducting Taylor cones*. Journal of Fluid Mechanics, 2006. **260**: p. 155-184.
17. Pantano, C., A.M. Gañán-Calvo, and A. Barrero, *Zeroth-order, electrohydrostatic solution for electro spraying in cone-jet mode*. Journal of Aerosol Science, 1994. **25**(6): p. 1065-1077.
18. Rayleigh, L., *XX. On the equilibrium of liquid conducting masses charged with electricity*. The London, Edinburgh, and Dublin Philosophical Magazine and Journal of Science, 1882. **14**(87): p. 184-186.
19. Kyritsis, D.C., et al., *Optimization of a catalytic combustor using electro sprayed liquid hydrocarbons for mesoscale power generation*. Combustion and Flame, 2004. **139**(1): p. 77-89.
20. Shapiro, M., C. Gutfinger, and G. Laufer, *Electrostatic mechanisms of aerosol collection by granular filters: A review*. Journal of Aerosol Science, 1988. **19**(6): p. 651-677.
21. Kraemer, H.F. and H.F. Johnstone, *Collection of Aerosol Particles in Presence of Electrostatic Fields*. Industrial & Engineering Chemistry, 1955. **47**(12): p. 2426-2434.
22. Valenti, M., et al., *Plasmonic nanoparticle-semiconductor composites for efficient solar water splitting*. Journal of Materials Chemistry A, 2016.
23. Fujishima, A. and K. Honda, *Electrochemical Photolysis of Water at a Semiconductor Electrode*. Nature, 1972. **238**(5358): p. 37-38.
24. Boddy, P.J., *Oxygen Evolution on Semiconducting TiO<sub>2</sub>*. Journal of The Electrochemical Society, 1968. **115**(2): p. 199-203.
25. Sivula, K. and R. van de Krol, *Semiconducting materials for photoelectrochemical energy conversion*. Nature Reviews Materials, 2016. **1**: p. 15010.
26. Maeda, K. and K. Domen, *Photocatalytic Water Splitting: Recent Progress and Future Challenges*. The Journal of Physical Chemistry Letters, 2010. **1**(18): p. 2655-2661.
27. Butler, M.A., R.D. Nasby, and R.K. Quinn, *Tungsten trioxide as an electrode for photoelectrolysis of water*. Solid State Communications, 1976. **19**(10): p. 1011-1014.
28. Su, J., et al., *Nanostructured WO<sub>3</sub>/BiVO<sub>4</sub> Heterojunction Films for Efficient Photoelectrochemical Water Splitting*. Nano Letters, 2011. **11**(5): p. 1928-1933.
29. Quinn, R.K., R.D. Nasby, and R.J. Baughman, *Photoassisted electrolysis of water using single crystal  $\alpha$ -Fe<sub>2</sub>O<sub>3</sub> anodes*. Materials Research Bulletin, 1976. **11**(8): p. 1011-1017.



30. Kay, A., I. Cesar, and M. Grätzel, *New Benchmark for Water Photooxidation by Nanostructured  $\alpha$ -Fe<sub>2</sub>O<sub>3</sub> Films*. Journal of the American Chemical Society, 2006. **128**(49): p. 15714-15721.
31. Kim, J.Y., et al., *Single-crystalline, wormlike hematite photoanodes for efficient solar water splitting*. Scientific Reports, 2013. **3**: p. 2681.
32. Nian, J.-N., C.-C. Hu, and H. Teng, *Electrodeposited p-type Cu<sub>2</sub>O for H<sub>2</sub> evolution from photoelectrolysis of water under visible light illumination*. International Journal of Hydrogen Energy, 2008. **33**(12): p. 2897-2903.
33. Paracchino, A., et al., *Highly active oxide photocathode for photoelectrochemical water reduction*. Nat Mater, 2011. **10**(6): p. 456-461.
34. Abdi, F.F., et al., *Efficient solar water splitting by enhanced charge separation in a bismuth vanadate-silicon tandem photoelectrode*. Nat Commun, 2013. **4**.
35. Kim, T.W. and K.-S. Choi, *Nanoporous BiVO<sub>4</sub> Photoanodes with Dual-Layer Oxygen Evolution Catalysts for Solar Water Splitting*. Science, 2014. **343**(6174): p. 990-994.
36. Shi, X., et al., *Efficient photoelectrochemical hydrogen production from bismuth vanadate-decorated tungsten trioxide helix nanostructures*. Nat Commun, 2014. **5**.
37. Pihosh, Y., et al., *Photocatalytic generation of hydrogen by core-shell WO<sub>3</sub>/BiVO<sub>4</sub> nanorods with ultimate water splitting efficiency*. Scientific Reports, 2015. **5**: p. 11141.
38. Youngblood, W.J., et al., *Photoassisted Overall Water Splitting in a Visible Light-Absorbing Dye-Sensitized Photoelectrochemical Cell*. Journal of the American Chemical Society, 2009. **131**(3): p. 926-927.
39. de Respinis, M., et al., *Solar Water Splitting Combining a BiVO<sub>4</sub> Light Absorber with a Ru-Based Molecular Cocatalyst*. The Journal of Physical Chemistry C, 2015. **119**(13): p. 7275-7281.
40. Li, J., et al., *Solar Hydrogen Generation by a CdS-Au-TiO<sub>2</sub> Sandwich Nanorod Array Enhanced with Au Nanoparticle as Electron Relay and Plasmonic Photosensitizer*. Journal of the American Chemical Society, 2014. **136**(23): p. 8438-8449.
41. Zhang, P., T. Wang, and J. Gong, *Mechanistic Understanding of the Plasmonic Enhancement for Solar Water Splitting*. Advanced Materials, 2015. **27**(36): p. 5328-5342.
42. Linic, S., P. Christopher, and D.B. Ingram, *Plasmonic-metal nanostructures for efficient conversion of solar to chemical energy*. Nat Mater, 2011. **10**(12): p. 911-921.
43. Warren, S.C. and E. Thimsen, *Plasmonic solar water splitting*. Energy & Environmental Science, 2012. **5**: p. 5133-5146.
44. Valenti, M., et al., *The Role of Size and Dimerization of Decorating Plasmonic Silver Nanoparticles on the Photoelectrochemical Solar Water Splitting Performance of BiVO<sub>4</sub> Photoanodes*. ChemNanoMat, 2016: p. n/a-n/a.

45. Mubeen, S., et al., *An autonomous photosynthetic device in which all charge carriers derive from surface plasmons*. Nat Nano, 2013. **8**(4): p. 247-251.
46. Cushing, S.K., et al., *Photocatalytic Activity Enhanced by Plasmonic Resonant Energy Transfer from Metal to Semiconductor*. Journal of the American Chemical Society, 2012. **134**(36): p. 15033-15041.
47. Chen, H.M., et al., *Plasmon Inducing Effects for Enhanced Photoelectrochemical Water Splitting: X-ray Absorption Approach to Electronic Structures*. ACS Nano, 2012. **6**(8): p. 7362-7372.
48. Haro, M., et al., *Plasmonic versus catalytic effect of gold nanoparticles on mesoporous TiO<sub>2</sub> electrodes for water splitting*. Electrochimica Acta, 2014. **144**: p. 64-70.
49. Valenti, M., et al., *Enhancement of the Photoelectrochemical Performance of CuWO<sub>4</sub> Thin Films for Solar Water Splitting by Plasmonic Nanoparticle Functionalization*. The Journal of Physical Chemistry C, 2014.
50. Thimsen, E., et al., *Influence of Plasmonic Au Nanoparticles on the Photoactivity of Fe<sub>2</sub>O<sub>3</sub> Electrodes for Water Splitting*. Nano Letters, 2011. **11**(1): p. 35-43.
51. Piot, A., et al., *Collective excitation of plasmonic hot-spots for enhanced hot charge carrier transfer in metal/semiconductor contacts*. Nanoscale, 2015. **7**(18): p. 8294-8298.
52. Erwin, W.R., et al., *Light trapping in mesoporous solar cells with plasmonic nanostructures*. Energy & Environmental Science, 2016.
53. Naldoni, A., et al., *Solar-Powered Plasmon-Enhanced Heterogeneous Catalysis, in Nanophotonics*. 2016. p. 112.
54. Cushing, S.K. and N. Wu, *Progress and Perspectives of Plasmon-Enhanced Solar Energy Conversion*. The Journal of Physical Chemistry Letters, 2016. **7**(4): p. 666-675.
55. Mie, G., *Articles on the optical characteristics of turbid tubes, especially colloidal metal solutions*. Annalen Der Physik, 1908. **25**(3): p. 377-445.
56. Kelly, K.L., et al., *The Optical Properties of Metal Nanoparticles: The Influence of Size, Shape, and Dielectric Environment*. The Journal of Physical Chemistry B, 2002. **107**: p. 668-677.
57. Sönnichsen, C., et al., *Drastic Reduction of Plasmon Damping in Gold Nanorods*. Physical Review Letters, 2002. **88**(7): p. 077402.
58. Quinten, M., *Fundamentals of Light Scattering by an Obstacle, in Optical Properties of Nanoparticle Systems*. 2011, Wiley-VCH Verlag GmbH & Co. KGaA. p. 55-74.
59. Bohren, C.F. and D.R. Huffman, *Particles Small Compared with the Wavelength, in Absorption and Scattering of Light by Small Particles*. 2007, Wiley-VCH Verlag GmbH. p. 130-157.

60. Pathak, N.K., et al., *Study of Light Extinction and Surface Plasmon Resonances of Metal Nanocluster: a Comparison Between Coated and Non-coated Nanogeometry*. Plasmonics, 2015. **10**(6): p. 1597-1606.
61. Huang, X., et al., *Cancer Cell Imaging and Photothermal Therapy in the Near-Infrared Region by Using Gold Nanorods*. Journal of the American Chemical Society, 2006. **128**(6): p. 2115-2120.
62. Kadkhodazadeh, S., et al., *Scaling of the Surface Plasmon Resonance in Gold and Silver Dimers Probed by EELS*. The Journal of Physical Chemistry C, 2014. **118**: p. 5478-5485.
63. Nordlander, P., et al., *Plasmon Hybridization in Nanoparticle Dimers*. Nano Letters, 2004. **4**(5): p. 899-903.
64. Jain, P.K., W. Huang, and M.A. El-Sayed, *On the Universal Scaling Behavior of the Distance Decay of Plasmon Coupling in Metal Nanoparticle Pairs: A Plasmon Ruler Equation*. Nano Letters, 2007. **7**(7): p. 2080-2088.
65. Quinten, M., et al., *Electromagnetic energy transport via linear chains of silver nanoparticles*. Optics Letters, 1998. **23**(17): p. 1331-1333.
66. Stiles, P.L., et al., *Surface-Enhanced Raman Spectroscopy*. Annual Review of Analytical Chemistry, 2008. **1**(1): p. 601-626.
67. Linic, S., P. Christopher, and D.B. Ingram, *Plasmonic-metal nanostructures for efficient conversion of solar to chemical energy*. Nat Mater, 2011. **10**: p. 911-921.
68. Hao, E. and G.C. Schatz, *Electromagnetic fields around silver nanoparticles and dimers*. The Journal of Chemical Physics, 2004. **120**(1): p. 357-366.
69. Willingham, B., D.W. Brandl, and P. Nordlander, *Plasmon hybridization in nanorod dimers*. Applied Physics B, 2008. **93**(1): p. 209-216.
70. Belkin, M., et al., *Plasmonic Nanopores for Trapping, Controlling Displacement, and Sequencing of DNA*. ACS Nano, 2015. **9**(11): p. 10598-10611.
71. Nicoli, F., et al., *DNA Translocations through Solid-State Plasmonic Nanopores*. Nano Letters, 2014. **14**(12): p. 6917-6925.
72. Atwater, H.A. and A. Polman, *Plasmonics for improved photovoltaic devices*. Nat Mater, 2010. **9**(3): p. 205-213.
73. Zhang, L., L.O. Herrmann, and J.J. Baumberg, *Size Dependent Plasmonic Effect on BiVO<sub>4</sub> Photoanodes for Solar Water Splitting*. Scientific Reports, 2015. **5**: p. 16660.
74. Callahan, D.M., J.N. Munday, and H.A. Atwater, *Solar Cell Light Trapping beyond the Ray Optic Limit*. Nano Letters, 2012. **12**(1): p. 214-218.
75. Cushing, S.K., et al., *Controlling Plasmon-Induced Resonance Energy Transfer and Hot Electron Injection Processes in Metal@TiO<sub>2</sub> Core-Shell Nanoparticles*. The Journal of Physical Chemistry C, 2015. **119**(28): p. 16239-16244.
76. Abdi, F.F., et al., *Plasmonic enhancement of the optical absorption and catalytic efficiency of BiVO<sub>4</sub> photoanodes decorated with Ag@SiO<sub>2</sub> core-shell nanoparticles*. Physical Chemistry Chemical Physics, 2014.

77. Shi, Y., et al., *Hot Electron of Au Nanorods Activates the Electrocatalysis of Hydrogen Evolution on MoS<sub>2</sub> Nanosheets*. Journal of the American Chemical Society, 2015. **137**(23): p. 7365-7370.
78. Baffou, G. and R. Quidant, *Nanoplasmonics for chemistry*. Chemical Society Reviews, 2014. **43**(11): p. 3898-3907.
79. Xuming, Z., et al., *Plasmonic photocatalysis*. Reports on Progress in Physics, 2013. **76**(4): p. 046401.
80. Subramanian, V., E.E. Wolf, and P.V. Kamat, *Catalysis with TiO<sub>2</sub>/Gold Nanocomposites. Effect of Metal Particle Size on the Fermi Level Equilibration*. Journal of the American Chemical Society, 2004. **126**(15): p. 4943-4950.
81. Xiaoguang, L., X. Di, and Z. Zhenyu, *Landau damping of quantum plasmons in metal nanostructures*. New Journal of Physics, 2013. **15**(2): p. 023011.
82. Sa, J., et al., *Direct observation of charge separation on Au localized surface plasmons*. Energy & Environmental Science, 2013. **6**(12): p. 3584-3588.
83. Govorov, A.O., H. Zhang, and Y.K. Gun'ko, *Theory of Photoinjection of Hot Plasmonic Carriers from Metal Nanostructures into Semiconductors and Surface Molecules*. The Journal of Physical Chemistry C, 2013. **117**(32): p. 16616-16631.
84. Knight, M.W., et al., *Photodetection with Active Optical Antennas*. Science, 2011. **332**(6030): p. 702-704.
85. Wu, K., et al., *Efficient hot-electron transfer by a plasmon-induced interfacial charge-transfer transition*. Science, 2015. **349**(6248): p. 632-635.
86. Knight, M.W., et al., *Embedding Plasmonic Nanostructure Diodes Enhances Hot Electron Emission*. Nano Letters, 2013. **13**(4): p. 1687-1692.
87. Amidani, L., et al., *Probing Long-Lived Plasmonic-Generated Charges in TiO<sub>2</sub>/Au by High-Resolution X-ray Absorption Spectroscopy*. Angewandte Chemie International Edition, 2015. **54**(18): p. 5413-5416.
88. Tian, Y. and T. Tatsuma, *Plasmon-induced photoelectrochemistry at metal nanoparticles supported on nanoporous TiO<sub>2</sub>*. Chemical Communications, 2004(16): p. 1810-1811.
89. Inagaki, T., K. Kagami, and E.T. Arakawa, *PHOTOACOUSTIC OBSERVATION OF NONRADIATIVE DECAY OF SURFACE-PLASMONS IN SILVER*. Physical Review B, 1981. **24**(6): p. 3644-3646.
90. Tian, Y. and T. Tatsuma, *Mechanisms and Applications of Plasmon-Induced Charge Separation at TiO<sub>2</sub> Films Loaded with Gold Nanoparticles*. Journal of the American Chemical Society, 2005. **127**(20): p. 7632-7637.
91. Tian, Y., et al., *Effects of electron donors on the performance of plasmon-induced photovoltaic cell*. Journal of Photochemistry and Photobiology A: Chemistry, 2008. **199**(2-3): p. 224-229.
92. Tian, Y., et al., *Charge separation in solid-state gold nanoparticles-sensitized photovoltaic cell*. Electrochemistry Communications, 2009. **11**(8): p. 1603-1605.

93. Yourey, J.E., J.B. Kurtz, and B.M. Bartlett, *Water Oxidation on a CuWO<sub>4</sub>–WO<sub>3</sub> Composite Electrode in the Presence of [Fe(CN)<sub>6</sub>]<sup>3-</sup>: Toward Solar Z-Scheme Water Splitting at Zero Bias*. The Journal of Physical Chemistry C, 2012. **116**(4): p. 3200-3205.
94. Cattarin, S., et al., *Electrodissolution and corrosion of CuInS<sub>2</sub> photoanodes with lamellar morphology*. Electrochimica Acta, 1995. **40**(8): p. 1041-1049.
95. Mubeen, S., et al., *Panchromatic Photoproduction of H<sub>2</sub> with Surface Plasmons*. Nano Letters, 2015. **15**(3): p. 2132-2136.
96. Chen, H.M., et al., *Quantum Dot Monolayer Sensitized ZnO Nanowire-Array Photoelectrodes: True Efficiency for Water Splitting*. Angewandte Chemie International Edition, 2010. **49**(34): p. 5966-5969.
97. Wang, H., et al., *Photoelectrochemical study of oxygen deficient TiO<sub>2</sub> nanowire arrays with CdS quantum dot sensitization*. Nanoscale, 2012. **4**(5): p. 1463-1466.
98. Yang, H.B., et al., *Stable Quantum Dot Photoelectrolysis Cell for Unassisted Visible Light Solar Water Splitting*. ACS Nano, 2014. **8**(10): p. 10403-10413.
99. Bernardi, M., et al., *Theory and computation of hot carriers generated by surface plasmon polaritons in noble metals*. Nat Commun, 2015. **6**.
100. Brown, A.M., et al., *Nonradiative Plasmon Decay and Hot Carrier Dynamics: Effects of Phonons, Surfaces, and Geometry*. ACS Nano, 2016. **10**(1): p. 957-966.
101. Manjavacas, A., et al., *Plasmon-Induced Hot Carriers in Metallic Nanoparticles*. ACS Nano, 2014. **8**(8): p. 7630-7638.
102. Sundararaman, R., et al., *Theoretical predictions for hot-carrier generation from surface plasmon decay*. Nat Commun, 2014. **5**.
103. Hung, S.-F., et al., *Iridium Oxide-Assisted Plasmon-Induced Hot Carriers: Improvement on Kinetics and Thermodynamics of Hot Carriers*. Advanced Energy Materials, 2016. **6**(8): p. 1501339-n/a.
104. Shiraishi, Y., et al., *Platinum Nanoparticles Supported on Anatase Titanium Dioxide as Highly Active Catalysts for Aerobic Oxidation under Visible Light Irradiation*. ACS Catalysis, 2012. **2**(9): p. 1984-1992.
105. Naldoni, A., et al., *The critical role of intragap states in the energy transfer from gold nanoparticles to TiO<sub>2</sub>*. Physical Chemistry Chemical Physics, 2015. **17**(7): p. 4864-4869.
106. Xiao, F.-X., et al., *Metal-Cluster-Decorated TiO<sub>2</sub> Nanotube Arrays: A Composite Heterostructure toward Versatile Photocatalytic and Photoelectrochemical Applications*. Small, 2015. **11**(5): p. 554-567.
107. Xiao, F.-X., Z. Zeng, and B. Liu, *Bridging the Gap: Electron Relay and Plasmonic Sensitization of Metal Nanocrystals for Metal Clusters*. Journal of the American Chemical Society, 2015. **137**(33): p. 10735-10744.
108. Harutyunyan, H., et al., *Anomalous ultrafast dynamics of hot plasmonic electrons in nanostructures with hot spots*. Nat Nano, 2015. **10**(9): p. 770-774.

109. Sousa-Castillo, A., et al., *Boosting Hot Electron-Driven Photocatalysis through Anisotropic Plasmonic Nanoparticles with Hot Spots in Au–TiO<sub>2</sub> Nanoarchitectures*. The Journal of Physical Chemistry C, 2016. **120**(21): p. 11690-11699.
110. Erwin, W.R., et al., *Plasmon enhanced water splitting mediated by hybrid bimetallic Au-Ag core-shell nanostructures*. Nanoscale, 2014. **6**(21): p. 12626-12634.
111. Gao, H., et al., *Plasmon-Enhanced Photocatalytic Activity of Iron Oxide on Gold Nanopillars*. ACS Nano, 2012. **6**(1): p. 234-240.
112. Yuriy, P., et al., *Ubiquitous element approach to plasmonic enhanced photocatalytic water splitting: the case of Ti@TiO<sub>2</sub> core-shell nanostructure*. Nanotechnology, 2014. **25**(31): p. 315402.
113. Wang, X., et al., *Silicon/Hematite Core/Shell Nanowire Array Decorated with Gold Nanoparticles for Unbiased Solar Water Oxidation*. Nano Letters, 2014. **14**(1): p. 18-23.
114. Nootchanat, S., et al., *Investigation of localized surface plasmon/grating-coupled surface plasmon enhanced photocurrent in TiO<sub>2</sub> thin films*. Physical Chemistry Chemical Physics, 2014. **16**(44): p. 24484-24492.
115. Enzhou, L., et al., *Plasmonic Ag deposited TiO<sub>2</sub> nano-sheet film for enhanced photocatalytic hydrogen production by water splitting*. Nanotechnology, 2014. **25**(16): p. 165401.
116. Zhang, X., et al., *Shape-dependent localized surface plasmon enhanced photocatalytic effect of ZnO nanorods decorated with Ag*. International Journal of Hydrogen Energy, 2014. **39**(16): p. 8238-8245.
117. Kim, H.J., et al., *Plasmon-Enhanced Photoelectrochemical Water Splitting with Size-Controllable Gold Nanodot Arrays*. ACS Nano, 2014. **8**(10): p. 10756-10765.
118. Archana, P.S., et al., *Plasmonic Enhancement of Photoactivity by Gold Nanoparticles Embedded in Hematite Films*. The Journal of Physical Chemistry C, 2015. **119**(27): p. 15506-15516.
119. Derkacs, D., et al., *Improved performance of amorphous silicon solar cells via scattering from surface plasmon polaritons in nearby metallic nanoparticles*. Applied Physics Letters, 2006. **89**: p. -.
120. Dotan, H., et al., *Probing the photoelectrochemical properties of hematite ([small alpha]-Fe<sub>2</sub>O<sub>3</sub>) electrodes using hydrogen peroxide as a hole scavenger*. Energy & Environmental Science, 2011. **4**: p. 958-964.
121. Green, M.A. and S. Pillai, *Harnessing plasmonics for solar cells*. Nat Photon, 2012. **6**(3): p. 130-132.
122. Novotny, L. and N. van Hulst, *Antennas for light*. Nat Photon, 2011. **5**(2): p. 83-90.
123. Schuller, J.A., et al., *Plasmonics for extreme light concentration and manipulation*. Nat Mater, 2010. **9**(3): p. 193-204.

124. Schaadt, D.M., B. Feng, and E.T. Yu, *Enhanced semiconductor optical absorption via surface plasmon excitation in metal nanoparticles*. Applied Physics Letters, 2005. **86**(6): p. 063106.
125. Thomann, I., et al., *Plasmon Enhanced Solar-to-Fuel Energy Conversion*. Nano Letters, 2011. **11**(8): p. 3440-3446.
126. Naldoni, A., et al., *Influence of TiO<sub>2</sub> electronic structure and strong metal-support interaction on plasmonic Au photocatalytic oxidations*. Catalysis Science & Technology, 2016. **6**(9): p. 3220-3229.
127. Fang, Y., et al., *Plasmon Enhanced Internal Photoemission in Antenna-Spacer-Mirror Based Au/TiO<sub>2</sub> Nanostructures*. Nano Letters, 2015. **15**(6): p. 4059-4065.
128. Dotan, H., et al., *Resonant light trapping in ultrathin films for water splitting*. Nat Mater, 2013. **12**(2): p. 158-164.
129. Li, J., et al., *Plasmon-induced photonic and energy-transfer enhancement of solar water splitting by a hematite nanorod array*. Nat Commun, 2013. **4**.
130. Abdi, F.F., et al., *Plasmonic enhancement of the optical absorption and catalytic efficiency of BiVO<sub>4</sub> photoanodes decorated with Ag@SiO<sub>2</sub> core-shell nanoparticles*. Physical Chemistry Chemical Physics, 2014. **29**(16).
131. Takai, A. and P.V. Kamat, *Capture, Store, and Discharge. Shuttling Photogenerated Electrons across TiO<sub>2</sub>-Silver Interface*. ACS Nano, 2011. **5**(9): p. 7369-7376.
132. Naseri, N., et al., *To What Extent Can Surface Morphology Influence the Photoelectrochemical Performance of Au:WO<sub>3</sub> Electrodes?* The Journal of Physical Chemistry C, 2015. **119**(3): p. 1271-1279.
133. Wang, J., et al., *Gold Nanorod-Enhanced Light Absorption and Photoelectrochemical Performance of  $\alpha$ -Fe<sub>2</sub>O<sub>3</sub> Thin-Film Electrode for Solar Water Splitting*. The Journal of Physical Chemistry C, 2013. **117**(42): p. 22060-22068.
134. Yuefan, W., et al., *Enhanced photoelectrochemical water-splitting effect with a bent ZnO nanorod photoanode decorated with Ag nanoparticles*. Nanotechnology, 2012. **23**(23): p. 235401.
135. Liu, G., et al., *Promoting Active Species Generation by Plasmon-Induced Hot-Electron Excitation for Efficient Electrocatalytic Oxygen Evolution*. Journal of the American Chemical Society, 2016. **138**(29): p. 9128-9136.
136. van de Krol, R., *Principles of Photoelectrochemical Cells*, in *Photoelectrochemical Hydrogen Production*, R. van de Krol and M. Grätzel, Editors. 2012, Springer US: Boston, MA. p. 13-67.
137. Subramanian, V., E. Wolf, and P.V. Kamat, *Semiconductor-Metal Composite Nanostructures. To What Extent Do Metal Nanoparticles Improve the Photocatalytic Activity of TiO<sub>2</sub> Films?* The Journal of Physical Chemistry B, 2001. **105**(46): p. 11439-11446.

138. Valenti, M., et al., *Hot Carrier Generation and Extraction of Plasmonic Alloy Nanoparticles*. ACS Photonics, 2017.
139. Fujishima, A. and K. Honda, *Electrochemical Photolysis of Water at a Semiconductor Electrode*. Nature, 1972. **238**: p. 37-38.
140. Mubeen, S., et al., *An autonomous photosynthetic device in which all charge carriers derive from surface plasmons*. Nat Nano, 2013. **8**: p. 247-251.
141. Cushing, S.K., et al., *Controlling Plasmon-Induced Resonance Energy Transfer and Hot Electron Injection Processes in Metal@TiO<sub>2</sub> Core-Shell Nanoparticles*. The Journal of Physical Chemistry C, 2015. **119**: p. 16239-16244.
142. Mubeen, S., et al., *Panchromatic Photoproduction of H<sub>2</sub> with Surface Plasmons*. Nano Letters, 2015. **15**: p. 2132-2136.
143. Cushing, S.K., et al., *Photocatalytic Activity Enhanced by Plasmonic Resonant Energy Transfer from Metal to Semiconductor*. Journal of the American Chemical Society, 2012. **134**: p. 15033-15041.
144. Clavero, C., *Plasmon-induced hot-electron generation at nanoparticle/metal-oxide interfaces for photovoltaic and photocatalytic devices*. Nature Photonics, 2014. **8**: p. 95-103.
145. Sundaraman, R., et al., *Theoretical predictions for hot-carrier generation from surface plasmon decay*. Nat Commun, 2014. **5**: p. 5788.
146. Brown, A.M., et al., *Nonradiative Plasmon Decay and Hot Carrier Dynamics: Effects of Phonons, Surfaces, and Geometry*. ACS Nano, 2016. **10**: p. 957-966.
147. Govorov, A.O., H. Zhang, and Y.K. Gun'ko, *Theory of Photoinjection of Hot Plasmonic Carriers from Metal Nanostructures into Semiconductors and Surface Molecules*. The Journal of Physical Chemistry C, 2013. **117**: p. 16616-16631.
148. Manjavacas, A., et al., *Plasmon-Induced Hot Carriers in Metallic Nanoparticles*. ACS Nano, 2014. **8**: p. 7630-7638.
149. Bernardi, M., et al., *Theory and computation of hot carriers generated by surface plasmon polaritons in noble metals*. Nat Commun, 2015. **6**: p. 7044.
150. Verbruggen, S.W., et al., *Predicting the Surface Plasmon Resonance Wavelength of Gold-Silver Alloy Nanoparticles*. The Journal of Physical Chemistry C, 2013. **117**: p. 19142-19145.
151. Khurgin, J.B., *How to deal with the loss in plasmonics and metamaterials*. Nat Nano, 2015. **10**: p. 2-6.
152. Schwyn, S., E. Garwin, and A. Schmidtott, *AEROSOL GENERATION BY SPARK DISCHARGE*. Journal of Aerosol Science, 1988. **19**: p. 639-642.
153. Feng, J., G. Biskos, and A. Schmidt-Ott, *Toward industrial scale synthesis of ultrapure singlet nanoparticles with controllable sizes in a continuous gas-phase process*. Scientific Reports, 2015. **5**: p. 15788.
154. Knutson, E.O. and K.T. Whitby, *Aerosol classification by electric mobility: apparatus, theory, and applications*. Journal of Aerosol Science, 1975. **6**: p. 443-451.



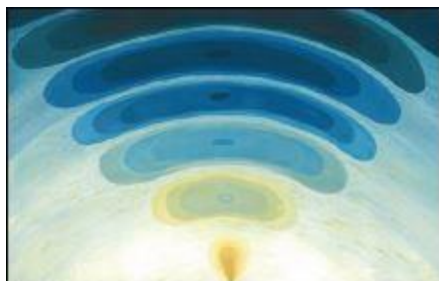
155. Atwater, H.A. and A. Polman, *Plasmonics for improved photovoltaic devices*. Nat Mater, 2010. **9**: p. 205-213.
156. Link, S., Z.L. Wang, and M.A. El-Sayed, *Alloy Formation of Gold-Silver Nanoparticles and the Dependence of the Plasmon Absorption on Their Composition*. The Journal of Physical Chemistry B, 1999. **103**(18): p. 3529-3533.
157. Mie, G., *Articles on the optical characteristics of turbid tubes, especially colloidal metal solutions*. Annalen Der Physik, 1908. **25**: p. 377-445.
158. Fowler, R.H., *The Analysis of Photoelectric Sensitivity Curves for Clean Metals at Various Temperatures*. Physical Review, 1931. **38**: p. 45-56.
159. Knight, M.W., et al., *Photodetection with Active Optical Antennas*. Science, 2011. **332**: p. 702-704.
160. Rioux, D., et al., *An Analytic Model for the Dielectric Function of Au, Ag, and their Alloys*. Advanced Optical Materials, 2014. **2**: p. 176-182.
161. Michaelson, H.B., *The work function of the elements and its periodicity*. Journal of Applied Physics, 1977. **48**: p. 4729-4733.
162. Rothenberger, G., D. Fitzmaurice, and M. Graetzel, *Spectroscopy of conduction band electrons in transparent metal oxide semiconductor films: optical determination of the flatband potential of colloidal titanium dioxide films*. The Journal of Physical Chemistry, 1992. **96**: p. 5983-5986.
163. Abdi, F.F. and R. van de Krol, *Nature and Light Dependence of Bulk Recombination in Co-Pi-Catalyzed BiVO4 Photoanodes*. The Journal of Physical Chemistry C, 2012. **116**: p. 9398-9404.
164. Narang, P., R. Sundararaman, and A. Atwater Harry, *Plasmonic hot carrier dynamics in solid-state and chemical systems for energy conversion*, in *Nanophotonics*. 2016. p. 96.
165. Baida, H., et al., *Quantitative Determination of the Size Dependence of Surface Plasmon Resonance Damping in Single Ag@SiO2 Nanoparticles*. Nano Letters, 2009. **9**(10): p. 3463-3469.
166. Novo, C., et al., *Contributions from radiation damping and surface scattering to the linewidth of the longitudinal plasmon band of gold nanorods: a single particle study*. Physical Chemistry Chemical Physics, 2006. **8**(30): p. 3540-3546.
167. Tanya, H., R.E. Stephen, and M. Sumeet, *Interaction of metallic nanoparticles with dielectric substrates: effect of optical constants*. Nanotechnology, 2013. **24**(3): p. 035201.
168. Hövel, H., et al., *Width of cluster plasmon resonances: Bulk dielectric functions and chemical interface damping*. Physical Review B, 1993. **48**(24): p. 18178-18188.
169. Klar, T., et al., *Surface-Plasmon Resonances in Single Metallic Nanoparticles*. Physical Review Letters, 1998. **80**(19): p. 4249-4252.

170. Hu, M., et al., *Dark-field microscopy studies of single metal nanoparticles: understanding the factors that influence the linewidth of the localized surface plasmon resonance*. Journal of Materials Chemistry, 2008. **18**(17): p. 1949-1960.
171. Hartland, G.V., et al., *What's so Hot about Electrons in Metal Nanoparticles?* ACS Energy Letters, 2017. **2**(7): p. 1641-1653.
172. Fowler, R.H., *The Analysis of Photoelectric Sensitivity Curves for Clean Metals at Various Temperatures*. Physical Review, 1931. **38**(1): p. 45-56.
173. Feng, J., et al., *Green manufacturing of metallic nanoparticles: a facile and universal approach to scaling up*. Journal of Materials Chemistry A, 2016. **4**(29): p. 11222-11227.
174. Valenti, M., et al., *The Role of Size and Dimerization of Decorating Plasmonic Silver Nanoparticles on the Photoelectrochemical Solar Water Splitting Performance of BiVO<sub>4</sub> Photoanodes*. ChemNanoMat, 2016. **2**(7): p. 739-747.
175. Mendes, M.J., et al., *Plasmonic light enhancement in the near-field of metallic nanospheroids for application in intermediate band solar cells*. Applied Physics Letters, 2009. **95**(7): p. 071105.
176. Lincic, S., et al., *Photochemical transformations on plasmonic metal nanoparticles*. Nat Mater, 2015. **14**(6): p. 567-576.
177. Chen, H.M., et al., *Plasmon Inducing Effects for Enhanced Photoelectrochemical Water Splitting: X-ray Absorption Approach to Electronic Structures*. Acs Nano, 2012. **6**(8): p. 7362-7372.
178. Mingce, L., et al., *Effect of gold nanoparticles on the photocatalytic and photoelectrochemical performance of Au modified BiVO<sub>4</sub>*. Nano-Micro Letters, 2011. **3**(3): p. 171-177.
179. Abdi, F.F., et al., *Plasmonic enhancement of the optical absorption and catalytic efficiency of BiVO<sub>4</sub> photoanodes decorated with Ag@SiO<sub>2</sub> core-shell nanoparticles*. Physical Chemistry Chemical Physics, 2014. **16**(29): p. 15272-15277.
180. Gao, H.W., et al., *Plasmon-Enhanced Photocatalytic Activity of Iron Oxide on Gold Nanopillars*. Acs Nano, 2012. **6**(1): p. 234-240.
181. Thimsen, E., et al., *Influence of Plasmonic Au Nanoparticles on the Photoactivity of Fe<sub>2</sub>O<sub>3</sub> Electrodes for Water Splitting*. Nano Letters, 2010. **11**: p. 35-43.
182. Valenti, M., et al., *Enhancement of the Photoelectrochemical Performance of CuWO<sub>4</sub> Thin Films for Solar Water Splitting by Plasmonic Nanoparticle Functionalization*. The Journal of Physical Chemistry C, 2015. **119**(4): p. 2096-2104.
183. Wang, T., et al., *Au nanoparticle sensitized ZnO nanopencil arrays for photoelectrochemical water splitting*. Nanoscale, 2015. **7**(1): p. 77-81.
184. Li, K., M.I. Stockman, and D.J. Bergman, *Self-Similar Chain of Metal Nanospheres as an Efficient Nanolens*. Physical Review Letters, 2003. **91**(22): p. 227402.

185. Marhaba, S., et al., *Surface Plasmon Resonance of Single Gold Nanodimers near the Conductive Contact Limit*. The Journal of Physical Chemistry C, 2009. **113**(11): p. 4349-4356.
186. Brown, L.V., et al., *Heterodimers: Plasmonic Properties of Mismatched Nanoparticle Pairs*. ACS Nano, 2010. **4**(2): p. 819-832.
187. Sheikholeslami, S., et al., *Coupling of Optical Resonances in a Compositionally Asymmetric Plasmonic Nanoparticle Dimer*. Nano Letters, 2010. **10**(7): p. 2655-2660.
188. Kadkhodazadeh, S., et al., *Coexistence of classical and quantum plasmonics in large plasmonic structures with subnanometer gaps*. Applied Physics Letters, 2013. **103**(8): p. 083103.
189. Koh, A.L., et al., *Electron Energy-Loss Spectroscopy (EELS) of Surface Plasmons in Single Silver Nanoparticles and Dimers: Influence of Beam Damage and Mapping of Dark Modes*. ACS Nano, 2009. **3**(10): p. 3015-3022.
190. Biskos, G., et al., *Generation and Sizing of Particles for Aerosol-Based Nanotechnology*. Kona Powder and Particle Journal, 2008. **26**: p. 13-35.
191. Schwyn, S., E. Garwin, and A. Schmidtott, *AEROSOL GENERATION BY SPARK DISCHARGE*. Journal of Aerosol Science, 1988. **19**(5): p. 639-642.
192. Lin, H.-Y., et al., *Direct near-field optical imaging of plasmonic resonances in metal nanoparticle pairs*. Optics Express, 2010. **18**(1): p. 165-172.
193. Anatoliy, P. and K. Uwe, *Interface decay channel of particle surface plasmon resonance*. New Journal of Physics, 2003. **5**(1): p. 151.
194. Liang, Y., C.S. Enache, and R. van de Krol, *Photoelectrochemical characterization of sprayed alpha-Fe(2)O(3) thin films: Influence of Si doping and SnO(2) interfacial layer*. International Journal of Photoenergy, 2008.
195. Kavan, L., et al., *Electrochemical and Photoelectrochemical Investigation of Single-Crystal Anatase*. Journal of the American Chemical Society, 1996. **118**: p. 6716-6723.
196. Kudo, A. and Y. Miseki, *Heterogeneous photocatalyst materials for water splitting*. Chemical Society Reviews, 2009. **38**: p. 253-278.
197. Dare-Edwards, M.P., et al., *Electrochemistry and photoelectrochemistry of iron(III) oxide*. Journal of the Chemical Society, Faraday Transactions 1: Physical Chemistry in Condensed Phases, 1983. **79**: p. 2027-2041.
198. Yourey, J.E. and B.M. Bartlett, *Electrochemical deposition and photoelectrochemistry of CuWO<sub>4</sub>, a promising photoanode for water oxidation*. Journal of Materials Chemistry, 2011. **21**: p. 7651-7660.
199. Chang, Y., et al., *Effect of Thermal Treatment on the Crystallographic, Surface Energetics, and Photoelectrochemical Properties of Reactively Cosputtered Copper Tungstate for Water Splitting*. The Journal of Physical Chemistry C, 2011. **115**: p. 25490-25495.

200. Varghese, O.K. and C.A. Grimes, *Appropriate strategies for determining the photoconversion efficiency of water photo electrolysis cells: A review with examples using titania nanotube array photoanodes*. Solar Energy Materials and Solar Cells, 2008. **92**: p. 374-384.
201. Gaillard, N., et al., *A nanocomposite photoelectrode made of 2.2 eV band gap copper tungstate (CuWO<sub>4</sub> and multi-wall carbon nanotubes for solar-assisted water splitting*. International Journal of Hydrogen Energy, 2013. **38**: p. 3166-3176.
202. Souza, F.L., et al., *The influence of the film thickness of nanostructured [small alpha]-Fe<sub>2</sub>O<sub>3</sub> on water photooxidation*. Physical Chemistry Chemical Physics, 2009. **11**: p. 1215-1219.
203. Pandey, P.K., N.S. Bhave, and R.B. Kharat, *Spray deposition process of polycrystalline thin films of CuWO<sub>4</sub> and study on its photovoltaic electrochemical properties*. Materials Letters, 2005. **59**: p. 3149-3155.
204. Yourey, J.E., J.B. Kurtz, and B.M. Bartlett, *Water Oxidation on a CuWO<sub>4</sub>-WO<sub>3</sub> Composite Electrode in the Presence of [Fe(CN)<sub>6</sub>]<sup>3-</sup>: Toward Solar Z-Scheme Water Splitting at Zero Bias*. The Journal of Physical Chemistry C, 2012. **116**: p. 3200-3205.
205. Yourey, J.E., et al., *Chemical Stability of CuWO<sub>4</sub> for Photoelectrochemical Water Oxidation*. The Journal of Physical Chemistry C, 2013. **117**: p. 8708-8718.
206. Ingram, D.B. and S. Linic, *Water Splitting on Composite Plasmonic-Metal/Semiconductor Photoelectrodes: Evidence for Selective Plasmon-Induced Formation of Charge Carriers near the Semiconductor Surface*. Journal of the American Chemical Society, 2011. **133**: p. 5202-5205.
207. Gomes Silva, C., et al., *Influence of Excitation Wavelength (UV or Visible Light) on the Photocatalytic Activity of Titania Containing Gold Nanoparticles for the Generation of Hydrogen or Oxygen from Water*. Journal of the American Chemical Society, 2010. **133**: p. 595-602.
208. Grabowska, E., et al., *Modification of Titanium(IV) Dioxide with Small Silver Nanoparticles: Application in Photocatalysis*. The Journal of Physical Chemistry C, 2013. **117**: p. 1955-1962.
209. Kamat, P.V., *Photophysical, Photochemical and Photocatalytic Aspects of Metal Nanoparticles*. The Journal of Physical Chemistry B, 2002. **106**: p. 7729-7744.
210. Schwyn, S., E. Garwin, and A. Schmidt-Ott, *Aerosol generation by spark discharge*. Journal of Aerosol Science, 1988. **19**: p. 639-642.
211. Hinds, W.C., *Chapter 15 Electrical Properties*, in *Aerosol Technology: Properties, Behavior, and Measurement of Airborne Particles*. 1999, John Wiley. p. 316-347.
212. Ritala, M. and J. Niinisto, *Chapter 4 Atomic Layer Deposition*, in *Chemical Vapour Deposition: Precursors*. 2009, The Royal Society of Chemistry. p. 158-206.
213. Didden, A.P., et al., *Fluidized-bed atomic layer deposition reactor for the synthesis of core-shell nanoparticles*. Review of Scientific Instruments, 2014. **85**.

214. Murphy, A.B., et al., *Efficiency of solar water splitting using semiconductor electrodes*. International Journal of Hydrogen Energy, 2006. **31**: p. 1999-2017.
215. Hu, S., et al., *Amorphous TiO<sub>2</sub> coatings stabilize Si, GaAs, and GaP photoanodes for efficient water oxidation*. Science, 2014. **344**: p. 1005-1009.
216. Yates Jr, J.T., *Photochemistry on TiO<sub>2</sub>: Mechanisms behind the surface chemistry*. Surface Science, 2009. **603**: p. 1605-1612.



## Invitation

to public defense of the  
doctoral thesis:

**Spark-Discharge as a  
Nanoparticle Source to Study  
Size-Dependent Plasmonic  
Properties for  
Photo-electrochemical  
Water Splitting**

On Monday June 4 at 12:30

Marco Valenti  
([m.valenti@tudelft.nl](mailto:m.valenti@tudelft.nl))

Paranymphs:  
Selma Causevic  
Caterina Valenti

